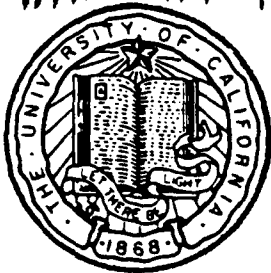


MMF FILE COPY



MARINE PHYSICAL LABORATORY

SCRIPPS INSTITUTION OF OCEANOGRAPHY

San Diego, California 92152

AD-A202 638

LOCALIZING AND BEAMFORMING FREELY-DRIFTING VLF ACOUSTIC SENSORS

Richard Lee Culver

DTIC
ELECTE
NOV 16 1988
S D
C7H

SIO REFERENCE 88-16

MPL-U-23/88

Approved for public release; distribution unlimited.

88 11 16 034

REPORT DOCUMENTATION PAGE

1a. REPORT SECURITY CLASSIFICATION UNCLASSIFIED			1b. RESTRICTIVE MARKINGS	
2a. SECURITY CLASSIFICATION AUTHORITY			3. DISTRIBUTION / AVAILABILITY OF REPORT Approved for public release; distribution unlimited.	
2b. DECLASSIFICATION / DOWNGRADING SCHEDULE				
4. PERFORMING ORGANIZATION REPORT NUMBER(S) SIO REFERENCE 88-16 [MPL-U-23/88]			5. MONITORING ORGANIZATION REPORT NUMBER(S)	
6a. NAME OF PERFORMING ORGANIZATION Marine Physical Laboratory		6b. OFFICE SYMBOL (If applicable) MPL		7a. NAME OF MONITORING ORGANIZATION Office of Naval Research Department of the Navy
6c. ADDRESS (City, State, and ZIP Code) University of California, San Diego Scripps Institution of Oceanography San Diego, CA 92152			7b. ADDRESS (City, State, and ZIP Code) 800 North Quincy Street Arlington, VA 22217-5000	
8a. NAME OF FUNDING / SPONSORING ORGANIZATION Office of Naval Research		8b. OFFICE SYMBOL (If applicable) ONR		9. PROCUREMENT INSTRUMENT IDENTIFICATION NUMBER N00014-82-K-0147; N00014-87-K-0010
8c. ADDRESS (City, State, and ZIP Code) Department of the Navy 800 North Quincy Street Arlington, VA 22217-5000			10. SOURCE OF FUNDING NUMBERS PROGRAM ELEMENT NO. PROJECT NO. TASK NO. WORK UNIT ACCESSION NO.	
11. TITLE (Include Security Classification) LOCALIZING AND BEAMFORMING FREELY-DRIFTING VLF ACOUSTIC SENSORS				
12. PERSONAL AUTHOR(S) Richard Lee Culver				
13a. TYPE OF REPORT Thesis		13b. TIME COVERED FROM TO		14. DATE OF REPORT (Year, Month, Day) September 1988
15. PAGE COUNT 149 pgs				
16. SUPPLEMENTARY NOTATION				
17. COSATI CODES FIELD GROUP SUB-GROUP			18. SUBJECT TERMS (Continue on reverse if necessary and identify by block number) Swallow floats, ambient ocean noise, Kalman tracking filter	
19. ABSTRACT (Continue on reverse if necessary and identify by block number) Self-contained, freely-drifting Swallow floats capable of recording ambient ocean noise in the 1 to 25 Hz band have been designed, built and deployed by the Marine Physical Laboratory, Scripps Institution of Oceanography, University of California, San Diego, California. The buoys are ballasted to neutral buoyancy at midwater depth where they record the components of particle velocity from which sound pressure levels may be derived. Float positions are estimated using an 8 kHz acoustic ranging system and a Kalman tracking filter. Individual float times series are then combined to obtain passive, directional acoustic measurements from 1 to 25 Hz which are not contaminated by flow noise or tether strumming. The float localization and beamforming techniques are illustrated using measurements from a September 1986 Swallow float experiment conducted approximately 50 miles west of San Diego, California. A distant target of opportunity (apparently a surface ship) provides six spectral lines between 9 and 22.5 Hz which are tracked for about 90 minutes. The complex bathymetry of the experiment site complicates signal propagation, but the signal level in the beamformer output indicates that the element time series are being properly combined. (CRH) 41				
20. DISTRIBUTION / AVAILABILITY OF ABSTRACT <input type="checkbox"/> UNCLASSIFIED / UNLIMITED <input checked="" type="checkbox"/> SAME AS RPT. <input type="checkbox"/> DTIC USERS			21. ABSTRACT SECURITY CLASSIFICATION UNCLASSIFIED	
22a. NAME OF RESPONSIBLE INDIVIDUAL William S. Hodgkiss			22b. TELEPHONE (Include Area Code) (619) 534-1798	
			22c. OFFICE SYMBOL MPL	

**UNIVERSITY OF CALIFORNIA
SAN DIEGO**

Localizing and Beamforming Freely-Drifting VLF Acoustic Sensors

*A dissertation submitted in partial satisfaction of the
requirements for the degree Doctor of Philosophy
in Electrical Engineering (Applied Ocean Science)*

by

Richard Lee Culver

Supported by
the Office of Naval Research
Contract N00014-82-K-0147 and
N00014-87-K-0010

SIO REFERENCE 88-16

MPL-U-23/88

September 1988

Table of Contents

	Page
Abstract	ix
Acknowledgements	x
1. Introduction	1
2. Swallow Float System Description	1
3. September 1986 Experiment	3
3.1 Experiment Summary	3
3.2 Acoustic Range Data	6
3.3 AGC Level and Float Heading	6
3.4 Geophone Data	12
3.5 Sound Speed Profile	14
4. Swallow Float Localization	17
4.1 Theoretical Development and Simulation Results	17
4.1.1 Summary of Previous Results	21
4.1.2 Obtaining Good Initial Position and Velocity Estimates	22
4.1.3 Relationship Between Actual and Predicted Error and the Innovation Sequence	24
4.1.4 Effect of Sound Speed Errors on Location Error	28
4.2 Application to Experimental Data	30
5. Beamforming With the Swallow Float Array	32
5.1 Theoretical Development and Simulation Results	35
5.1.1 Single Element Arrays	35
5.1.2 Multi-Element Arrays	39
5.1.3 Sparse Multi-Element Arrays	41
5.1.4 Three-Dimensional Beamforming	41
5.1.5 Swallow Float Array	51
5.2 Application to Experimental Data	51
5.2.1 Processing the Time Series	51
5.2.2 Horizontal Bearing Levels	62
5.2.3 Enhancing Bearing Levels	62
5.2.4 Three-Dimensional Bearing Levels	72
5.2.5 Beamformer Gain	72
5.2.6 Correlating Geophone Signals	77
6. Analysis and Conclusions	80
References	84
Appendix A AGC Corrected Geophone Time Series	87
Appendix B Geophone Power Spectra	93
Appendix C Comparison of Kalman and Least Squares Filters for Locating Autonomous Very Low Frequency Acoustic Sensors	99
Appendix D Three-Dimensional Beamforming Results	127
Appendix E Geophone Cross-Correlation Results	137

List of Figures

	Page
Chapter 2.	
2.1 Swallow float hardware	2
Chapter 3.	
3.1 Location of the September 1986 experiment	4
3.2 Bathymetry of the September 1986 experiment site	5
3.3 Approximate float deployment and recovery positions	7
3.4 Range pulses transmitted by float 10 and received by float 10	8
3.5 Range pulses transmitted by float 3 and received by float 0	9
3.6 Range pulses transmitted by float 2 and received by float 0	10
3.7 Battery voltage, AGC level and heading of float 3.....	11
3.8 RMS geophone power for float 5	13
3.9 Exact frequency of spectral lines	15
3.10 Spectral level of the line near 9 Hz	17
3.11 Magnitude of the vertical arrival angles	18
3.12 Sound speed profile for the September 1986 experiment	20
Chapter 4.	
4.1 Coordinate system for the Swallow float localization	23
4.2 Predicted and actual rms error in the least squared filter results	25
4.3 Mean magnitude of the innovation, predicted and actual rms error, Cases 1 and 2	26
4.4 Mean magnitude of the innovation, predicted and actual rms error, Cases 6 and 7	27
4.5 Plan view of the localizaton coordinate system	30
4.6 Results of the Kalman and least squares filter, Case 11 and experiment data	31
4.7 Swallow float positions, September 1986 experiment	33
4.8 Swallow float positions, September 1986 experiment	34
Chapter 5.	
5.1 Coordinate system used for the beamforming	36
5.2 Single geophone geometry	37
5.3 Collocated geophone pair geometry	38
5.4 Multi-element array geometry	39
5.5 Comparison of magnitude bearing response, $d = 100$ m, $\theta_s = 0^\circ$	40
5.6 Comparison of magnitude bearing response, $d = 100$ m, $\theta_s = 60^\circ$	42
5.7 Comparison of magnitude bearing response, $d = 350$ m, $\theta_s = 0^\circ$	43
5.8 Comparison of magnitude bearing response, $d = 350$ m, $\theta_s = 60^\circ$	44
5.9 Omni-directional element bearing response, $d = 100$ m, $\theta_s = 0^\circ$, $\phi_s = 0^\circ$	47
5.10 Geophone bearing response, $d = 100$ m, $\theta_s = 0^\circ$, $\phi_s = 0^\circ$	48
5.11 Omni-directional element bearing response, $d = 100$ m, $\theta_s = 60^\circ$, $\phi_s = 0^\circ$	49
5.12 Geophone bearing response, $d = 100$ m, $\theta_s = 60^\circ$, $\phi_s = 0^\circ$	50
5.13 Omni-directional element bearing response, $d = 350$ m, $\theta_s = 60^\circ$, $\phi_s = 20^\circ$	52
5.14 Geophone bearing response, $d = 350$ m, $\theta_s = 60^\circ$, $\phi_s = 20^\circ$	53
5.15 Geophone bearing response, record 1830, $\theta_s = 0^\circ$, $\phi_s = 0^\circ$	54
5.16 Geophone bearing response, record 1830, $\theta_s = 60^\circ$, $\phi_s = -10^\circ$	55
5.17 Plan view of beamforming coordinate system	57
5.18 Comparison of time bases	59

5.19	Spectral level versus azimuthal bearing	63
5.20	Average spectral level versus azimuthal bearing	67
5.21	Product of spectral levels versus azimuthal bearing	71
5.22	Horizontal beamforming results	73
5.23	Highest bearing levels and incoherent sum	78
Chapter 6.		
6.1	Simulated bearing response with shading error	81
6.2	Simulated bearing response with position and shading error	82
Appendix C		
1	Swallow float hardware	119
2	Range pulses transmitted by float 5 and received by float 4	120
3	Edge detector output of range pulses shown in Figure 2	121
4	Processing Swallow float travel time measurements	122
5	Simulating Swallow float travel time measurements	123
6	Swallow float localization simulations	124
7	Effect of process and measurement noise on filter performance	125
8	Effect of deployment geometry on filter performance	125

List of Tables

		Page
Chapter 3.		
3.1	Deployment depths	12
Chapter 4.		
4.1	Float location simulations	22



Accession For	
NTIS GRA&I	<input checked="" type="checkbox"/>
DTIC TAB	<input type="checkbox"/>
Unannounced	<input type="checkbox"/>
Justification	
By	
Distribution/	
Availability Codes	
Dist	Avail and/or Special
A-1	

ABSTRACT OF THE DISSERTATION

Localizing and Beamforming Freely-Drifting VLF Acoustic Sensors

by

Richard Lee Culver

**Doctor of Philosophy in Electrical Engineering
(Applied Ocean Science)**

University of California, San Diego, 1988

Dr. William S. Hodgkiss, Chairman

Self-contained, freely-drifting Swallow floats capable of recording ambient ocean noise in the 1 to 25 Hz band have been designed, built and deployed by the Marine Physical Laboratory, Scripps Institution of Oceanography, University of California, San Diego, California. The buoys are ballasted to neutral buoyancy at midwater depth where they record the components of particle velocity from which sound pressure levels may be derived. Float positions are estimated using an 8 kHz acoustic ranging system and a Kalman tracking filter. Individual float times series are then combined to obtain passive, directional acoustic measurements from 1 to 25 Hz which are not contaminated by flow noise or tether strumming.

The float localization and beamforming techniques are illustrated using measurements from a September 1986 Swallow float experiment conducted approximately 50 miles west of San Diego, California. A distant target of opportunity (apparently a surface ship) provides six spectral lines between 9 and 22.5 Hz which are tracked for about 90 minutes. The complex bathymetry of the experiment site complicates signal propagation, but the signal level in the beamformer output indicates that the element time series are being properly combined.

Acknowledgements

This work was funded by the Office of Naval Research, Code 122, under contract N00014-82-K-0147, and Code 1125OA, under contract N00014-87-K-0010. The knowledgeable and patient assistance of Dr. Bill Hodgkiss, my committee chairman, was an essential and principle support to this work, and is sincerely appreciated. My mother and father taught me persistence and much more. My lovely wife [REDACTED] gave me her whole-hearted support and encouragement from start to finish. She is my best friend and partner. My brother set a stiff pace which I am endeavoring to match.

Messrs. George Coleman and Cliff Skinner of Integrated Systems Analysts, Inc. encouraged me to pursue my doctorate. They, along with Mr. Lloyd Maudlin and the president of ISA, Mr. Mike Gooden, encouraged me continuously along the way. I look forward to continued association with them all.

The very competent John McInerney made our computer environment a reliable, productive and friendly place to work. Greg Edmonds designed most of the Swallow float hardware and Marv Darling fabricated the floats. The success of our experiments is evidence of their expertise.

My student friends at Scripps, Gerald D'Spain, Barb Sotirin, Jean-Marie Tran, Phil Hammer, and Dr. Chris de Moustier, have contributed significantly to my education. In particular, Dr. Rick Brienzo has set a professional standard and been a personal friend.

Good friends R. Ben McCloud and Rev. Burt Smith never doubted my ability and never let me sell myself short. I am indebted to my Bible study brothers for nourishment and inspiration. No man has ever had better friends.

1. Introduction

Under Office of Naval Research sponsorship, the Marine Physical Laboratory has designed, built and deployed a set of 12 acoustic sensors which are neutrally buoyant and drift freely when deployed in the ocean. The sensors are called *Swallow floats* after J. C. Swallow who used freely-drifted floats to measure deep ocean currents.¹ The MPL Swallow floats also drift freely, but are used to measure acoustic energy in the very low frequency (VLF) band, which is generally defined as 1 to 20 Hz.

The Swallow floats are designed to operate without tethers so that their measurements are not contaminated by tether strumming noise and so that they drift with the ocean current and are not subject to flow noise. Each float possesses an 8 kHz acoustic transducer for measuring interfloat and float-to-surface travel times. The travel times may be used to estimate time-varying, relative float positions. Several floats deployed in the same general area form a freely-drifting, randomly-spaced array whose acoustic measurements may be combined, or *beamformed*.

The MPL Swallow floats have been deployed several times annually since 1982 as part of the system development process. In terms of analyzing and interpreting Swallow float measurements, single float measurements of ambient ocean noise have been shown to be consistent with other, similar measurements found in the literature.² This thesis describes how float positions are estimated from interfloat travel time measurements, and demonstrates the correct way to beamform signals from the directional geophones. The localization and beamforming procedures are illustrated using measurements from a September 1986 Swallow float experiment conducted approximately 50 miles west of San Diego, California.

2. Swallow Float System Description

A number of articles have been published to date providing details of the Swallow float hardware and operation.³⁻¹⁵ Reference [6] is probably the most complete system description. The intent here is to provide sufficient detail to enable the reader to understand the results which follow.

As illustrated in Figure 2.1, the Swallow float system consists of a 17 inch (0.432 meter) diameter, 9/16 inch (14.3 mm) thick glass sphere which contains

- 3 orthogonally-oriented velocity sensors, known as *geophones*;
- a control processor unit and electronic circuitry to condition, sample and record the geophone signal, and to control other float activities such as ballast release;
- a compass which measures the direction of the y axis geophone relative to magnetic north;
- a solid state memory buffer and a digital cartridge tape recorder;
- a battery pack power supply.

External to the sphere are

- an 8 kHz acoustic transducer for transmitting and receiving ranging signals;
- an optical flasher and a radio beacon used to locate the float when it is on the surface;

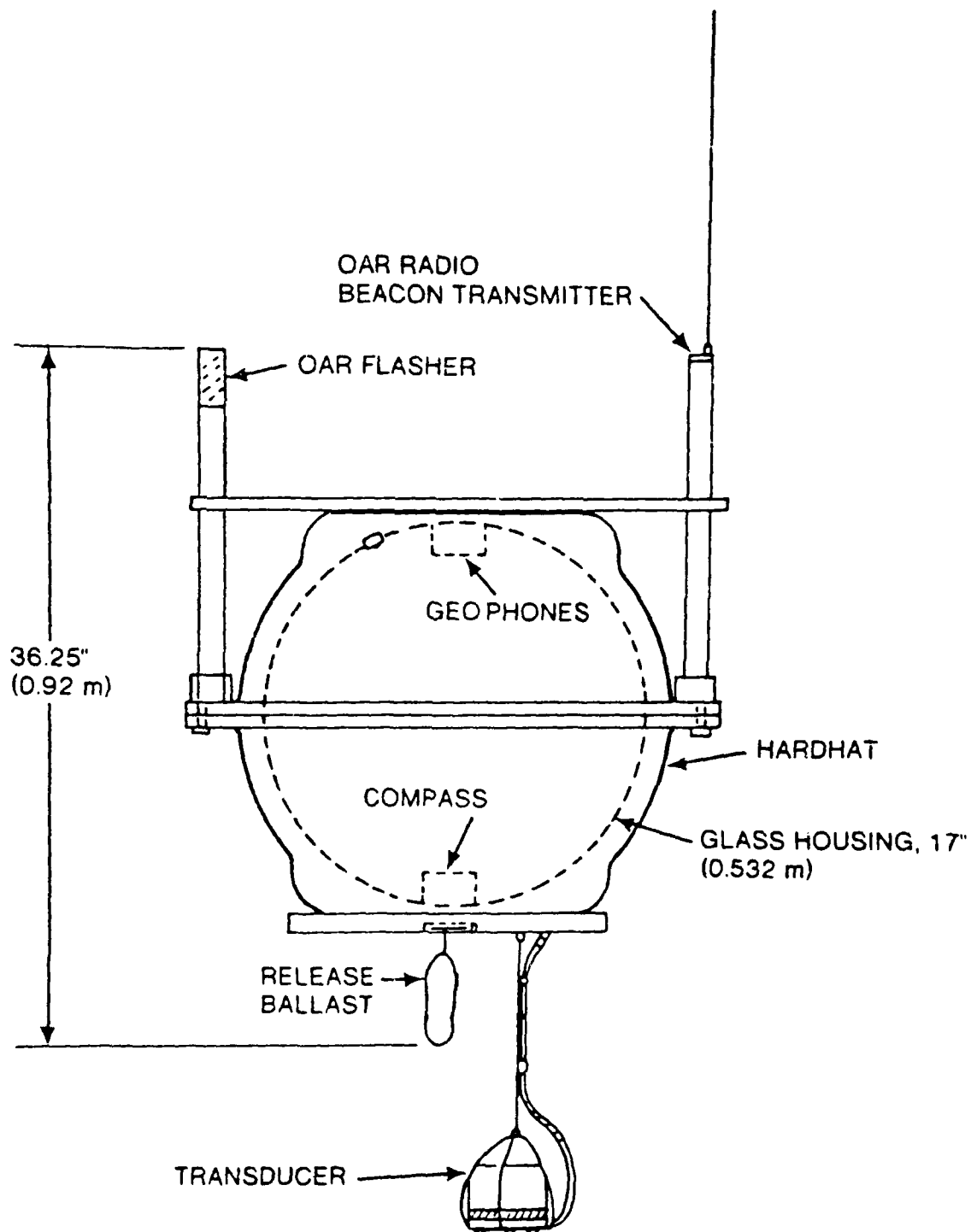


Figure 2.1 Swallow float hardware

- expendable ballast and a ballast release mechanism;
- a plastic *hardhat* which protects the glass sphere.

In operation the floats are lowered into the water from the deck of a ship after which they sink to a preset depth and operate autonomously. They are ballasted to neutral buoyancy at a particular depth, or in some cases, to sink to the ocean bottom. Recent experiments have utilized 3 floats positioned on the ocean bottom to provide a stationary coordinate system within which the remaining floats can be localized. Upon command from the surface, or failing to receive that command, according to a preset timer, the floats release a portion of their ballast and ascend to the surface.

While deployed, each float samples and internally records signals from the 3 geophones, the compass, and the 8 kHz range pulse detection circuit. The floats divide time into 45 second records consisting of 44 seconds during which data are sampled and stored in the buffer and 1 second during which the buffer contents are written to tape. No geophone data are sampled during the 1 second buffer dump. Appendix 1 of Reference [13] contains a detailed description of the conditioning applied to the geophone signal. Briefly, the geophones produce a signal proportional to their velocity, which is then amplified, low-pass filtered, and sampled at 50 Hz. Float data storage capacity is limited to 17 Mbytes, which corresponds to about 25 hours of operation.

Once a float has surfaced and been retrieved, its data tape is extracted and read. The 8 kHz acoustic pulse arrival times provide interfloat and float-to-surface travel time measurements which may be used to determine the float positions. Geophone signals provide float velocity measurements from which acoustic pressure may be estimated. Float compass heading measurements are made because the geophones are directional sensors and we must know the direction in which they were pointed when the measurements were made.

3. September 1986 Experiment

Data presented in this thesis were acquired between 16 and 19 September 1986, approximately 50 miles west of San Diego, California and approximately 20 miles southeast of San Clemente Island ($32^{\circ}35'N$, $118^{\circ}10'W$). Figure 3.1 shows the location of the deployment site. A detailed look at individual float data from this experiment is contained in Reference [9]. This Chapter contains a summary of [9] and some additional information necessary to localize the floats and beamform their outputs.

3.1. Experiment Summary

The experiment began on Tuesday, 16 September 1986, when 6 MPL personnel with 12 Swallow floats sailed from the University of California's Nimitz Marine Facility in San Diego aboard the 110' chartered vessel *Scorpius*. The experiment site was the northwest corner of San Clemente Basin, where the water depth is about 1000 fathoms (about 2000 meters). Three of the floats (0, 1, and 2) were ballasted to descend to the ocean bottom. The remainder were ballasted for neutral buoyancy at 1000 meters depth. The experiment was scheduled to begin on the morning of 17 September and to last about 24 hours. Inside each buoy, the backup ballast release timers had been set to release on 19 September.

Figure 3.2 shows the bottom elevation contours in the vicinity of the experiment site. San Clemente Basin is bounded to the east by a series of underwater cliffs which lead up to very

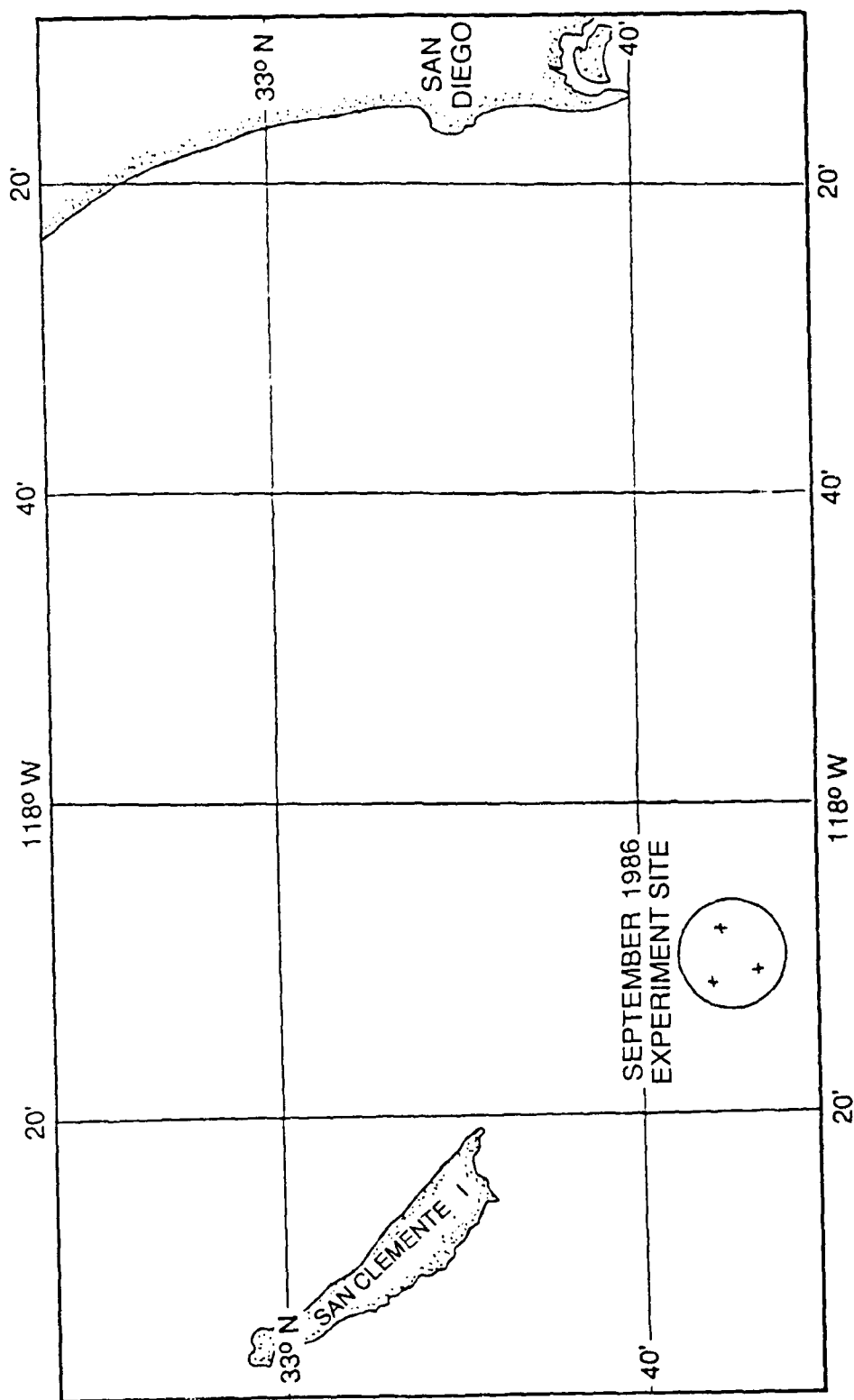


FIGURE 3.1 Location of the September 1986 experiment

shallow water, less than 100 meters deep in some places. The Basin is bounded to the north by upward sloping ground which rises to San Clemente Island. To the west and south, the bottom slopes upward more gradually.

The *Scorpius* arrived on station early on the 17th. The floats were checked out and found to be operating satisfactorily. They were initialized synchronously at 0515, and by 1000 all 12 floats had been deployed. Floats 6, 7, 8 and 11 encountered problems and had to be dropped from the experiment. Figure 3.3 (taken from Figure I.3 of [9]) shows where the floats were put in the water and later recovered.

Scorpius remained in the general vicinity of the experiment site throughout the day on the 17th, and in the evening sailed to San Clemente Island, where she was anchored for the night. The ship got underway again at 0400 on the 18th and arrived at the experiment site at about 0630. The day was spent recalling and recovering floats one at a time. By 1600 the last float was aboard and the ship sailed for San Diego.

3.2. Acoustic Range Data

Acoustic range pulses transmitted by a float are reflected by the surface and received by that same float. Figure 3.4, taken from Figure III.12 of [9], shows float 10's surface echoes. The vertical axis has been scaled from round trip travel time to depth using one-half the sound speed, approximately 750 meters/second. The horizontal axis is elapsed deployment time. The echoes from the surface descend gradually from the left and level off at about 1000 meters depth. The echoes from the ocean bottom rise from the left and obscure the surface bounce pulse arrival between records 1000 and 1150. This establishes record 1150 as the first record where we can begin to localize the floats. Table 3.1 shows the depths to which the floats deployed based upon their surface echo data.

Figure 3.5, taken from Figure IV.1c of [9], shows float 0's record of pulses received from float 3 (freely-drifting float to bottomed float). The short dashes extending across the page are the direct path pulse (10 msec, or 150 meters long) and the longer dashes are the surface bounce arrivals. Scattering by the rough sea surface is thought to be responsible for the extended duration of the surface bounce arrivals. The direct and surface bounce arrivals come together quickly beginning about record 1900, marking float 3's ballast release and ascent to the surface and also indicating the end of the period during which we may localize the floats.

Direct path acoustic range pulses are clearly visible between all pairs of floats except between the bottomed floats. The upward refracting sound speed gradient apparently caused severe attenuation of direct path transmission between the bottomed floats. However, the surface bounce path is clearly visible for these floats. Figure 3.6, taken from Figure IV.1b of [9], shows the arrival of pulses transmitted by float 2, reflected by the surface, and received by float 0.

Distinct pulse arrival times are seen for all pairs of floats and the surface echoes between records 1150 and 1870. The positions of the floats during this interval will be estimated in Chapter 4.

3.3. AGC Level and Float Heading

Reference [9] contains plots of automatic gain control (AGC) level and float compass heading for each float during the deployment. One such plot, for float 3, is presented in Figure 3.7. The AGC indicates the amount of gain applied to the geophone signals. It is programmed to increase as signal decreases, and vice versa, in order to optimize the dynamic range of the analog to digital converter (ADC). The AGC level is thus inversely proportional to, and a rough measure of, geophone signal level. In Figure 3.7, the AGC level is zero during the float's descent because of the descent motion, and higher thereafter once the float's depth becomes stable. The drop in AGC level between records 1400 and 1600 was caused by high level signals received from a passing ship.

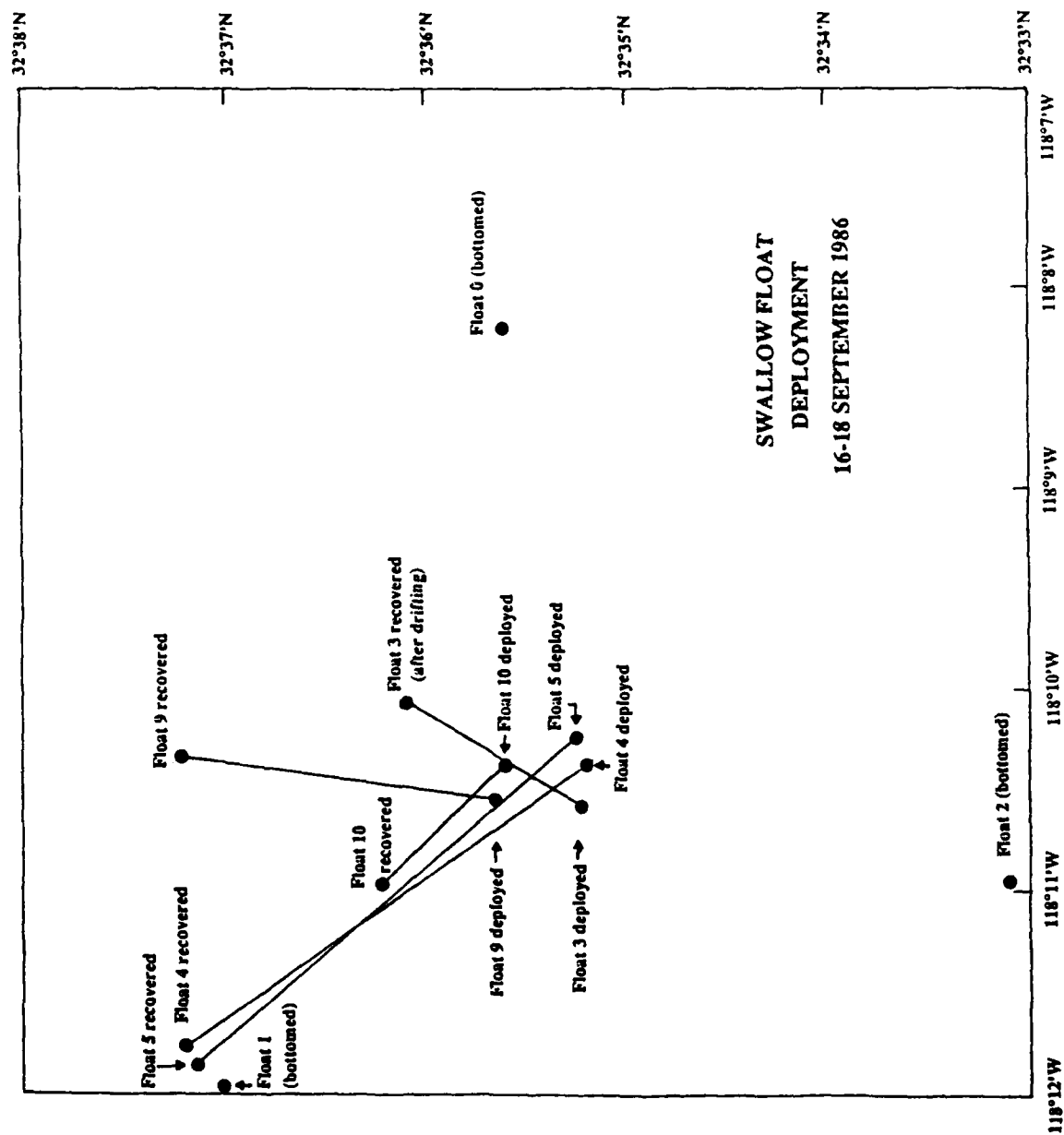


Figure 3.3 Approximate float deployment and recovery positions

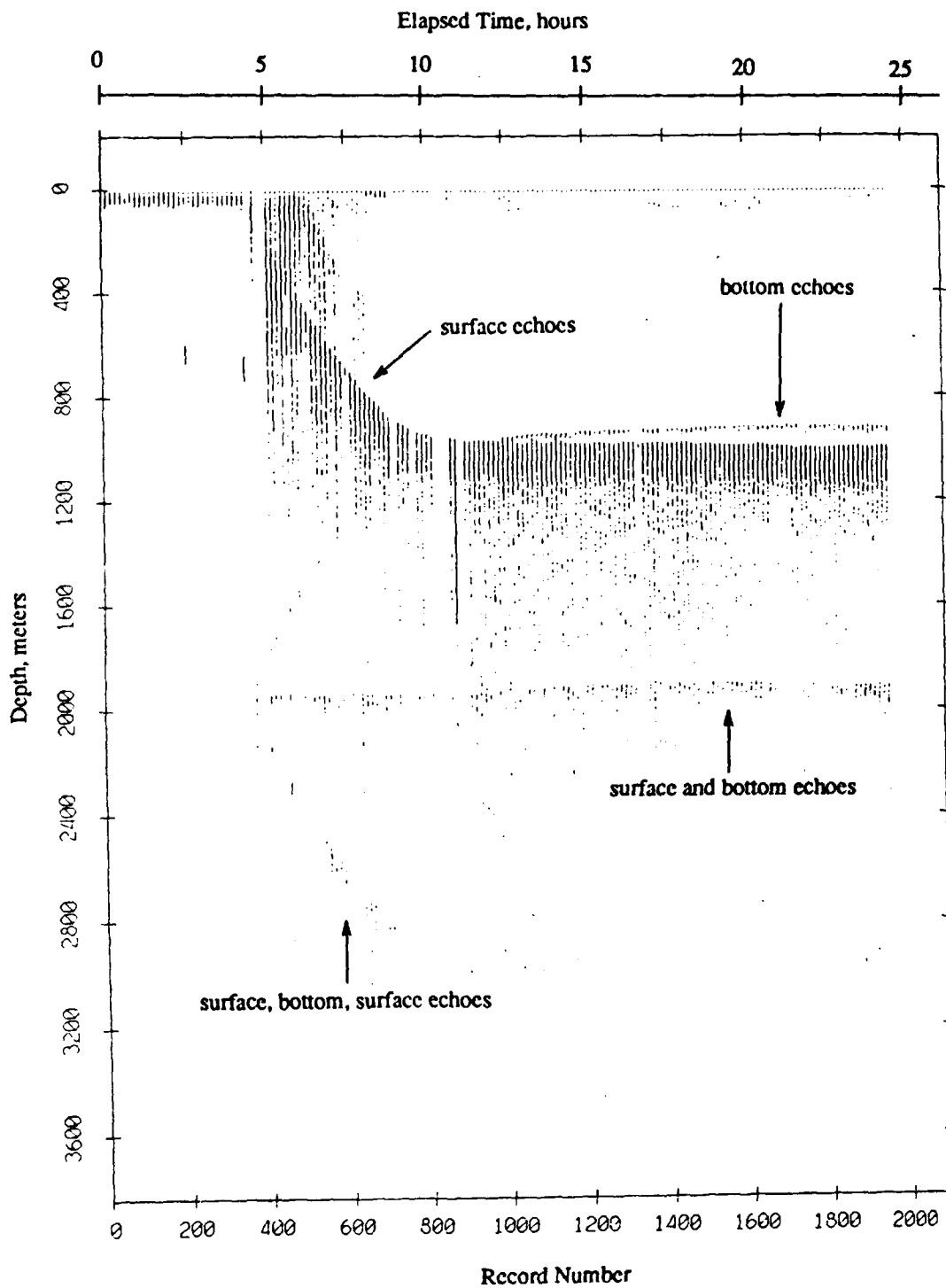


Figure 3.4 8 kHz acoustic range pulses transmitted by float 10 (freely-drifting), reflected by the ocean surface, and received by float 10

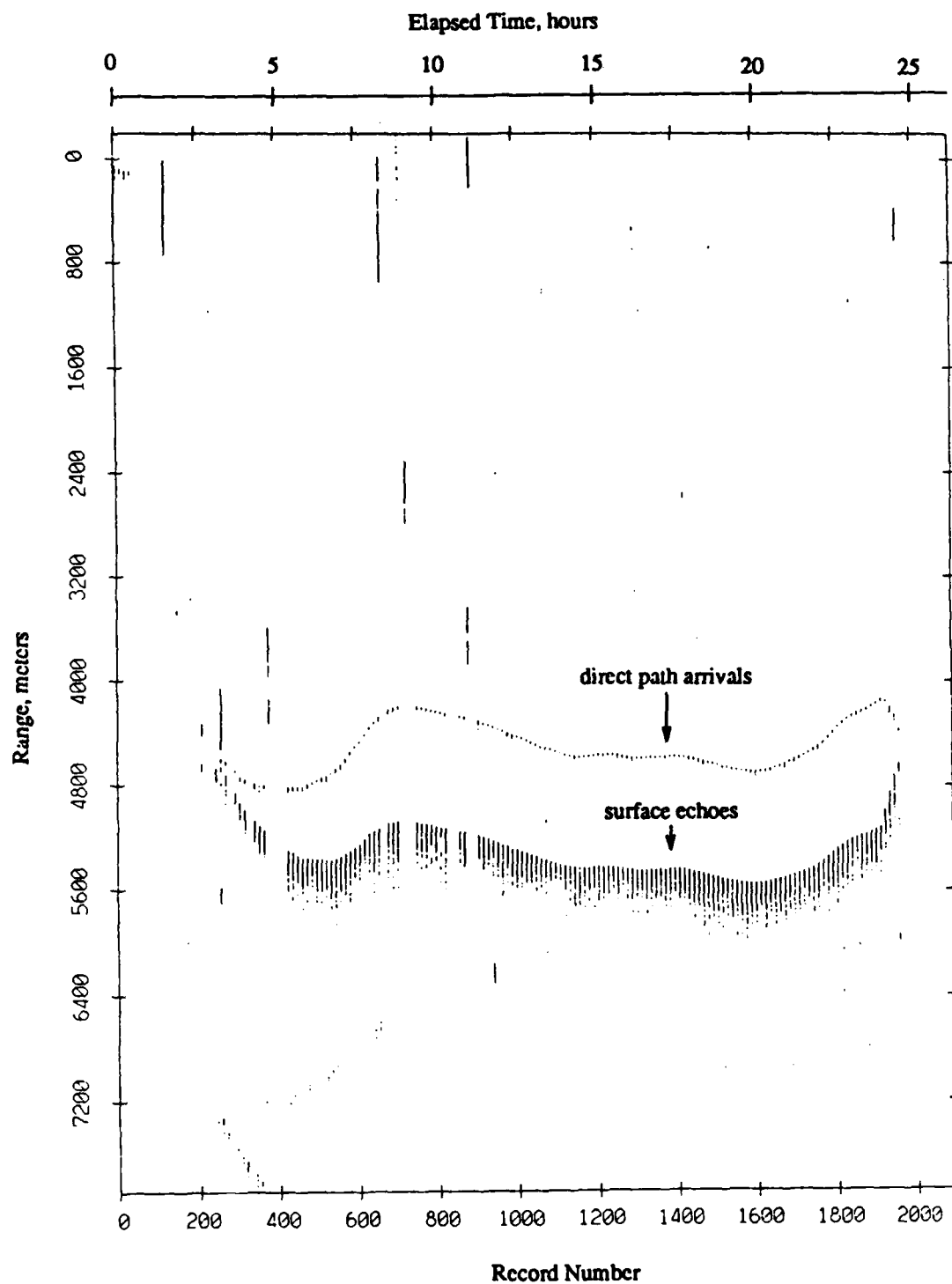


Figure 3.5 8 kHz acoustic range pulses received by float 0 (on the bottom) from float 3 (freely-drifting)

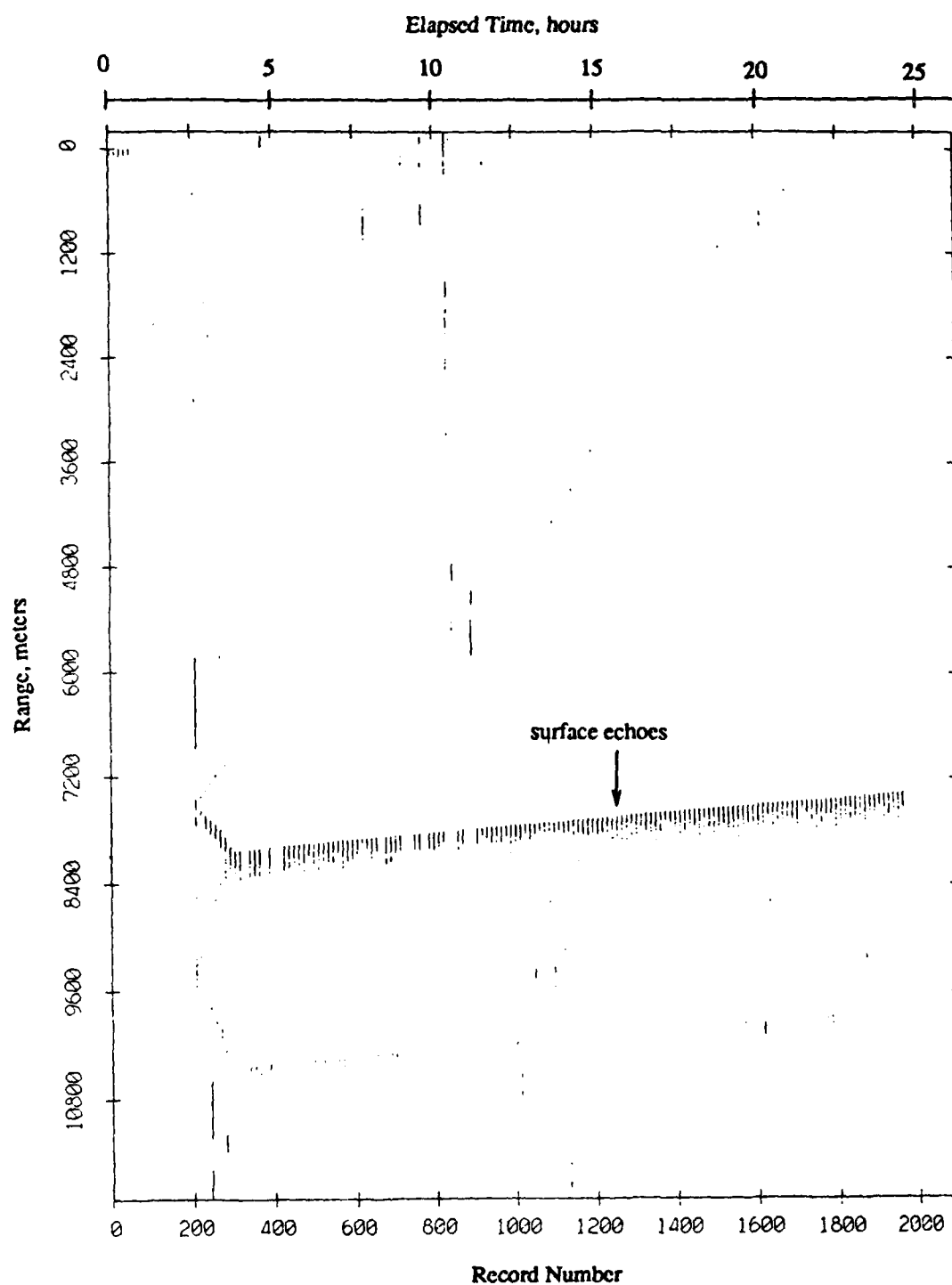


Figure 3.6 8 kHz acoustic range pulses transmitted by float 2 (on the bottom), reflected by the ocean surface, and received by float 0 (also on the bottom)

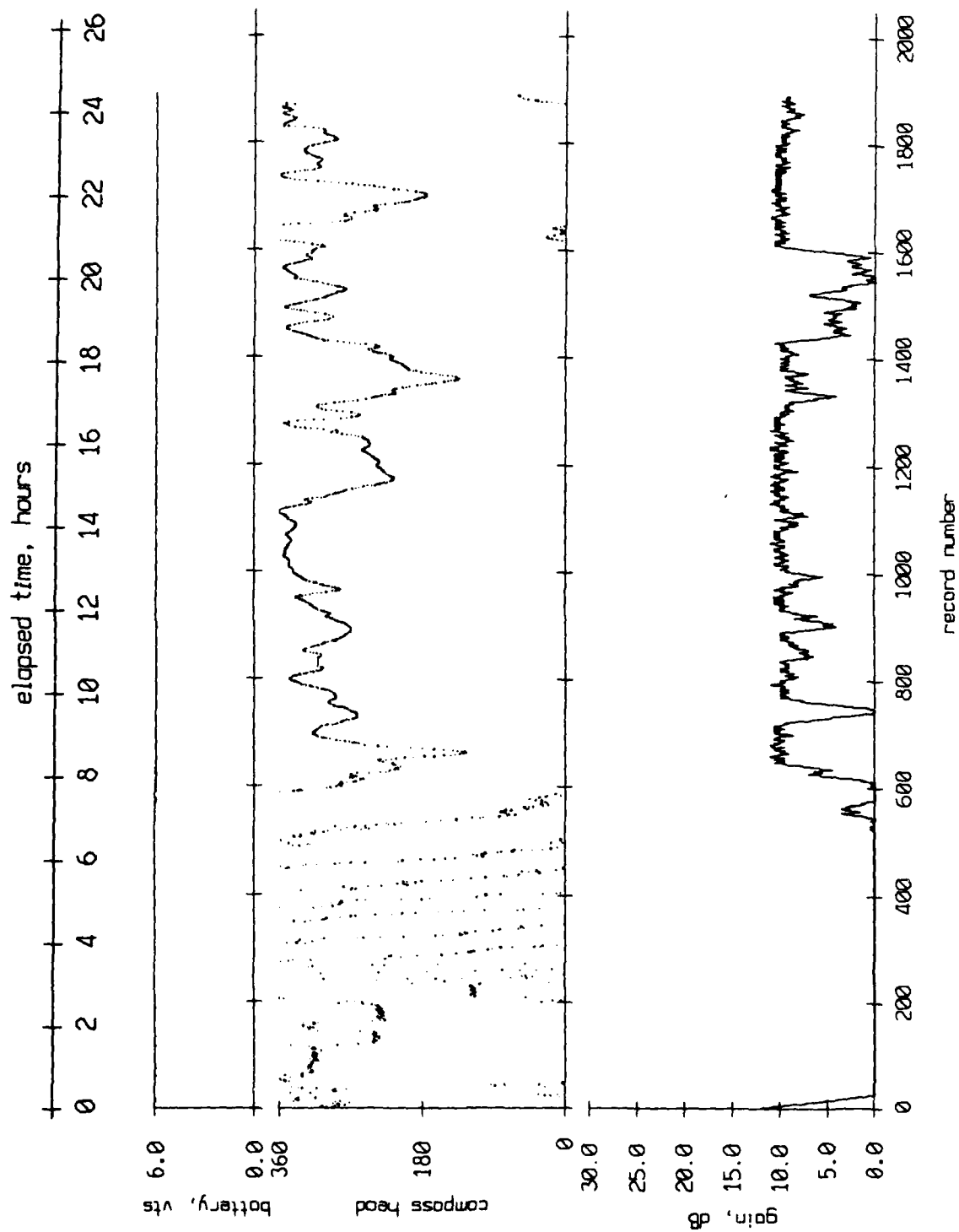


Figure 3.7 Battery voltage, AGC level and heading of float 3 during the September 1986 experiment

Table 3.1: Deployment Depths

Float	Depth, meters	
0	2010	(bottom)
1	1820	(bottom)
2	1900	(bottom)
3	960	
4	1040	
5	1060	
9	800	
10	990	

Float compass heading is the direction of the y axis geophone, measured clockwise from magnetic north. The compass heading trace in Figure 3.7 shows that float 3 was on the deck of the ship until about record 200, that it rotated as it descended between records 200 and 750, and that its depth (and to a large degree, its heading) stabilized after about record 750.

3.4. Geophone Data

As a first step in evaluating Swallow float geophone data, the rms power in 5 second segments is computed. The resulting power series, which are shown in [9], show gross signal characteristics. One such plot, for records 1750 through 1980 from float 5, is shown in Figure 3.8. The power series showed that three of the floats (0, 2 and 4) had connector problems which grounded one geophone channel. This was not a problem in the case of floats 0 and 2, since they were tethered to the bottom and their geophone signals are almost entirely clipped due to motion from tether strumming. For float 4, however, it meant that the float could not be used in the beamforming.

A problem discussed in [9] is the presence of strong oscillatory signals at the start of each record which decay exponentially. These signals are attributed to mechanical oscillation of the float, apparently excited by the internal tape recorder when it cycles on and off between records. They can cause velocity data to be clipped for up to 8 seconds at the beginning of the record, obscuring the ambient ocean noise signal and reducing the dynamic range with which the ambient ocean noise is measured during the remainder of the record.

Since the September 1986 deployment, the Swallow floats have been modified to eliminate or greatly attenuate mechanical vibrations. It was also desirable to remove these signals from the 1986 data set to permit its further use. Reference [10] derives a method of removing or significantly reducing resonant oscillation present in data, which may be applied if certain conditions are met. The method is shown to be effective on the 1986 deployment data set and was applied to data from floats 3, 9, and 10 before continuing with the analysis.

A related problem, which is addressed separately in Reference [11], is resonant float oscillation at frequencies below 0.6 Hz. Oscillation at these frequencies appears to consist of an irregular rocking or wobble which is strongly excited as the floats descend, weakly but consistently excited by the tape recorder at the start of each record, and occasionally excited by the receipt of strong acoustic pulses. We are not directly concerned with this problem here because it is below the band of immediate interest.

The focus of the beamforming in Chapter 5 will be on records 1760 through 1870, which is the last 110 records, or 82.5 minutes, of the period during which the float positions will be estimated in Chapter 4. This portion of the data record was chosen with the hope of seeing propulsion tonals from *Scorpius* as she steamed down from San Clemente Island early on the morning of 18 September. Since both engines were running at 1750 rpm and the reduction gear

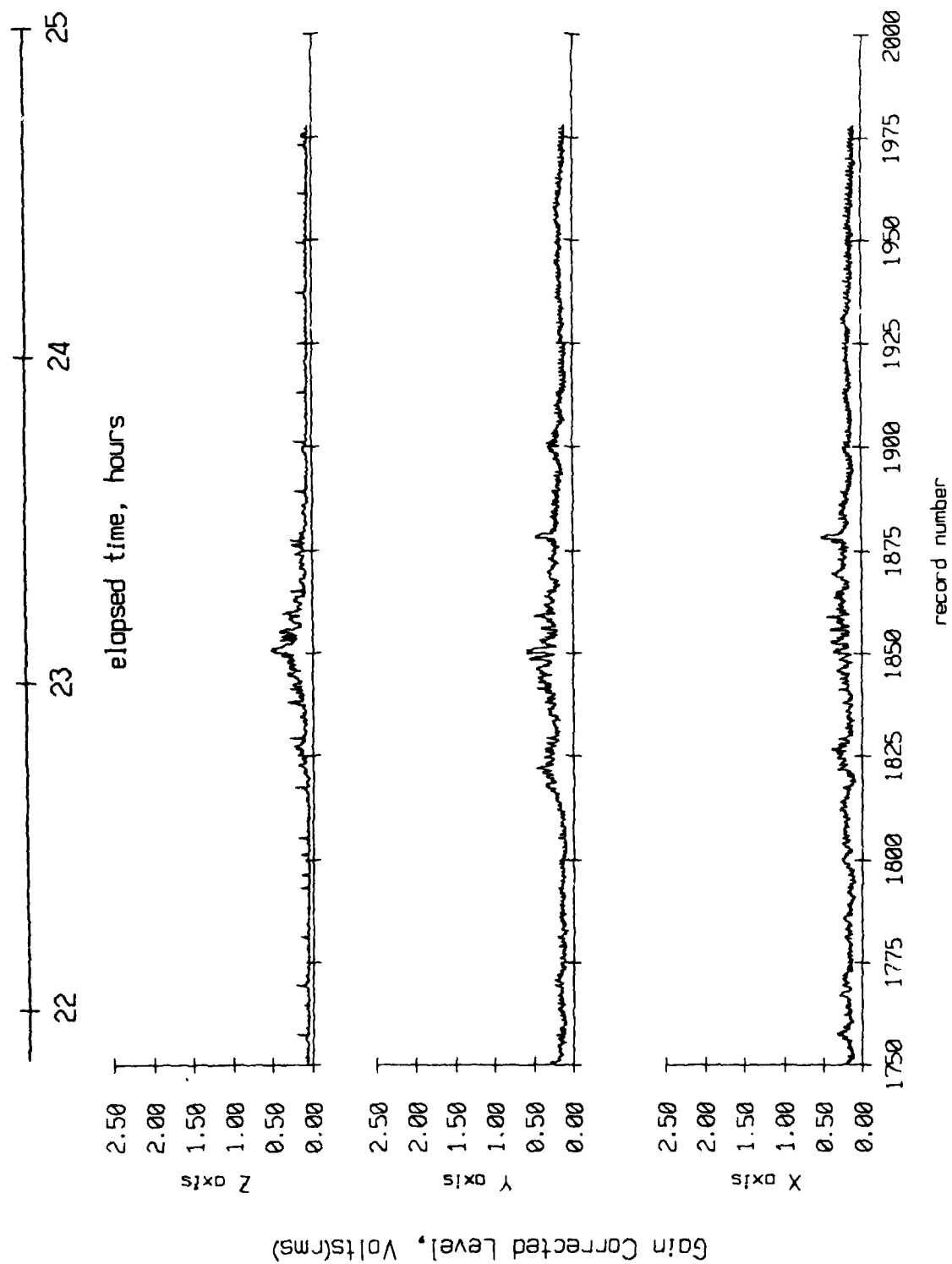


Figure 3.8 RMS geophone power for float 5 during a portion of the September 1986 experiment

ratio is known to be 3.8:1, the shaft rate may be expected to be

$$f_{\text{shaft rate}} = (1750 \text{ engine rev./min.}) \cdot \left(\frac{1}{3.8 \text{ engine rev./shaft rev.}} \right) \cdot \left(\frac{1 \text{ min.}}{60 \text{ sec}} \right) = 7.67 \text{ Hz} \quad (3.1)$$

The propeller has 4 blades so that the blade pass rate is 30.7 Hz, which is out of band.

Appendix A contains plots of some of the time series from the selected period and Appendix B contains the corresponding spectra. Data from floats 3, 9 and 10 have been processed as described in Reference [10] to remove resonant mechanical oscillation signals excited by the tape recorder turning on and off. A 2048 point (40.96 second) FFT was used in Appendix B, and data were windowed with a Kaiser-Bessel window ($\alpha \approx 2.5$). Only positive frequencies are shown. Reference [2] discussed calibrating the spectra.

Several spectral lines are visible in all the records. A tone is seen at 6.7 Hz in some records, which may be *Scorpius's* shaft rate, but there are other spectral lines at much higher levels. A set of lines at 9, 13.5, 18 and 22.5 Hz are harmonically related, although the fundamental frequency, 4.5 Hz, is absent. Two other lines, at 10.3 and 12.2 Hz, are also prominent.

Figure 3.9 shows how the frequencies of these lines vary with time. The plots were made by searching a small part of the spectrum near each frequency for the exact bin at which the peak occurs. Note that the frequency of the lines at approximately 9 and 13.5 Hz slowly decreases during the 110 record interval. All the floats record rather abrupt shifts in these frequencies near records 1850 and 1865, and in the 9 Hz line only, near record 1808. These abrupt frequency shifts also occur in the lines at approximately 18 Hz and 22.5 Hz, indicating that the 9, 13.5, 18 and 22.5 Hz lines are all harmonically related. The 10.3 and 12.2 Hz lines are stable throughout the interval, indicating that they are not harmonically related to the other lines.

The source of all of the lines is assumed to be a single surface ship. It will become apparent in Chapter 5 that all of the lines arrive from approximately the same bearing. The 9 Hz and harmonics line set is thought to be propulsion related because the fundamental frequency (4.5 Hz) is normal for a merchant ship blade pass frequency and is usually accompanied by strong harmonics.¹⁶ The reason for the absence of the fundamental is hypothesized in Chapter 6. The 10.3 and 12.2 Hz lines are likely to be auxiliary machinery tones.

Figure 3.10 shows the level of the 9 Hz line, which rises by about 10 dB during the interval. The levels of the other lines are not shown here, but they decrease or remain approximately constant during the interval. Thus nothing about the range to the source can be concluded. However, the transmission losses are apparently different for different frequencies emanating from the same source.

Figure 3.11 shows the vertical angle of arrival for the 9, 10.3, 12.2, and 13.5 Hz signals during the interval. The arrival angle was obtained by comparing the horizontal and vertical spectral levels. For a particular frequency and during any one record, the arrival angle is different at each float. Also, for a particular float and during any one record, the arrival angle is different at each frequency. This indicates that the sound field is far from homogeneous, and that sound is not propagating across the Swallow float array as plane waves. The beamforming results of Chapter 5 will be more understandable in light of Figure 3.11.

3.5. Sound Speed Profile

The sound speed profile for the upper 500 meters was obtained from temperature measurements made by the California Cooperative Oceanic Fisheries Investigations (CalCOFI) Cruise 8609 on 19 September 1986 at (32° 30.9' N, 118° 13.3' W),¹⁷ which is within a few miles of the deployment site. Historical data archived by the National Oceanographic Data Center were used for salinity in the upper 500 meters and temperature and salinity in the lower 1500 meters.¹⁸ Using the equation given by Mackenzie,¹⁹ the composite sound speed profile shown in Figure 3.12 was calculated.

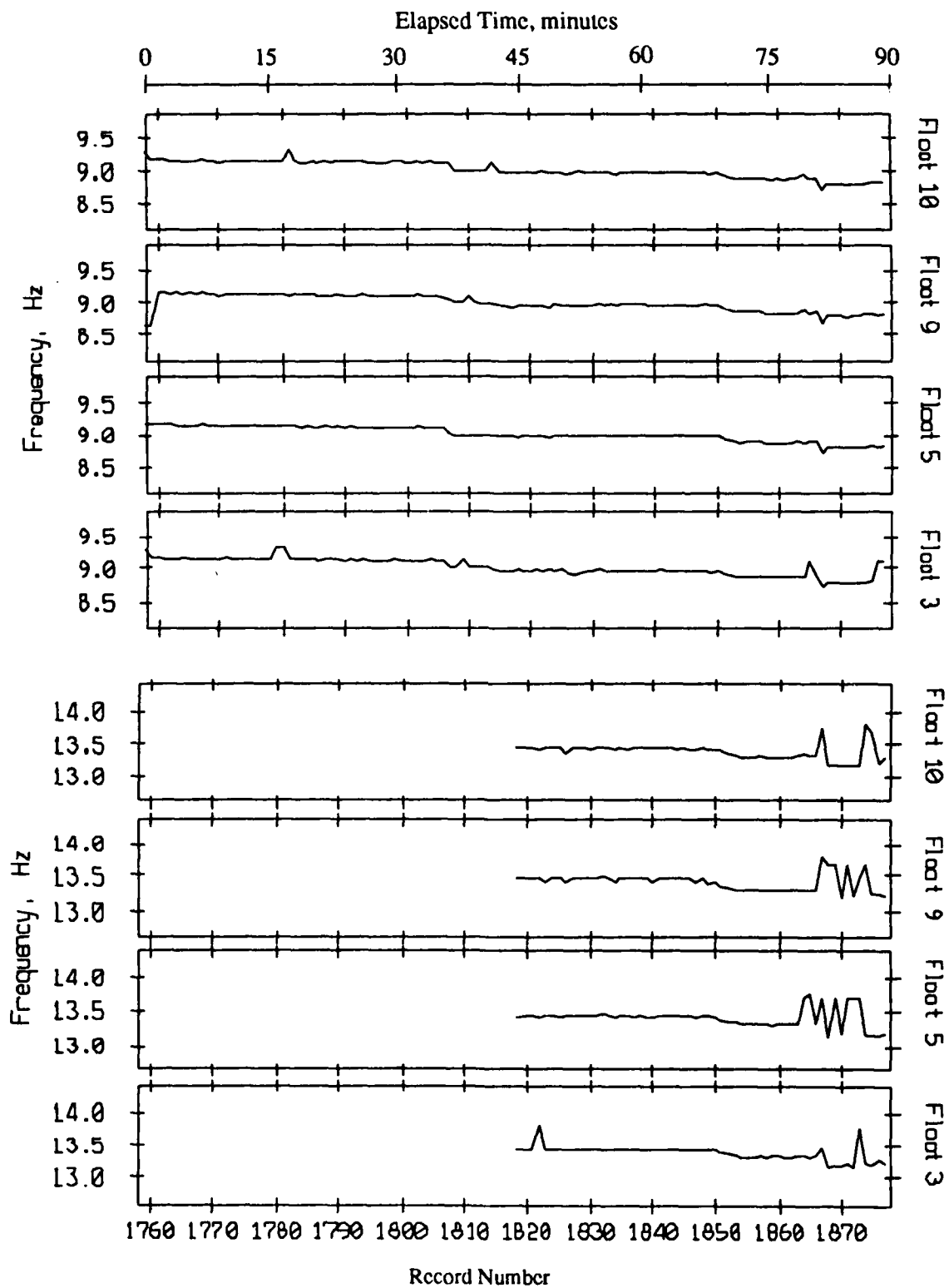


Figure 3.9a Exact frequency of spectral lines near 9 Hz (upper) and 13.5 Hz (lower panel)

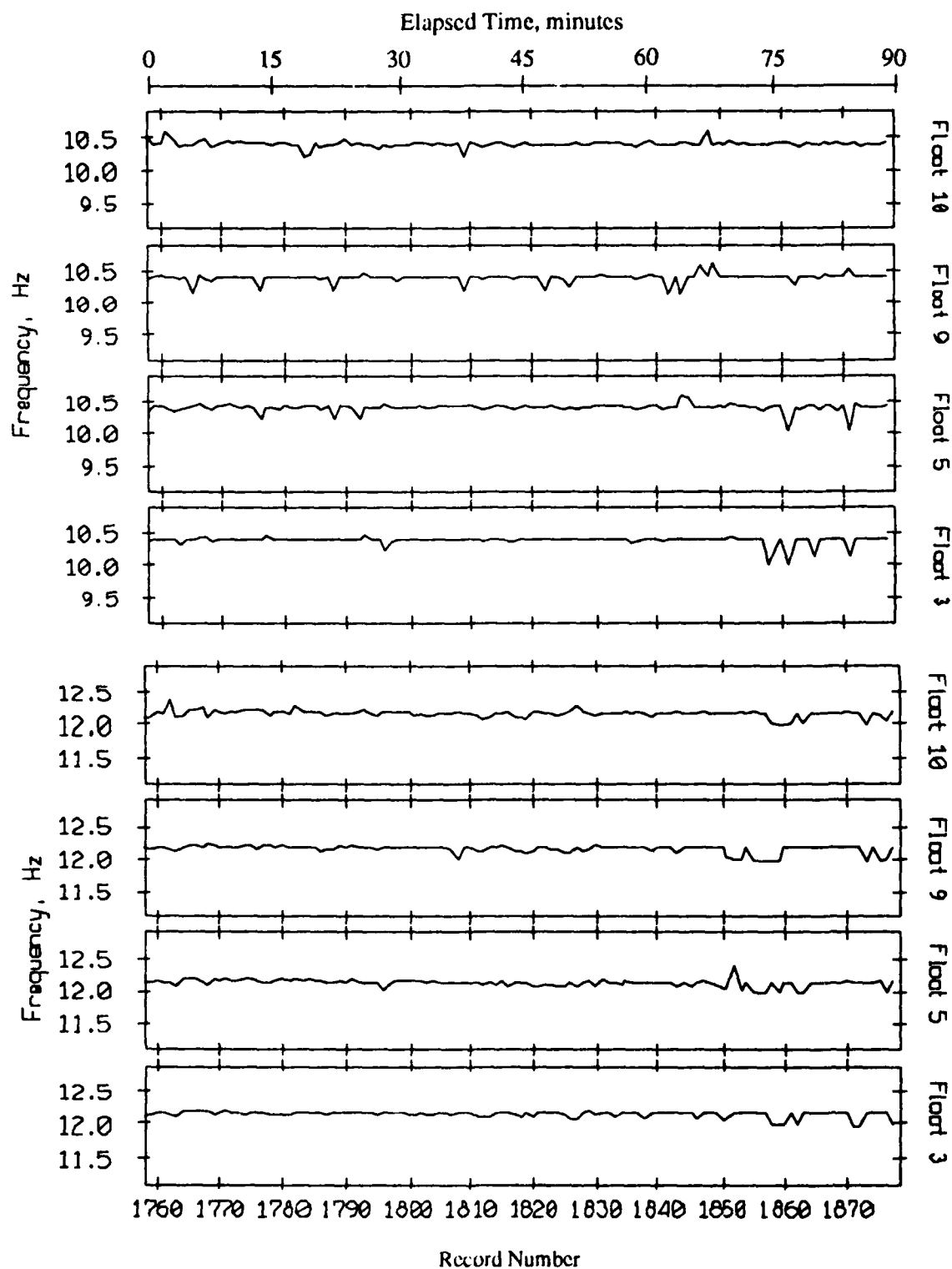


Figure 3.9b Exact frequency of spectral lines near 10.3 Hz (upper) and 12.2 Hz (lower panel)

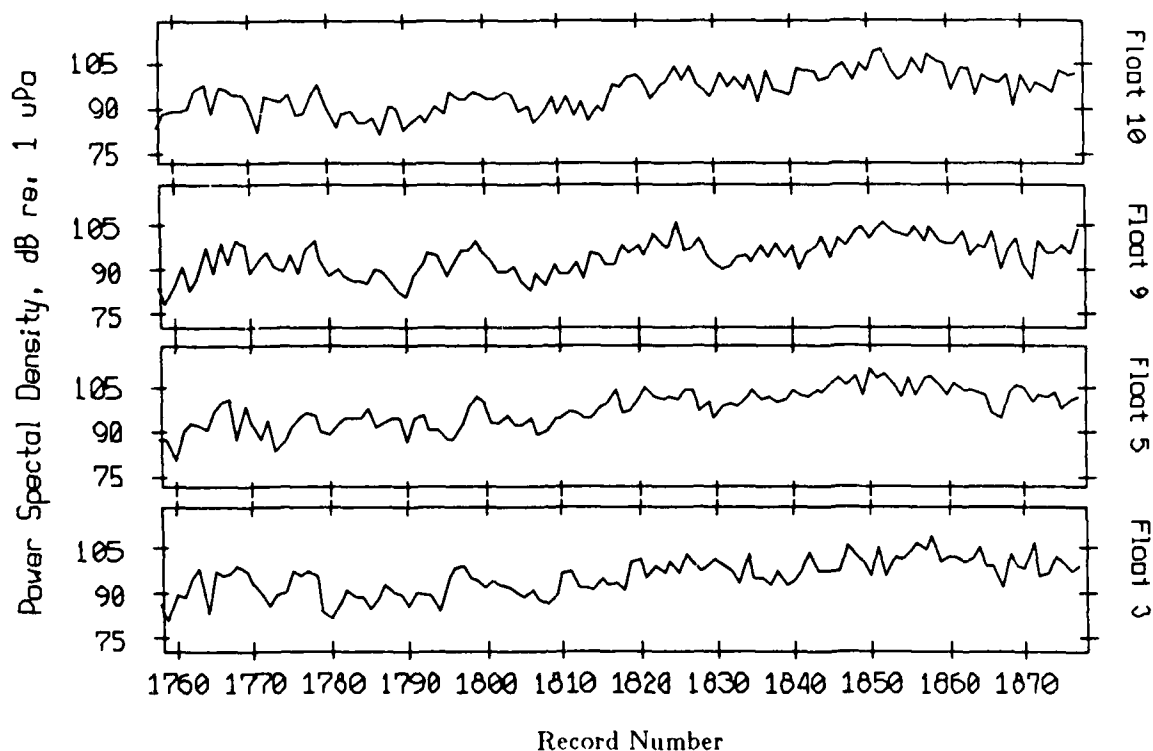


Figure 3.10 Spectral level of the line near 9 Hz

4. Swallow Float Localization

In this Chapter, the time-varying locations of the Swallow floats are estimated for records 1150 to 1870 of the September 1986 experiment. The rms position error is also estimated. The goal of the localization is to obtain a position estimate with an rms error of less than $\lambda/10$ at the highest frequency of interest, since theory predicts that beamforming results will be degraded by less than 1 dB if this condition is met.²⁰ Since the highest frequency of interest is 20 Hz, the condition to be satisfied is

$$\text{rms position error} \leq \frac{\lambda}{10} = \frac{c/f}{10} = \frac{1500 \text{ m/sec}}{10(20 \text{ Hz})} = 7.5 \text{ meters} \quad (4.1)$$

4.1. Theoretical Development and Simulation Results

Aspects of the localization problem are addressed in an MPL Technical Memorandum²¹ and in a Journal of Oceanic Engineering (JOE) submission,²² the latter of which is included here as Appendix C. The earlier results are summarized below and extended in subsequent subsections.

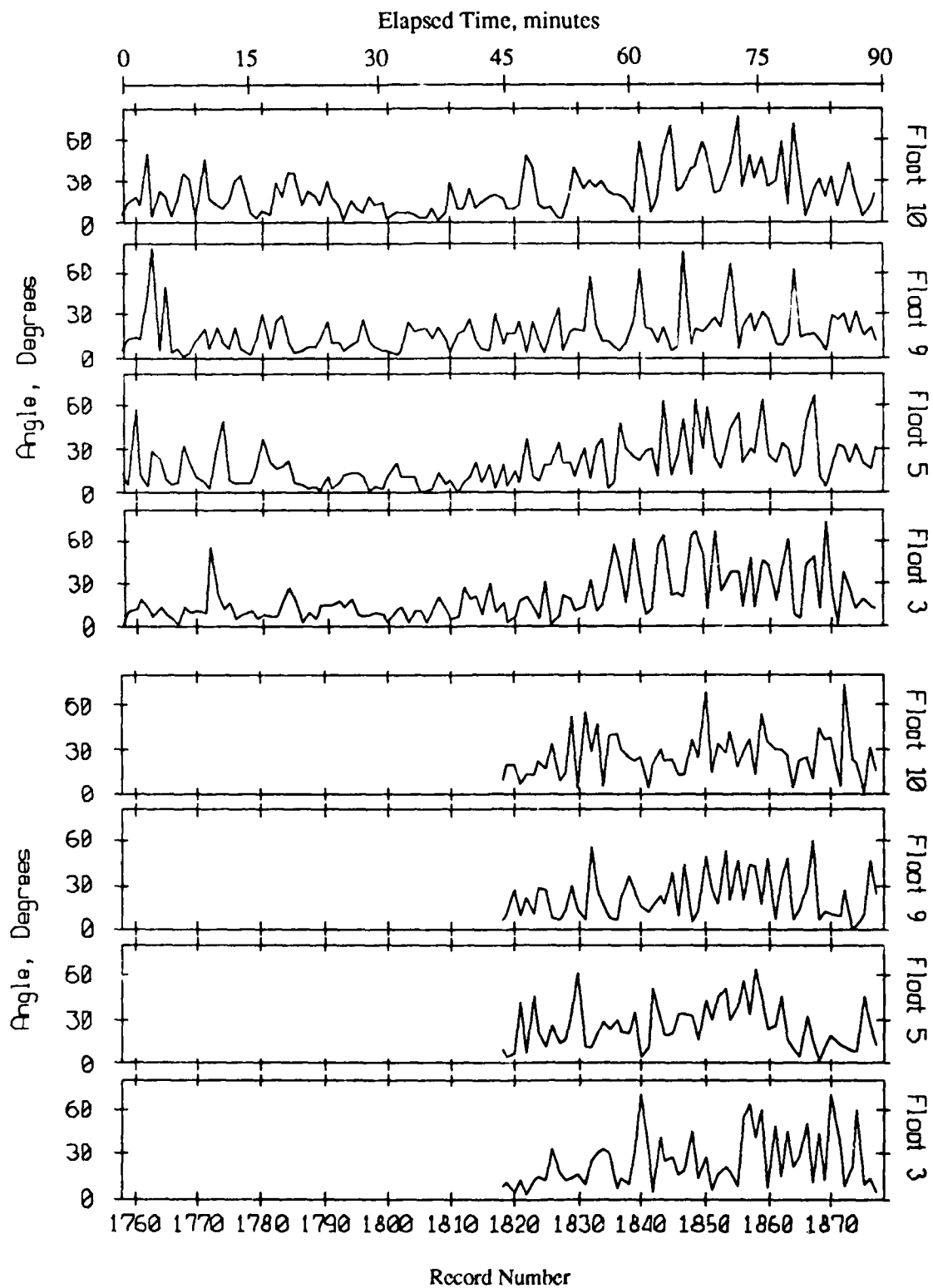


Figure 3.11a Magnitude of the vertical arrival angle at 9 Hz (upper) and 13.5 Hz (lower panel)

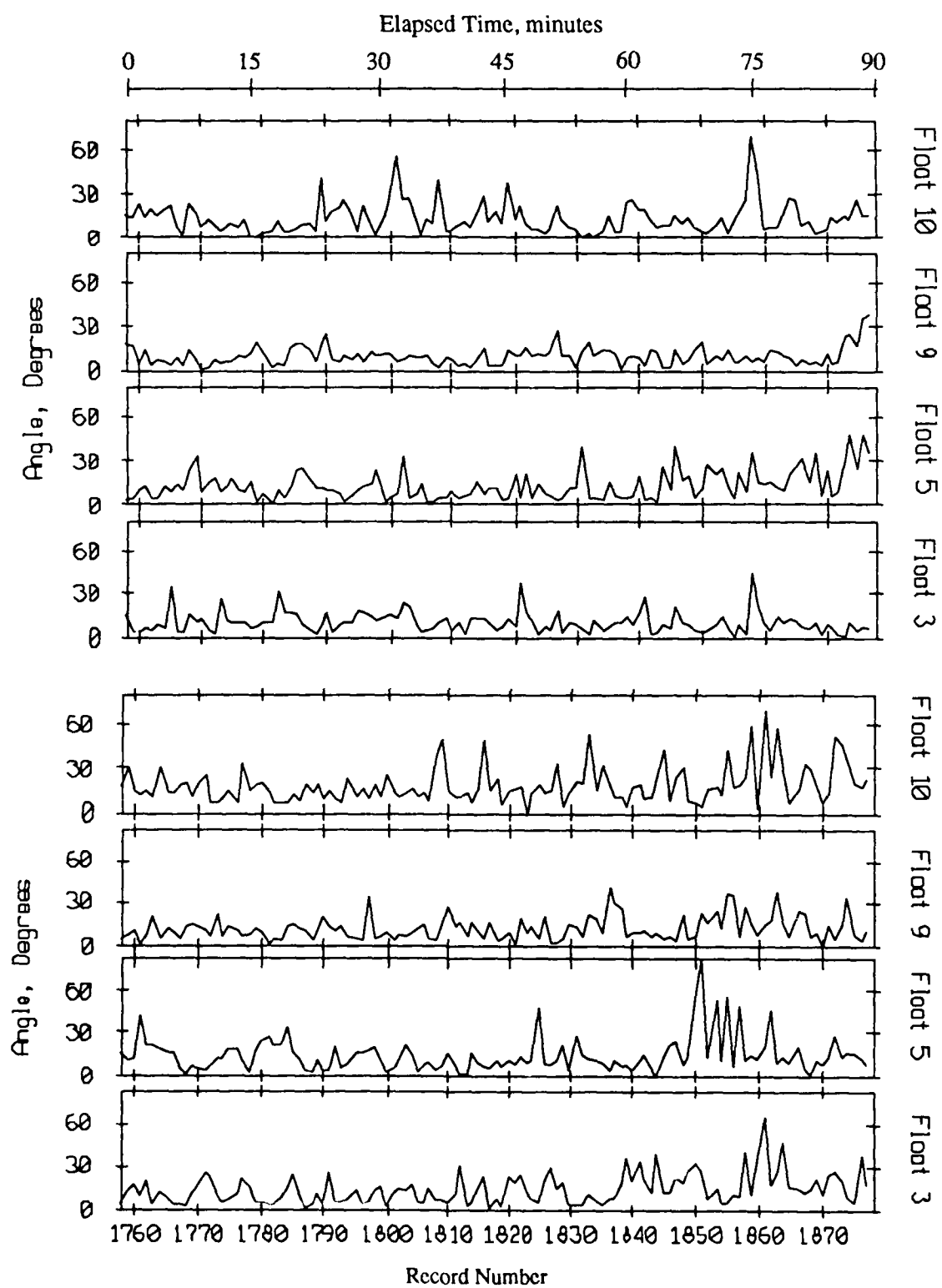


Figure 3.11b Magnitude of the vertical arrival angle at 10.3 Hz (upper) and 12.2 Hz (lower panel)

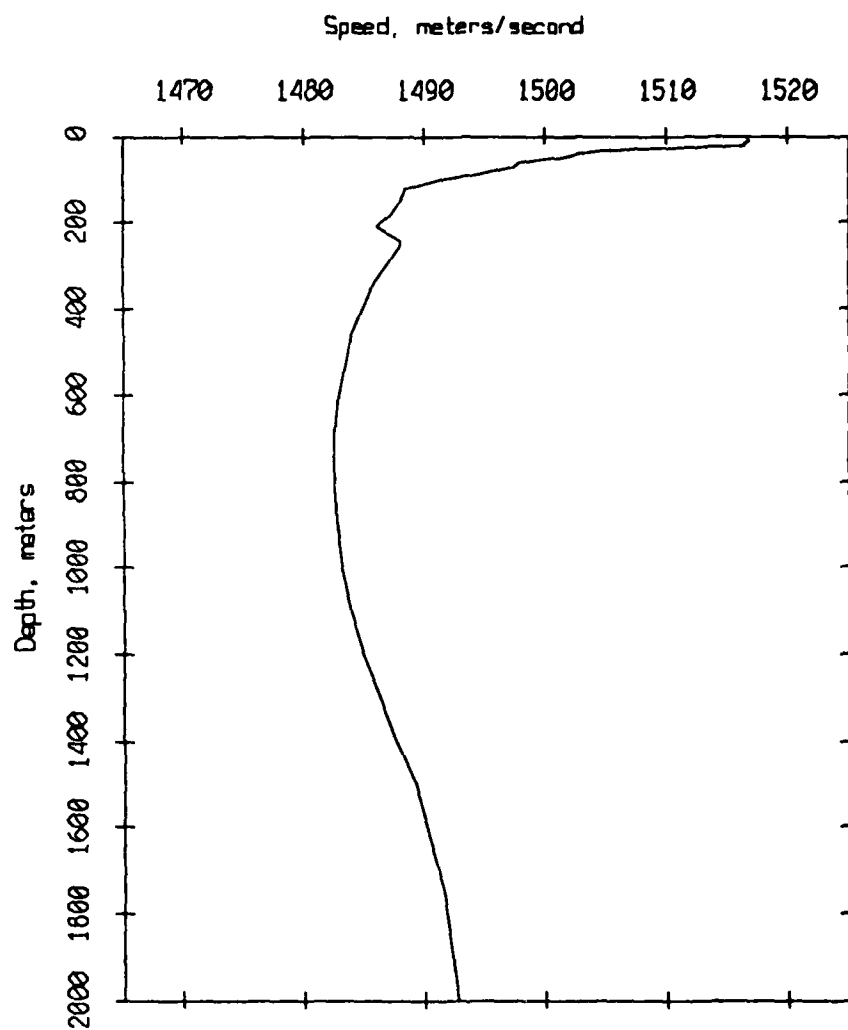


Figure 3.12 Sound speed profile for the September 1986 experiment

4.1.1. Summary of Previous Results

Reference [21] describes how interfloat travel times and travel time error variance are obtained from the acoustic range data. Briefly, the pulse arrival times are detected, and the pulse transmit time subtracted from them, to obtain measurements of the travel time between each float pair and between each float and the surface. Only one float transmits during each record, so a particular travel time measurement is made at N record intervals, where N is the number of floats. The travel time measurements must be interpolated to obtain a measurement for each record. Reciprocal path measurements are then averaged to obtain travel time estimates. The difference between the reciprocal path measurements is used to estimate the travel time error, as shown in [21]. A diagram showing the processing steps may be found in Figure 4 of Appendix C.

Two methods are derived in Appendix C for estimating float positions from travel time and travel time error estimates:

- A *generalized least squares* filter which estimates current position using the current set of travel time measurements. The filter uses only that set of measurements and an estimate of the rms measurement error.
- A *Kalman* filter which estimates current position by weighting the current set of measurements against the previous position estimate propagated forward in time. Position estimates are propagated forward in time using equations of motion for the floats. The filter must also be supplied with estimates of the rms measurement error and float accelerations.

Simulations are employed in Appendix C to test the filters under a variety of deployment geometries and noise conditions. Four simulation deployment geometries are shown in Figure 6 of Appendix C. Filter performance is evaluated for four combinations of process and measurement noise. Process noise parameterizes how erratically the floats move between travel time measurements, and measurement noise is the error in the travel time measurements. For the simulations, float accelerations were modeled as normally distributed white noise, and process noise is actually the variance of the acceleration used in the simulation.

Cases 1, 2, 6 and 7 test the most frequently used Swallow float deployment geometry in which 3 floats are deployed to the ocean bottom and the remainder in a planar array somewhere in the water column. Case 1 uses low process and measurement noise in order to establish the baseline for evaluating how the filters respond to increased noise or other deployment geometries. Cases 2, 6, and 7 test the filters' performance when the process and measurement noise are increased. The rms measurement noise is raised by a factor of 2 in Cases 2 and 7, and the rms process noise is raised by a factor of about 100 in Cases 6 and 7.

Both the process and measurement noise are low in Cases 3, 4 and 5. Case 3 tests the filters' performance when the mid-water column floats drift out of the net formed by the bottomed floats. The bottomed floats are the same as in Case 1, but the planar array is now outside the triangle formed by the bottomed floats. Case 4 tests the effect of one of the bottomed floats failing. The remaining bottomed floats and planar array are the same as in Case 1. Case 5 tests the effect of deploying the mid-water column floats in a vertical line array rather than a planar array. The three bottomed floats were put at about 4000 meters depth and 5 other floats spaced between 700 and 2200 meters depth. The simulation cases are summarized in Table 4.1.

The coordinate system for the localization is shown in Figure 4.1. The origin is fixed at the surface directly above one of the bottomed floats. This fixes the location of the Z axis. The horizontal axes are then rotated until a second bottomed float lies in the XZ plane.

The results of the simulations are shown in Figures 7 and 8 of Appendix C. Figure 7 compares the results of Cases 1, 2, 6 and 7 and shows the effects of increased process and measurement noise. The horizontal axis is process noise and the vertical axis is rms position error. The two lower lines show the results when the measurement noise is low, and the upper two when the measurement noise is high. The dotted lines, which depict the least squares filter results, are parallel to the horizontal axis because the filter is insensitive to the level of process

Table 4.1. Float Location Simulations.

Case	Process Noise	Measurement Noise	Tests the Effect of:
1	low	low	filter performance baseline
2	low	high	increased measurement noise
7	high	low	increased process noise
6	high	high	increased process and measurement noise
3	low	low	large array drift
4	low	low	losing a bottomed float
5	low	low	vertical line array

noise. The filter processes one set of measurements at a time and is not affected by what happens to the floats between measurements.

We see that the error in the Kalman filter estimate is smaller than that in the least squares estimate as long as the process noise is low. This is because the Kalman filter tracks the floats' motion when the process noise is low. As the process noise is increased, the Kalman filter is less able to maintain a track and the error in its position estimate increases. At sufficiently high process noise, the two filters perform comparably. The effect of increasing the measurement error is to increase the error in the output of both filters.

Figure 8 compares the results of Cases 1, 3, 4 and 5 which show the effect of different float deployment geometries on the filters' performance. The Kalman filter performs somewhat better than the least squares filter in all of the deployment geometries simulated. Since these simulations were conducted with low process noise, the performance differential is probably due to the tracking capability of the Kalman filter.

There remain three issues which must be addressed prior to applying the Kalman and least squares filters to experimental data. They are:

- obtaining a good initial estimate of float positions and velocities,
- determining the relationship between actual position error and the error estimates produced by the filters;
- determining how error in the sound speed estimate impacts the performance of both filters;

These issues are discussed below.

4.1.2. Obtaining Good Initial Position and Velocity Estimates

Both filters require a good initial estimate of the float positions and velocities in order to perform well. Their respective responses to bad initial estimates, which are discussed below, include becoming stuck at a bad position estimate, slowly converging to a good position estimate, and no effect at all. Nearly perfect initial estimates of the floats' initial positions and velocities were used in the simulations presented in Appendix C in order to isolate the effects of changes in process noise, measurement noise, and deployment geometry. In this Section, a method is developed for obtaining sufficiently good initial estimates of float positions and velocities to enable both filters to produce good position estimates beginning almost immediately.

The filter's perform differently when given poor initial estimates. A really bad initial estimate can cause the least squares filter to converge to, and remain stuck at, the wrong

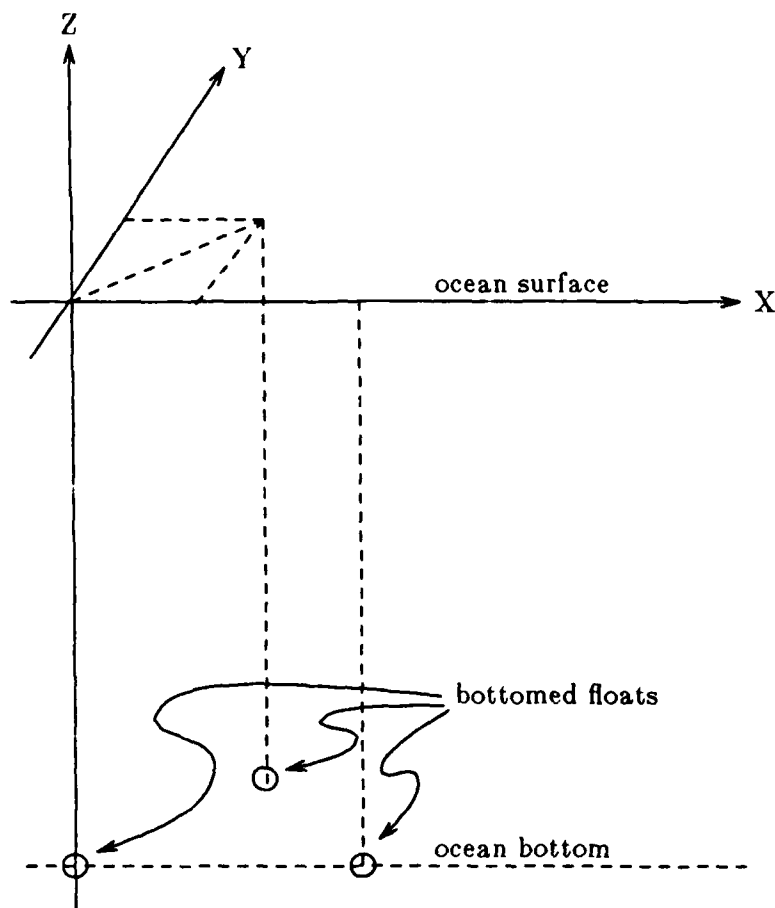


Figure 4.1 Coordinate system for the Swallow float localization

position. This position is called a *local minimum* because it is a local minimum in the loss function, but not the global minimum (see Equation 3.9 of Appendix C). However, if we provide the least squares filter with only a moderately poor initial estimate, so that it does not get stuck at a local minimum, then its first position estimate will be very good. In terms of the estimate error, a really bad initial estimate can result in a large initial error which remains large for subsequent measurements. However, a moderately poor initial estimate will result in a small initial error which remains small.

The Kalman filter's response to a poor initial estimate depends upon two other parameters, the estimated initial position error and the estimated initial velocity error, which are supplied to the filter separately. If the estimated initial position error is large, then the filter relies primarily on the measurement to estimate float positions. Likewise for the initial velocity error. If the measurement is noisy, the filter's estimate may jump around considerably. The error in the filter's estimate depends entirely upon the measurement error.

If the initial position and velocity error estimates are set small, the Kalman filter will estimate float positions and velocities based upon the process and measurement noise estimates which it has been given. If there was, in fact, error in the initial estimate, the filter will converge very slowly to the correct position estimate. In terms of the estimate error, a bad initial estimate causes a large initial error which slowly decreases. On the other hand, a good initial

estimate results in a small initial error which stays small.

To summarize, the least squares filter may respond to a very bad initial estimate by becoming stuck at a local minimum. However, it will converge immediately to a good position estimate if the initial estimate is not too bad. The Kalman filter's response to a poor initial estimate depends upon the values of the estimated initial position and velocity errors. If they are large, the filter depends entirely upon the measurements. If they are small, the filter will slowly converge to the correct position estimate.

Good initial estimates can be obtained by taking advantage of the strengths of both filters. The following procedure was found to work well in simulations:

- (1) Starting with arbitrary initial float position and velocity estimates and large values for the estimated initial position and velocity errors, the Kalman filter is run on the first 2 to 4 measurements. Using the filter's estimates after the last measurement as the new initial estimates, the filter is again run on the same set of measurements. This step is repeated, each time using the filter's estimate at the end of the previous run as the starting point for the next run, until the filter's position estimate stops changing much.
- (2) Using the position estimate obtained in (1) above, the least squares filter is run on the first measurement. This produces the best estimate of float positions for that measurement and becomes the initial position estimate for both filters.
- (3) Using the result of (2) as the initial position estimate, an arbitrary initial velocity estimate, a small estimated initial position error and a large estimated initial velocity error, the Kalman filter is again run on the first 2 to 4 measurements. The filter's position estimate does not change much but the velocity estimate does. Using the filter's velocity estimate after the last measurement, the filter is again run on the same set of measurements. This step is repeated, each time using the filter's velocity estimate at the end of the previous run as the starting point for the next run, until the filter's velocity estimate stops changing much.

4.1.3. Relationship Between Actual and Predicted Error and the Innovations Sequence

The performances of the Kalman and least squares filters are compared in Appendix C on the basis of the rms error in their position estimates. However, both filters also estimate the error in their output. We might ask the question "What is the relationship between the error estimates produced by the filters and the actual position errors?" The answer to this question will permit us to predict the estimate error with some confidence when we process experimental data.

The least squares filter produces an estimate of the error (actually the *mean magnitude of the residual*), which is defined in equation (3.25) of Appendix C. It is analogous to the mean square difference between the measurement and position estimate, normalized by the number of measurements.

The Kalman filter produces an estimate of the position error covariance, identified in equation (4.29) of Appendix C. Also produced is the *mean magnitude of the innovation*, which is a measure of the difference between the predicted float positions and the positions indicated by the measurement, and is identified below equation (4.13) in Appendix C. The latter is similar to the residual produced by the least squares filter.

The error estimates produced by the filters are now compared to the actual rms errors for the simulations presented in Appendix C. Figure 4.2 compares the predicted and actual rms error in the least squares filter result for the 7 Cases simulated. The filter's estimate of the error comes quite close to the actual error in Cases 1, 2 and 7, where the deployment geometry was normal and either or both the process and measurement noise were low. The actual and estimated errors are higher in Cases 2 and 6 than in Cases 1 and 7 because the measurement

noise is higher in Cases 2 and 6. The filter slightly underestimates the error in Case 6, when the process and measurement noise are higher. Cases 3, 4, and 5 show that the filter underestimates the error when the deployment geometry becomes less optimal. Under these circumstances the error estimate is about a factor of 2 lower than the actual error.

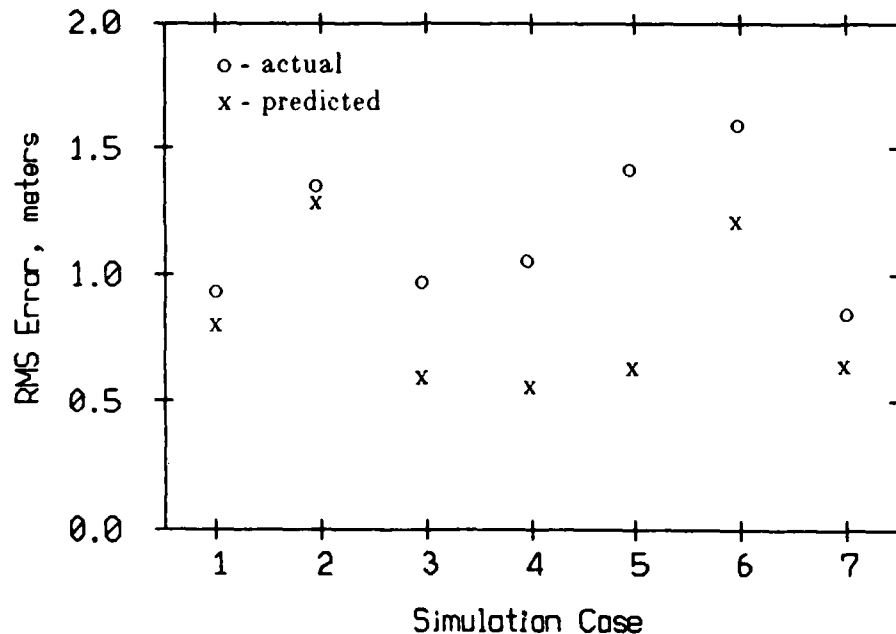


Figure 4.2 Predicted and actual rms error in the least squares filter results for the seven simulated cases.

Figures 4.3 and 4.4 compare the mean magnitude of the innovation and the predicted and actual rms error obtained using the Kalman filter in the 4 Cases involving changes in process and measurement noise. The vertical axes are rms error or mean innovation magnitude, in meters. The horizontal axes are the estimate of process noise given to the filter as a parameter. The process noise estimate is used to control the filter. It is denoted q and will be the subject of considerable discussion below.

Each panel in Figures 4.3 and 4.4 contains 3 curves. The top curve is the mean innovation magnitude and is indicated by $|I|$. The middle curve is the true rms error, and is labeled e . The bottom curve is the estimate of the standard deviation of the error produced by the filter and is labeled \hat{e} .

The Cases shown in Figure 4.3 have low underlying process noise. The actual error is bracketed by the innovation and the predicted error, and their relative values are approximately constant. The error in the estimate varies with q : as q is lowered, and the error decreases, and vice versa. The lowest error is obtained by setting q very low.

Increasing the measurement noise increases the spacing between the 3 curves, as may be seen by comparing the upper and lower plots in Figure 4.3.

The Cases shown in Figure 4.4 show the innovation and rms error when the underlying process noise is high. When q is set large, the curves resemble the low process noise cases. When q is set low, however, the innovation and actual error rise but the estimated error remains low. This phenomenon is called *divergence* because the filter's estimate of position error diverges from the true position error.

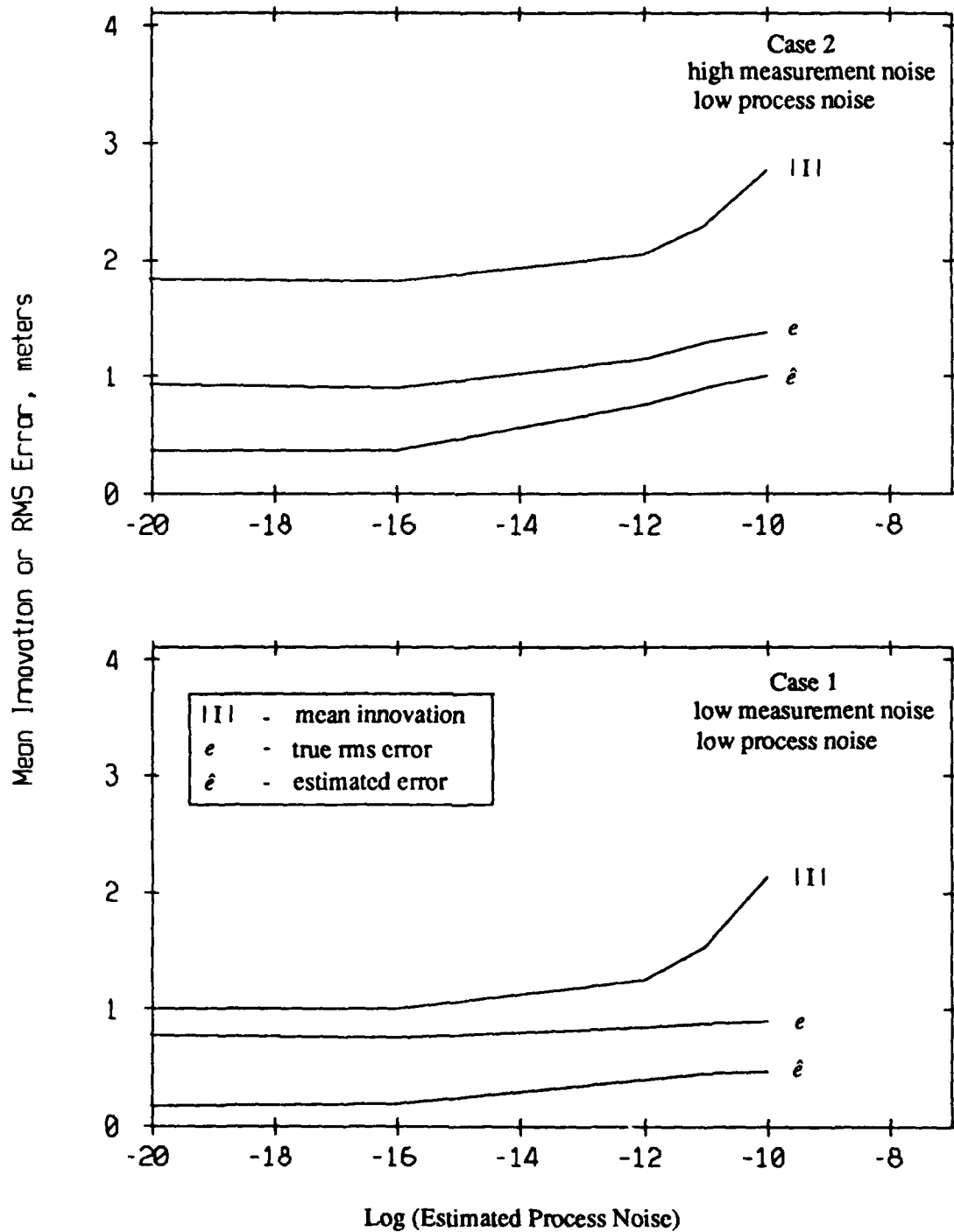


Figure 4.3 Mean magnitude of the innovation, predicted and actual rms error using the Kalman filter on simulation Cases 1 and 2

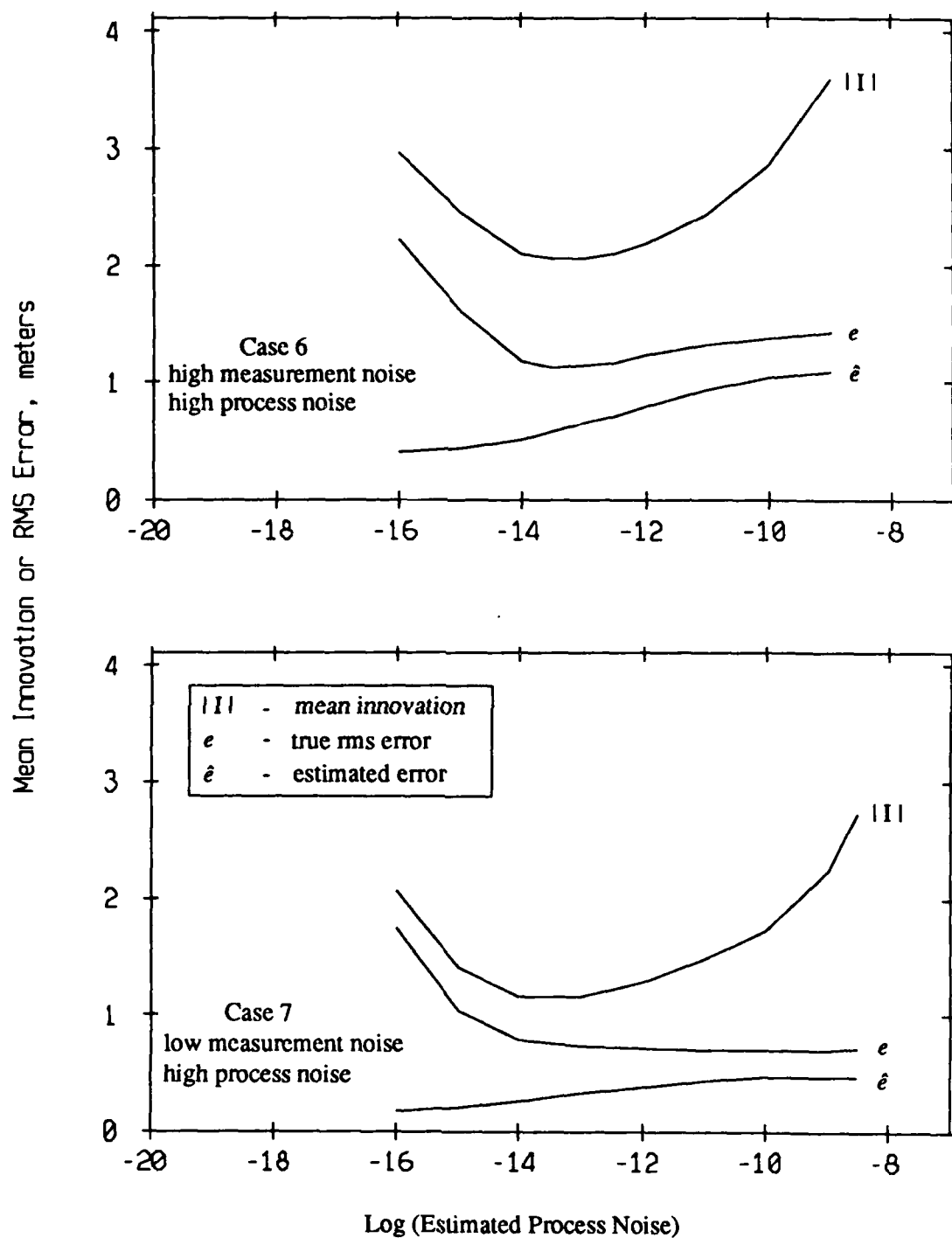


Figure 4.4 Mean magnitude of the innovation, predicted and actual rms error using the Kalman filter on simulation Cases 6 and 7

Figures 4.3 and 4.4 show that the error in the Kalman filter estimate, the mean innovation magnitude and the estimated error vary as a function of q , the estimate of process noise given to the filter. Thus q is the parameter which is used to control the filter's performance. The filter uses q to determine how much weight to give to its own track of the float positions, relative to the measurements. When q is set high, indicating that the process noise is thought to be high, the filter gives greater weight to the measurements and less to its own track of the floats. In this case, the Kalman filter result approaches that of the least squares filter in that the position error depends upon the measurement noise.

When q is set low, indicating that the process noise is thought to be low, the filter gives greater weight to its own track of the floats and less to the new measurements coming in. If the process noise really is low, the filter works fine. If the process noise is actually high, however, divergence can occur and the position error becomes large. This is seen when $q \leq 10^{14}$ in Figure 4.4.

The optimal value of q , which minimizes the rms error in the filter's estimate, is readily apparent in the simulations shown in Figures 4.3 and 4.4 because the true rms position error is known. Figure 4.4, however, shows how to determine q when processing experiment data and the true position error is unknown. The optimum value for q is seen to correspond to the minimum mean innovation magnitude. This suggests that when experimental data are being processed, the filter can be run several times using different values for q , and the optimum value of q selected as the one which minimizes the innovation.

The error in the resulting position estimate will be bracketed by the mean magnitude of the innovation and the estimated standard deviation of the error. A reasonable estimate for the rms position error would be the average of the mean innovation and estimate of rms error. A conservative estimate for the rms error would be the mean magnitude of the innovation.

4.1.4. Effect of Sound Speed Errors on Location Error

The simulations in Appendix C included travel time error but no sound speed error. What remains is to (1) estimate the sound speed error and (2) determine its impact on the filters' performance.

4.1.4.1. Sound Speed Errors

The sound speed estimate is usually based upon ocean temperature versus depth measurements made at the experiment site using expendable bathythermographs (XBT's). The sound speed profile is then calculated using historical values for salinity. There will be errors in the sound speed profile and it will fluctuate somewhat during the experiment. Typical measurements of maximum sound speed fluctuations reported in the literature are 0.75 and 1.0 m/sec.^{23,24}

An estimate of the errors and variation found in typical sound speed estimates was obtained using a series of 12 XBT measurements made during a 26 hour period by MPL personnel from FLIP during September 1987 at 35° N, 126° W, about 265 miles west of Point Conception, California. The standard deviation of the sound speed at a particular depth was just under 0.6 meters/sec. This number is taken as representative of the rms sound speed error at a particular depth for experiments lasting approximately 24 hours.

It is shown in Appendix C that the filters utilize the average sound speeds over the paths separating each pair of floats. To calculate the average sound speeds, the sound speed measurements are first used to develop a multi-layer ocean model with constant sound speed in each layer. Then, for each float pair, the average sound speed is found from

$$\bar{c} = \frac{\sum_{i=1}^N d_i}{\sum_{i=1}^N \frac{d_i}{c_i}} \quad (4.2)$$

where d_i and c_i are the thickness and sound speed for the i^{th} layer and the summation is over all of the layers between the float pair.

Equation (4.2) is a good approximation so long as the ray paths are approximately straight. The Generic Sonar Model (GSM) ray tracing program²⁵ was employed to determine if that condition is satisfied during the September 1986 deployment. Interfloat travel times were calculated for representative pairs of floats using the sound speed profile shown in Figure 3.12 and the approximate positions of the floats during the September 1986 experiment. The *effective* sound speed was computed by dividing the geometric distances separating the floats by the GSM-produced travel times. The average and effective sound speeds differed by less than 0.5 meters/sec, indicating that equation (4.2) is a good approximation.

The rms error of the average sound speed \bar{c} is a complicated function of the errors in the sound speeds c_i 's. However, since (4.2) is essentially an average, and since the sound speed errors are taken to be approximately mean zero, the error in the average sound speed would be expected to be less than that in the sound speed for a particular layer.

4.1.4.2. Effect On Position Error

In Appendix C, the measurement noise is defined to be the error in the interfloat or float to surface *ranges*, that is, to include the error made in measuring the travel time as well as the error made in estimating the sound speed along the path over which the range pulse travels. From equation (3.8) of Appendix C, the rms sound speed and measurement errors for floats i and j are related according to

$$\sigma_{r_{ij}} = \left[(\hat{r}_{ij}^2) \sigma_{\bar{c}_{ij}}^2 + (\bar{c}_{ij})^2 \sigma_{\tau_{ij}}^2 \right]^{1/2} \quad (4.3)$$

where $\sigma_{\bar{c}} = 0.6$ m/sec is the estimated rms error in the average sound speed, \bar{c} is the average sound speed estimate, \hat{r} is the travel time estimate, σ_{τ} is the rms travel time error estimate, and σ_r is the rms measurement error. It is shown in [21] that the rms travel time error during the September 1986 experiment is approximately 0.0013 seconds. Take the average sound speed to be 1500 m/sec. If the path length between floats i and j is approximately 3 km, so that the travel time is about 2 seconds, then the rms measurement error is

$$\begin{aligned} \sigma_{r_{ij}} &= \left[(4 \text{ sec}^2) (0.36 \text{ m}^2/\text{sec}^2) + (2.25 \times 10^6 \text{ m}^2/\text{sec}^2) (1.69 \times 10^{-6} \text{ sec}^2) \right]^{1/2} \\ &= \left(1.44 + 3.8 \right)^{1/2} \text{ meters} = 2.3 \text{ meters} \quad (\tau = 2 \text{ seconds}) \end{aligned} \quad (4.4)$$

The second term, which involves the rms travel time error, is about twice as large. If the range is increased to 7.5 km, so that the travel time increases to 5 seconds, then

$$\sigma_{r_{ij}} = \left(9 + 3.8 \right)^{1/2} \text{ meters} = 3.6 \text{ meters} \quad (\tau = 5 \text{ seconds}) \quad (4.5)$$

The first term now dominates and the rms measurement error is increased by about 2/3.

The effect of sound speed errors is to increase measurement noise, which we have seen increases error in the filters' results. However, the increase in measurement noise is apparently not significant except for the largest travel times. Since both filters accept estimates of the rms sound speed and travel time error and use equation (3.8) of Appendix C to calculate measurement error variance, they give less weight to longer ranges and thus properly respond to sound speed errors.

4.2. Application to Experiment Data

September 1986 experiment acoustic range data between records 1150 and 1870 are now applied to the least squares and Kalman filters. A coordinate system is established in which the origin lies at the surface directly above float 0, and float 1 lies in the XZ plane. This is shown in Figure 4.5. The Z axis is vertical and extends through float 0. The directions of the X and Y axes relative to magnetic north are determined from Figure 3.3 to be approximately 280° and 190° , respectively.

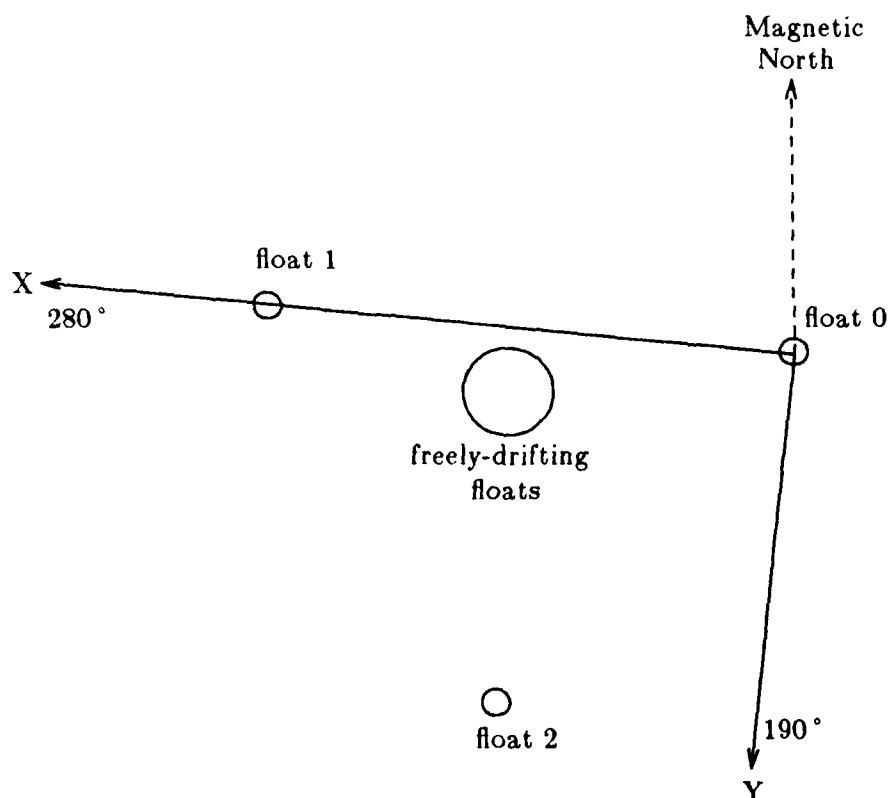


Figure 4.5 Plan view of the coordinate system established for localizing Swallow floats during the September 1986 experiment.

The processing steps shown in Figure 4 of Appendix C were followed to obtain travel times estimates between each float pair and between each float and the surface. The rms travel time error was also estimated for each pair and for the surface echoes. The average rms error is found to be 1.3 msec.

The procedure described in Section 4.1.1 was used to obtain initial position and velocity estimates. Using an rms sound speed error of 0.6 m/sec, the travel times were applied to the least squares and Kalman filters, and the results shown in the upper panel of Figure 4.6. The mean innovation magnitude and predicted standard error produced by the Kalman filter are labeled $|I|$ and \hat{e}_k , respectively. The mean error predicted by the least squares filter is indicated by a dotted line and labeled \hat{e}_L .

The innovation magnitude and predicted rms error look much like the high process noise plots in Figure 4.4, except shifted up and to the right. The right shift suggests that the

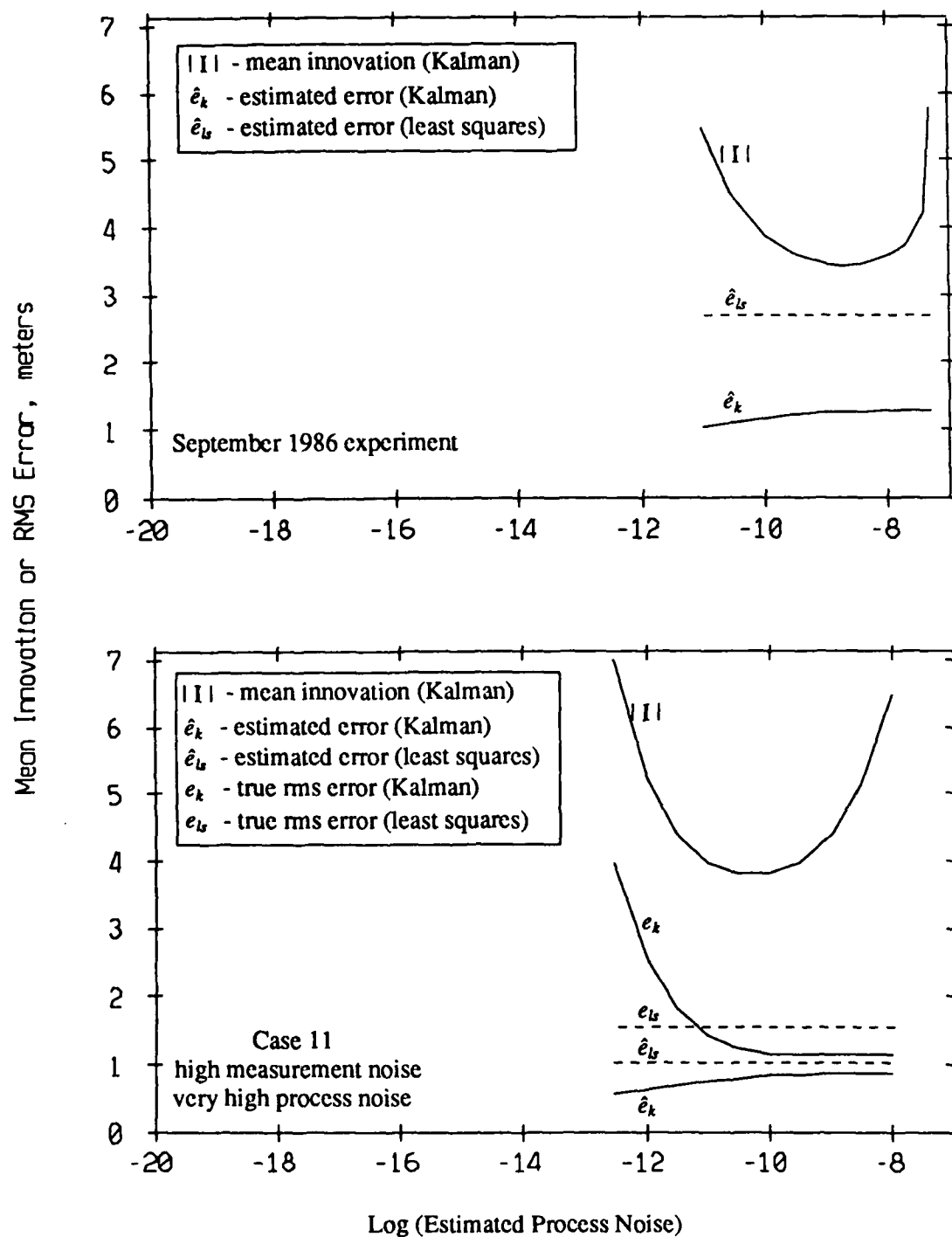


Figure 4.6 Results of the Kalman and least squares filters applied to the September 1986 experiment and simulation Case 11

process noise in the experiment data was higher than that used in the simulations, and the shift up indicates likewise for the measurement noise. However the rms travel time error found in the experiment data (1.3 msec) is approximately equal to that used in the high measurement noise simulations (1.4 msec). The shift up, then, is apparently due to sound speed errors in the experimental data.

In order to match the experimental results more closely, another simulation was run in which the rms process noise was increased by a factor of about 30 and the rms travel time error increased from about 1.4 to 1.7 msec. The results are shown in the bottom panel of Figure 4.6, labeled as in the upper panel except that e_k and e_{t_k} are the true rms errors in the estimates. The Case 11 Kalman filter results are quite similar to the experimental results. The mean innovation and predicted error have approximately the same shape and location in both plots. The optimal value of q appears to be 10^{-9} for the experiment data and 10^{-10} for Case 11. The difference between these two numbers could be a result of the order of the simulation model being too low.

Based upon the mean innovation magnitude and predicted standard deviation of the error, the rms error in the Kalman filter's position estimate for the September 1986 experiment is estimated to be about 2.4 meters. It is certainly less than 3.5 meters. The rms difference between the Kalman filter and the least squares position estimates was found to be about 3 meters. Based upon the error estimates produced by both filters, and given the apparent high process noise in the experimental data, it is impossible to determine whether one estimate is better than the other. Both apparently satisfy the condition in (4.1). The Kalman filter positions were chosen for the beamforming in Chapter 5.

Plan views of the float positions as a function of time are shown in Figures 4.7 and 4.8. The former shows all of the floats and the latter shows only the freely-drifting floats. It is interesting to note that four of the floats (3, 4, 5 and 10) drifted in a generally counter-clockwise direction, while float 9 drifted generally in a generally clockwise direction. According to Table 3.1, the four floats which drifted together all deployed to about 1000 meters depth, while float 9 deployed to about 800 meters depth.

All five of the floats drifted with an average speed of approximately 200 meters/hour, which is about 0.1 kt or 5 cm/sec.

5. Beamforming With the Swallow Float Array

Having determined the float positions during the September 1986 experiment, the mid-water column floats may now be treated as an array of sensors and their time series beamformed. In general, arrays of spatially separated sensors are employed in measuring a sound field in order to determine its *directionality*, which is the direction from which sound is arriving. This is the goal of beamforming with the Swallow floats.

Beamforming with an array of Swallow floats turns out to be considerably different from beamforming with an array of omni-directional hydrophones. This is because each float contains 3 orthogonally-oriented geophones, and each geophone's response depends upon the angle between the source direction and the geophone axis. Simulations are used to demonstrate differences between the results obtained using omni-directional and directional sensors. The experimental results are thus interpretable, although the large array aperture and an inhomogeneous sound field cause them to be somewhat confusing.

Float Positions, September 1986 Experiment

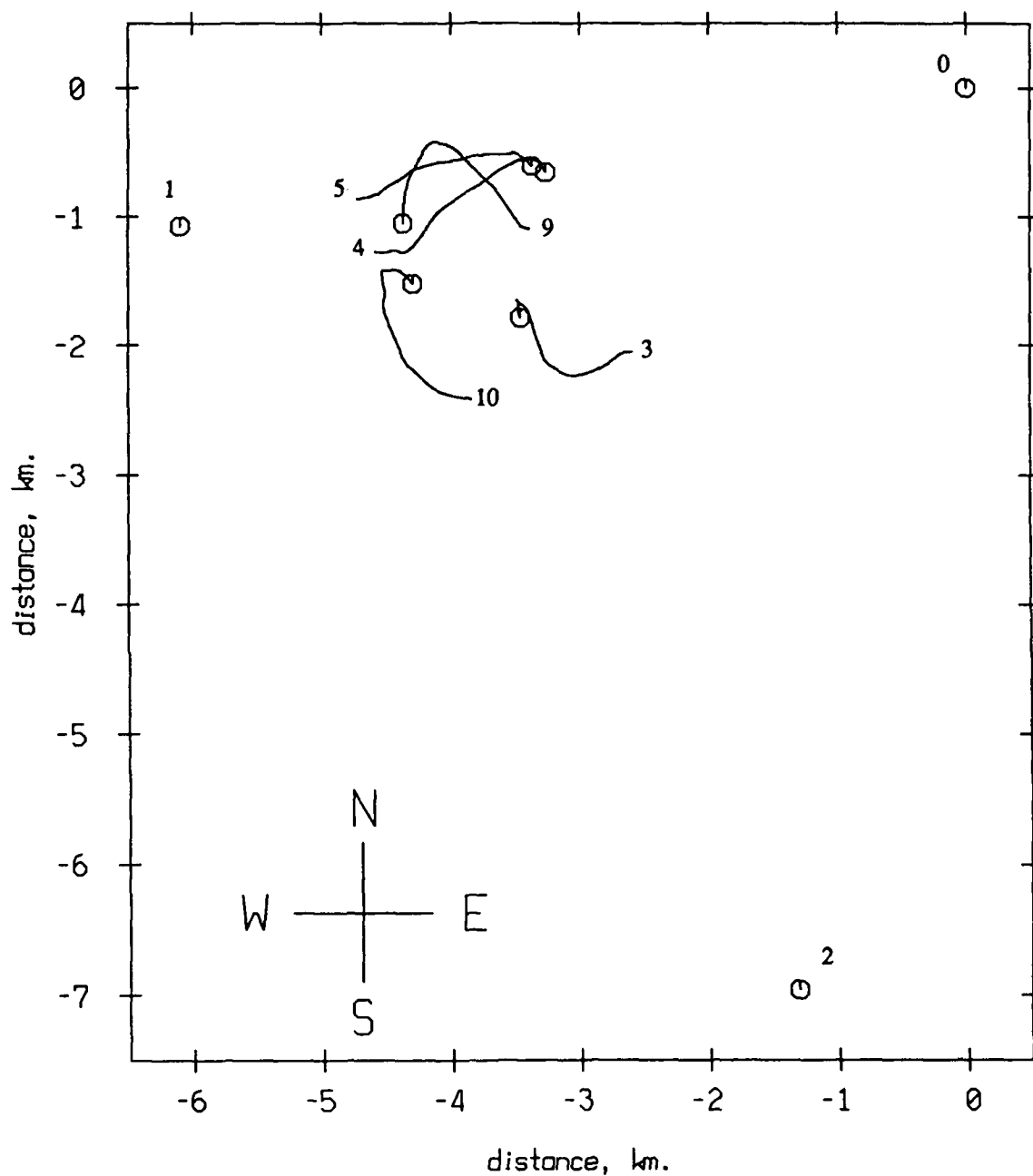


Figure 4.7 Kalman filter estimate of time-varying float positions between records 1150 and 1870 (approximately 9 hours duration) for the September 1986 experiment. Floats 0, 1 and 2 are on the bottom; floats 3, 4, 5, 9 and 10 are freely-drifting. "O" marks the starting position.

Float Positions, September 1986 Experiment

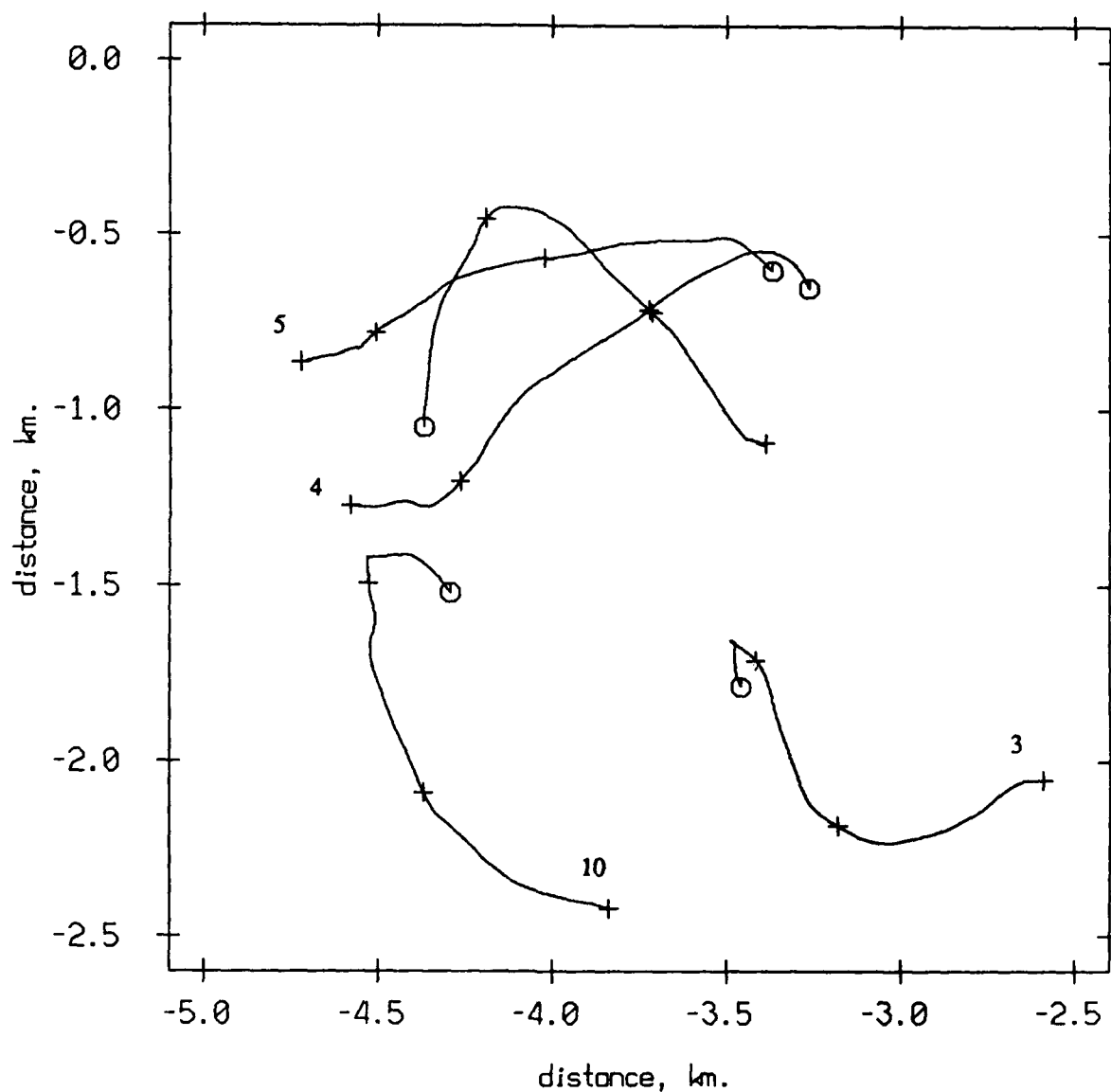


Figure 4.8 Kalman filter estimate of time-varying float positions between records 1150 and 1870 (approximately 9 hours duration) for the September 1986 experiment. Depths are approximately 1000 meters for floats 3, 4, 5, and 10, and approximately 800 meters for float 9. "O" marks the starting position. "+" marks 3 hour intervals.

5.1. Theoretical Development and Simulation Results

The job of a time delay and sum beamformer is to combine array element signals to produce beams which listen preferentially in particular directions, called *look* directions. For each look direction, a set of delays must be calculated which, when applied to the element time series, cause signals arriving from that direction to be aligned in phase, or *co-phased*. The amplitude of the sum of harmonic signals with the same phase is the sum of their amplitudes. This is greater than the sum of harmonic signals which do not have the same phase.

Consider an array of sensors and one or more harmonic sources. Assume that all of the sources are located far from the array so that wavefront curvature is minimal over the array aperture. As defined in Figure 5.1, the azimuthal bearing from the array to the source is measured counterclockwise from the X axis and denoted by θ_s . The source elevation angle is measured from the horizontal and denoted ϕ_s . If the array is excited by a complex exponential signal

$$s(t) = e^{i\omega t} \quad (5.1)$$

whose bearing is θ_s, ϕ_s from the array, then the beamformer output can be written

$$b(t) = br(\theta_l, \phi_l, \theta_s, \phi_s) \cdot e^{i\omega t} \quad (5.2)$$

where the array *bearing response* $br(\theta_l, \phi_l, \theta_s, \phi_s)$ is a complex quantity which contains the amplitude and phase of the response.²⁶ This is a useful notation because the bearing responses of different sensors and arrays can be compared to each other without reference to the $e^{i\omega t}$ term.

5.1.1. Single Element Arrays

Consider first a simple array composed of a single, omni-directional element. For simplicity, start with a source which is in the XY plane ($\phi_s = 0$) and constrain the look direction to also lie in the XY plane ($\phi_l = 0$). Since the array contains only one sensor whose response does not depend upon the direction to the source, the array bearing response does not depend upon either the source or look direction azimuth angles.

$$br(\theta_l, \theta_s) = 1 \quad (\text{single omni-directional element}) \quad (5.3)$$

Now substitute a single geophone for the omni-directional sensor. The geophone's response is directional, i.e. it depends upon the angle between its axis and the bearing to the source. Denote the geophone azimuth angle relative to the array X axis as θ_H as shown in Figure 5.2, and set the geophone elevation angle ϕ_H equal to zero. The geophone bearing response is

$$br(\theta_l, \theta_s) = \cos(\theta_H - \theta_s) \quad (\text{single geophone}) \quad (5.4)$$

This is called a *dipole* response because it has the same form as the field of an electric dipole.²⁷ If the geophone axis is rotated until it is parallel to the X axis of the array, its bearing response becomes

$$br(\theta_l, \theta_s) = \cos(\theta_s) \quad (\text{single geophone parallel to X axis}) \quad (5.5)$$

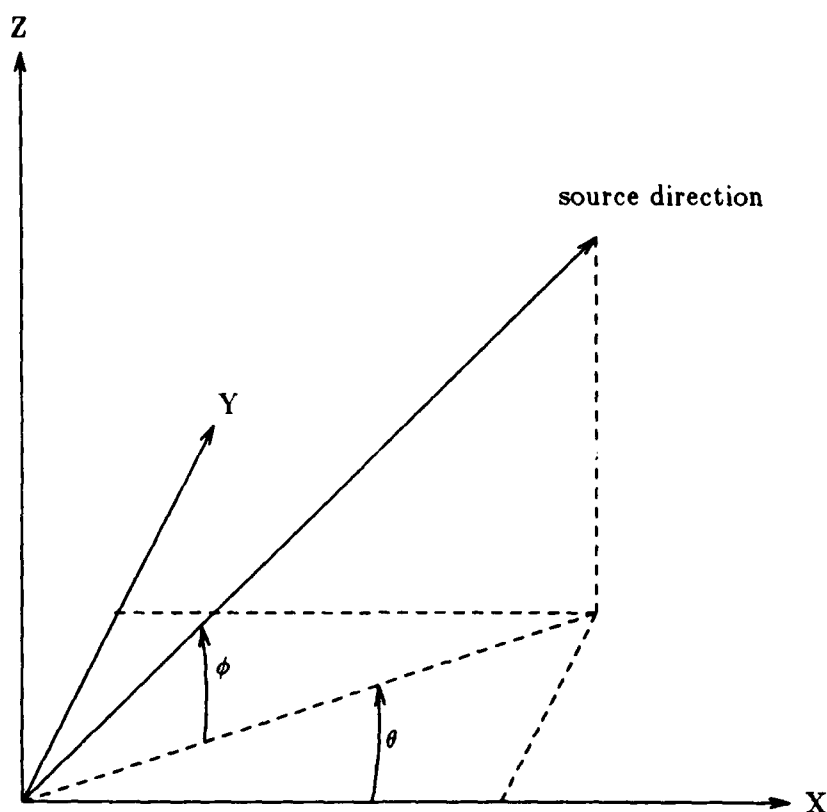


Figure 5.1 Coordinate system used for beamforming.
 θ - azimuth angle in the XY plane
 ϕ - elevation angle out of the XY plane.

Each Swallow float contains three orthogonally-oriented, collocated geophones whose axes are assumed for now to coincide with the X, Y and Z axes of the array. For the geophone whose axis is parallel to the Y axis, $\theta_H = 90^\circ$ and its bearing response is:

$$br(\theta_i, \theta_s) = \cos(90 - \theta_s) = \sin(\theta_s) \quad (\text{single geophone parallel to Y axis}) \quad (5.6)$$

Now consider an array of two, collocated geophones, one parallel to the X and the other parallel to the Y axis, as shown in Figure 5.3. The array bearing response can be maximized in the direction of the source by forming a time series for each look direction in which each sensor signal is multiplied by the cosine of the angle between its axis and the look direction (the *look direction cosines*).

$$\begin{aligned} \left[br(\theta_i, \theta_s) \right]_{\text{X and Y axis geophones}} &= \left[br(\theta_i, \theta_s) \right]_{\text{X axis geophone}} \cdot \cos(\theta_i) \\ &+ \left[br(\theta_i, \theta_s) \right]_{\text{Y axis geophone}} \cdot \cos(90^\circ - \theta_i) \end{aligned}$$

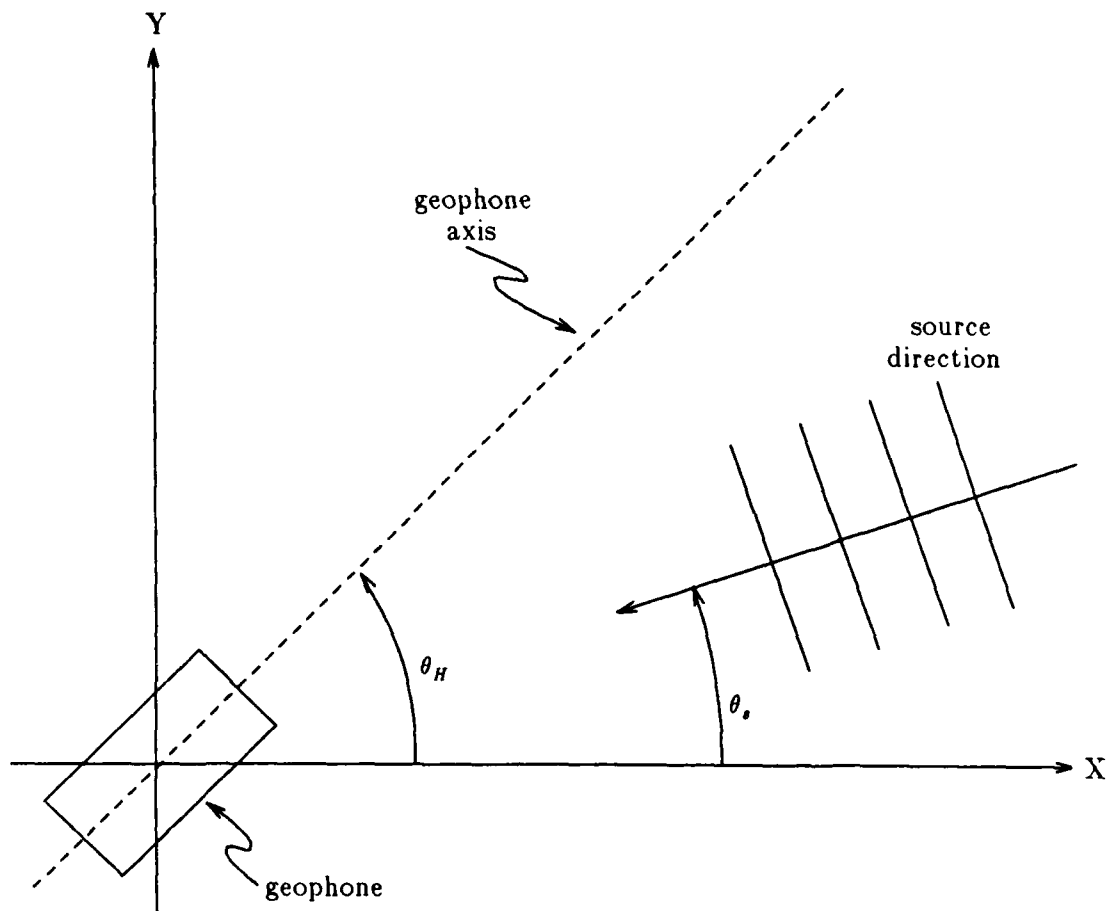


Figure 5.2 Single geophone geometry.

Substituting (5.5) and (5.6) for the bearing responses of the individual geophones and using $\cos(90^\circ - \theta_i) = \sin(\theta_i)$

$$\begin{aligned} \left[br(\theta_i, \theta_s) \right]_{\text{X and Y axis geophones}} &= \cos(\theta_s) \cdot \cos(\theta_i) + \sin(\theta_s) \cdot \sin(\theta_i) \\ &= \cos(\theta_s - \theta_i) \quad (\text{X and Y axis geophones}) \end{aligned} \quad (5.7)$$

It is clear from equation (5.7) that the bearing response of the collocated, orthogonally-oriented geophone pair can provide information about the source azimuth, whereas the omni-directional element bearing response of (5.3) does not. Comparing the bearing response of two geophones to that of one omni-directional sensor may seem unfair. However, the geophone pair are packaged as one unit, so that it is actually the bearing responses of two sensor packages which are being compared.

This is an important comparison because a major part of the effort in measuring sound in the ocean is in getting the sensor in place, getting power to it, storing its output, and retrieving it. Deploying two separate packages requires very nearly twice the hardware and effort of deploying one package. Deploying two geophones packaged as one unit requires about the same

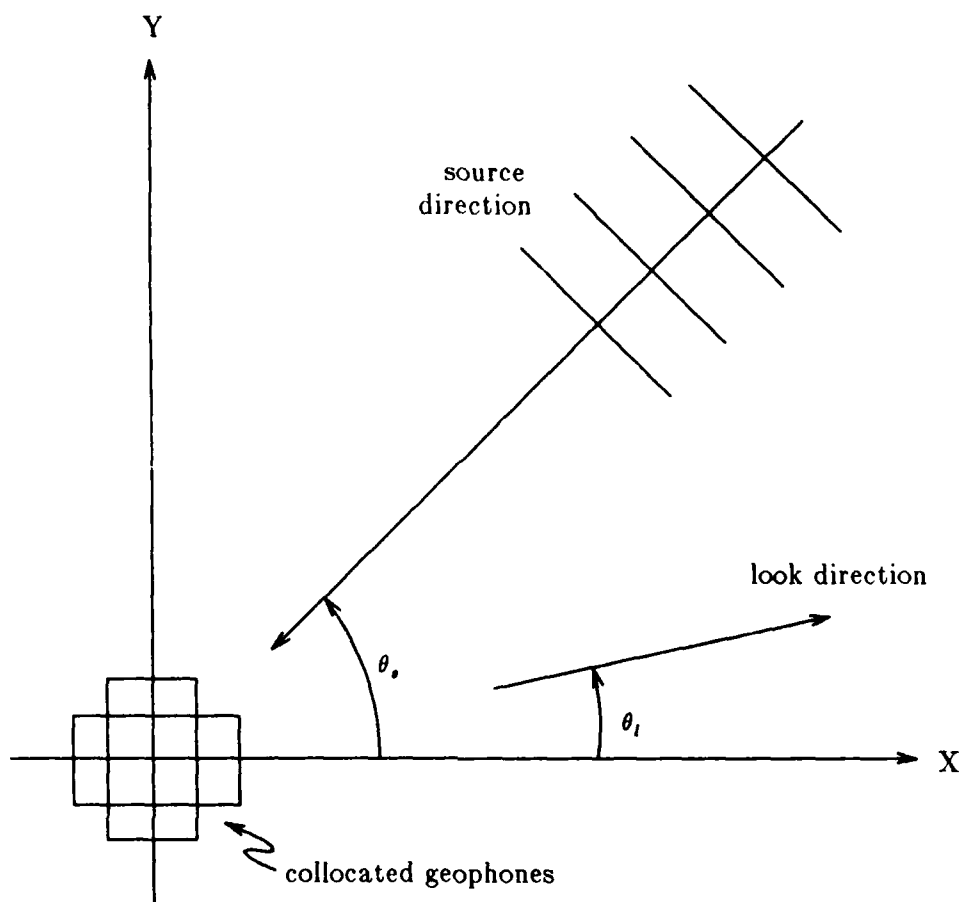


Figure 5.3 Geometry for two collocated geophones, one parallel to the X axis and one parallel to the Y axis.

hardware and effort as deploying one omni-directional element. Thus the advantage accrued by deploying geophone pairs (or as we will see shortly, geophone triplets), is that source bearing information is obtained with just a single package.

If there is more than one source transmitting a signal to the array, then the bearing response of the single omni-directional sensor is the sum of the responses to the sources individually, which is independent of the source bearing angles.

$$br(\theta_l, \theta_{s1}) + br(\theta_l, \theta_{s2}) = 2 \quad (\text{single omni-directional element}) \quad (5.8)$$

Similarly, the bearing response of the collocated, orthogonally-oriented geophone pair is the sum of the responses to the sources individually:

$$br(\theta_l, \theta_{s1}) + br(\theta_l, \theta_{s2}) = \cos(\theta_l - \theta_{s1}) + \cos(\theta_l - \theta_{s2}) \quad (\text{X and Y axis geophones}) \quad (5.9)$$

Equation (5.9) has a peak when the look direction equals either of the source directions.

5.1.2. Multi-Element Arrays

Now consider an array of sensors. The elements are uniformly spaced on the Y axis at 100 meters intervals as shown in Figure 5.4. The array bearing response is no longer independent of the source and look directions because the elements are spatially separated and the beamformer can co-phase signals coming from the look direction. For simplicity in the development, the source and look direction continue to be constrained to the XY plane. The results will be expanded to three dimensions subsequently.

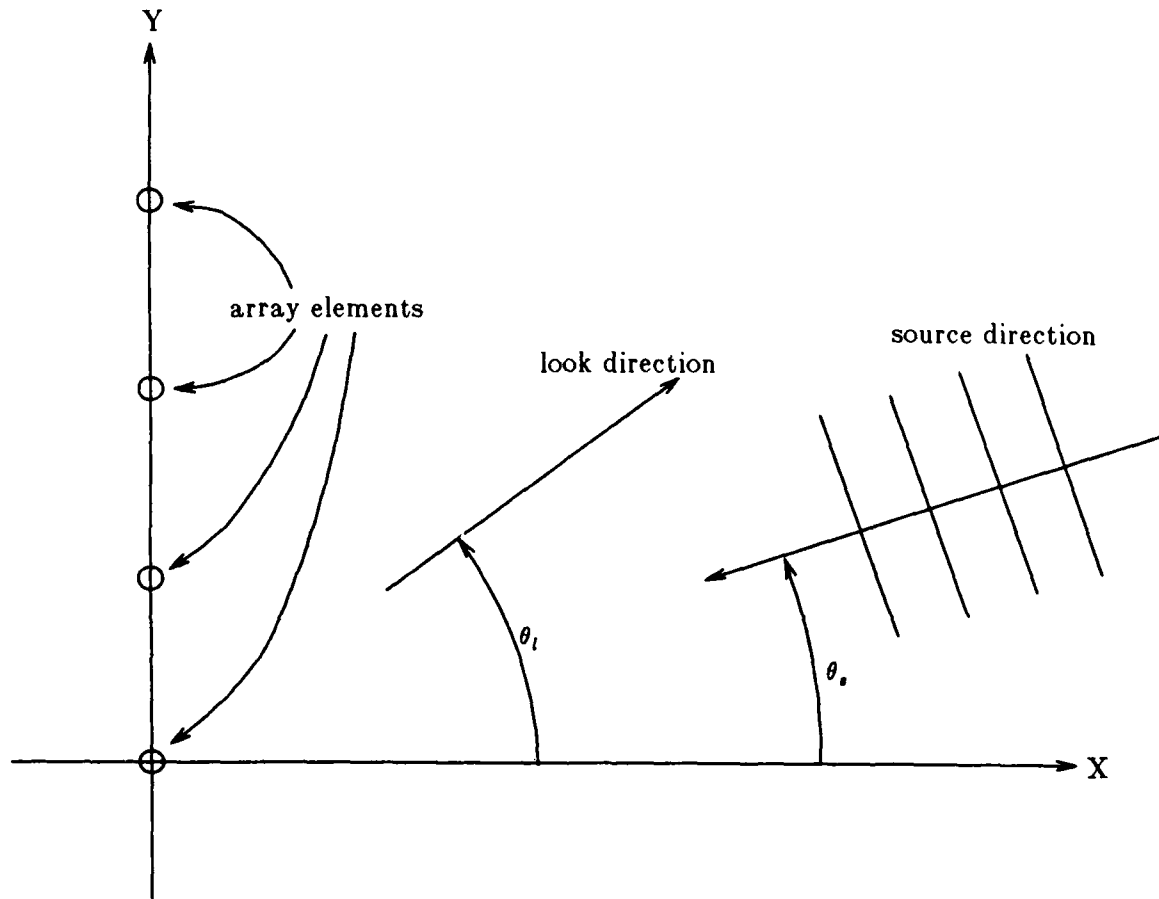


Figure 5.4 Multi-element array geometry.

Figure 5.5 compares the magnitude of the bearing responses of the omni-directional element and orthogonally-oriented geophone arrays with a 6.7 Hz source at $\theta_s = 0^\circ$. Both bearing responses have peaks in the source direction, which is desirable. However, both bearing responses also have peaks in another direction too, which indicates *directional ambiguity* with respect to the array axis (the Y axis of the coordinate system). When the source bearing is 0° (source broadside to the array), we know that it is broadside but we cannot determine which side it is on (0° or 180°). This is known as the *right-left ambiguity* of a line array because if we stand at the origin and look down the array axis, we cannot tell rather the source is coming from our right or left. The ambiguity (0° or 180°) persists in the geophone array bearing response because the magnitude of the geophone's $\cos(\theta_l)$ response has a 180° (forward-backward) ambiguity, which, when the source angle is 0° , coincides with the line array's right-left ambiguity.

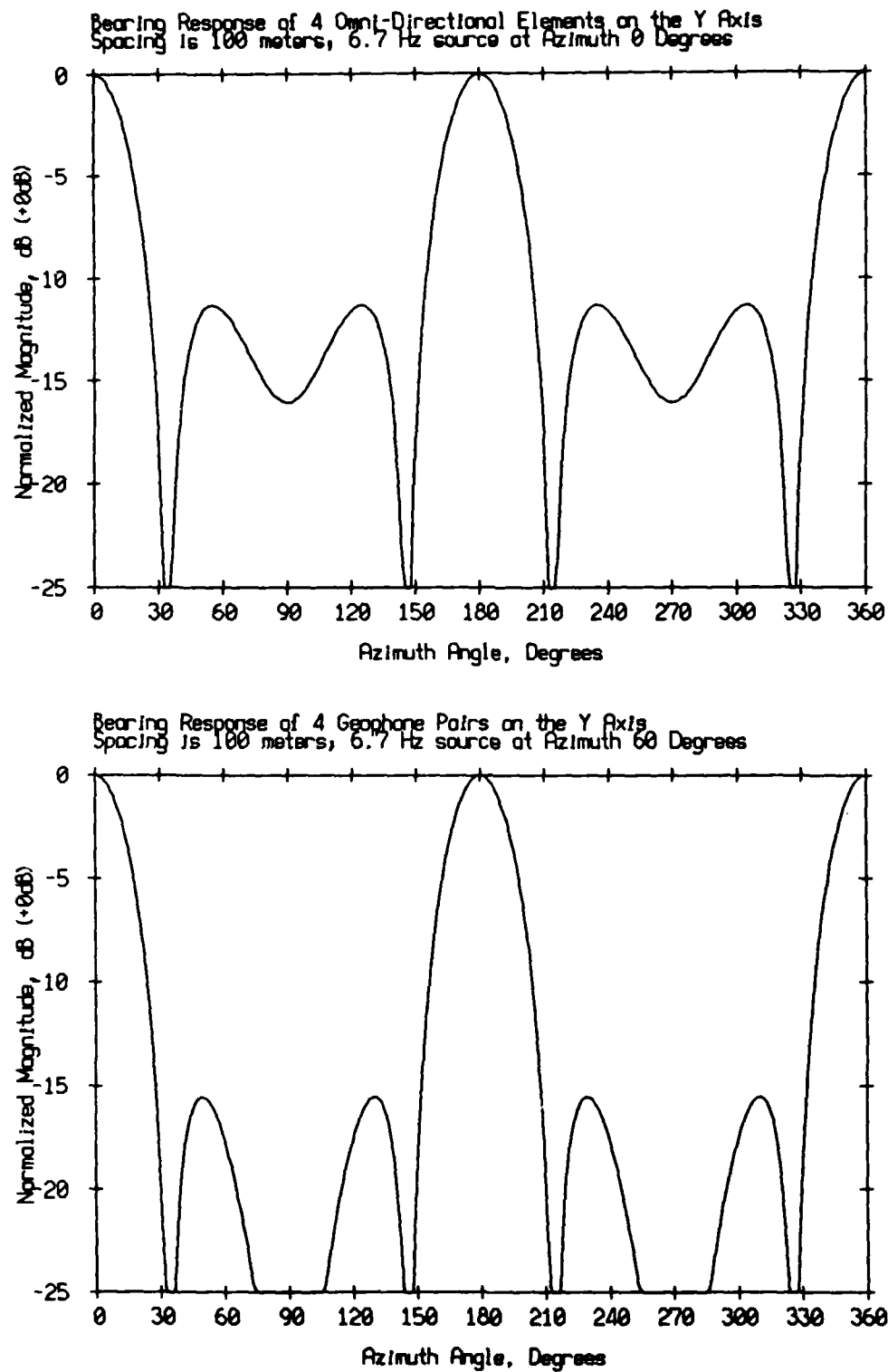


Figure 5.5 Comparison of the magnitude of the bearing responses of omni-directional element and geophone arrays with a 6.7 Hz source at $\theta_s = 0^\circ$. The array elements are uniformly spaced at 100 meter intervals.

The half-wavelength spacing for this frequency, with $c = 1500$ meters/sec, is

$$\frac{\lambda}{2} = \frac{c/f}{2} = \frac{1500 \text{ meters/sec}}{2 \cdot 6.7 \text{ Hz}} = 112 \text{ meters} \quad (5.10)$$

Thus the element spacing of 100 meters used in the simulations is less than $\lambda/2$. This is why in the omni-directional bearing response, the two side lobes merge at $\theta_l = 90^\circ$ and $\theta_l = 270^\circ$ rather than going to zero as they would if the element spacing were exactly $\lambda/2$.

Note from Figure 5.5 that the geophone array achieves about 5 dB side lobe level reduction. This is because of the directionality of the geophones parallel to the X axis, and because the geophones parallel to the Y axis do not detect the signal at all.

Figure 5.6 compares the magnitude of the bearing responses of the omni-directional element and orthogonally-oriented geophone arrays with a 6.7 Hz source at $\theta_s = 60^\circ$. The directional ambiguity in the omni-directional element bearing response is such that a source bearing 60° from the array cannot be distinguished from one bearing 120° . This ambiguity is reduced by 5 dB in the geophone array bearing response because the geophone and array ambiguities are not pointed in the same direction. The geophone array is again seen to achieve considerable side lobe reduction.

5.1.3. Sparse Multi-Element Arrays

The advantages offered by Swallow floats in closely-spaced, uniform arrays are clear enough, but we saw in Chapter 4 that the mid-water column floats were 1000 to 2200 meters apart during the September 1986 experiment. Arrays whose element spacing is greater than one-half the wavelength of sound at the highest frequency of interest are said to be *sparse*. The bearing response of sparse, uniformly-spaced arrays may contain lobes whose levels are as high as main lobe, in directions other than the source direction. They are called *grating lobes*.²⁰

Figures 5.7 and 5.8 compare the bearing responses of omni-directional element and geophone arrays with a 350 meter element spacing and with 6.7 Hz sources at 0° and 60° . The numerous grating lobes make it impossible to determine the source direction using the omni-directional element array. The geophone array reduces grating lobes and makes it much easier to recognize the source bearing. The 180° ambiguity persists with the source at 0° because the X axis geophones and the array both have ambiguities in this direction. The source direction ambiguity is reduced 5 dB when the source is at 60° .

5.1.4. Three-Dimensional Beamforming

The comparison made thus far in this Chapter is now expanded to include look directions and source bearings not restricted to the XY plane. As in equation (5.3), the single, omni-directional element bearing response is independent of look or source bearing angles

$$br(\theta_l, \phi_l, \theta_s, \phi_s) = 1 \quad (\text{single omni-directional element}) \quad (5.11)$$

Also as in the two-dimensional case, the bearing response of the geophone depends upon the angle between the geophone axis and the source direction. If that angle is denoted α , then

$$br(\theta_l, \phi_l, \theta_s, \phi_s) = \cos(\alpha) \quad (\text{single omni-directional element}) \quad (5.12)$$

The definition of the dot product can be used to obtain an expression for $\cos(\alpha)$ in terms of θ_l ,

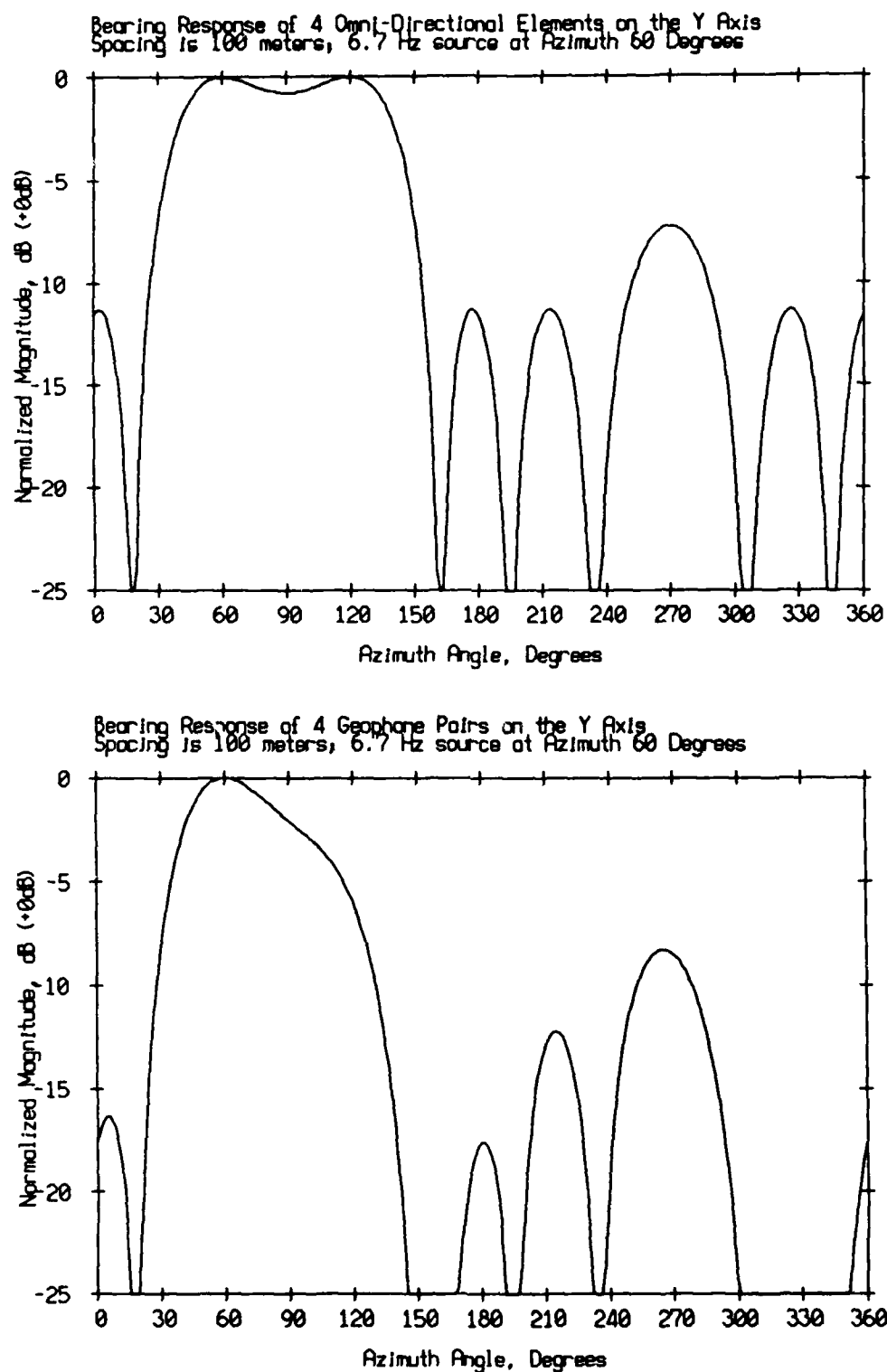


Figure 5.6 Comparison of the magnitude of the bearing responses of omni-directional element and geophone arrays with a 6.7 Hz source at $\theta_s = 60^\circ$. The array elements are uniformly spaced at 100 meter intervals.

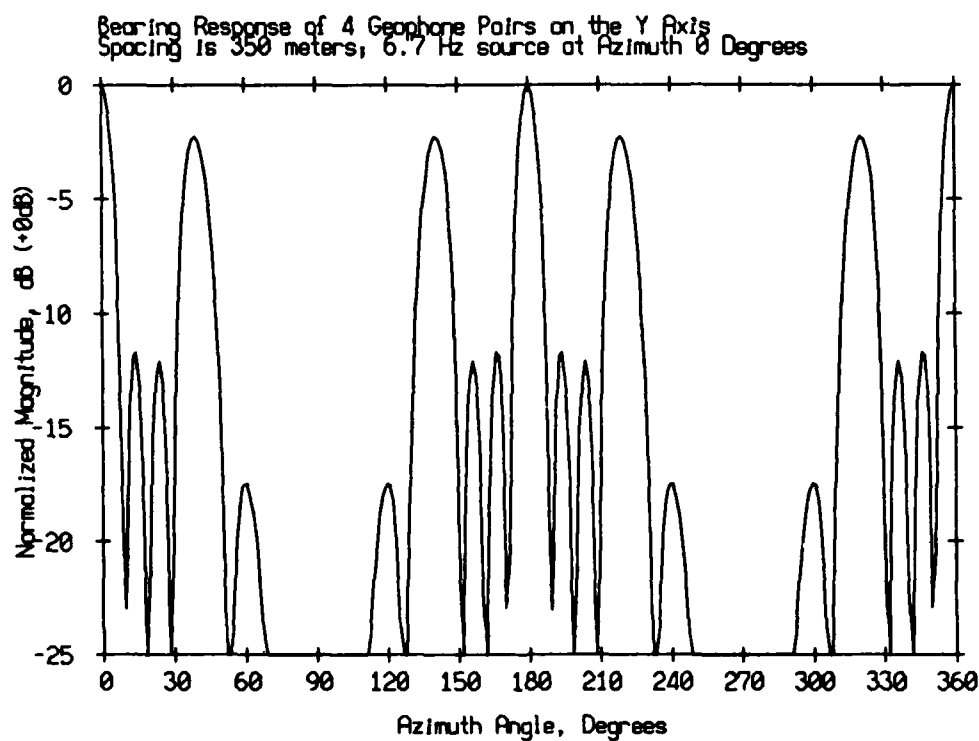
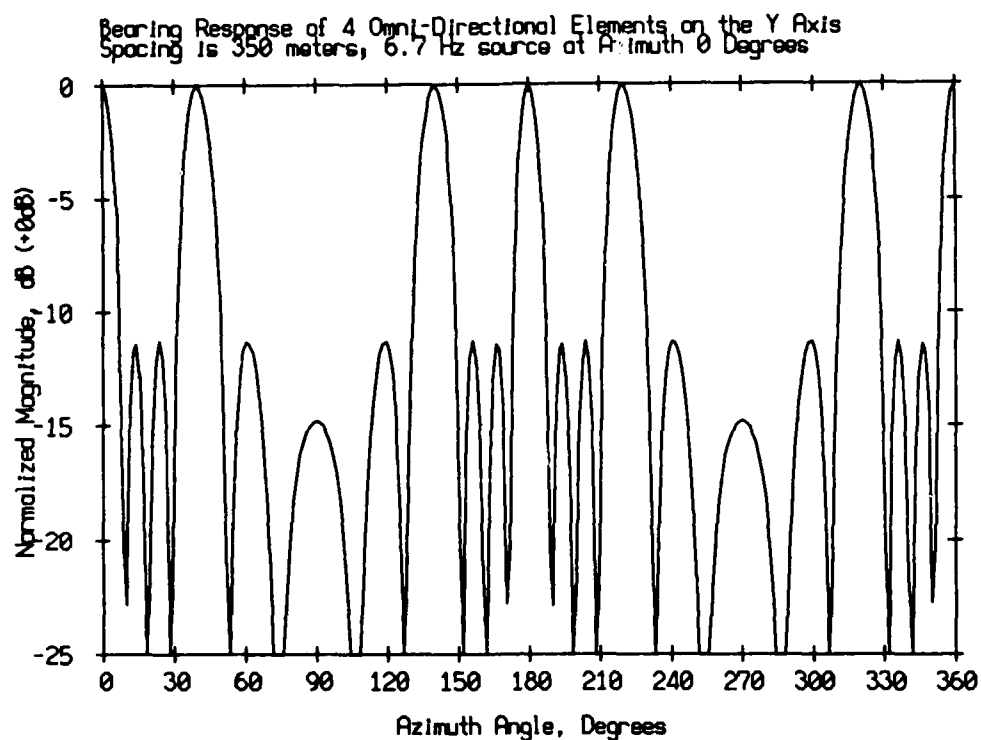


Figure 5.7 Comparison of the magnitude of the bearing responses of omni-directional element and geophone arrays with a 6.7 Hz source at $\theta_s = 0^\circ$. The array elements are uniformly spaced at 350 meter intervals.

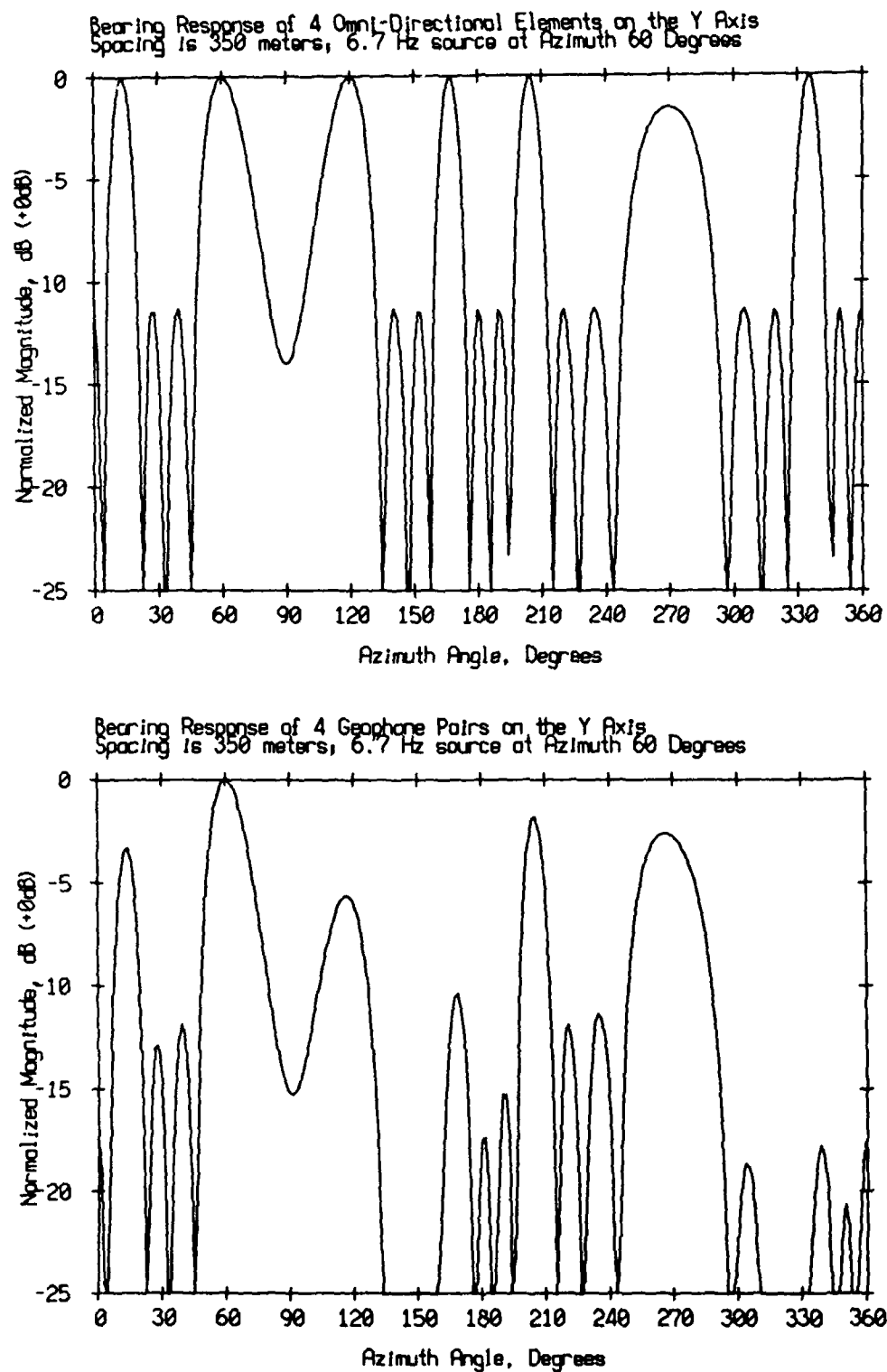


Figure 5.8 Comparison of the magnitude of the bearing responses of omni-directional element and geophone arrays with a 6.7 Hz source at $\theta_s = 60^\circ$. The array elements are uniformly spaced at 350 meter intervals.

ϕ_l , θ_s , and ϕ_s . If \vec{H} and \vec{S} are unit vectors in the geophone axis and source directions, respectively, then

$$\vec{H} \cdot \vec{S} = |\vec{H}| |\vec{S}| \cos(\alpha) \quad (5.13)$$

Denoting the geophone azimuth and elevation angles θ_H and ϕ_H , respectively, then using the coordinate system defined in Figure 5.1, the components of \vec{H} are

$$\vec{H} = \cos(\theta_H) \cos(\phi_H) \vec{e}_x + \sin(\theta_H) \cos(\phi_H) \vec{e}_y + \sin(\phi_H) \vec{e}_z \quad (5.14)$$

where \vec{e}_x , \vec{e}_y and \vec{e}_z are unit vectors along the axes. Similarly, the components of \vec{S} are

$$\vec{S} = \cos(\theta_S) \cos(\phi_S) \vec{e}_x + \sin(\theta_S) \cos(\phi_S) \vec{e}_y + \sin(\phi_S) \vec{e}_z \quad (5.15)$$

The dot product is thus

$$\begin{aligned} \cos(\alpha) = \vec{H} \cdot \vec{S} &= \cos(\theta_H) \cos(\phi_H) \cos(\theta_S) \cos(\phi_S) + \sin(\theta_H) \cos(\phi_H) \sin(\theta_S) \cos(\phi_S) \\ &+ \sin(\phi_H) \sin(\phi_S) \end{aligned}$$

so that

$$br(\theta_l, \phi_l, \theta_s, \phi_s) = \cos(\theta_H - \theta_s) \cos(\phi_H) \cos(\phi_s) + \sin(\phi_H) \sin(\phi_s) \quad (\text{single geophone}) \quad (5.16)$$

If the geophone is rotated until its axis is parallel to the array X axis ($\theta_H = 0^\circ$, $\phi_H = 0^\circ$), its bearing response becomes

$$br(\theta_l, \phi_l, \theta_s, \phi_s) = \cos(\theta_s) \cos(\phi_s) \quad (\text{single geophone parallel to X axis}) \quad (5.17a)$$

Similarly, the bearing response of a geophone parallel to the Y axis ($\theta_H = 90^\circ$, $\phi_H = 0^\circ$) will be

$$br(\theta_l, \phi_l, \theta_s, \phi_s) = \sin(\theta_s) \cos(\phi_s) \quad (\text{single geophone parallel to Y axis}) \quad (5.17b)$$

and that of a geophone parallel to the Z axis ($\phi_H = 90^\circ$) will be

$$br(\theta_l, \phi_l, \theta_s, \phi_s) = \sin(\phi_s) \quad (\text{single geophone parallel to Z axis}) \quad (5.17c)$$

Now consider three ~~collocated~~ geophones, one oriented parallel to each axis. The bearing response of the combination is formed by multiplying the sensor signals by the look direction cosines, which are

$$l_x = \cos(\theta_l) \cos(\phi_l)$$

$$l_y = \sin(\theta_l) \cos(\phi_l)$$

$$l_z = \sin(\phi_l) \quad (5.18)$$

The combined bearing response is thus

$$\begin{aligned} \left[br(\theta_l, \phi_l, \theta_s, \phi_s) \right]_{X, Y \text{ and } Z \text{ axis geophones}} &= \left[br(\theta_l, \phi_l, \theta_s, \phi_s) \right]_{X \text{ axis geophone}} \cdot \cos(\theta_l) \cos(\phi_l) \\ &+ \left[br(\theta_l, \phi_l, \theta_s, \phi_s) \right]_{Y \text{ axis geophone}} \cdot \sin(\theta_l) \cos(\phi_l) \\ &+ \left[br(\theta_l, \phi_l, \theta_s, \phi_s) \right]_{Z \text{ axis geophone}} \cdot \sin(\phi_l) \\ &= \cos(\theta_s) \cos(\phi_s) \cos(\theta_l) \cos(\phi_l) + \sin(\theta_s) \cos(\phi_s) \sin(\theta_l) \cos(\phi_l) + \sin(\phi_s) \sin(\phi_l) \\ &= \cos(\theta_s - \theta_l) \cos(\phi_s) \cos(\phi_l) + \sin(\phi_s) \sin(\phi_l) \end{aligned} \quad (5.19)$$

Equation (5.19) has a maximum when the source and look directions are equal. When the source and look direction azimuth angles are equal, equation (5.19) reduces to $\cos(\phi_s - \phi_l)$, which has a maximum when the look and source direction elevation angles are equal.

Figure 5.9 shows the bearing response of a four omni-directional element array to a 6.7 Hz source at azimuth $\theta_s = 0^\circ$ and elevation $\phi_s = 0^\circ$. The array elements are uniformly spaced at 100 meter intervals. The look direction azimuth angle ranges from 0° to 360° , and the elevation angle varies from -30° to 30° . Each trace indicates the bearing response for a particular look direction elevation angle ϕ_l . The vertical scale for each trace is -10 to 0 dB, i.e. the trace is clipped at -10 dB.

Several points can be made about this bearing response. First, the $\phi_l = 0$ trace is identical to the top 10 dB of the upper plot in Figure 5.5, which was also made with $\phi_l = 0$. Second, the levels of the peaks at $\theta_l = 0^\circ$ and 180° is independent of ϕ_l . This is due to the array's right-left ambiguity, which becomes conical in 3 dimensions. When the source is broadside, the directional ambiguity is circular so that the cone angle is 180° . Third, the lobe width increases as $|\phi_l|$ increases. (This can be seen by looking closely at the Figure). This is due to the coordinate system used in the beamforming. As the elevation angle increases, and as we sweep through a 360° azimuth angle, an increasingly greater percentage of the sweep is within the main lobe. When the look elevation angle is straight up or straight down ($\phi = \pm 90^\circ$, not shown in Figure 5.9), the entire sweep is pointed toward the peak of the main lobe and the level of the trace is 0 dB independent of azimuth angle.

Now replace each omni-directional element with three collocated, orthogonally-oriented geophones, one parallel to each axis. Figure 5.10 shows the bearing response of the array to the same source as in Figure 5.9. The geophone array response appears quite similar to the omni-directional element array except that the peak response at $\theta_l = 0^\circ$ and $\theta_l = 180^\circ$ is attenuated as $|\phi_l|$ increases. This is due to the X axis geophone's directional response and because the Z axis geophone does not receive the signal at all. At $\phi_l = 90^\circ$ the trace is clipped at -10 dB. Note that the response at $\phi_l = 0$ is the same as the top 10 dB of the bottom panel in Figure 5.5.

Figures 5.11 and 5.12 are the bearing responses of the omni-directional and geophone element arrays with the source at $\theta_s = 60^\circ$, $\phi_s = 0^\circ$ as in Figures 5.6. The response along the cone swept out when $\phi_l \neq 0^\circ$ and θ_l goes from 0° to 360° is hard to visualize. However, one can see that the $\phi_l = 0^\circ$ traces correspond to the top 10 dB of the plots in Figure 5.6. Also, comparing Figures 5.11 and 5.12 shows that the source direction ambiguity at $\theta_l = 120^\circ$ is reduced by the geophone's directionality.

The array bearing response is even harder to interpret when $\phi_s \neq 0^\circ$. However, a comparison of sparse omni-directional and geophone arrays serves to emphasize the enhanced

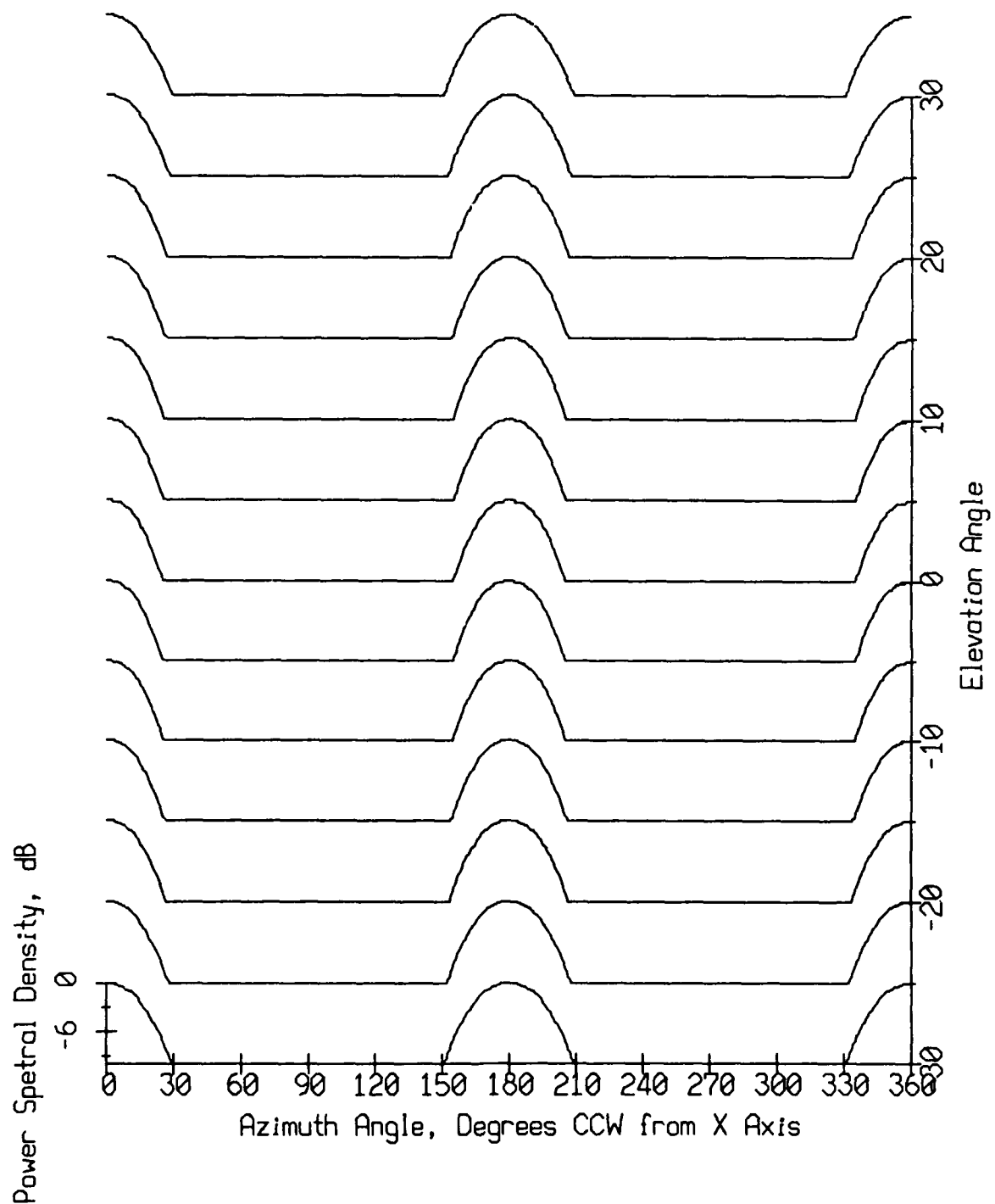


Figure 5.9 Bearing response of a four omni-directional element array to a 6.7 Hz source at azimuth $\theta_s = 0^\circ$ and elevation $\phi_s = 0^\circ$. The array elements are uniformly spaced at 100 meter intervals.

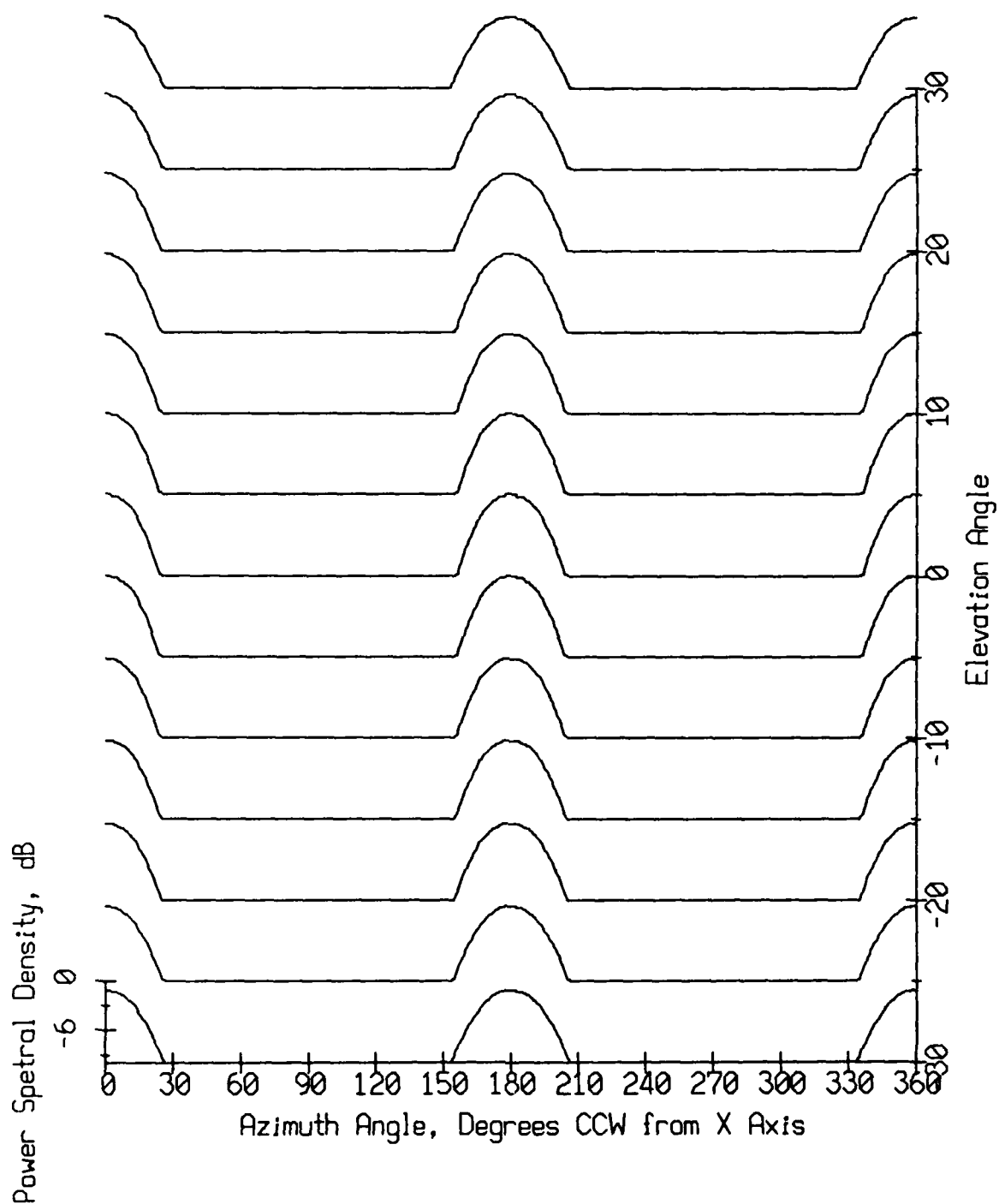


Figure 5.10 Bearing response of a four element array of orthogonally-oriented geophone triplets. A 6.7 Hz source is located at azimuth $\theta_s = 0^\circ$ and elevation $\phi_s = 0^\circ$. The array elements are uniformly spaced at 100 meter intervals.

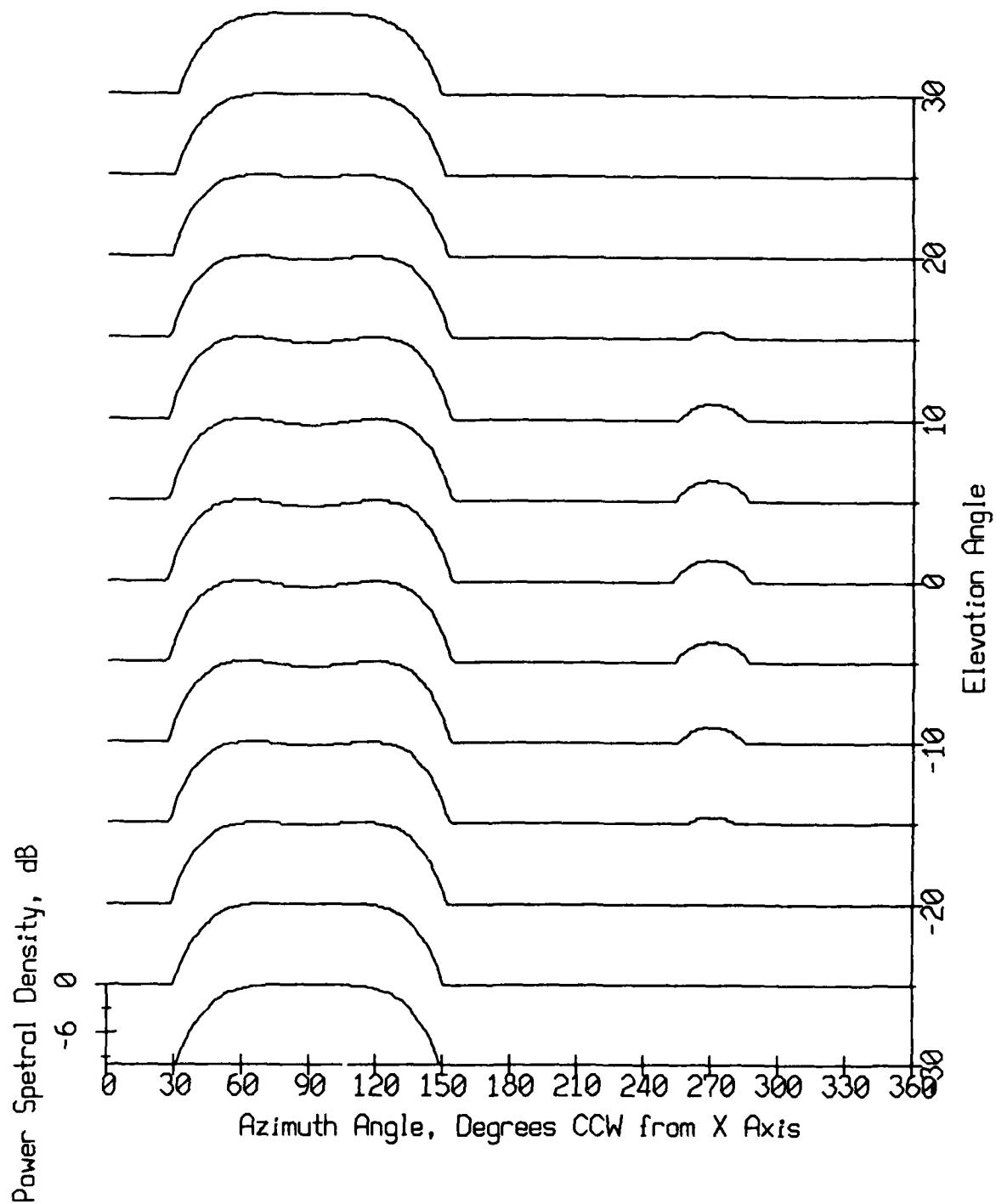


Figure 5.11 Bearing response of a four omni-directional element array to a 6.7 Hz source at azimuth $\theta_s = 60^\circ$ and elevation $\phi_s = 0^\circ$. The array elements are uniformly spaced at 100 meter intervals.

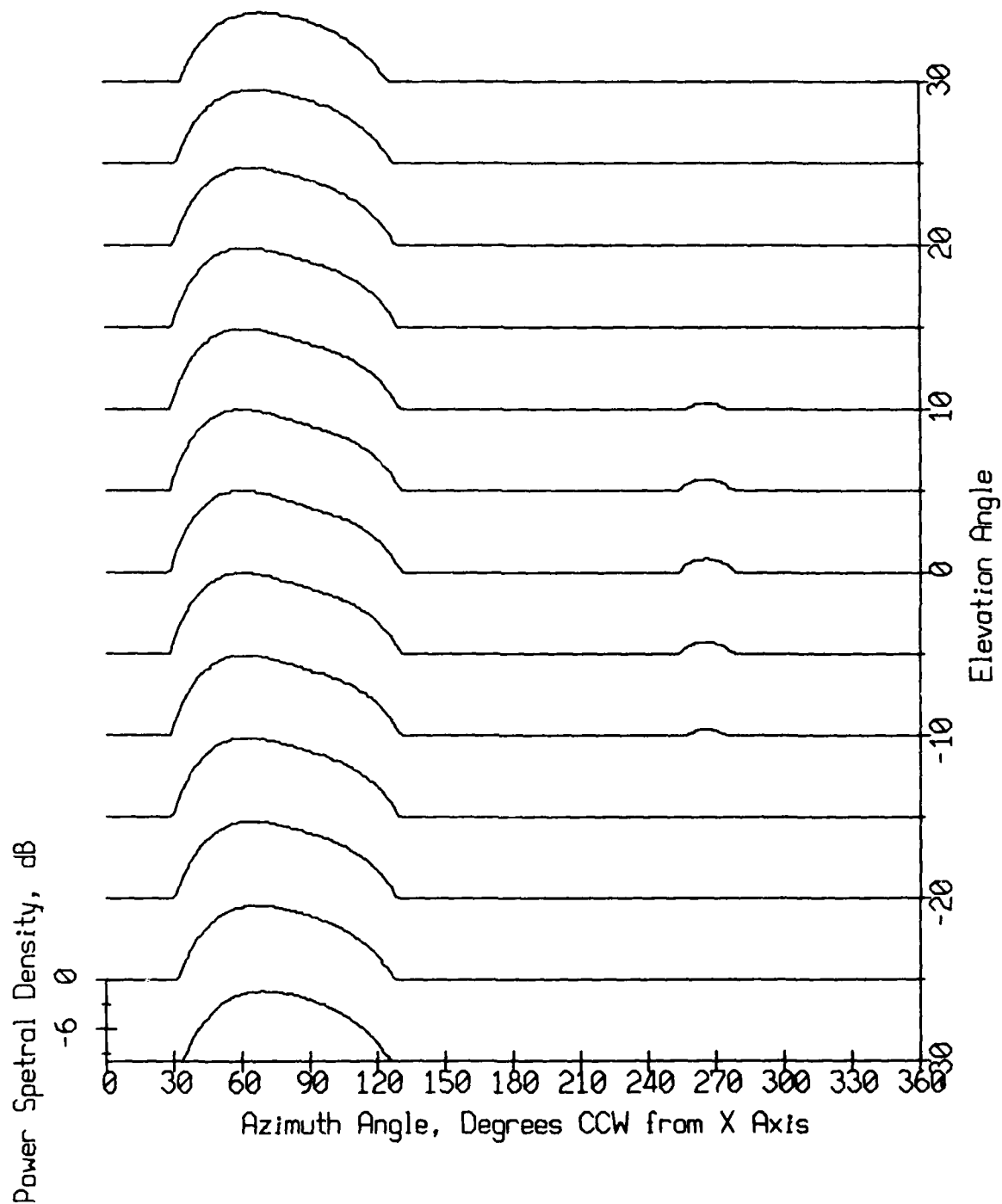


Figure 5.12 Bearing response of a four element array of orthogonally-oriented geophone triplets. A 6.7 Hz source is located at azimuth $\theta_s = 60^\circ$ and elevation $\phi_s = 0^\circ$. The array elements are uniformly spaced at 100 meter intervals.

capability of the geophone array to resolve source direction. Figure 5.13 shows the bearing response of the omni-directional element array with the source at $\theta_s = 60^\circ$, $\phi_s = 20^\circ$. The array is sparse and the bearing response contains numerous grating lobes like those seen in Figure 5.7. The line array directional ambiguity is near $\theta_l = 120^\circ$ as long as the look elevation is small. As the look elevation angle becomes large (positive or negative), the ambiguity and source direction peaks move closer together.

Figure 5.14 shows the bearing response of the geophone array to the same source. The geophone array clearly provides an enhanced capability to determine source direction. The level in the direction of the array ambiguity, $\theta_l = 120^\circ$, $\phi_s = 20^\circ$, is 5 dB lower than in the omni-directional element array. The strong grating lobe seen at $\theta_s \approx 205^\circ$, $\phi_s \approx -20^\circ$ is also seen in Figure 5.8 and 5.13, as are the lower level grating lobes. There has been significant grating lobe level reduction, although there remain a few high level lobes which, in the presence of noise, might be confused with the main lobe.

5.1.5. Swallow Float Array

As a last simulation, consider the array formed by the mid-water column floats during the September 1986 experiment. The element spacing is about 1000 to 2200 meters, so the array is sparse, and the elements are randomly located in three dimensions. On the average, sparse randomly-spaced arrays are not subject to grating lobes, but may have side lobes whose levels are nearly as high as the main lobe.²⁰ Thus, the Swallow float array bearing response may be expected to contain high level side lobes.

Figures 5.15 and 5.16 show the three-dimensional bearing response of a four element array of Swallow floats located at the estimated float positions for record 1830 of the September 1986 experiment. The two Figures contain 6.7 Hz sources at azimuth $\theta_s = 0^\circ$ and elevation $\phi_s = 0^\circ$, and azimuth $\theta_s = 60^\circ$ and elevation $\phi_s = -10^\circ$, respectively. Both Figures contain numerous, high level side lobes, many only 1 dB lower than the main lobe level.

The bearing response for small elevation angles is composed of ridges which are narrow in azimuth, about 5° , and broad in elevation, about 20° . This vertical ridge structure will also be seen in the experiment data.

Other prominent features are a strong 180° ambiguity and a weak response at $\pm 90^\circ$ from the source direction. Both of these features are due to geophone's directionality, and they too will be seen in the experimental data.

5.2. Application to Experiment Data

It has been shown that the proper way to combine orthogonally-oriented geophone signals is to multiply by the look direction cosines and sum. There are, however, some preliminary steps which must be taken when processing experimental data. The geophone axes are not, in general, parallel to the array axes, and all of the floats do not have the same time base. The steps required to align the float axes with the array axes and float time bases with each other are discussed below, after which the experimental data are beamformed. The experimental results turn out to look much like noisy versions of the simulation results.

5.2.1. Processing the Time Series

The processing steps are listed below and described in more detail in subsequent paragraphs.

- each float's geophone time series is operated on to effectively rotate the floats so that they are all aligned with the array coordinate system;

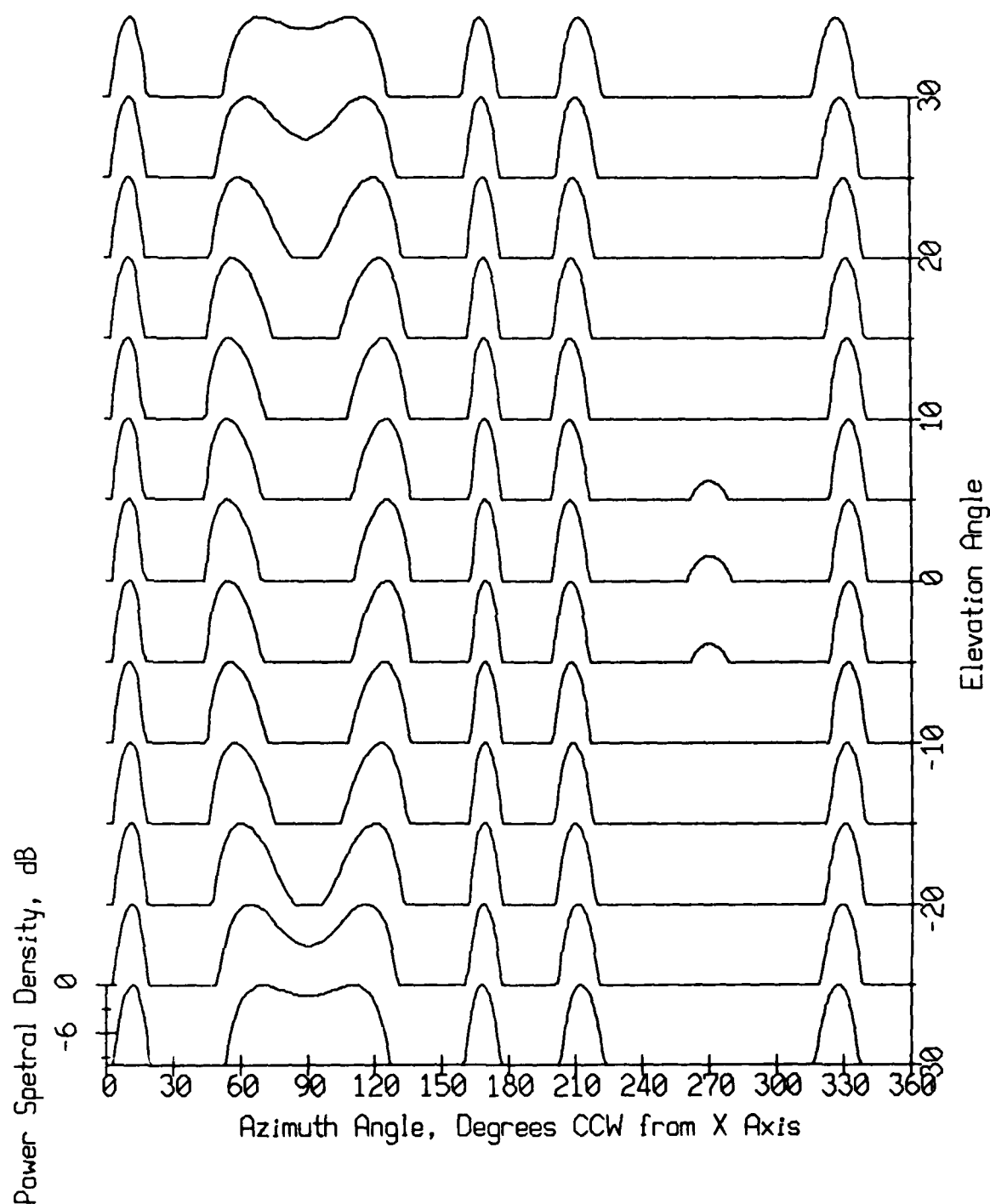


Figure 5.13 Bearing response of a four omni-directional element array to a 6.7 Hz source at azimuth $\theta_s = 60^\circ$ and elevation $\phi_s = 20^\circ$. The array elements are uniformly spaced at 350 meter intervals.

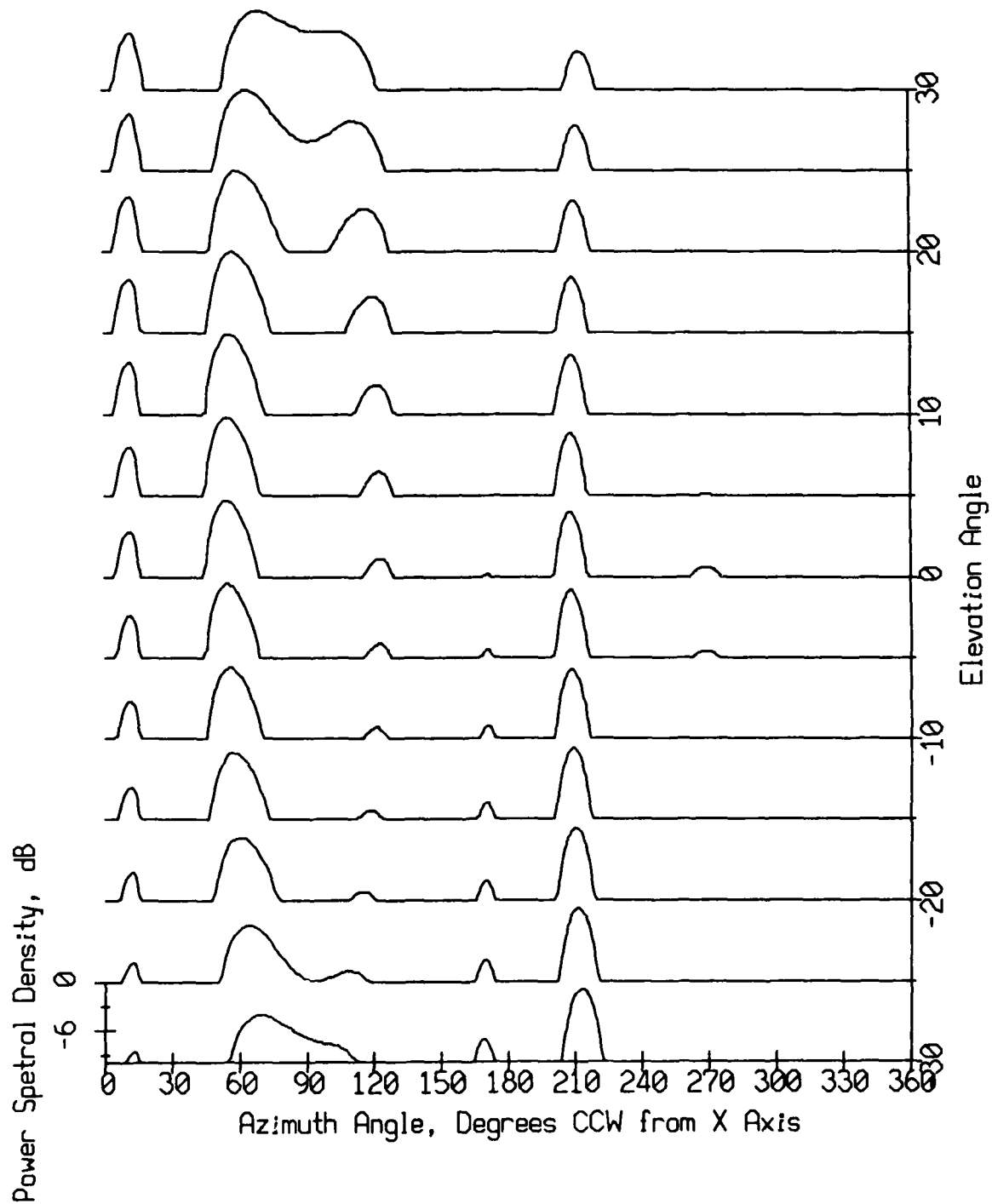


Figure 5.14 Bearing response of a four element array of orthogonally-oriented geophone triplets. A 6.7 Hz source is located at azimuth $\theta_s = 60^\circ$ and elevation $\phi_s = 20^\circ$. The array elements are uniformly spaced at 350 meter intervals.

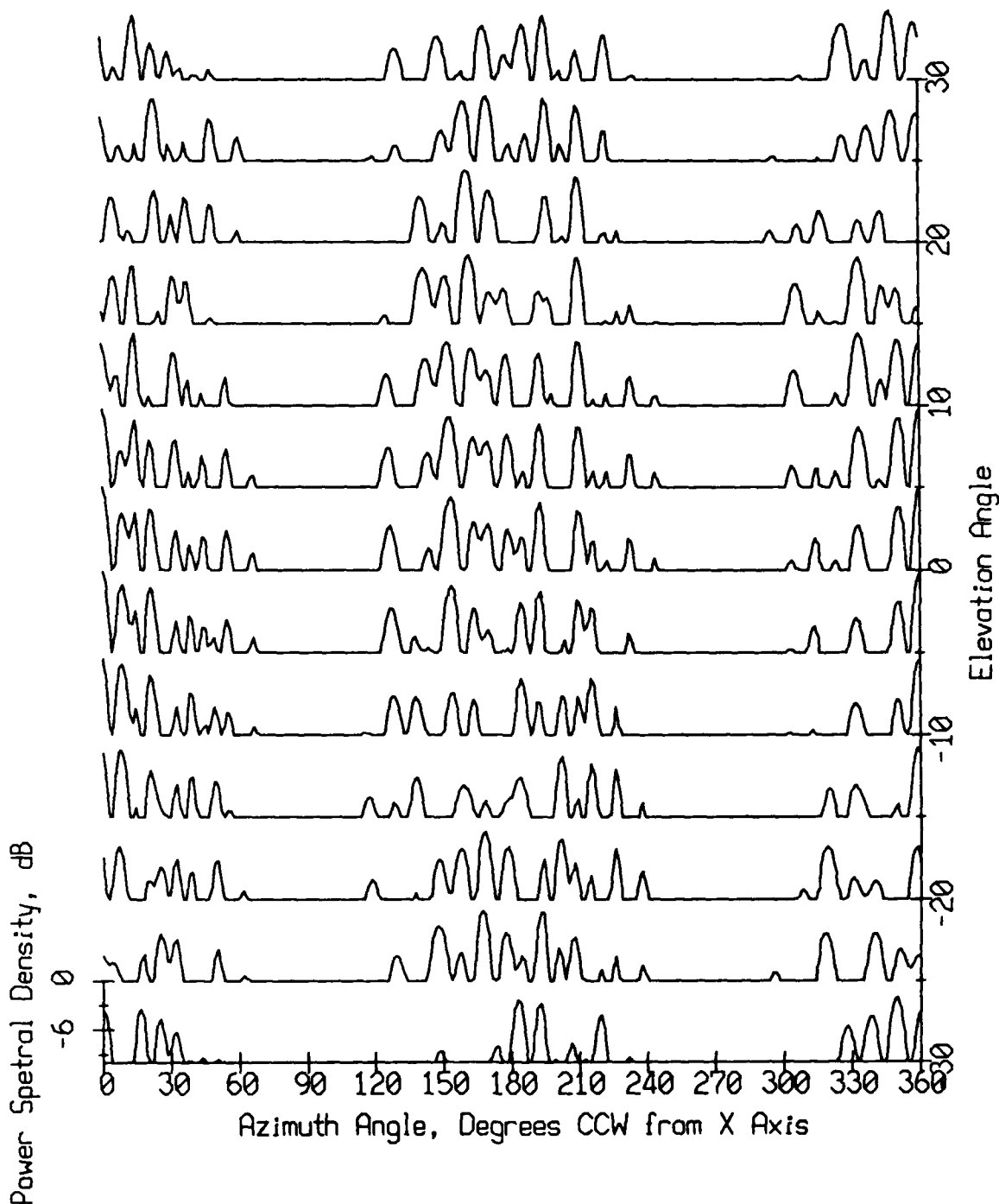


Figure 5.15 Bearing response of a four element array of Swallow floats located at estimated float positions for record 1830 of the September 1986 experiment. There is a 6.7 Hz source at azimuth $\theta_s = 0^\circ$ and elevation $\phi_s = 0^\circ$. The array aperture is approximately 2000 meters.

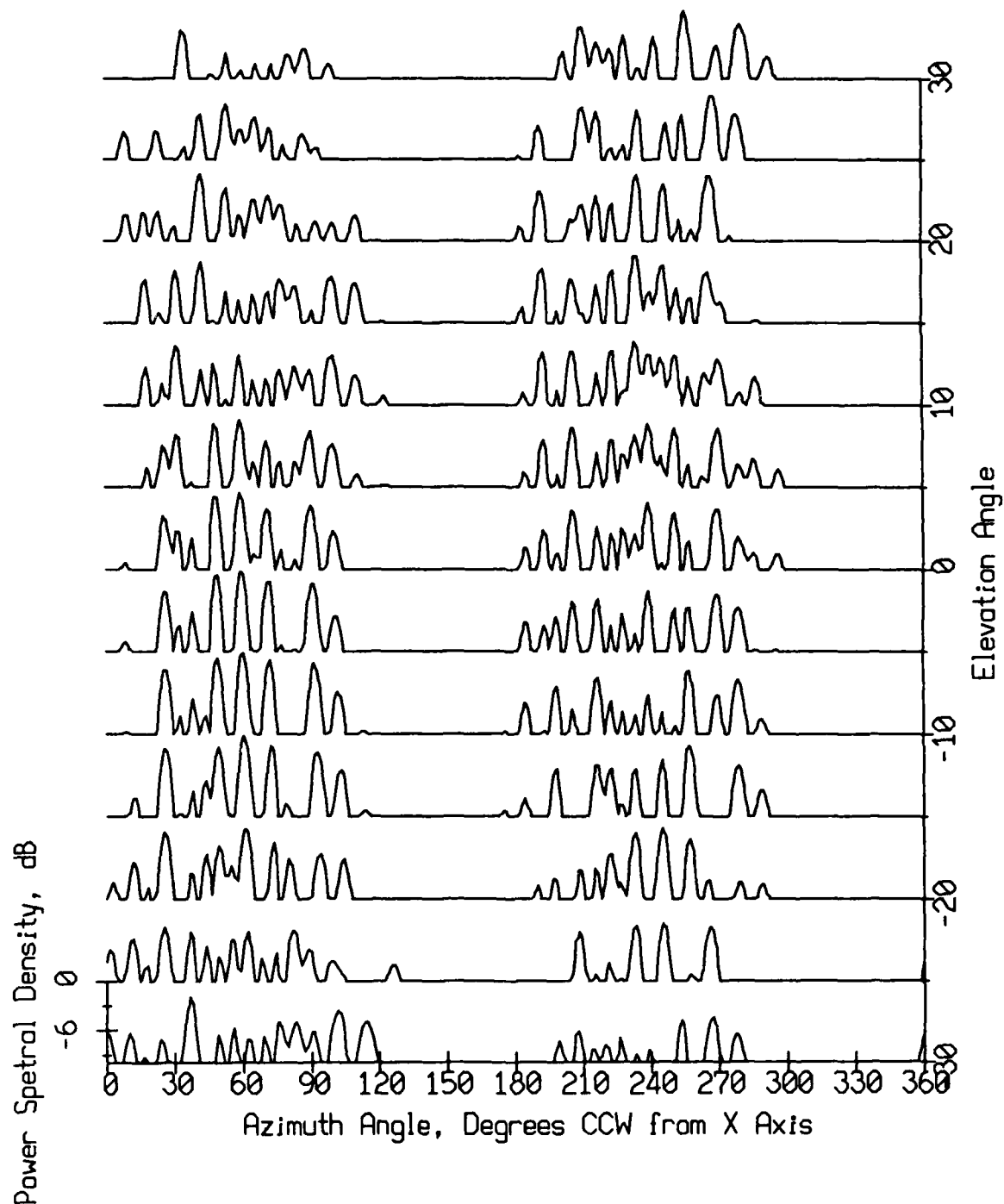


Figure 5.16 Bearing response of a four element array of Swallow floats located at estimated float positions for record 1830 of the September 1986 experiment. There is a 6.7 Hz source at azimuth $\theta_s = 60^\circ$ and elevation $\phi_s = -10^\circ$. The array aperture is approximately 2000 meters.

- the time bases of all but one of the floats' time series are shifted to align them with the reference float's time base;
- each axis is beamformed separately; the X axis time series from all of the floats are beamformed together, and likewise for the Y and Z axis time series;
- the beamformer output for the 3 axes are multiplied by the look direction cosines and summed to form a time series for each look direction;
- the time series are Fourier transformed and a calibration curve applied;
- the levels of selected spectral peaks are selected from the beam spectra, yielding *bearing levels*, which are spectral levels as a function of bearing. The bearing level is analogous to the magnitude of the bearing response used earlier.

5.2.1.1. Rotating Float Axes

The most straightforward approach to beamforming Swallow float data might be to combine each float's time series separately to form a beam for each look direction, and run the beamformer once for each direction. However, this approach would require the formation of a time series for each float and look direction, which would be voluminous, and would require running the beamformer separately for each look direction, which is inefficient and time consuming.

An equivalent approach is to operate on each float's time series to align their axes with the array axes, beamform each axis from all the floats separately, and combine the beamformer outputs using the look direction cosines. Using this latter approach, the beamformer is only run once for each axis and only one time series per look direction is produced. This is the method used in this thesis.

Rotating the floats to align their axes with the array axes can be understood by referring to Figure 5.17, which is a plan view of a freely-drifting float within the coordinate system established for localizing the floats. The direction of the float's y axis is denoted α_{float} , and is shown in the Figure to be about 120° magnetic. The float's z axis is vertical and parallel to the Z axis of the coordinate system.

The time series from the float geophones which are parallel to the float's x and y axes, are denoted $x(n)$ and $y(n)$. They must be combined to obtain new geophone time series in the directions of the array X and Y axes, call them $x'(n)$ and $y'(n)$. By inspection,

$$x'(n) = \left[y(n) \cos (280^\circ - \alpha_{float}) + x(n) \sin (280^\circ - \alpha_{float}) \right]$$

and

$$y'(n) = \left[y(n) \sin (280^\circ - \alpha_{float}) - x(n) \cos (280^\circ - \alpha_{float}) \right] \quad (5.20)$$

Equations (5.20) show how each float's geophone time series can be combined to effectively rotate the float axes to align them with the array axes. The angle α_{float} is the float heading, which the float measures at the start of each record. The directions of the coordinate system axes are determined by plotting the positions of the bottomed floats on a nautical chart.

5.2.1.2. Aligning Float Time Bases

The floats have different time bases because their internal clocks are not identical, i.e., the clock rates vary slightly from float to float. Consider floats i and j . Denote time according to float j 's clock as T_j . According to float j , record $n+1$ starts at

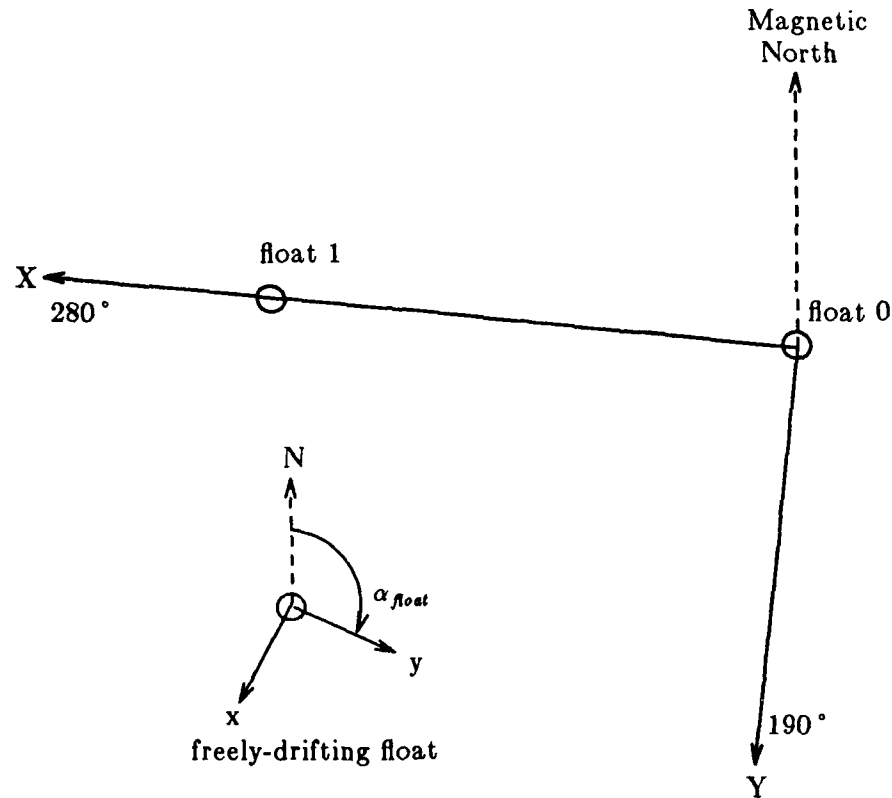


Figure 5.17 Plan view of a freely-drifting Swallow float, whose heading is denoted α_{float} , and the coordinate system defined by the positions of bottomed floats 0 and 1.

$$T_j = 45 n \quad (5.21)$$

which is 45 n of float j 's seconds. In [21] it is shown that once the float temperatures stabilize, the relationship between elapsed time according to a float, and true elapsed time since synchronization, is linear. Let true elapsed time be t . Then

$$T_j(t) = g_j t + a_j \quad (5.22)$$

where g_j and a_j are constants unique to each float. Note that g_j is dimensionless and the units of a_j are time.

Equation (5.22) can be solved for true time t in terms of T_j , g_j and a_j , and if g_j and a_j are known, the float time base can be aligned to true time. However, it is shown in [21] that the g_j 's and a_j 's cannot be measured directly. It is further shown in [21] that reciprocal path travel times can be combined to estimate the clock rate and offset differences, $(g_i - g_j)$ and $(a_i - a_j)$. Therefore, the approach is to pick one of the floats as the reference time base and align all of the other floats to it.

Solving (5.22) for true time t and using (5.21) yields the true elapsed time at the start of record $n+1$ aboard float j .

$$t(T_j) = \frac{T_j - a_j}{g_j} = \frac{45n - a_j}{g_j} \equiv t(j, n) \quad (5.23)$$

Changing only the subscript yields the true elapsed time at the start of record $n+1$ aboard float i .

$$t(i, n) = \frac{T_i - a_i}{g_i} = \frac{45n - a_i}{g_i} \quad (5.24)$$

The difference between (5.24) and (5.23) gives the difference between the time bases of the two floats in true time.

$$\Delta t(i, j, n) = t(j, n) - t(i, n)$$

$$\begin{aligned} &= \frac{45n - a_j}{g_j} - \frac{45n - a_i}{g_i} \\ &= 45n \left[\frac{1}{g_j} - \frac{1}{g_i} \right] + \frac{a_i}{g_i} - \frac{a_j}{g_j} \quad (\text{true time dif. between time bases}) \end{aligned} \quad (5.25)$$

Figure 5.18 depicts the time bases of floats i and j and that of true time when float i 's clock rate is somewhat faster than float j 's. The horizontal axes in the top panel are time according to float i , time according to float j , and true time. All are increasing to the right, which means that $t(j, n) > t(i, n)$ and $\Delta t(i, j, n) > 0$.

The event indicated by $t(e)$ in Figure 5.18 occurs simultaneously at the two floats. However the time of the event according to float i is later than the time of the event according to float j .

$$[T_i(e) - T_i(n)] > [T_j(e) - T_j(n)]$$

If the time series are simply aligned using the record start times, as shown in the bottom panel of Figure 5.18, then the event does not occur simultaneously in the two time series but occurs first at float j . In order for the two events to add coherently, they must occur simultaneously in the time series presented to the beamformer. One or the other of the float time bases must be shifted to align it with the other.

Let float j be chosen as the reference time base, so that float i 's time base is to be shifted $\Delta t(i, j, n)$ seconds. To find the amount of the shift in terms of float i 's clock, denoted ΔT_i , use equation (5.22) and substitute $\Delta t(i, j, n)$ for t :

$$\Delta T_i \left(\Delta t(i, j, n) \right) = g_i \left(\Delta t(i, j, n) \right) + a_i$$

Using (5.25),

$$\Delta T_i \left(\Delta t(i, j, n) \right) = g_i \left[45n \left(\frac{1}{g_j} - \frac{1}{g_i} \right) + \frac{a_i}{g_i} - \frac{a_j}{g_j} \right]$$

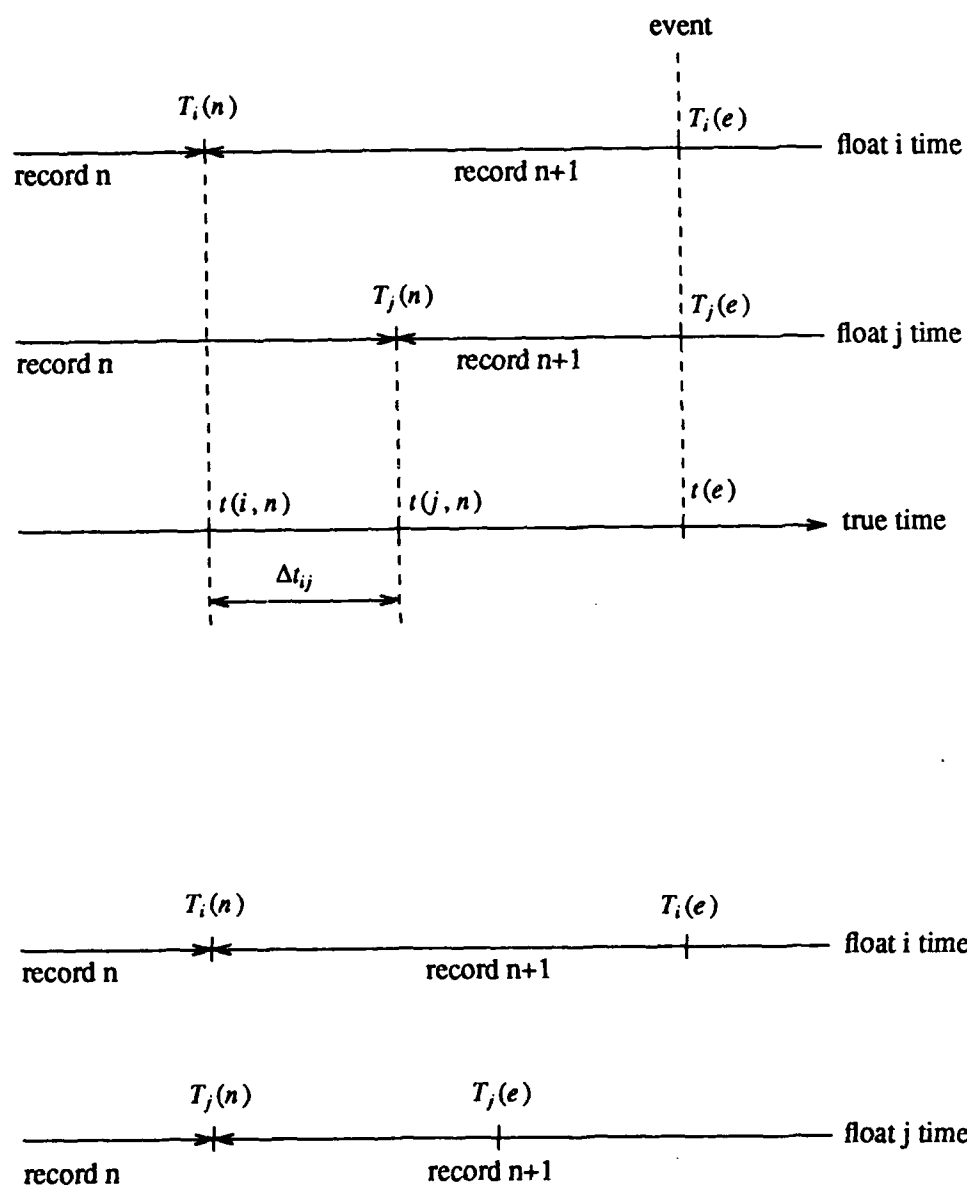


Figure 5.18 Comparison of the time bases of floats i and j and true time. The upper panel shows their relationship when the floats were deployed. The bottom panel shows the effect of simply aligning the record start times.

$$= 45 n \left(\frac{g_i - g_j}{g_j} \right) + a_i - \frac{g_i}{g_j} a_j \quad (5.26)$$

Note that if $g_j = g_i$ and $a_j = a_i$, which is to say that the two time bases are the same, then $\Delta T_i = 0$ as expected.

It is shown in [21] that the values of g_i are very close to 1, such that if we write $g_i \equiv 1 + \epsilon$, then ϵ is of order 10^{-6} . Thus (5.26) can be simplified using the Taylor series expansion

$$f(x + a) = f(x) + f'(x) a + f''(x) \frac{a^2}{2} + \dots$$

of

$$f(x) = \frac{1}{x}$$

Using

$$f'(x) = -\frac{1}{x^2} \quad \text{and} \quad f''(x) = \frac{2}{x^3}$$

the expansion is

$$\frac{1}{x + a} = \frac{1}{x} - \frac{a}{x^2} + \frac{a^2}{x^3} + \dots$$

Substituting $x = 1$ and $a = \epsilon$, to first order in ϵ ,

$$\frac{1}{g_i} = \frac{1}{1 + \epsilon_i} \approx 1 - \epsilon_i$$

Therefore, to first order in ϵ ,

$$\frac{g_i - g_j}{g_j} = \frac{1 + \epsilon_i - 1 - \epsilon_j}{1 + \epsilon_j} \approx (\epsilon_i - \epsilon_j) (1 - \epsilon_j) \approx \epsilon_i - \epsilon_j = g_i - g_j \quad (5.27a)$$

and

$$\frac{g_i}{g_j} = \frac{1 + \epsilon_i}{1 + \epsilon_j} \approx (1 + \epsilon_i) (1 - \epsilon_j) \approx 1 + \epsilon_i - \epsilon_j \approx 1 + g_i - g_j \quad (5.27b)$$

Putting equations (5.27) into (5.26) yields

$$\Delta T_i \approx 45 n \left(g_i - g_j \right) + a_i - \left(1 + g_i - g_j \right) a_j = \left(45 n - a_j \right) \left(g_i - g_j \right) + a_i - a_j \quad (5.28)$$

It is shown in [21] that

$$|a_j| \leq 1 \text{ second} \ll 45 n \text{ seconds}, \quad n > 1 \quad (5.29)$$

Equation (5.28) therefore becomes

$$\Delta T_i \approx 45 n (g_i - g_j) + (a_i - a_j) \quad (5.30)$$

It is now shown that $\Delta t(i, j, n)$ changes negligibly over the course of one record so that it is sufficient to realign the time series once for each record. To see this, use (5.25) to find the change in $\Delta t(\cdot)$ over the course one record.

$$\Delta t(i, j, n+1) - \Delta t(i, j, n) = 45 \left(\frac{1}{g_j} - \frac{1}{g_i} \right)$$

To first order in ϵ ,

$$\frac{1}{g_j} - \frac{1}{g_i} \approx 1 - \epsilon_j - 1 + \epsilon_i = \epsilon_i - \epsilon_j$$

so that

$$\Delta t(i, j, n+1) - \Delta t(i, j, n) \approx 45 (\epsilon_i - \epsilon_j) \approx 45 \cdot 10^{-6} \text{ seconds} \approx 0.5 \text{ msec.} \quad (5.31)$$

Equation (5.30) thus shows how to calculate how much float i 's time base must be shifted at the start of each record in order to align it with the corresponding record in float j 's geophone data. It requires knowing the differences between the clock rates and offsets in the two floats, $\{g_i - g_j\}$ and $\{a_i - a_j\}$. Reference [21] shows how the differences between the clock rates and offsets are calculated, and contains values for them for all float pairs during the September 1986 deployment. The procedure for aligning the float time bases is:

- chose one float as a reference whose time base will not be shifted;
- using measured values for $(g_i - g_j)$ and $(a_i - a_j)$, and equation (5.30), calculate how much each record of the other float's geophone data must be shifted, and in what direction;
- interpolate and shift the three geophone time series for all but the reference float.

5.2.1.3. Remaining Processing Steps

Having aligned the geophone time series in direction and time, they can now be delayed and summed to listen selectively in particular directions. A time delay beamformer is applied to the time series from each axis of all the floats, producing three time series for each look direction. Let $b_i(t, \theta_l, \phi_l)$ denote the time series for look direction (θ_l, ϕ_l) , obtained by combining the geophones parallel to the i axis. The three sets of time series are then multiplied by the look direction cosines and summed.

$$b(t, \theta_l, \phi_l) = b_x(t, \theta_l, \phi_l) \cos(\theta_l) \cos(\phi_l) + b_y(t, \theta_l, \phi_l) \sin(\theta_l) \cos(\phi_l) + b_z(t, \theta_l, \phi_l) \sin(\phi_l) \quad (5.32)$$

The time series for each look direction is Fourier transformed using the same length transform (40.96 seconds) and window used for the spectra in Appendix B.

$$B(f, \theta_l, \phi_l) = F \left\{ b(t, \theta_l, \phi_l) \right\} \quad (5.33)$$

After applying a calibration curve, the levels of selected spectral lines may be picked from all of the beam spectra to obtain the spectral level as a function of bearing or bearing level. The bearing level is analogous to the magnitude of the bearing response which was used in Section 5.1. It indicates the directionality of sound at particular frequencies.

5.2.2. Horizontal Bearing Levels

The initial effort is to beamform only in the horizontal direction, that is, for θ_l between 0° and 360° and $\phi_l = 0^\circ$. This is considered a reasonable approach because the bearing responses in Figures 5.15 and 5.16 show that the horizontal and low elevation angle bearing responses look much alike as long as the source arrival angle is small, and according to Figure 3.10, the vertical arrival angles are small for many records at the frequencies of interest.

Horizontal bearing levels for a 20 record (15 minute) period beginning with record 1800 are shown in Figure 5.19. The upper 5 dB of the bearing levels at 9, 10.3, 12.2 and 13.5 Hz are shown. The azimuth angle is degrees relative to magnetic north and the look elevation is 0° .

The four plots in Figure 5.19 contain numerous, high level side lobes and a 180° ambiguity much like Figures 5.15 and 5.16. The azimuth angle of the highest lobe is not constant for more than a few records (3 to 5 minutes) at a time. In general, however, the source bearing appears to be near either 090° or 270° magnetic. A means of enhancing the main lobe and reducing the level of the side lobes is needed in order to better resolve the source direction.

5.2.3. Enhancing Bearing Levels

Figure 5.20 contains the result of averaging the bearing levels of five consecutive records at each frequency. The entire 110 record period selected for analysis is shown in these plots. Averaging appears to smooth the bearing levels, so that the source direction is approximately the center of a rounded mass of peaks. Gross changes in the approximate source bearing during the 110 record period are approximately the same at all frequencies. For example, the source azimuth increases about 20° between records 1780 and 1800. This indicates that all of the signals originate from the same source.

As another approach to enhancing the bearing levels, Figure 5.21 contains the product of the 9, 10.3 and 12.2 Hz bearing levels. If different frequency signals arrive at the array from the same direction, their main lobes will line up but their side lobes, whose spacing is frequency dependent, will not. Figure 5.21 shows that multiplying bearing levels together thins the peaks out considerably, but the 180° ambiguity persists. This implies that the signal arrival angles are, to some extent, frequency dependent.

Figure 5.22 summarizes the horizontal direction beamforming results. The top panels show the highest bearing level during the 110 record period. Comparing the top panel of Figure 5.22a with Figure 3.10 shows that the gross rise in signal level evident in the individual float spectral lines is also seen in the bearing levels. This is true for the other frequencies as well.

Normalized Bearing Levels at 9 Hz.

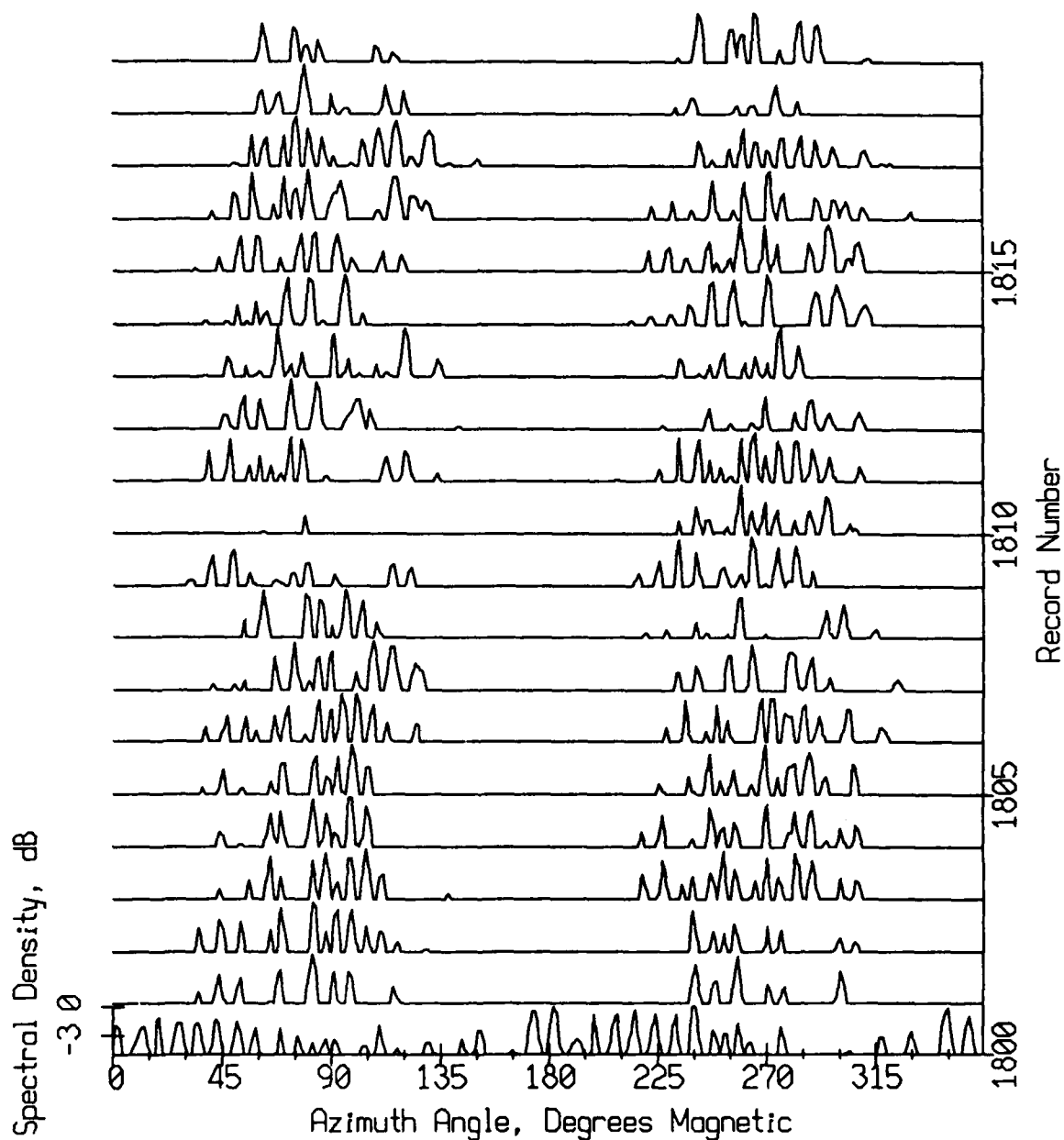


Figure 5.19a Spectral level versus azimuthal bearing at 9 Hz from four freely-drifting Swallow floats during records 1800 - 1819 of the September 1986 experiment (15 minutes duration). The look elevation angle is zero (horizontal).

Normalized Bearing Levels at 10.3 Hz.

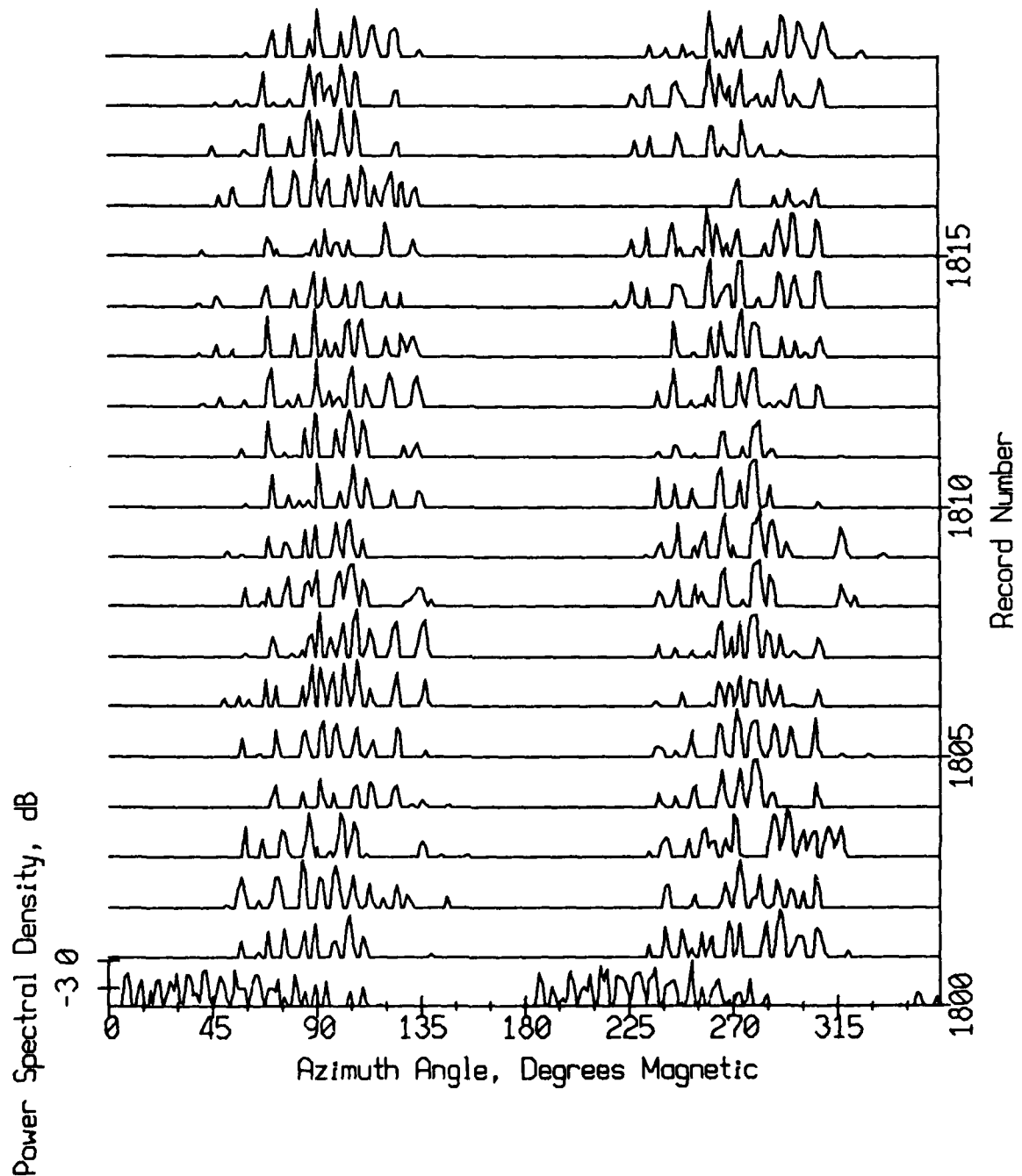


Figure 5.19b Spectral level versus azimuthal bearing at 10.3 Hz from four freely-drifting Swallow floats during records 1800 - 1819 of the September 1986 experiment (15 minutes duration). The look elevation angle is zero (horizontal).

Normalized Bearing Levels at 12.2 Hz.

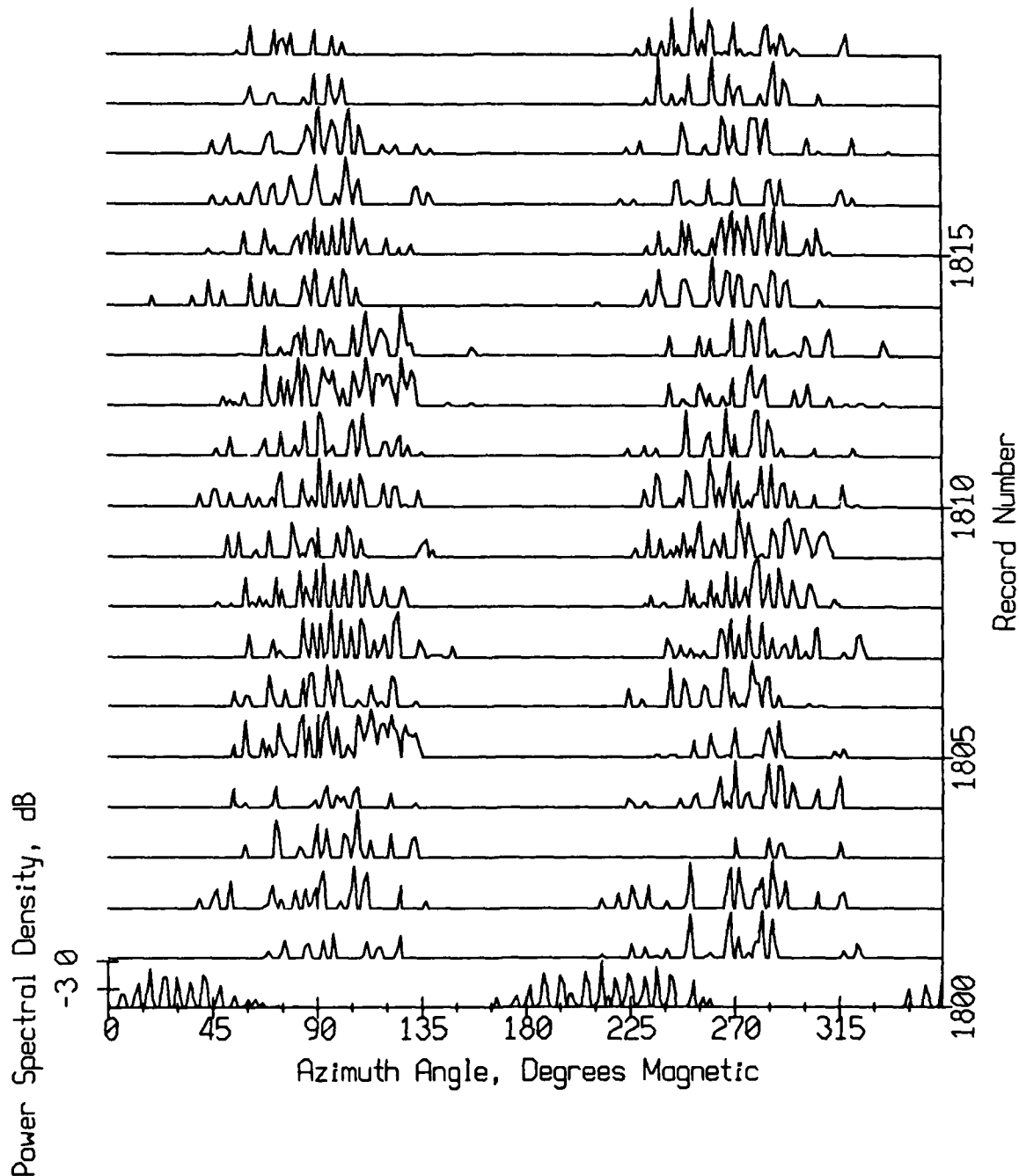


Figure 5.19c Spectral level versus azimuthal bearing at 12.2 Hz from four freely-drifting Swallow floats during records 1800 - 1819 of the September 1986 experiment (15 minutes duration). The look elevation angle is zero (horizontal).

Normalized Bearing Levels at 13.5 Hz.

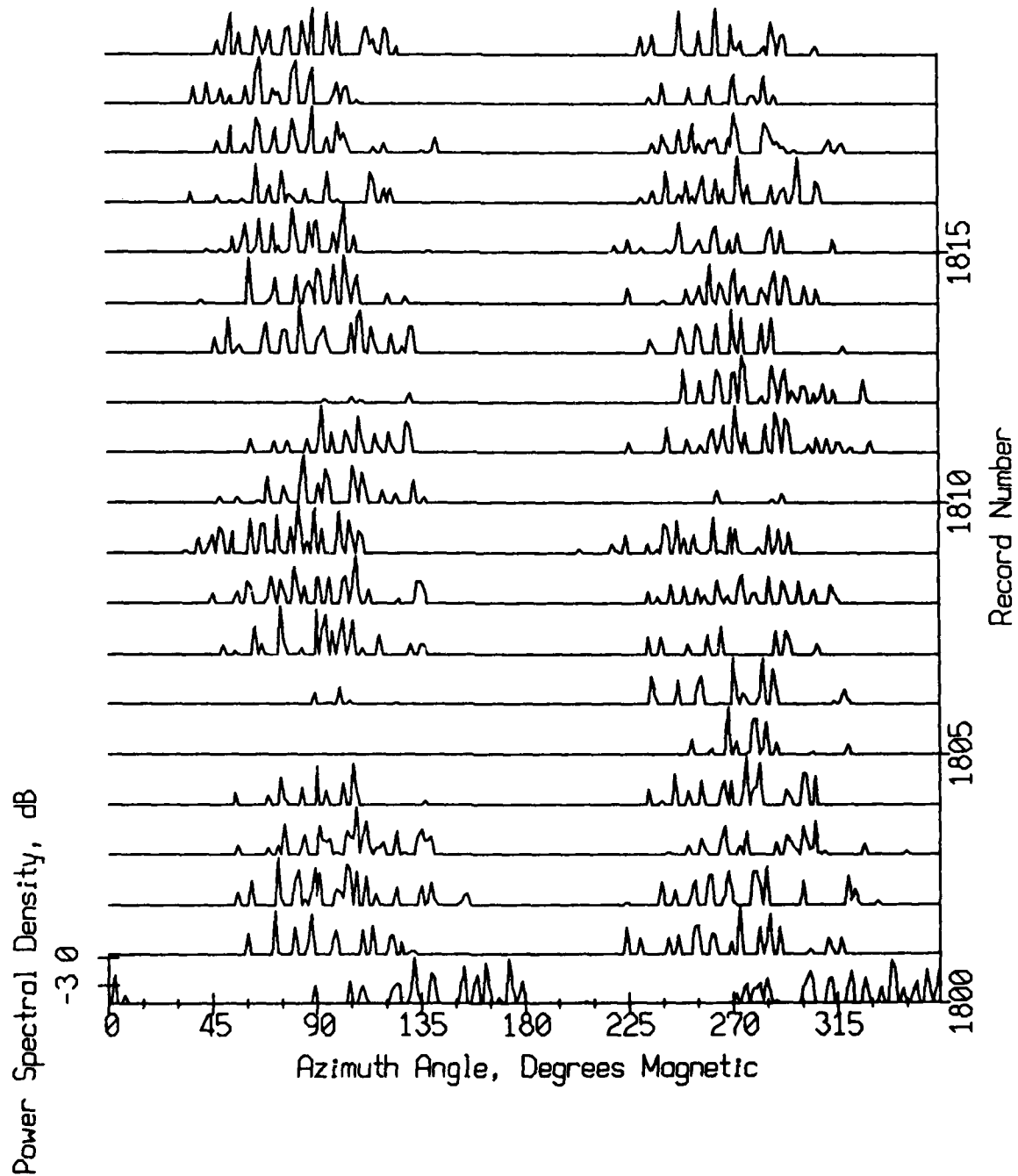


Figure 5.19d Spectral level versus azimuthal bearing at 13.5 Hz from four freely-drifting Swallow floats during records 1800 - 1819 of the September 1986 experiment (15 minutes duration). The look elevation angle is zero (horizontal).

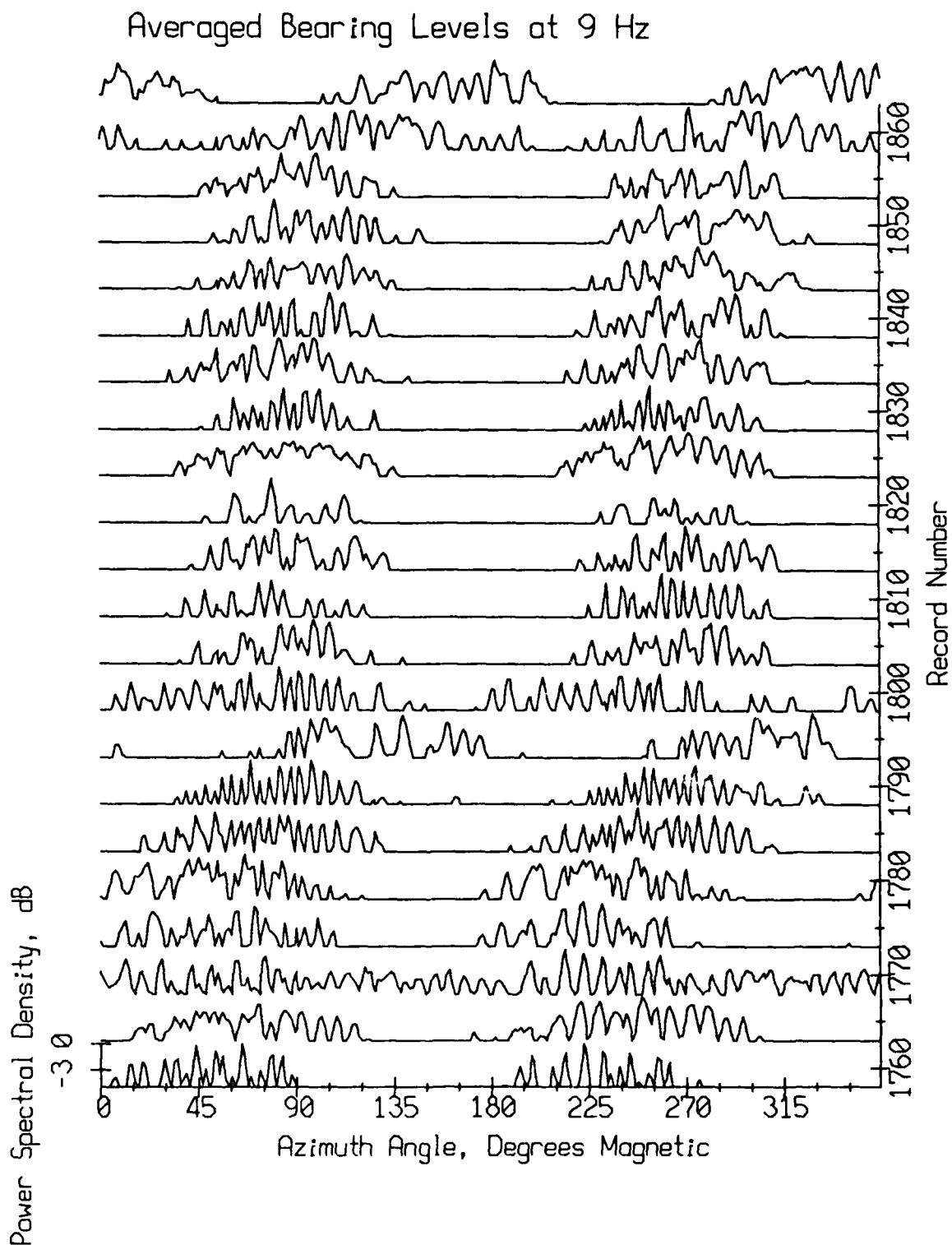


Figure 5.20a Averaged spectral levels versus azimuthal bearing at 9 Hz from four freely-drifting Swallow floats during records 1758 - 1868 of the September 1986 experiment (82.5 minutes duration). The look elevation angle is zero (horizontal). Each trace is the average of five records.

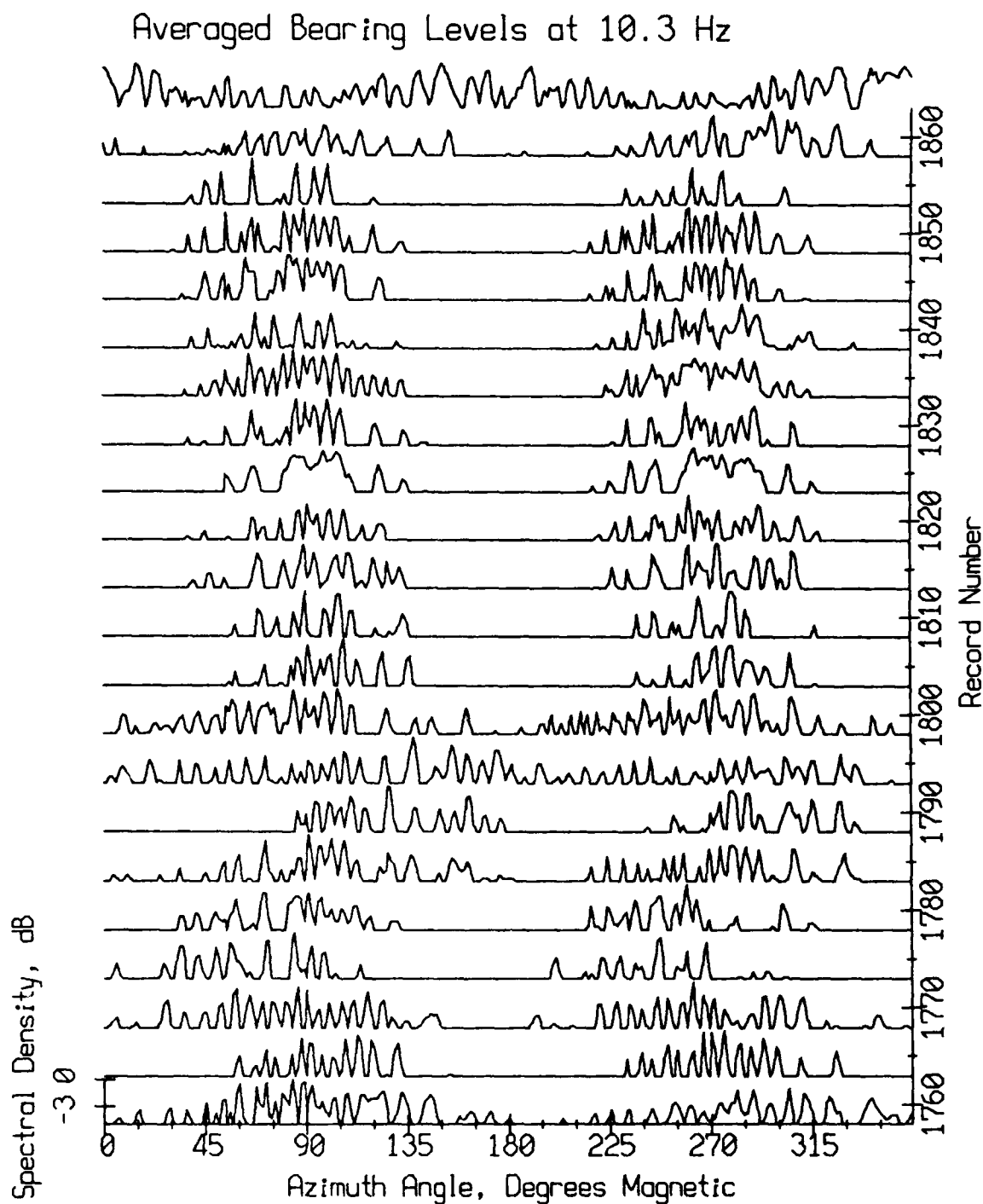


Figure 5.20b Averaged spectral levels versus azimuthal bearing at 10.3 Hz from four freely-drifting Swallow floats during records 1758 - 1868 of the September 1986 experiment (82.5 minutes duration). The look elevation angle is zero (horizontal). Each trace is the average of five records.

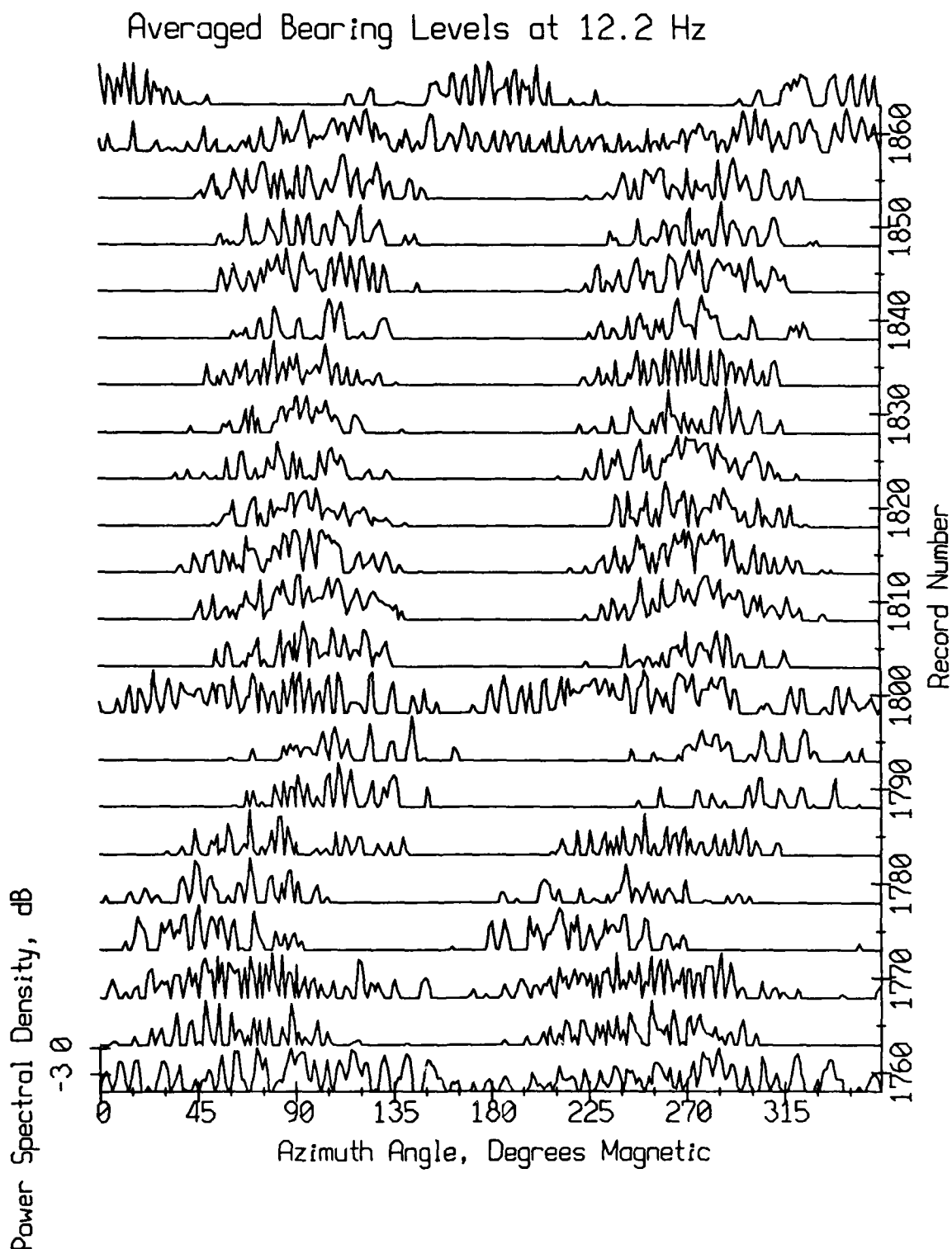


Figure 5.20c Averaged spectral levels versus azimuthal bearing at 12.2 Hz from four freely-drifting Swallow floats during records 1758 - 1868 of the September 1986 experiment (82.5 minutes duration). The look elevation angle is zero (horizontal). Each trace is the average of five records.

Averaged Bearing Levels at 13.5 Hz

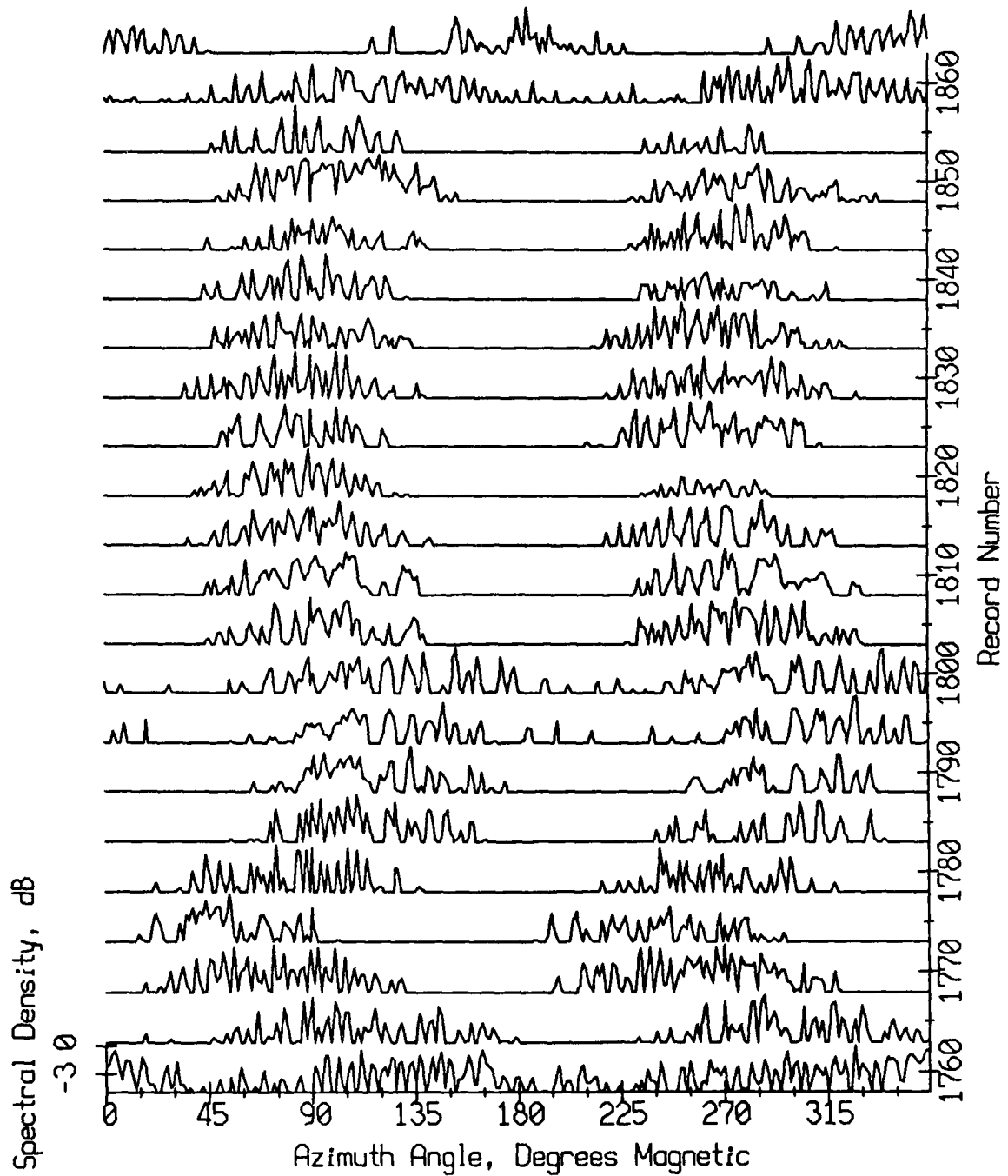


Figure 5.20d Averaged spectral levels versus azimuthal bearing at 13.5 Hz from four freely-drifting Swallow floats during records 1758 - 1868 of the September 1986 experiment (82.5 minutes duration). The look elevation angle is zero (horizontal). Each trace is the average of five records.

Product of 9, 10.3 and 12.2 Hz Bearing Levels

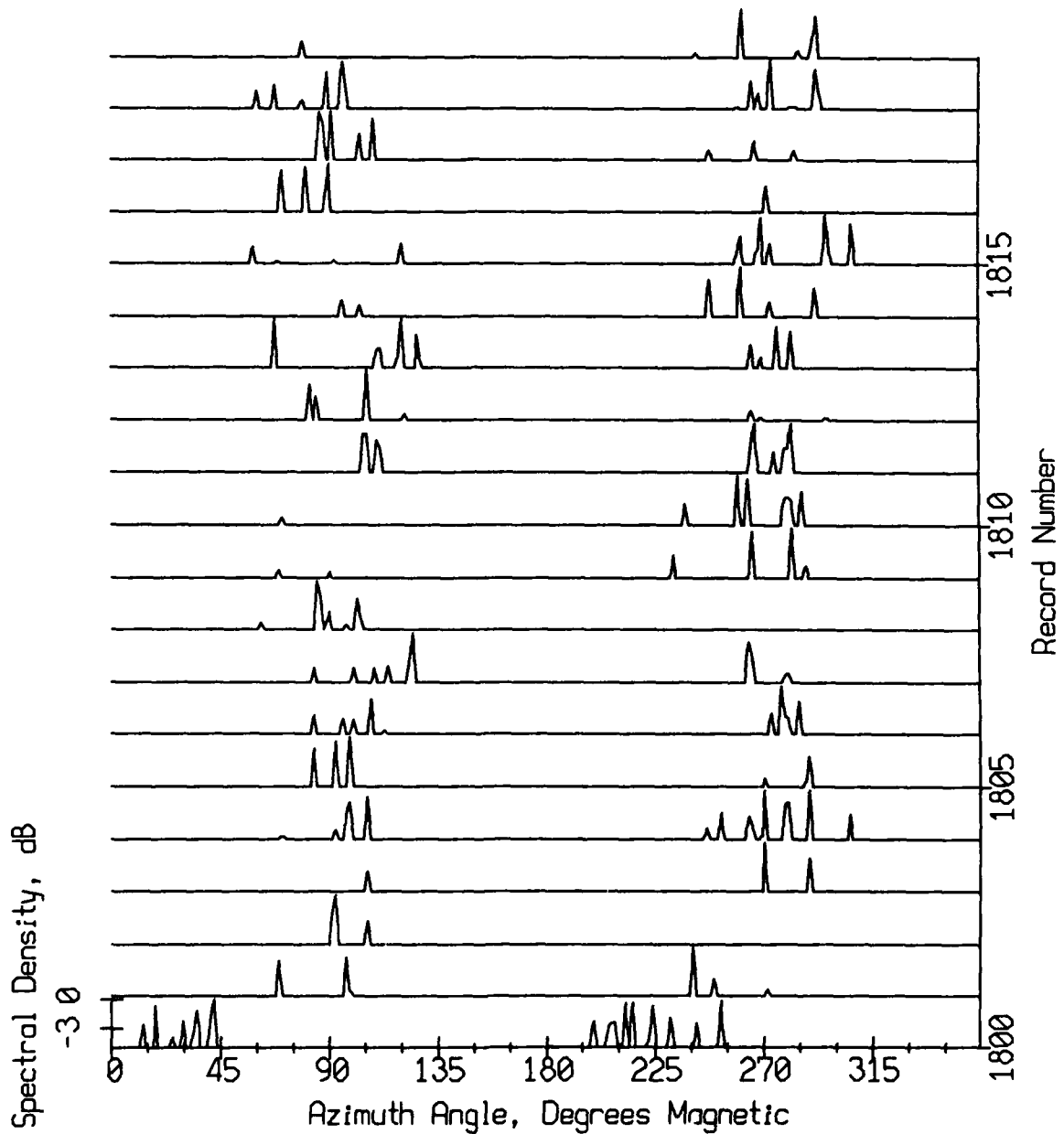


Figure 5.21 Product of 9, 10.3 and 12.2 Hz spectral levels versus azimuthal bearing from four freely-drifting Swallow floats during records 1800 - 1819 of the September 1986 experiment (15 minutes duration). The look elevation angle is zero (horizontal).

The middle panels in Figure 5.22 show the exact frequency at which the peaks occur. Comparing them with Figure 3.9 shows that changes in signal frequency which are apparent in the individual float spectra also appear in the bearing levels. The bottom panels in Figure 5.22 show the apparent direction to the source based upon the azimuth of the highest bearing level. The source direction jumps between 90° and approximately 270° , indicating a 180° ambiguity.

5.2.4. Three-Dimensional Bearing Levels

Appendix D contains bearing levels for record 1802 for azimuth angles between 150° and 240° relative to the array X axis and elevation angles between -20° and 20° . The arrival angles during this record were seen in Figure 3.11 to be nearly horizontal. The three-dimensional bearing levels display the same vertical ridge structure seen in Figures 5.15 and 5.16. The bearing levels at different frequencies all display main lobes at azimuth angle $\theta_i \approx 187^\circ$, but the elevation angles vary between 0° and 15° .

Appendix D also contains bearing levels for record 1844 for azimuth angles between 150° and 240° (relative to the array X axis) and elevation angles between -60° and 60° . This record was selected because the magnitude of the arrival angle at 9 Hz is seen in Figure 3.11 to be greater than 30° for three of the floats. The 9 Hz bearing level indicates that considerable energy is arriving at large positive and negative elevation angles during record 1844. This indicates that the signal is propagating to the array over multiple paths. Energy at 10.3 Hz is concentrated between -15° and 15° elevation. The other two signals, at 12.2 and 13.5 Hz, are arriving at -45° to 20° elevation and -35° to 40° elevation, respectively. We see that the vertical angle arrival varies considerably with frequency.

5.2.5. Beamformer Gain

One method of evaluating how well signals are being co-phased is to compare the highest bearing level with the levels at the individual floats. If the beamformer is perfectly co-phasing each float's signals, then the highest bearing level will be equal to the coherent sum of the signals. The level in dB of a sinusoidal signal with amplitude x , is $10 \log \left(\frac{x^2}{2} \right)$. The coherent sum of N equal strength signals having the same phase is

$$10 \log \frac{(N x)^2}{2} = 20 \log N + 10 \log \left(\frac{x^2}{2} \right) \quad (5.30)$$

which shows a gain of $20 \log N$ over the level of one signal. When there are 4 elements, the gain is 12 dB.

When the signals do not all have the same amplitude, as is the case with the Swallow floats, but they are co-phased, the coherent sum is

$$10 \log (x_1 + x_2 + x_3 + x_4)^2 \quad (\text{coherent sum}) \quad (5.31)$$

where x_i is the signal amplitude at float i . When the signals have approximately the same amplitude, the coherent sum is something less than 12 dB higher than the level of the individual signals.

Figure 5.23 compares the highest horizontal bearing levels to the coherent sum of the spectral levels of each float's x and y axis geophones. The coherent sum has been subtracted from the highest bearing level. Also shown is the incoherent sum of the x and y axis geophone levels. If all of the signals are of equal strength, the incoherent sum is

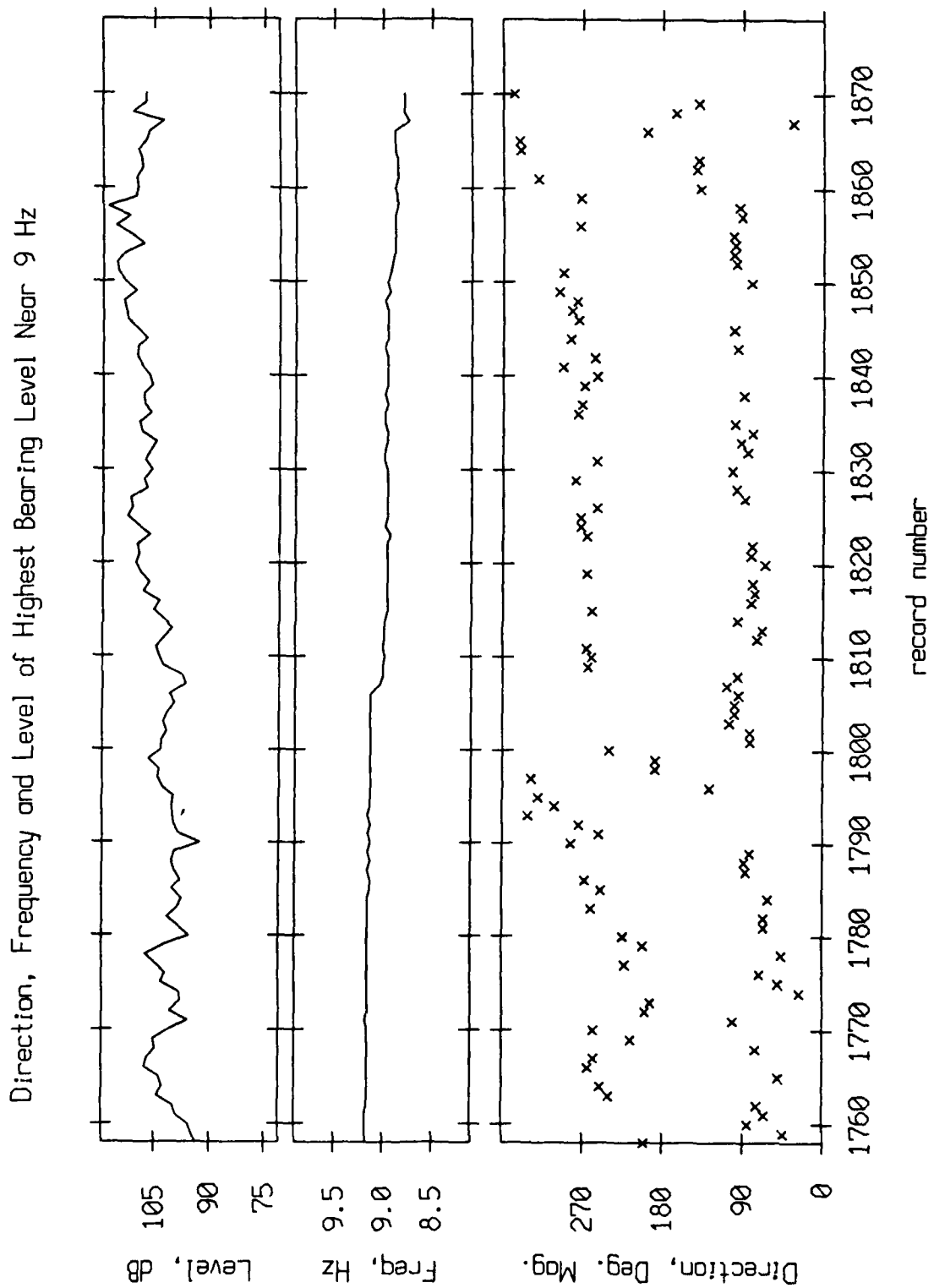


Figure 5.22a Horizontal beamforming results. Direction, frequency and level of the highest horizontal bearing level for the 9 Hz spectral line.

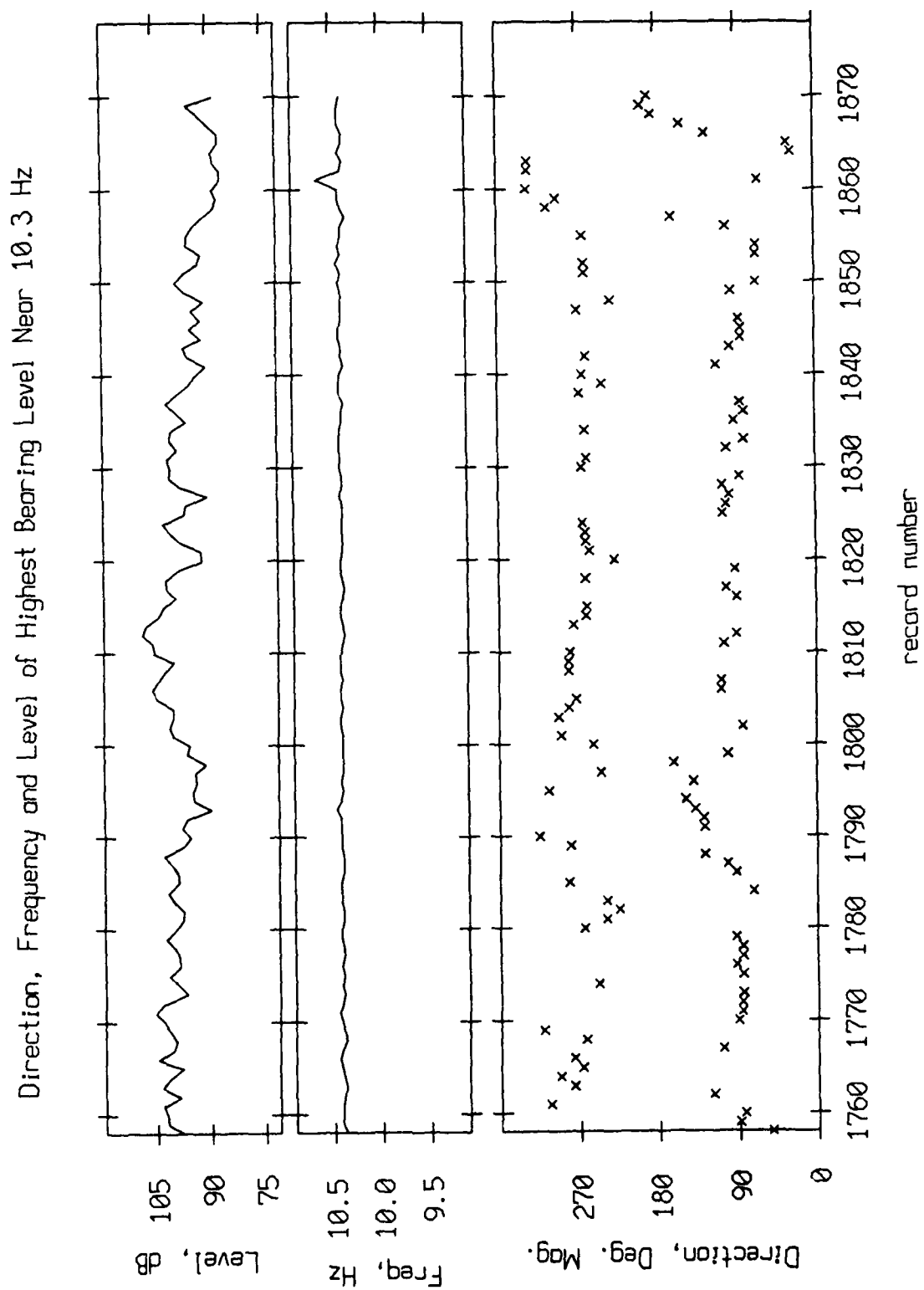


Figure 5.22b Horizontal beamforming results. Direction, frequency and level of the highest horizontal bearing level for the 10.3 Hz spectral line.

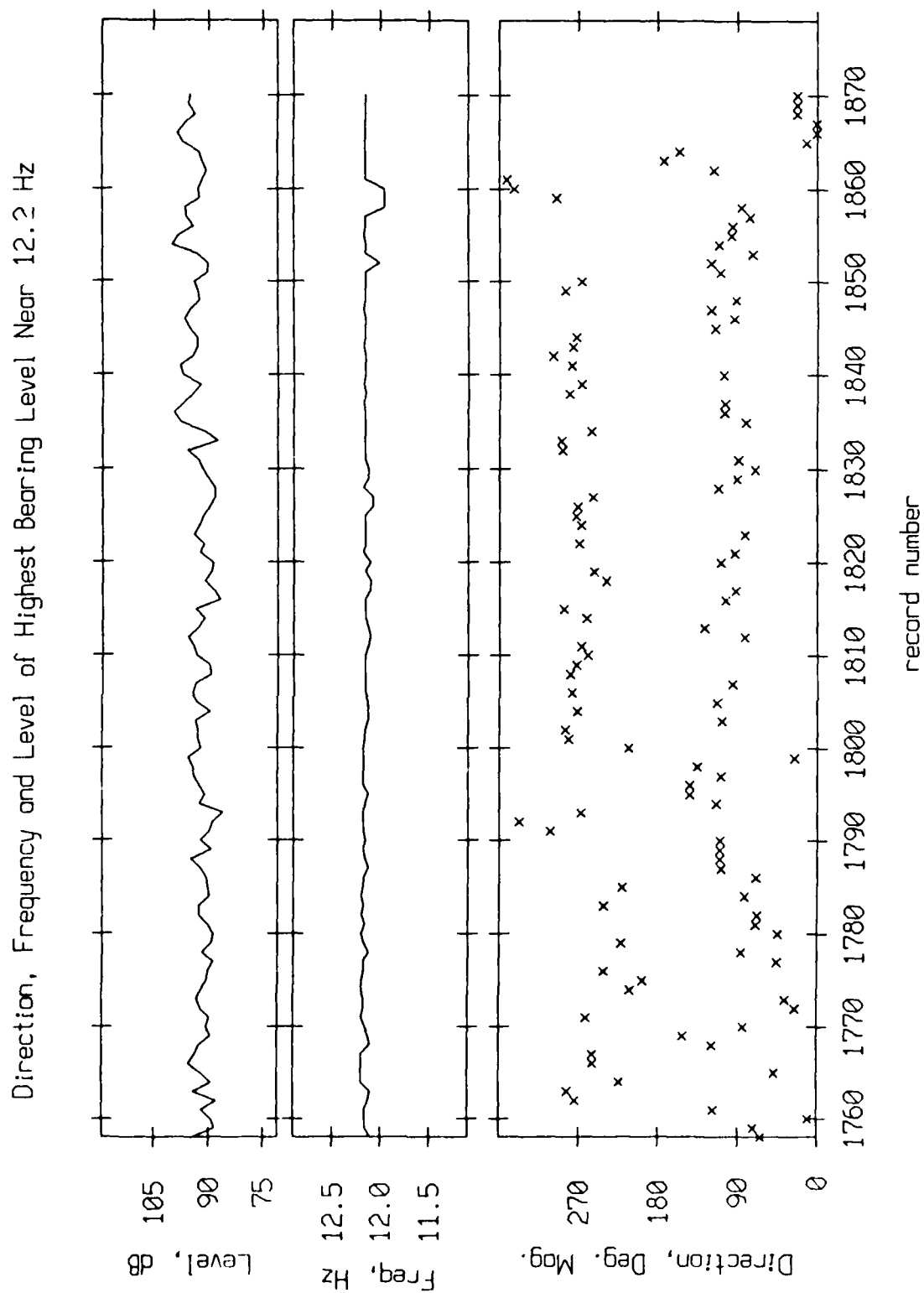


Figure 5.22c Horizontal beamforming results. Direction, frequency and level of the highest horizontal bearing level for the 12.2 Hz spectral line.

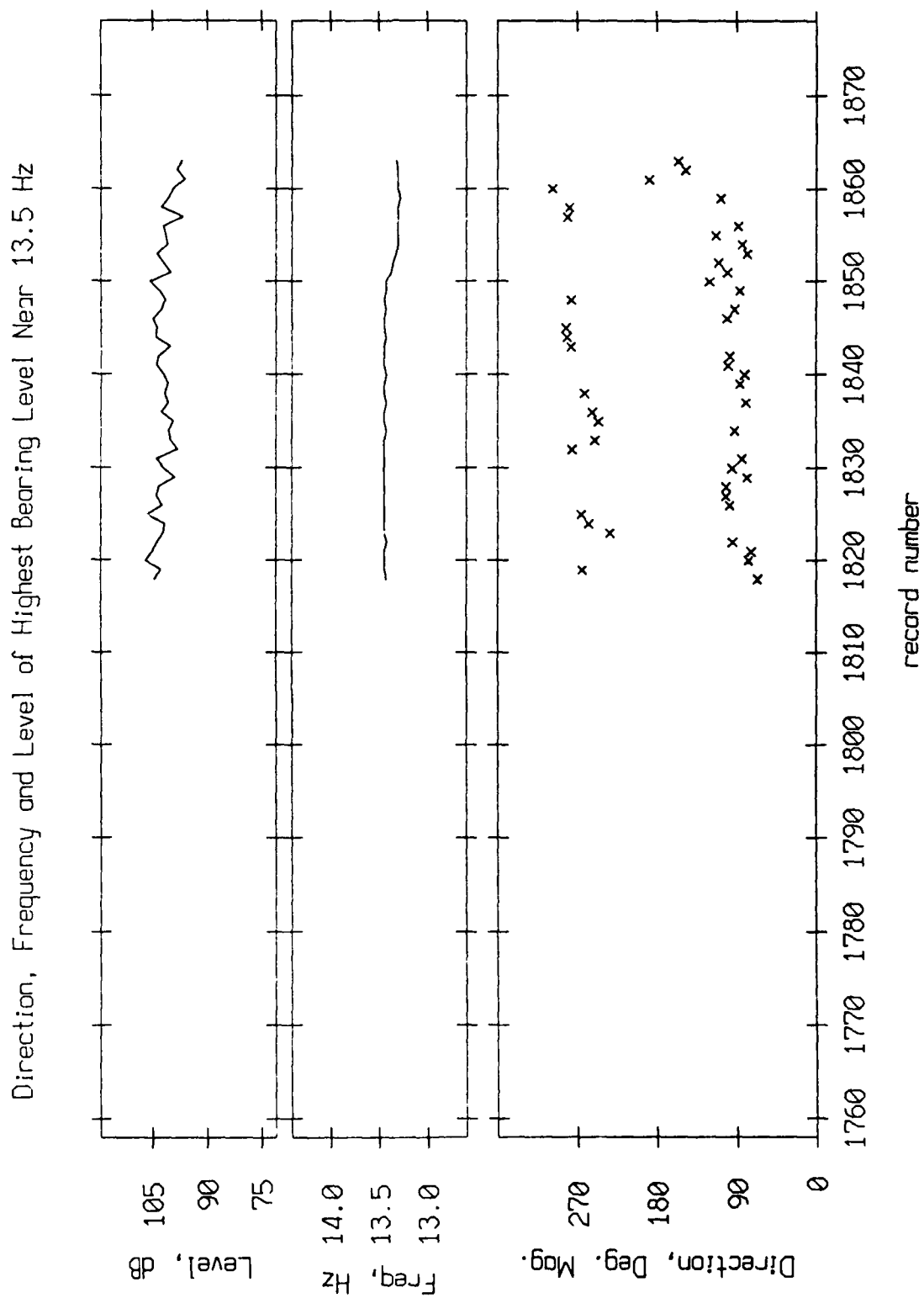


Figure 5.22d Horizontal beamforming results. Direction, frequency and level of the highest horizontal bearing level for the 13.5 Hz spectral line.

$$10 \log \left(N \frac{x^2}{2} \right) = 10 \log N + 10 \log \left(\frac{x^2}{2} \right)$$

so that the signal gain with $N = 4$ is $10 \log 4 = 6$ dB. The coherent sum has also been subtracted from the incoherent sum in Figure 5.23, and we see that the incoherent sum is roughly 6 dB lower than the coherent sum.

The highest bearing levels are, on the average, about 3 dB lower than the coherent sum and about 3 dB above the incoherent sum. This indicates that the bearing level gain is about 9 dB. The signals are apparently being co-phased well enough for the highest bearing level to be higher than the incoherent sum, but are not being perfectly co-phased, in that the highest bearing level is lower than the coherent sum.

The three x's on the first three plots in Figure 5.23 mark the highest three-dimensional bearing levels, normalized by the coherent sum of the horizontal and vertical geophone spectral levels. Including the vertical channel does not change the conclusion regarding bearing level gain.

5.2.6. Correlating Geophone Signals

In a somewhat separate effort to determine the direction to the source, geophone signals from pairs of floats were correlated. The correlation of two broadband signals is a spike at a particular time delay. Narrowband signals have a sinusoidal correlation function. The experimental data contain ship-generated signals, which are approximately sinusoidal, but it was hoped that they had sufficient bandwidth for the correlation functions to yield unique time delays. The delays for all float pairs might then be used to estimate the source bearing from each pairs of floats.

The time series from the 4 floats were Fourier transformed and pairwise multiplied together to obtain their cross power spectra. The cross power spectra were then divided by the power spectrum of one of the pair to obtain the transfer functions of the channels separating each float pair. The channel transfer functions were inverse Fourier transformed to obtain the channel impulse responses.²⁸ In order to restrict the correlation to frequencies originating from the source, only the 17 bins centered at each frequency were used.

The correlation results are shown in Appendix E. They contain many peaks, indicating that there was insufficient bandwidth to the source lines for the correlation method to yield useful information about source direction.

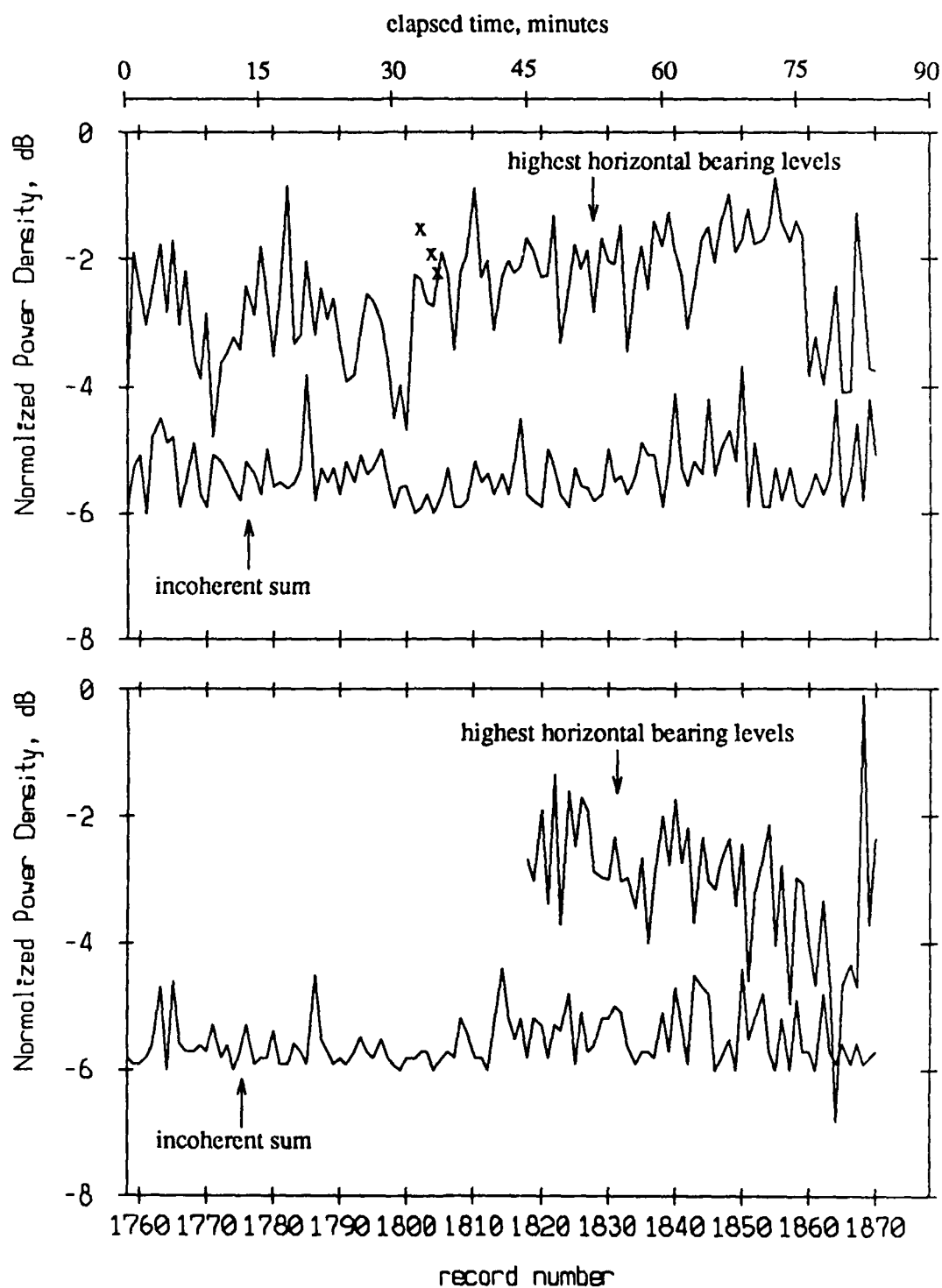


Figure 5.23a Highest horizontal bearing level and incoherent sum of the 9 Hz (upper panel) and 13.5 Hz (lower panel) spectral levels of each float's x and y axis geophones. Both are normalized by the coherent sum of all floats' horizontal spectral levels. X's mark the highest normalized 3-d bearing levels.

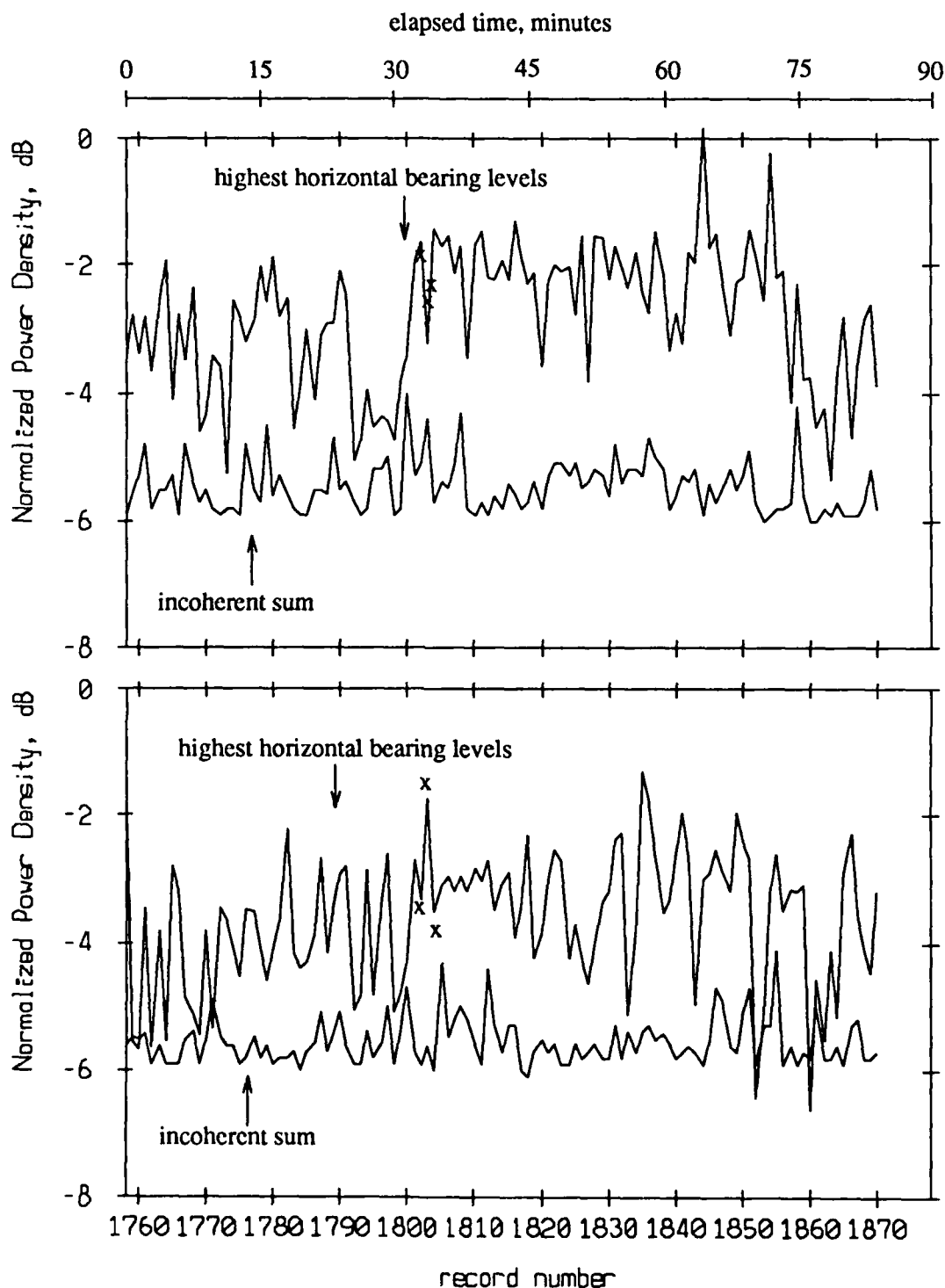


Figure 5.23b Highest horizontal bearing level and incoherent sum of the 10.3 Hz (upper panel) and 12.2 Hz (lower panel) spectral levels of each float's x and y axis geophones. Both are normalized by the coherent sum of all floats' horizontal spectral levels. X's mark the highest normalized 3-d bearing levels.

6. Analysis and Conclusions

The beamforming results shown in Chapter 5 indicate that different frequency signals emanating from the same source arrive at the array at different azimuth and elevation angles, and at different strengths. Also, because the floats are so widely dispersed and the array aperture so large, the azimuth and elevation arrival angles at a particular frequency vary considerably from float to float. This indicates that signals are propagating to the array by frequency-dependent paths, and are not propagating across the array as plane waves. Since the beamformer calculates delays to co-phase signals propagating across the array as plane waves, this may explain why the peak bearing levels are not as high as the coherent sum.

The effect of improperly co-phasing the time series (due to non-plane wave propagation) can be simulated by feeding the beamformer erroneous float positions, causing it to calculate an erroneous set of time delays. The effect of different strength signals can be simulated by introducing shading errors. The difference in float spectral levels at the frequencies of interest was found to be 14 dB or less, except when an anomaly such as clipping occurs. Figure 6.1 shows the effect of shading errors alone on the horizontal bearing response of the four Swallow float array during record 1830 with a 10.3 Hz source at azimuth 202°, elevation 0°. Shading errors uniformly distributed between 0 and 14 dB have been introduced into each trace. It is apparent that this type of error by itself does not produce results like those seen in the experimental data, e.g. Figure 5.19.

Figure 6.2 shows the bearing response of the same array to the same source, but here position errors have been combined with shading errors. The position errors used in this simulation are mean zero and have a standard deviation of 20 meters. Shading errors are uniformly distributed between 0 and 14 dB. This Figure looks much like the experimental bearing level plots in Figure 5.19.

The experimental bearing levels in Figure 5.19 indicate that the source is either to the east or to the west of the array. The rough underwater terrain to the east makes it more likely that the source is actually east of the array, so that the high bearing levels at azimuth 270° magnetic are due to the 180° ambiguity. Relatively steep underwater cliffs begin about 5 miles east of the array and rise to quite shallow water, approximately 100 meters deep, about 14 miles to the east. These rough features may cause sound to be scattered in many directions, so that from the array, the source direction appears to change erratically with time.

The shallow water east of the array also offers a plausible explanation for the absence of the 4.5 Hz fundamental frequency in the Swallow float data. The cutoff frequency may be higher than 4.5 Hz over some portion of the transmission path between the source and the array. To calculate the water depth required to block transmission of a 4.5 Hz signal, assume a 3 layer model consisting of a constant sound speed water layer bounded from above by an air half-space and from below by a sediment half-space. As shown in Chapter 9 of Medwin and Clay,²⁹ the equation which sets the minimum depth for a particular frequency to propagate is

$$(m-1)\pi + \phi_u + \phi_l \leq \frac{2\pi h}{\lambda} \left[1 - \left(\frac{c_0}{c_1} \right)^2 \right]^{1/2} \quad (6.1)$$

where m is the mode number, $2\phi_u$ is the phase angle of the reflection coefficient at the upper (air-water) boundary, $2\phi_l$ is the phase angle of the reflection coefficient at the lower (water-sediment) boundary, h is the water depth, c_0 and c_1 are the sound speeds in the water and sediment, respectively, and λ is the wavelength of sound at the frequency of interest. Assuming an ideal pressure release air-water interface, $2\phi_u = \pi$. Assuming an ideal rigid bottom, $\phi_l = 0$. Set m equal to 1 because the first mode must propagate for any mode to propagate. The wavelength at 4.5 Hz, assuming a sound speed of 1500 meters/sec, is approximately 330 meters. Substituting these values into equation (6.1) yields

$$\frac{\pi}{2} \leq \frac{2\pi h}{300} \left[1 - \left(\frac{c_0}{c_1} \right)^2 \right]^{1/2}$$

Bearing Response, Record 1830, 10.3 Hz. Source @ 202
 No Position Error, < 14 dB Shading Error

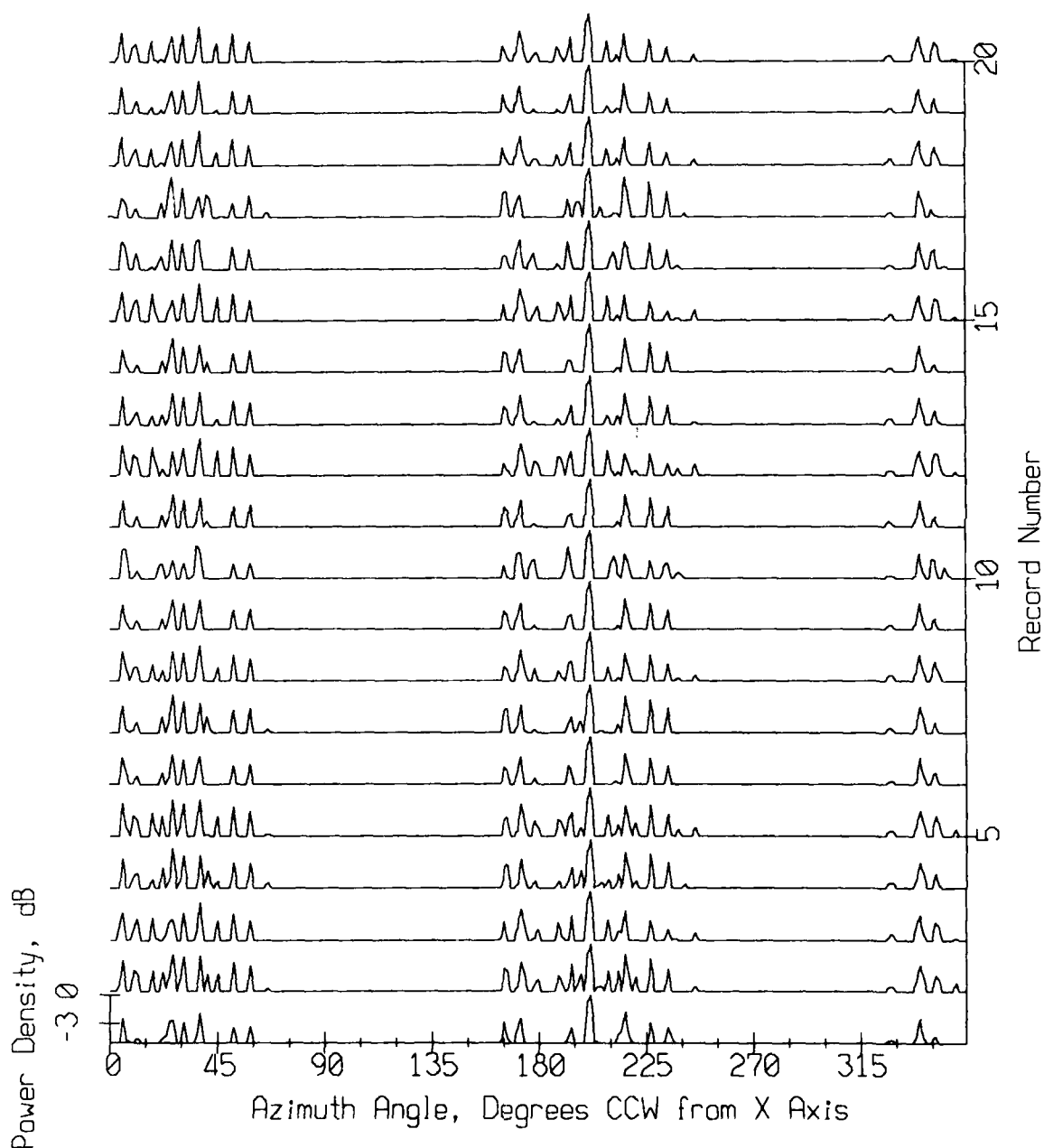


Figure 6.1 Horizontal bearing response of the four Swallow float array during record 1830 to a 10.3 Hz source at azimuth 202°, elevation 0°, showing the effect of 0 to 14 dB, uniformly distributed shading errors.

Bearing Response, Record 1830, 10.3 Hz. Source @ 202
20 M. RMS Position Errors and Random Shading

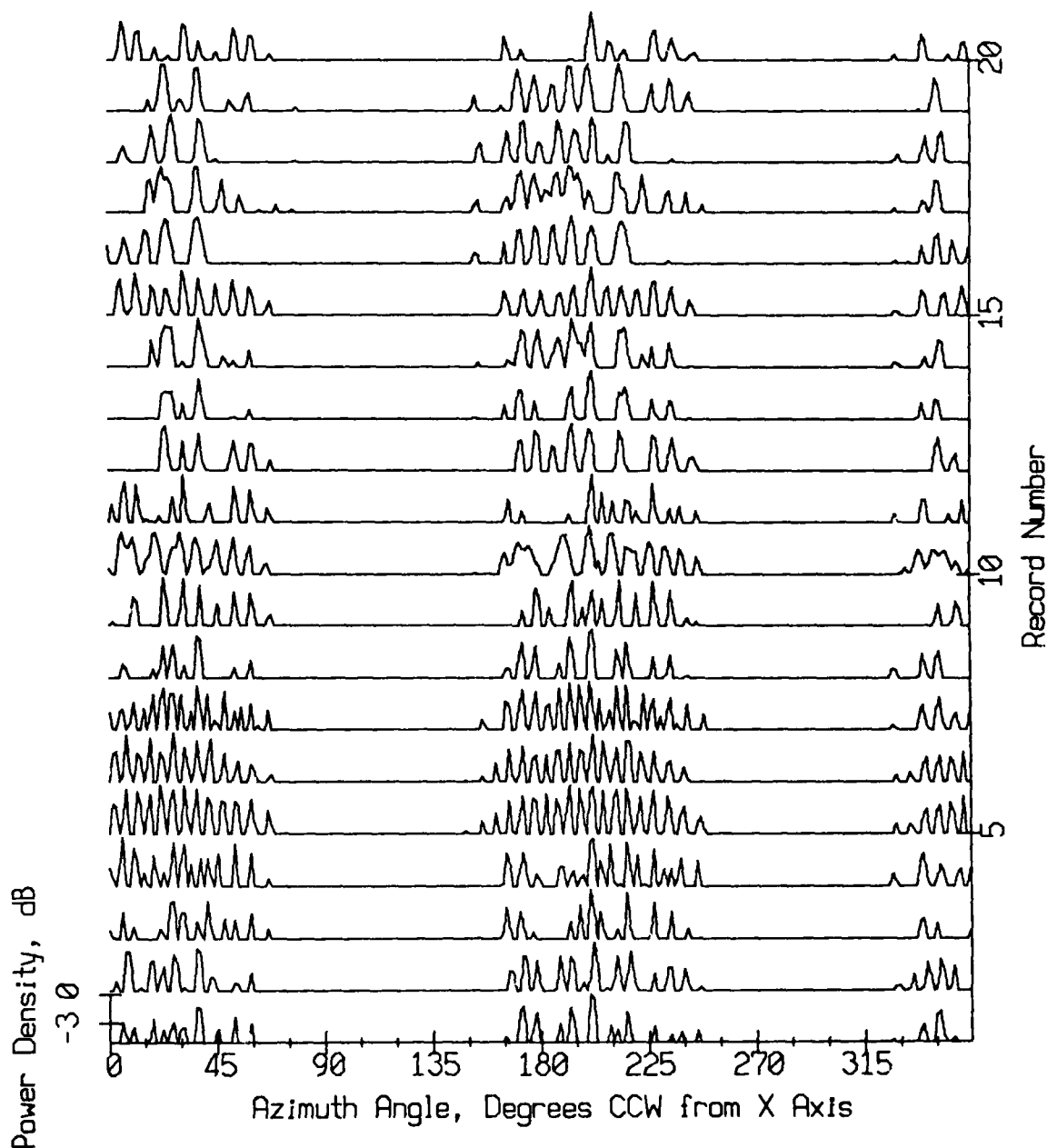


Figure 6.2 Horizontal bearing response of the four Swallow float array during record 1830 to a 10.3 Hz source at azimuth 202°, elevation 0°, showing the effect of shading errors and mean zero, normally distributed position errors (standard deviation = 20 meters).

and the condition on h is

$$h \geq 75 \left[1 - \left(\frac{c_0}{c_1} \right)^2 \right]^{-1/2} \quad (6.2)$$

If $c_1 \gg c_0$, then

$$h \geq 75 \text{ meters} \quad c_1 \gg c_0$$

If $c_1 = 1.2 c_0$, then

$$h \geq 135 \text{ meters} \quad c_1 = 1.2 c_0$$

Thus depending upon the values chosen for c_1 and c_0 , the water depth would need to be shallower than about 150 meters in order to block a 4.5 Hz signal. We saw in Figure 3.2 that this condition is met to the east of the array. It is not necessary that the source be in shallow water, only that the transmission path include shallow water.

The variation in vertical arrival angle seen in Figure 3.11 may have something to do with the radiation pattern of the source. If the 9 Hz line set are blade pass harmonics, they are radiated by the tip of each blade of the ship's propeller as it passes the hull. The sound radiates strongly outward and downward. If the other lines at 10.3 and 12.2 Hz are auxiliary machinery tonals, they tend to radiate primarily outward rather than downward. Thus we might expect the 9, 13.5 Hz, etc. lines to arrive at higher angles than the 10.3 and 12.2 Hz signals.

References

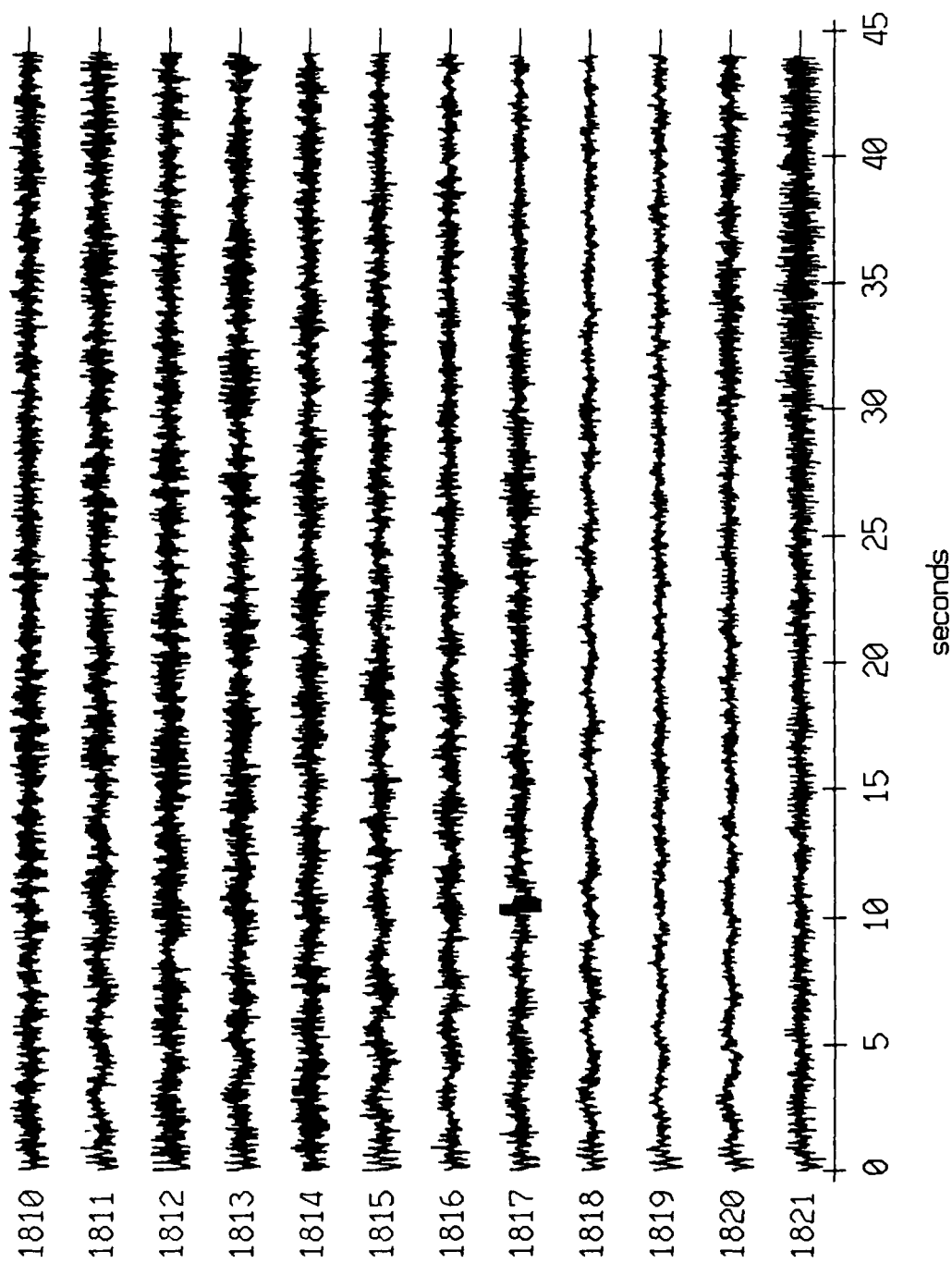
1. Swallow, J. C., "A neutral-buoyancy float for measuring deep currents," *Deep-Sea Research*, vol. 3, pp. 74-81, London, 1955.
2. Culver, R. L., "Infrasonic ambient ocean noise spectra from freely drifting sensors," SIO Reference 85-22, Scripps Institution of Oceanography, San Diego, CA, 1985. Also, Master's thesis, University of California, San Diego, 1988.
3. Hawes, R., W. S. Hodgkiss, V. C. Anderson, J. C. Nickles, and G. L. Edmonds, "Freely Drifting Swallow float Array: Surface Echo Detection and Tracking," MPL TM-348, Marine Physical Laboratory, Scripps Institution of Oceanography, San Diego, CA, 1982.
4. Hodgkiss, W. S. and V. C. Anderson, "Acoustic positioning for an array of freely drifting sensors," *IEEE J. Oceanic Eng.*, vol. OE-8, no. 3, pp. 116-119, 1983.
5. Culver, R. L., "Infrasonic ambient ocean noise spectra from freely drifting sensors," SIO Reference 85-22, Scripps Institution of Oceanography, San Diego, CA, 1985. Also, Master's thesis, University of California, San Diego, 1988.
6. Culver, R. L., W. S. Hodgkiss, V. C. Anderson, J. C. Nickles, and G. L. Edmonds, "Freely drifting Swallow float array: Initial estimates of interelement range," MPL TM-380, Marine Physical Laboratory, Scripps Institution of Oceanography, San Diego, CA, 1985.
7. Hodgkiss, W. S., V. C. Anderson, G. Edmonds, J. C. Nickles, and R. L. Culver, "A freely drifting infrasonic sensor system," *Fourth Working Symposium on Oceanographic Data Systems*, February 4-6, 1986.
8. Culver, R. L., G. L. Edmonds, W. S. Hodgkiss, V. C. Anderson, and J. C. Nickles, "Freely Drifting Swallow Float Array: September 1985 Trip Report," MPL TM-383, Marine Physical Laboratory, Scripps Institution of Oceanography, San Diego, CA, 1986.
9. Culver, R. L., W. S. Hodgkiss, G. L. Edmonds, and V. C. Anderson, "Freely Drifting Swallow Float Array: September 1986 Trip Report," MPL TM-391, Marine Physical Laboratory, Scripps Institution of Oceanography, San Diego, CA, 1987.
10. Culver, R. L., W. S. Hodgkiss, V. C. Anderson, J. C. Nickles, and G. L. Edmonds, "Removing Resonant Oscillation Signals from Swallow Float Data," MPL TM-395, Marine Physical Laboratory, Scripps Institution of Oceanography, San Diego, CA, 1987.
11. Culver, R. L., W. S. Hodgkiss, V. C. Anderson, and G. L. Edmonds, "Low Frequency Oscillations in 1986 Swallow Float Data," MPL TM-394, Marine Physical Laboratory, Scripps Institution of Oceanography, San Diego, CA, 1988.
12. Culver, R. L., G. L. D'Spain, and William S. Hodgkiss, "Vertical Oscillation in Freely Drifting Swallow Floats," MPL TM, Marine Physical Laboratory, Scripps Institution of Oceanography, San Diego, CA, under preparation.
13. D'Spain, G. L., R. L. Culver, W. S. Hodgkiss, and G. L. Edmonds, "Freely Drifting Swallow Float Array: April 1987 Trip Report," MPL TM-397, Marine Physical Laboratory, Scripps Institution of Oceanography, San Diego, CA, 1987.
14. D'Spain, G. L., R. L. Culver, W. S. Hodgkiss, and G. L. Edmonds, "Swallow Float Experiment May 1987," MPL TM-402, Marine Physical Laboratory, Scripps Institution of Oceanography, San Diego, CA, 1987.
15. D'Spain, G. L., W. S. Hodgkiss, and G. L. Edmonds, *Trip Report - August 1987 Swallow Float Deployment with RUM*, Marine Physical Laboratory, Scripps Institution of Oceanography, San Diego, CA, December 1987.
16. Ross, D., *Mechanics of Underwater Noise*, Pergamon Press, New York, 1976.
17. *Physical, Chemical and Biological Data: CalCOFI Cruise 8609 18 September - 3 October 1986*, University of California, Scripps Institution of Oceanography, San Diego, CA., 14 April 1987.

18. National Oceanographic Data Center, *archival data*, Scripps Institution of Oceanography, La Jolla, Ca..
19. Mackenzie, K. V., "Nine-term equation for sound speed in the oceans," *J. Acoust. Soc. Am.*, vol. 70, No. 3, September 1981.
20. Steinberg, B. D., *Principles of Aperture and Array System Design*, Wiley, New York, 1976.
21. Culver, R. L., G. L. D'Spain, and William S. Hodgkiss, "Estimating Travel Times and Travel Time Errors from Swallow Float Acoustic Range Data," MPL TM, Marine Physical Laboratory, Scripps Institution of Oceanography, San Diego, CA, under preparation.
22. Culver, R. L. and W. S. Hodgkiss, "Comparison of Kalman and Least Squares Filters for Locating Autonomous Very Low Frequency Acoustic Sensors," *submitted to JOE*, 1988.
23. Munk, W. H. and F. Zachariasen, "Sound propagation through a fluctuating stratified ocean: theory and observation," *J. Acoust. Soc. Am.*, 1976.
24. Piip, A. T., "Fine structure and stability of the sound channel in the ocean," *J. Acoust. Soc. Am.*, vol. 36, No. 10, 1964.
25. Weinberg, H., *Generic Sonar Model*, Naval Underwater Systems Center, New London, CT., 1985.
26. DeFatta, D., J. Lucas, and W. S. Hodgkiss, *Digital Signal Processing*, Wiley, New York, 1988.
27. Halliday, D. and R. Resnick, *Fundamentals of Physics*, Wiley & Sons, New York, 1981.
28. Roth, P. R., "Effective measurements using digital signal analysis," *IEEE Spectrum*, April 1971.
29. Clay, C. S. and H. Medwin, *Acoustical Oceanography: Principles and Applications*, Wiley & Sons, New York, 1977.

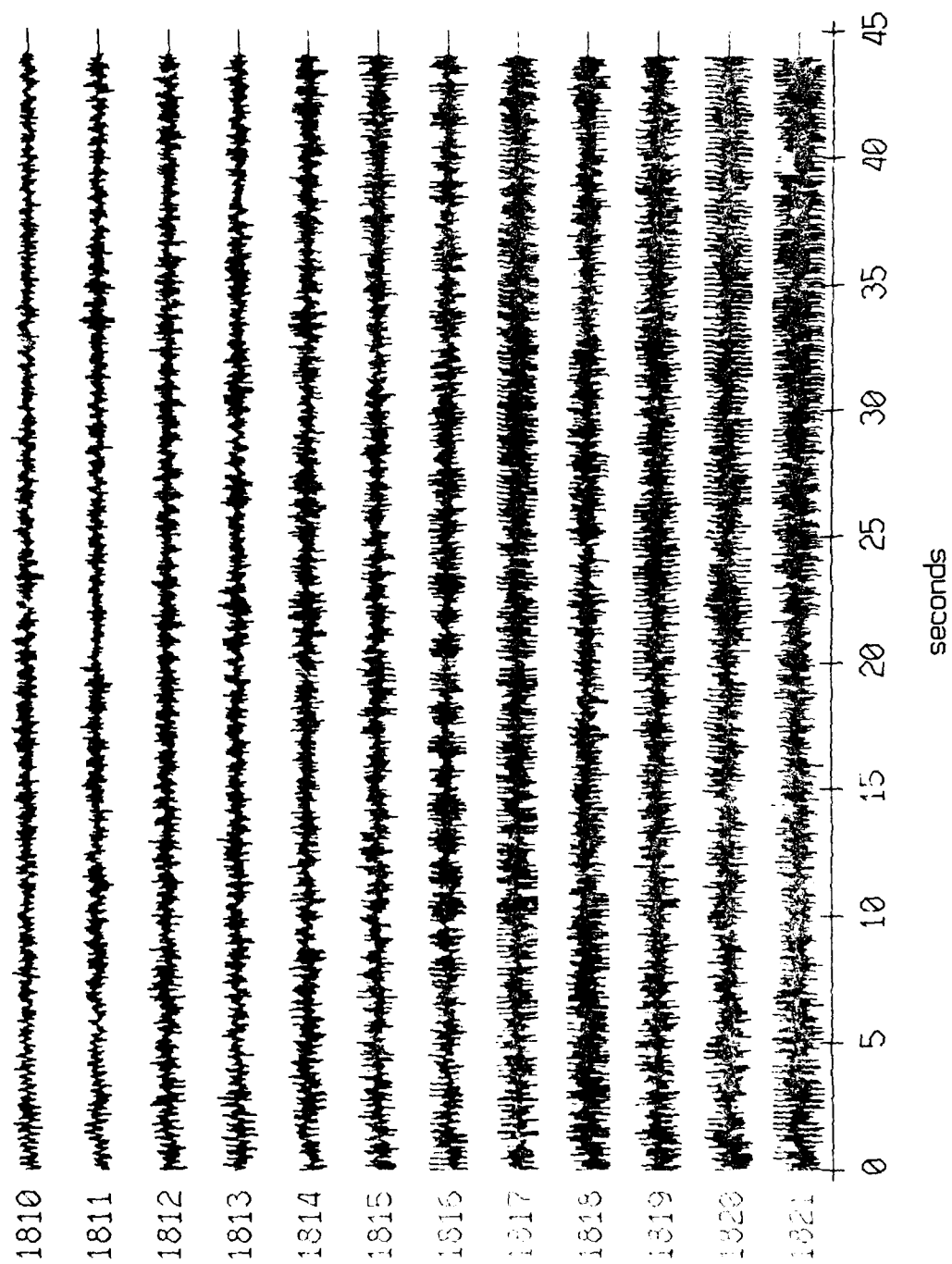
APPENDIX A

AGC Corrected Geophone Time Series

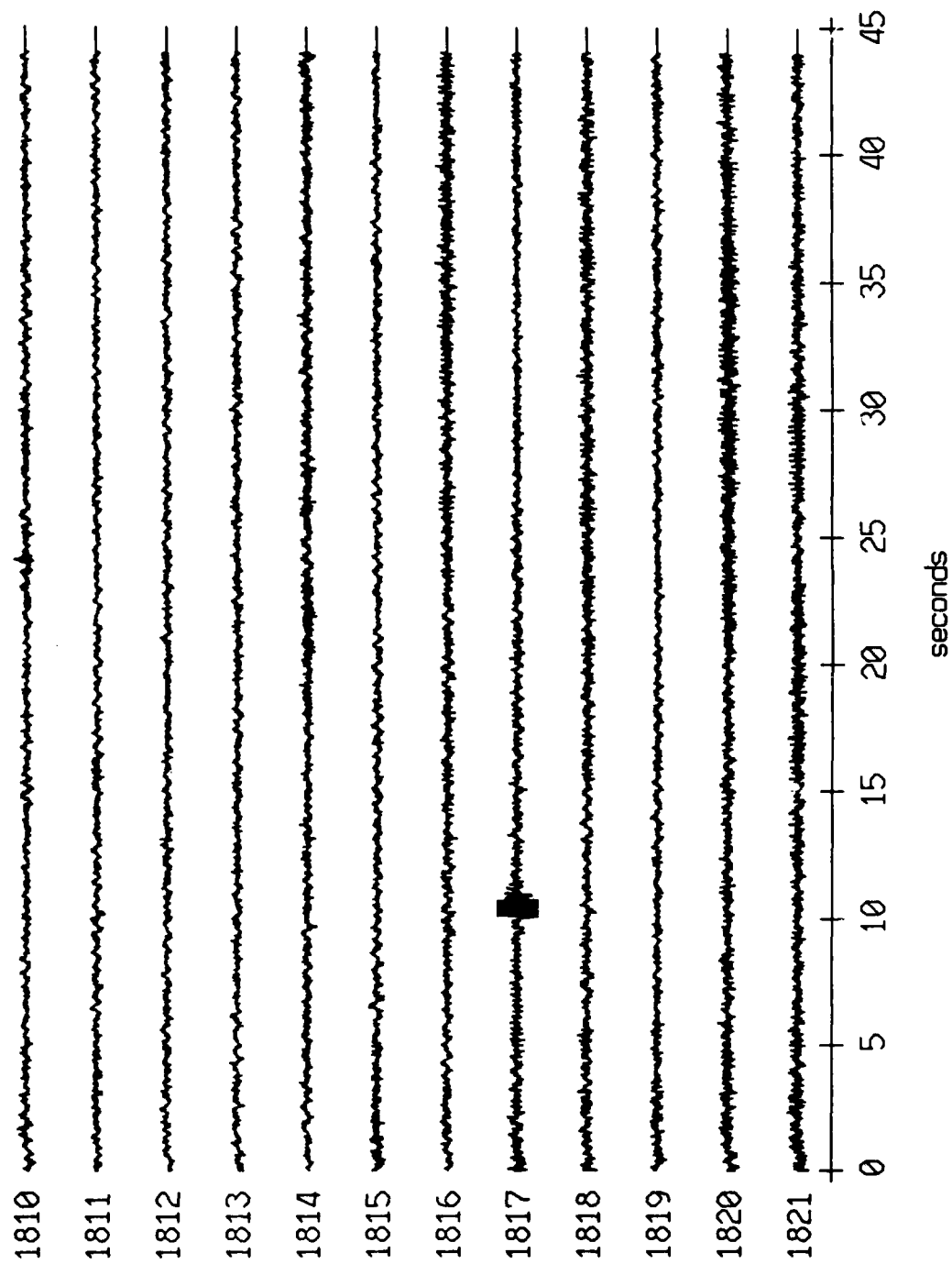
AGC Corrected Geophone Time Series, Float 5, x-axis



AGC Corrected Geophone Time Series, Float 5, y-axis



AGC Corrected Geophone Time Series, Float 5, z-axis

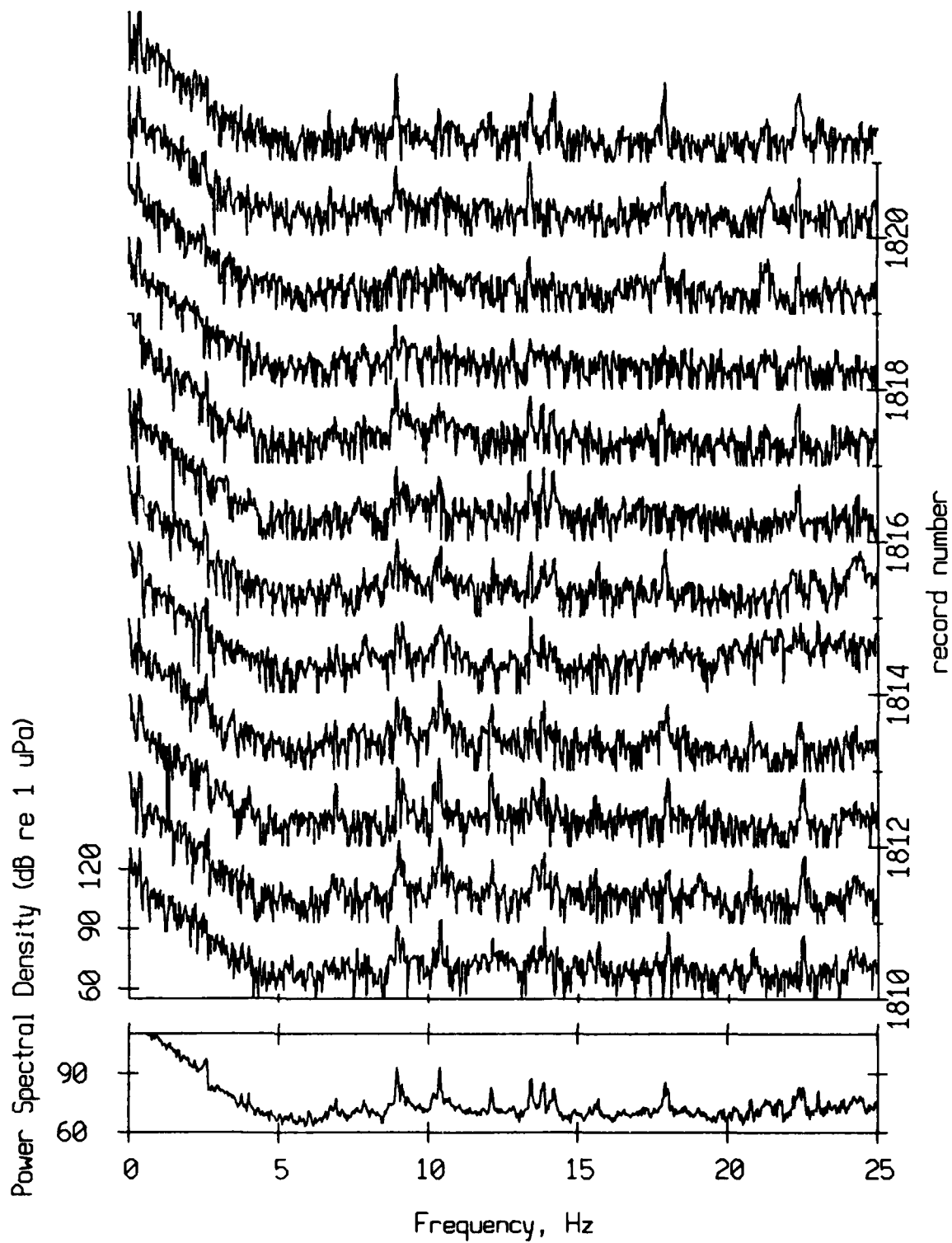


APPENDIX B

Geophone Power Spectra

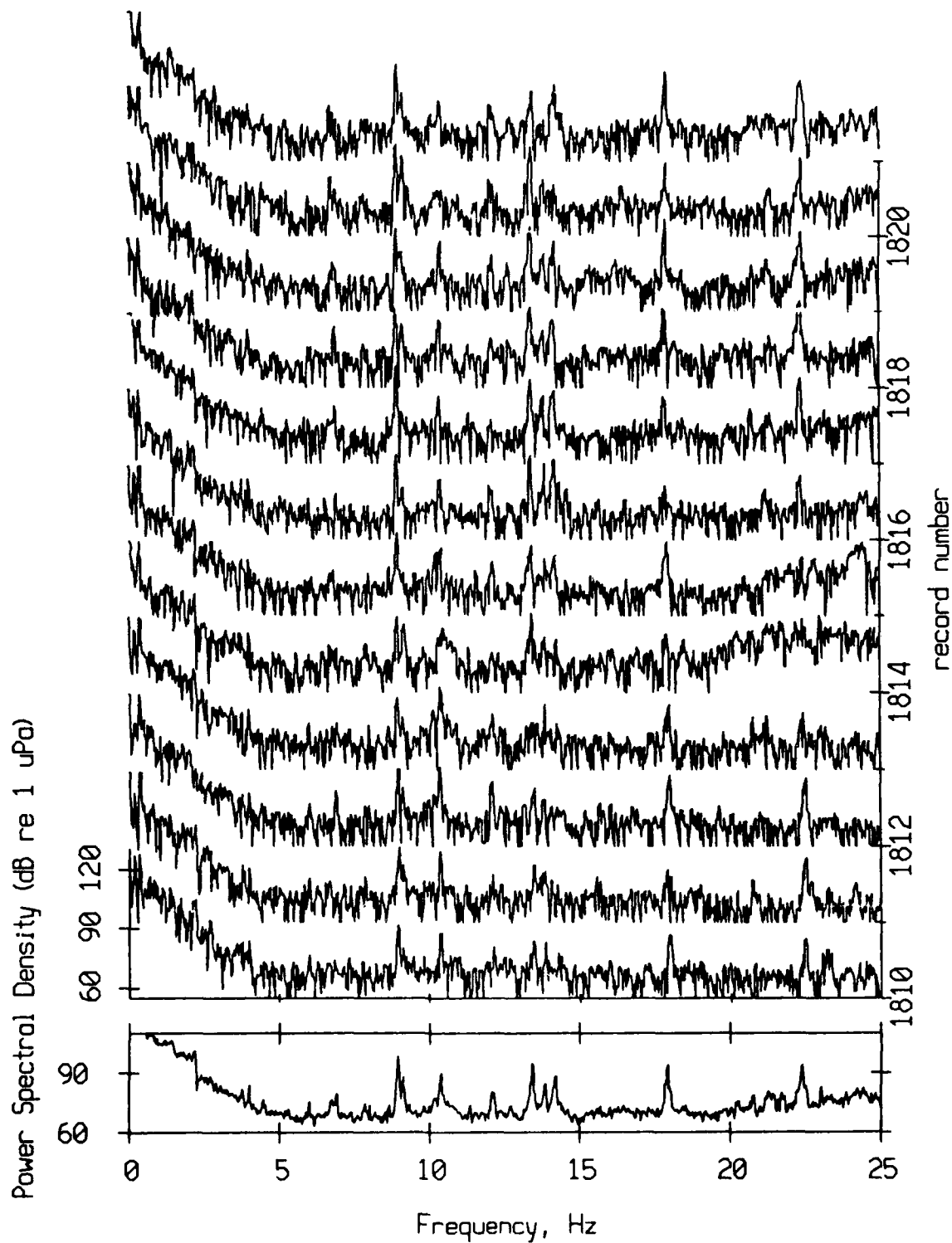
Float 5, X Axis Geophone Power Spectra

Records 1810 - 1821 and the 12 Record Average



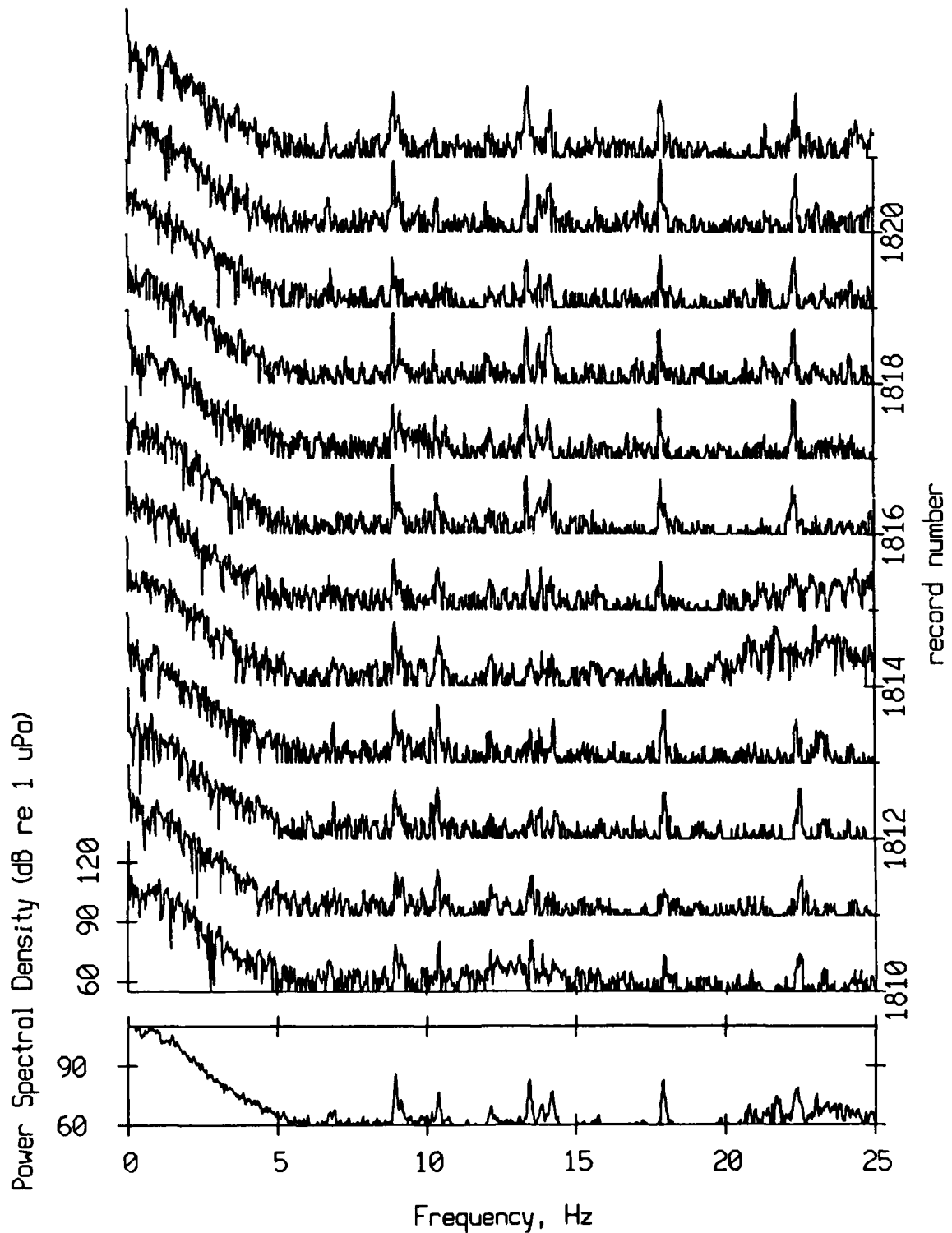
Float 5, Y Axis Geophone Power Spectra

Records 1810 - 1821 and the 12 Record Average



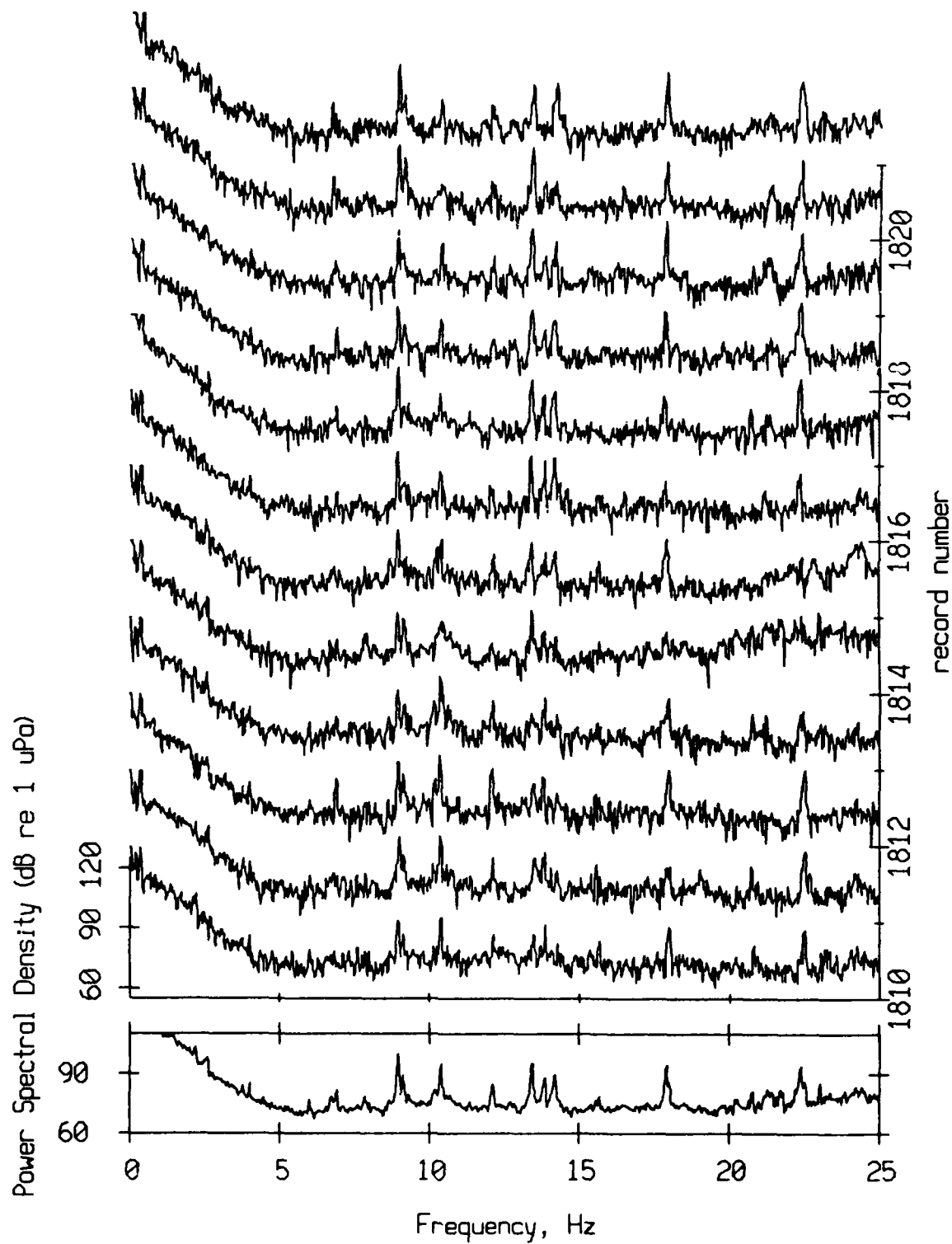
Float 5, Z Axis Geophone Power Spectra

Records 1810 - 1821 and the 12 Record Average



Float 5, Sum of Three Geophone Power Spectra

Records 1810 - 1821 and the 12 Record Average



Appendix C

Comparison of Kalman and Least Squares Filters for Locating Autonomous Very Low Frequency Acoustic Sensors

R. L. Culver and W. S. Hodgkiss

Marine Physical Laboratory
Scripps Institution of Oceanography
San Diego, CA 92152

1. Introduction

Under Office of Naval Research sponsorship, the Marine Physical Laboratory has designed and built self-contained, freely-drifting Swallow floats which can measure ambient ocean noise in the 1 to 20 Hz band for up to 25 hour periods. The floats are ballasted for neutral buoyancy at a specified depth. The deployment of several floats forms a freely-drifting array of noise sensors whose outputs may be combined after the experiment with a beamformer. [1]

Float locations must be known in order to beamform their outputs. The floats generate and receive acoustic pulses and thereby measure float to surface and float to float travel times. A series of signal processing routines have been developed to estimate float position from these travel time measurements. This paper compares two localization methods:

- A *generalized least squares* filter estimates current position using the current set of travel time measurements. The filter uses only that set of measurements and an estimate of the mean square measurement error.
- A *Kalman* filter estimates current position by weighting the current set of measurements against the previous position estimate propagated forward in time. Position estimates are propagated forward in time using equations of motion developed for the floats. The filter also uses estimates of the measurement error variance and float accelerations.

Computer simulation is used to compare filter performance under several deployment scenarios. The effects of increasing the randomness of float movement and the measurement error are also investigated. Results show that the Kalman filter performs better than the least squares filter as long as the floats are only subjected to small magnitude accelerations between measurements. This is true even when there are large measurement errors. Neither filter was found to be sensitive to relatively major changes in deployment geometry as long as the sound speed profile is known exactly. However, deploying the floats in a vertical array does degrade

the performance of both filters.

MPL has been deploying Swallow floats since 1982. A number of articles and technical reports have been written describing various aspects of the project. [2-11] The reader is referred to articles cited in the reference list for details about Swallow float construction and functioning not found in this paper.

2. Travel Time Measurements and Mean Square Measurement Error

In this section we discuss the travel time measurements made by the floats and show data from a September 1986 Swallow float experiment. We describe how the measurements are processed to remove errors caused by differences among float clock rates and estimate mean square measurement error. The resulting float to float and float to surface travel time and mean square error estimates are the inputs to the Kalman and least squares filters.

The general Swallow float hardware configuration is shown in Figure 1. Suspended about 1 meter below the glass sphere is an acoustic transducer which generates and receives 8 kHz tone bursts. Pulses 10 milliseconds long are transmitted by the floats in a pre-programmed sequence. A different float transmits every 45 seconds. When there are N floats deployed, each float transmits every $45 \cdot N$ seconds. Twelve floats are normally deployed, and each float normally transmits every 9 minutes.

The floats are listening whenever they are not transmitting. They receive pulses transmitted by other floats as well as reflections of their own pulses. They ordinarily detect reflections from the ocean surface, and often from the ocean bottom.

The float pulse detection circuit outputs an analog signal indicating whether or not a pulse is detected. The signal is sampled by the float at 1 kHz (1000 times per second) and a bit is set to 1 if a pulse is present, 0 otherwise. Groups of eight detection circuit samples are inspected by the float for the presence of range pulses (bits which are set). Bytes which contain bits set are stored internally along with their time according to the float's internal clock.

After a deployment, the stored pulse arrival information may be used to reconstruct the sampled pulse detection circuit output. We can display this information directly by converting it to a raster image. Figure 2 is one such plot, taken from the September 1986 deployment of 12 Swallow floats in the Pacific ocean 50 miles west of San Diego, Ca. The vertical scale of the plot has been changed from travel time (in seconds) to range (in meters) using the approximate speed of sound, 1500 meters/second. The plot shows detections made by float 4 during records when float 3 transmitted. The depth of both floats was about 1000 meters and water depth was 2000 meters. [8]

The line of very short dashes running across the upper part of the plot mark the arrival of the direct path pulse from float 3 at float 4. These dashes are about 15 meters (10 msec) in length and are separated by 12 records. The much longer vertical lines running across the plot at greater range mark the arrival of pulses which bounced off the ocean surface and then traveled to the float. These lines are 150 to 600 meters (100 to 400 msec) long and are also separated by 12 records. The arrival of surface bounce pulses is spread out in time because of scattering by the sea surface.

A computer program has been developed to detect the upper edge of each dash or line, which corresponds to when the pulse first arrives. The program is referred to as the *edge detector* [5] in that it outputs the time corresponding to each pulse's leading edge. Applying the edge detector to the pulse arrival information shown in Figure 2, we obtain the time series shown in Figure 3. Both Figures are plotted on the same scale so that they may be compared to verify edge detector performance.

Noise in the edge detector output is evidenced by the bad point at about record 1850. Smaller magnitude measurement noise, too small to be visible on this scale, is also present in the edge detector output. [12]

The pulse arrival time according to the edge detector minus the time when the pulse was transmitted is the travel time measurement. Each float determines the pulse transmission time according to its own internal clock. However, the clock rates vary slightly among the floats so that reciprocal path travel time measurements must be interpolated and averaged to obtain the true interfloat travel time. There are, in fact, several processing steps which the measurement time series must pass through before being fed into the Kalman or least squares filters. These steps are shown in Figure 4. The dotted line shows how simulated travel time measurements are introduced in order to validate the processing and filtering under different conditions.

A *one-step forward adaptive linear predictor* [5] is used to reject noisy points (like the one evident in Figure 3) and fill gaps which sometimes occur in the travel time series. The linear predictor must be told the maximum allowable difference between the predicted value and a data point for the data to be considered valid. Predictor output is monitored to ensure that it is functioning properly and if necessary, the maximum difference parameter is adjusted.

We must interpolate the travel time measurements before averaging reciprocal path measurements because the measurements are not made simultaneously. They are separated in time by at least 45 seconds, and by as much as $N/2 * 45$ seconds, where N is the number of floats deployed. A cubic spline interpolation is used.

Reciprocal path interfloat travel times are then averaged. The averaged interfloat travel times and float to surface travel times are ready for input to the least squares or Kalman filter.

An estimate of the mean square measurement error is obtained by taking the mean square of the difference between reciprocal path travel time measurements minus a least squares linear fit to the difference. [12] The mean square measurement error estimate is used by both filters to weight the measurements, that is, give greater weight to those with smaller mean square error.

3. The Least Squares Filter

Our problem is to use the travel time measurements and measurement error estimates just described to estimate float positions. The least squares filter operates on one set of travel time measurements and produces a set of float positions which minimizes the square of the differences between the measurements and the interfloat travel times calculated using the position estimate. A generalized least squares estimator is employed, allowing greater weight to be applied to certain measurements. The measurement error estimates determine the weights, with greater weight applied to measurements whose error is thought to be lower.

The derivation of the least squares estimator and the loss function linearization method presented here closely follows that given by Sorenson. [13] We start by identifying the n^{th} measurement vector

$$Z_n = C' \begin{bmatrix} \hat{r}_{12}^n \\ \hat{r}_{13}^n \\ \vdots \\ \hat{r}_{N-1,N}^n \\ \hat{r}_1^n \\ \vdots \\ \hat{r}_N^n \end{bmatrix} \quad (3.1)$$

where \hat{r}_{ij}^n is the averaged travel time estimate between floats i and j , \hat{r}_i^n is the round trip travel time estimate between float i and the surface, and C is a matrix whose diagonal elements are the estimated average sound speeds for the paths over which the travel times were measured.

$$C = \begin{bmatrix} \hat{c}_{12} & & & & 0 & 0 \\ & \ddots & & & & 0 \\ & & \hat{c}_{N-1N} & & & \\ & & & \frac{\hat{c}_1}{2} & & \\ 0 & & & & \ddots & \\ 0 & 0 & & & & \frac{\hat{c}_N}{2} \end{bmatrix} \quad (3.2)$$

The last N elements of (3.2), which are divided by 2, correspond to round trip travel times.

The measurement vector is related to the float position vector according to

$$Z_n = h(X_n) + V_n \quad (3.3)$$

X_n is the vector of float positions at time n

$$X_n^T = [x_1^n \ y_1^n \ z_1^n \ \cdots \ x_N^n \ y_N^n \ z_N^n] \quad (3.4)$$

and x_1^n is the x coordinate of float 1 at time n , etc. The origin of the coordinate system is at the ocean surface directly above float 1, and z is positive downward. The axes are rotated so that float 2 is in the xy plane.

$h(X_n)$ indicates a nonlinear transformation on X_n from position space to measurement space (ranges and depths).

$$h(X_n) = \begin{bmatrix} \left[(x_2^n - x_1^n)^2 + (y_2^n - y_1^n)^2 + (z_2^n - z_1^n)^2 \right]^{\frac{1}{2}} \\ \left[(x_3^n - x_1^n)^2 + (y_3^n - y_1^n)^2 + (z_3^n - z_1^n)^2 \right]^{\frac{1}{2}} \\ \vdots \\ \left[(x_N^n - x_{N-1}^n)^2 + (y_N^n - y_{N-1}^n)^2 + (z_N^n - z_{N-1}^n)^2 \right]^{\frac{1}{2}} \\ z_1^n \\ z_2^n \\ \vdots \\ z_N^n \end{bmatrix} \quad (3.5)$$

The first group of elements of $h(X_n)$ are the interfloat ranges and the second group are the float to surface distances, or depths.

V_n in equation (3.3) is the measurement error or noise vector

$$V_n^T = [\hat{c}_{12} v_{12}^n \quad \hat{c}_{13} v_{13}^n \quad \cdots \quad \hat{c}_{N-1N} v_{N-1N}^n \quad \hat{c}_1 v_1^n \quad \cdots \quad \hat{c}_N v_N^n] \quad (3.6)$$

whose elements are, or are made to be, mean zero. The subscripts of the v 's are the same as those of the \hat{c} 's and \hat{r} 's described below (3.1). The covariance of V_n is R , where

$$E [V_n V_m^T] = R_n \delta_{nm} \quad (3.7)$$

We assume that the noise is uncorrelated from measurement to measurement, an assumption which has been demonstrated to be reasonable. [12] R is thus diagonal, with elements [12]

$$\sigma_{r_{ij}}^2 = (\hat{r}_{ij}^n)^2 \sigma_{c_{ij}}^2 + (\hat{c}_{ij})^2 \sigma_{r_{ij}}^2 \quad (3.8)$$

where \hat{r}_{ij}^n and \hat{c}_{ij} are identified in (3.1) and (3.2), and $\sigma_{c_{ij}}^2$ and $\sigma_{r_{ij}}^2$ are the variances of the uncertainties in c_{ij} and r_{ij} , respectively.

The least squares estimate of X_n , given measurements Z_n , is defined as the value \hat{X}_n which minimizes the following loss function:

$$\begin{aligned} l_{LS} &= [Z_n - h(X_n)]^T R_n [Z_n - h(X_n)] \\ &= Z_n^T R_n Z_n - 2Z_n^T R_n h(X_n) + h(X_n)^T R_n h(X_n) \end{aligned} \quad (3.9)$$

Necessary and sufficient conditions for \hat{X}_n to minimize l_{LS} are that $\partial l_{LS} / \partial X = 0$ and $\partial^2 l_{LS} / \partial X^2$ is positive-definite. Thus to determine the least squares estimate \hat{X} , form

$$\begin{aligned} \frac{\partial l_{LS}}{\partial X} &= -2Z_n^T R_n \frac{\partial h(X)}{\partial X} + 2h(X_n)^T R_n \frac{\partial h(X)}{\partial X} \\ &= 2 \left[h(X_n) - Z_n \right]^T R_n \frac{\partial h(X)}{\partial X} = 0 \end{aligned} \quad (3.10)$$

Equation (3.10) says that the *residual* $h(X_n) - Z_n$ must be orthogonal to the columns of $\partial h(X) / \partial X$. If $h(X)$ is a linear function of X

$$h(X_n) = H X_n$$

and

$$\frac{\partial h(X_n)}{\partial X} = H$$

then (3.10) represents a linear equation in X with solution

$$\hat{X}_{LS} = \left[H^T R H \right]^{-1} H^T R Z \quad \left[h(X) \text{ linear in } x \right] \quad (3.11)$$

However, when $h(X)$ is a nonlinear function of X , as in (3.5), (3.10) represents a system of nonlinear algebraic equations for which, in general, there is no closed form solution. As a result, we must linearize the loss function and solve the problem numerically. A numerical procedure will not in general provide an exact solution to (3.10). Our hope is that it provides an improved estimate of X , so that repeated application may yield a satisfactory estimate.

Three numerical methods were considered for estimating \hat{X}_n given Z_n and R_n . In what follows, we identify k as a step-size parameter which must be chosen. To simplify the notation, define

$$H_i \triangleq \left. \frac{\partial h(X)}{\partial X} \right|_{X=\hat{X}_i} \quad (3.12)$$

In order of increasing complexity, the methods considered are the *steepest descent procedure*

$$\hat{X}_{i+1} = \hat{X}_i + k_i H_i^T R \left[Z - h(\hat{X}_i) \right] \quad (3.13)$$

the *Gauss procedure*

$$\hat{X}_{i+1} = \hat{X}_i + k_i \left[H_i^T R H_i \right]^{-1} H_i^T R \left[Z - h(\hat{X}_i) \right] \quad (3.14)$$

and the *Newton procedure*

$$\hat{X}_{i+1} = \hat{X}_i + k_i \left\{ H_i^T R H_i - \sum_{j=1}^M \left[Z_j - h_j(\hat{X}_i) \right] R_{jj} \frac{\partial^2 h_j}{\partial X^2}(\hat{X}_i) \right\}^{-1} \cdot H_i^T R \left[Z - h(\hat{X}_i) \right] \quad (3.15)$$

Here the subscript i is the iteration index.

Newton's method was chosen for our use because it provides the most rapid convergence in the vicinity of the minimum value of l_{LS} . [13] Newton's method does entail more computation than the other methods, but that is not a problem for us at this time.

We now derive the *Newton procedure* to see what assumptions are made. We start with an initial estimate of X_n , which we call \hat{X}_n , a vector of interfloat range and float depth measurements Z_n , and a covariance matrix R_n . We want to find a new estimate of X_n which reduces the value of the loss function identified in equation (3.9). First we use a Taylor series to expand the loss function in the vicinity of \hat{X}_n , keeping terms of order 2 or less in $(X_n - \hat{X}_n)$.

$$l(X_n) \approx l(\hat{X}_n) + \left. \frac{\partial l(X)}{\partial X} \right|_{X_n = \hat{X}_n} (X_n - \hat{X}_n) + \frac{1}{2} (X_n - \hat{X}_n)^T \left[\left. \frac{\partial^2 l(X)}{\partial X^2} \right|_{X_n = \hat{X}_n} \right] (X_n - \hat{X}_n) \quad (3.16)$$

Necessary and sufficient conditions for the loss function to be minimized are that $\partial^2 l / \partial X^2$ is positive definite and that the gradient of the loss function vanish. The gradient of (3.16) is

$$\left[\frac{\partial}{\partial X} l(X) \right]^T = \left[\left. \frac{\partial l(X)}{\partial X} \right|_{X_n = \hat{X}_n} \right]^T + \left[\left. \frac{\partial^2 l(X)}{\partial X^2} \right|_{X_n = \hat{X}_n} \right] (X_n - \hat{X}_n) \quad (3.17)$$

Defining

$$\left. \frac{\partial l(X)}{\partial X} \right|_{x_n = \hat{x}_n} \triangleq g_n^T \quad (3.18)$$

$$\left. \frac{\partial^2 l(X)}{\partial X^2} \right|_{x_n = \hat{x}_n} = \frac{\partial}{\partial X} \left[\left. \frac{\partial l(X)}{\partial X} \right] \right|_{x_n = \hat{x}_n}^T \triangleq N_n \quad (3.19)$$

and

$$X_n - \hat{X}_n \triangleq P_n \quad (3.20)$$

the requirement that (3.17) vanish may be written compactly:

$$g_n + N_n P_n = 0 \quad (3.21)$$

g_n and P_n are vectors; N_n is a matrix. g_n and N_n are calculated using \hat{X}_n . Equation (3.21) is solved using the least squares method discussed below to obtain P_n . We then substitute it into (3.20) to obtain a new estimate of X_n .

$$(\text{old}) \hat{X}_n + P_n \triangleq (\text{new}) \hat{X}_n \quad (3.22)$$

We must now check our new value of \hat{X}_n against some criterion and decide if it is a satisfactory estimate of X_n . The criterion used is discussed below. If \hat{X}_n is satisfactory, we are finished and can go on to find an estimate for X_{n+1} , the float positions at the time of the $(n+1)^{\text{th}}$ measurement. If it is not, we recalculate g_n and N_n using the new value of \hat{X}_n , obtain a new least squares solution for P_n , and obtain still a newer value of \hat{X}_n using (3.22). This procedure may be repeated until a satisfactory estimate of X_n is found.

In summary, the estimate of X_n is found from Z_n and R_n using the following steps:

Summary of Least Squares Procedure

- | | |
|---------|---|
| Step 1: | Pick \hat{X}_n . |
| Step 2: | Determine if \hat{X}_n is a satisfactory estimate of X_n . If so, terminate the search, increment n and go to Step 1. If not, go to Step 3. |
| Step 3: | Calculate g_n and N_n using equations (3.18) and (3.19) and obtain a least squares solution for P_n . |
| Step 4: | Calculate a new value for \hat{X}_n using equation (3.22) and return to Step 2 |

Fixing the Coordinate System

We fix the coordinate system so that the origin lies at the surface directly above float 1, and float 2 lies in the xz plane. This is accomplished by specifying that the coordinates of floats 1 and 2 in the initial estimate \hat{X}_n are such that float 1 is on the z axis and float 2 is in the xz plane.

$$x_1^n = y_1^n = y_2^n = 0 \quad (3.23)$$

Then P_n is constrained such that

$$P_n^T \begin{bmatrix} 1 & 0 & 0 \\ 0 & 1 & 0 \\ 0 & 0 & 0 \\ 0 & 0 & 1 \\ 0 & 0 & 0 \\ \vdots \\ 0 & 0 & 0 \end{bmatrix} = \begin{bmatrix} 0 \\ 0 \\ 0 \end{bmatrix} \quad (3.24)$$

Since each new estimate \hat{X}_n is the sum of the old \hat{X}_n and P_n , the constraint (3.24) ensures that equation (3.23) continues to be satisfied.

The Least Squares Solution for P_n

Obtaining the least squares solution to (3.21) subject to the constraint (3.24) is accomplished using a method recommended by Lawson and Hanson. [14] We first derive an $(N-1) \cdot 3$ dimensional unconstrained least squares problem, solve the derived problem, and finally transform the solution of the derived problem to obtain a solution to the original constrained problem. The QR method, which involves repeated application of the Householder transformation, is used to solve the derived least squares problem.

Search Termination Criterion

The search termination criterion is used to decide if \hat{X}_n is a satisfactory estimate of X_n . We specify that the search will stop when the mean magnitude of the *residual* changes by less than 1 meter for 10 consecutive values of \hat{X}_n . The mean magnitude of the residual is

$$\text{mean magnitude of the residual} = \frac{|Z_n - h(\hat{X}_n)|}{M} \quad (3.25)$$

where M is the number of elements in the vector Z . When 10 consecutive values of (3.25) change by less than 1 meter, we stop the search and accept the current value of \hat{X}_n .

4. The Kalman Filter

The Kalman filter represents an attempt to obtain a better estimate of the float positions by taking advantage of additional information which may be available. This additional information consists of:

- a model of how the floats propagate through the water,
- an estimate of the magnitude of the accelerations to which the floats are subjected while they are deployed, and
- an estimate of the variance of the error in the initial estimate of the float positions.

When these additional pieces of information are incorporated in the Kalman filter, it can perform better than the least squares filter under conditions which we will determine.

The form of the Kalman filter is

$$\hat{X}_n = \Phi \hat{X}_{n-1} + K_n \left[Z_n - h(\Phi \hat{X}_{n-1}) \right] \quad (4.1)$$

Here \hat{X}_n is the current estimate of the float positions and velocities. \hat{X}_{n-1} is the previous estimate. The vectors Z_n and $h(\Phi \hat{X}_{n-1})$ are unchanged from the definitions in (3.1) and (3.5), respectively. The vector X_n is now twice as long as it was in the least squares filter derivation because it now includes float velocities as well as positions.

Φ is called the *transition matrix* and it propagates the float positions forward in time. K is called the *Kalman gain matrix*. Its magnitude determines how much the current float position estimate is influenced by the current measurements as opposed to relying primarily upon the previous estimate propagated forward in time.

There are many books and articles dealing with the Kalman filter. [15-20] The derivation given here closely follows Sorenson. [17]

We start with a model of the floats as they propagate through the ocean. For simplicity, consider for the moment only one float. Its position at time n is (x^n, y^n, z^n) and its velocity components are $(\dot{x}^n, \dot{y}^n, \dot{z}^n)$. The position coordinates and velocity components are combined into the vector X_n , called the *state vector*.

$$X_n^T \triangleq \begin{bmatrix} x^n & y^n & z^n & \dot{x}^n & \dot{y}^n & \dot{z}^n \end{bmatrix} \quad (4.2)$$

We model the float's movement through the water with the following linear difference equations:

$$\begin{aligned} x^{n+1} &= x^n + \dot{x}^n T + a_x^n \frac{T^2}{2} & \dot{x}^{n+1} &= \dot{x}^n + a_x^n T \\ y^{n+1} &= y^n + \dot{y}^n T + a_y^n \frac{T^2}{2} & \dot{y}^{n+1} &= \dot{y}^n + a_y^n T \\ z^{n+1} &= z^n + \dot{z}^n T + a_z^n \frac{T^2}{2} & \dot{z}^{n+1} &= \dot{z}^n + a_z^n T \end{aligned} \quad (4.3)$$

where T is the elapsed time between n and $n + 1$. The accelerations

$$\begin{bmatrix} a_x & a_y & a_z \end{bmatrix} \triangleq A^T \quad (4.4)$$

are unknown, but have zero mean

$$E(A) = 0 \quad (4.5a)$$

and known covariance

$$E \left[A_n A_m^T \right] \triangleq Q_n \delta_{nm} \quad (4.5b)$$

Equation (4.5b) is part of the new information which is used by the Kalman filter but not by the least squares filter. We define the transition matrix

$$\Phi \triangleq \begin{bmatrix} 1 & 0 & 0 & T & 0 & 0 \\ 0 & 1 & 0 & 0 & T & 0 \\ 0 & 0 & 1 & 0 & 0 & T \\ 0 & 0 & 0 & 1 & 0 & 0 \\ 0 & 0 & 0 & 0 & 1 & 0 \\ 0 & 0 & 0 & 0 & 0 & 1 \end{bmatrix} \quad (4.6)$$

and

$$\Gamma \triangleq \begin{bmatrix} \frac{T^2}{2} & 0 & 0 \\ 0 & \frac{T^2}{2} & 0 \\ 0 & 0 & \frac{T^2}{2} \\ T & 0 & 0 \\ 0 & T & 0 \\ 0 & 0 & T \end{bmatrix} \quad (4.7)$$

Using (4.6) and (4.7), we can combine equations (4.3) into one vector equation:

$$X_{n+1} = \Phi X_n + \Gamma A_n \quad (4.8)$$

Equation (4.8) is referred to as the *dynamic* or *plant* equation or process. We can expand X_n , Φ , and Γ so that equation (4.8) describes the motion of all of the floats. Equation (4.8) is a new equation which was not used by the least squares filter and which will be incorporated into the Kalman filter.

The exact value of the state at time 0 is unknown. However, we assume that its expected value

$$E(X_0) = \hat{X}_0 \quad (4.9a)$$

and covariance matrix

$$P_0 \triangleq E \left[(X_0 - \hat{X}_0) (X_0 - \hat{X}_0)^T \right] \quad (4.9b)$$

are known. Equation (4.9b) is also new information which is used by the Kalman filter.

The Kalman filter makes use of the plant equation (4.8) and the measurement equation identified in (3.3). Our goal is to determine an estimate of X_n which is a linear combination of the estimate X_{n-1} and the measurements Z_n and which minimizes the expected value of the sum of the squares of the errors in the estimate. That is,

$$E \left[(X_n - \hat{X}_n)^T (X_n - \hat{X}_n) \right] \text{ is minimized} \quad (4.10)$$

The condition (4.10) is equivalent to minimizing the trace of P_n , the covariance of the estimate error.

$$E \left[(X_n - \hat{X}_n)^T (X_n - \hat{X}_n) \right] = \text{trace} \left\{ E \left[(X_n - \hat{X}_n) (X_n - \hat{X}_n)^T \right] \right\} = \text{trace } P_n \quad (4.11)$$

We know that the state of the floats, that is their positions and velocities, evolves according to (4.8). Because the accelerations A are mean zero, one would not *expect* them to influence the state from one measurement to the next. Thus given \hat{X}_{n-1} , it is reasonable to predict, in the absence of any measurement, that

$$\hat{X}_n = \Phi \hat{X}_{n-1} \quad (\text{before any measurement}) \quad (4.12)$$

The measurement at time n can be used to modify this estimate. Based upon (4.12), one would expect the n^{th} measurement to be $h(\Phi \hat{X}_{n-1})$. The difference between Z_n and $h(\Phi \hat{X}_{n-1})$ is the new information, sometimes called the *innovation*, contained in the measurement. We define the estimate of X_n to be

$$\hat{X}_n = \Phi \hat{X}_{n-1} + K_n \left[Z_n - h(\Phi \hat{X}_{n-1}) \right] \quad (4.13)$$

where the matrix K_n will be determined to satisfy the condition (4.10).

The error in \hat{X}_n is, using (4.13) and (3.3),

$$\begin{aligned} \tilde{X}_n &\triangleq \hat{X}_n - X_n \\ &= \Phi \hat{X}_{n-1} + K_n \left[Z_n - h(\Phi \hat{X}_{n-1}) \right] - X_n \\ &\approx \Phi \hat{X}_{n-1} + K_n \left[Z_n - h(\Phi \hat{X}_{n-1}) \right] - \Phi X_{n-1} \end{aligned}$$

$$\approx \Phi \tilde{X}_{n-1} + K_n \left[h(\Phi X_{n-1}) - h(\Phi \hat{X}_{n-1}) + V_n \right] \quad (4.14)$$

We need to linearize $h(X)$ in order to simplify (4.14). We can use a Taylor series to expand $h(X)$ about its nominal value, which we call X' .

$$h(X) \approx h(X') + \left. \frac{\partial h(X)}{\partial X} \right|_{X=X'} (X - X') \quad (4.15)$$

Using (4.15) to simplify $h(\Phi X_{n-1}) - h(\Phi \hat{X}_{n-1})$, we get

$$\begin{aligned} h(X_n) - h(\hat{X}_n) &\approx \left[h(X'_n) + \left. \frac{\partial h(X)}{\partial X} \right|_{X=X'_n} (X_n - X'_n) \right] - \left[h(\hat{X}'_n) + \left. \frac{\partial h(X)}{\partial X} \right|_{X=\hat{X}'_n} (\hat{X}_n - \hat{X}'_n) \right] \\ &\approx h(X'_n) - h(\hat{X}'_n) + \left. \frac{\partial h(X)}{\partial X} \right|_{X=X'_n} (X_n - X'_n) \\ &\quad - \left. \frac{\partial h(X)}{\partial X} \right|_{X=\hat{X}'_n} (\hat{X}_n - \hat{X}'_n) \end{aligned} \quad (4.16)$$

It seems reasonable in light of (4.12) to choose for our nominal values

$$X'_n = \hat{X}'_n = \Phi \hat{X}_{n-1} \quad (4.17)$$

This reduces (4.16) to

$$h(X_n) - h(\hat{X}_n) \approx \left. \frac{\partial h(X)}{\partial X} \right|_{X=\Phi \hat{X}_{n-1}} \tilde{X}_n$$

Putting this result into (4.14) yields

$$\begin{aligned} \tilde{X}_n &\approx \Phi \tilde{X}_{n-1} - K_n \left[\left. \frac{\partial h(X)}{\partial X} \right|_{X=\Phi \hat{X}_{n-1}} \right] \tilde{X}_n + K_n V_n \\ &\approx \Phi \tilde{X}_{n-1} - K_n \left[\left. \frac{\partial h(X)}{\partial X} \right|_{X=\Phi \hat{X}_{n-1}} \right] \Phi \tilde{X}_{n-1} + K_n V_n \\ &\approx \left\{ I - K_n \left[\left. \frac{\partial h(X)}{\partial X} \right|_{X=\Phi \hat{X}_{n-1}} \right] \right\} \Phi \tilde{X}_{n-1} + K_n V_n \end{aligned} \quad (4.18)$$

Now we form the covariance of the estimate error

$$E \left[\tilde{X}_n \tilde{X}_n^T \right] \triangleq P_n \quad (4.19)$$

Putting (4.18) into (4.19), using (3.7), and assuming that X and V are uncorrelated, we can eventually obtain [17]

$$P_n = \left\{ I - K_n \left[\frac{\partial h(X)}{\partial X} \right] \Big|_{x = \Phi \dot{x}_{n-1}} \right\} M_n \left\{ I - K_n \left[\frac{\partial h(X)}{\partial X} \right] \Big|_{x = \Phi \dot{x}_{n-1}} \right\}^T + K_n R_n K_n^T \quad (4.20)$$

where we have identified

$$M_n \triangleq \Phi P_{n-1} \Phi^T + \Gamma A \Gamma^T \quad (4.21)$$

To simplify the notation, define

$$H_n \triangleq \frac{\partial h(X)}{\partial X} \Big|_{x = \Phi \dot{x}_{n-1}} \quad (4.22)$$

Then (4.20) can be written

$$P_n = M_n - K_n H_n M_n - M_n H_n^T K_n^T + K_n \left[H_n M_n H_n^T + R_n \right] K_n^T \quad (4.23)$$

The term $\left(H_n M_n H_n^T + R_n \right)$ is symmetric and non-negative definite, so it can be written as the product of a matrix S_n and its transpose (i.e. a matrix square root).

$$S_n S_n^T \triangleq H_n M_n H_n^T + R_n \quad (4.24)$$

Substituting (4.24) into (4.23) and postulating the existence of an array A in order to complete the square, we obtain

$$\begin{aligned} P_n &= M_n - K_n H_n M_n - M_n H_n^T K_n^T + K_n S_n S_n^T K_n^T \\ &= M_n + K_n S_n S_n^T K_n^T - K_n S_n A_n^T - A_n S_n K_n + A_n A_n^T \\ &\quad - K_n H_n M_n - M_n H_n^T K_n^T + K_n S_n A_n^T + A_n S_n K_n - A_n A_n^T \\ &= M_n + \left(K_n S_n - A_n \right) \left(K_n S_n - A_n \right)^T + K_n \left[S_n A_n^T - H_n M_n \right] + \left[A_n S_n^T - M_n H_n^T \right] K_n^T - A_n A_n^T \end{aligned}$$

Now define A_n so that

$$S_n A_n^T - H_n M_n = 0$$

or

$$A_n = M_n H_n^T (S_n^{-1})^T \quad (4.25)$$

When S_n is singular, the pseudo inverse S_n^\dagger is used instead of S_n^{-1} . Using (4.25), the error covariance becomes

$$P_n = M_n + \left(K_n S_n - A_n \right) \left(K_n S_n - A_n \right)^T - A_n A_n^T \quad (4.26)$$

Only the product term of (4.26) involves K_n . The product of a matrix and its transpose is positive-definite. Thus the trace of P is minimized by choosing

$$K_n S_n = A_n \quad (4.27)$$

The Kalman gain matrix is then

$$\begin{aligned} K_n &= M_n H_n^T (S_n^{-1})^T S_n^{-1} \\ &= M_n H_n^T (S_n^T S_n)^{-1} \\ &= M_n H_n^T \left[H_n M_n H_n^T + R_n \right]^{-1} \end{aligned} \quad (4.28)$$

In terms of K_n , the covariance of the estimate error is

$$P_n = M_n - K_n H_n M_n \quad (4.29)$$

The *matrix inversion lemma* [17] may be used to rewrite K_n in terms of the covariance matrix

$$K_n = P_n H_n^T R_n^{-1} \quad (4.30)$$

where

$$P_n = M_n - M_n H_n^T \left[H_n M_n H_n^T + R_n \right]^{-1} H_n M_n \quad (4.31)$$

Equations (4.13), (4.21), (4.30), and (4.31) comprise the Kalman filter estimator. In summary, we obtain the estimate \hat{X}_n using the following steps:

Fixing the Coordinate System

We want the coordinate system to be fixed as in the least squares filter. To do this, we specify

- \hat{X}_0 such that float 1 is on the z axis and has zero horizontal velocity, and float 2 is on the xy plane and has zero velocity in the y direction;

Summary of Kalman Filter Procedure

- Step 1: Pick \hat{X}_0 and P_0 . Set $n = 1$. Go to step 4.
- Step 2: Using (4.21), calculate the estimate error covariance before the measurement.
- Step 3: Using (4.31), calculate the estimate error covariance after the measurement.
- Step 4: Calculate $h(\Phi \hat{X}_{n-1})$ using (3.5) and H_n using (4.22).
- Step 5: Calculate the Kalman gain using (4.30).
- Step 6: Calculate the position and velocity estimates using (4.13).
- Step 7: Increment n and go to Step 2.

- P_0 such that the errors in the initial estimates of float 1's x and y coordinate and velocity and the errors in the initial estimates of float 2's y coordinate and velocity are known to be zero.
- Q_0 such that float 1 is known to experience zero horizontal acceleration and float 2 is known to experience zero acceleration in the y direction.

5. Float Location Simulations

We now proceed to test the functioning of the travel time measurement processing discussed in Section 2 and programs implementing the least squares and Kalman filters derived in Sections 3 and 4. Test cases are developed by simulating float motion on the computer and calculating the distance between the floats at periodic intervals to simulate travel time measurements. The measurements are then processed and fed to the filters. The resulting position estimates are compared to the actual float positions. We calculate the rms position error for each float and average over all of the floats to obtain a performance measure.

Figure 5 shows the steps taken to simulate travel time measurements. We first establish the initial float positions. Four different deployment geometries are simulated in order to investigate their effect on filter performance. We then simulate float motion, propagating them through space by applying mean-zero random accelerations in the horizontal directions and oscillatory motion in the vertical direction, simulating the influence of internal waves in the ocean. Our experience deploying and tracking Swallow floats in the ocean has given us a feel for how much the floats can be expected to move horizontally when they are drifting freely and the kind of vertical motion amplitudes and frequencies which can be expected to occur. We increase the horizontal and vertical excitation (called *process noise*) in two simulations in order to see its effect on filter performance.

Simulated travel time measurements are derived from the float positions by calculating the distance between each pair of floats and dividing by the speed of sound. Of course we must introduce errors into the measurements in order to make the simulation realistic. We add errors (usually called *measurement noise*) to these measurements and delete a few points to simulate data dropouts because they occasionally occur in real travel time measurements. The measurement noise variance in two simulations was varied in order to determine its effect on filter performance. No errors were introduced in the sound speed estimates.

The four float deployment geometries used in the simulations are depicted in Figure 6. Cases 1, 2, 6 and 7 used our normal Swallow float deployment configuration in which we deploy 3 floats to the ocean bottom (2000 meters in this case) and 5 (or more) floats to somewhere in the water column (1000 meters depth in this case). The bottomed floats form a triangular base for locating the freely drifting floats. The mid-water column floats form an approximately planar array which is used to measure ambient ocean noise.

Case 1 establishes the baseline for evaluating how the filters respond to increased noise or special deployment geometries. Both the process and measurement noise are low in Case 1. Cases 2, 6, and 7 test the filters' performance when the process and measurement noise are increased. The process noise is raised by a factor of 100 in Cases 6 and 7. The measurement noise is raised by a factor of 2 in Cases 2 and 6.

Case 3 tests the filters' performance when the mid-water column floats drift out of the net formed by the bottomed floats. The bottomed floats are the same as in Case 1, but the planar array has been moved considerably outside the triangle formed by the bottomed floats. Low process and measurement noise are used for this simulation.

Case 4 tests the effect of one of the bottomed floats failing. The remaining bottomed floats and planar array are the same as in Case 1, and low process and measurement noise are used.

Case 5 tests our localization capability when the mid-water column floats are deployed in a vertical line array rather than a planar array. This geometry was used during the September 1987 experiment conducted in the Pacific Ocean approximately 260 miles west of Point Conception, California. In this simulation, the three bottomed floats were put at about 4000 meters depth and 5 other floats were spaced between 700 and 2200 meters depth. Low process and measurement noise were used for this simulation.

Table 5.1. Float Location Simulations.

Case	Process Noise	Measurement Noise	Tests the Effect of:
1	low	low	filter performance baseline
2	low	high	increased measurement noise
3	low	low	large array drift
4	low	low	losing a bottomed float
5	low	low	vertical line array
6	high	high	increased process noise
7	high	low	increased process and measurement noise.

The least squares filter requires an initial estimate of the float positions and the Kalman filter requires an initial estimate of the float positions and velocities. We used estimates which were nearly identical to the actual float positions and velocities for our simulations. This was done in order to isolate their response to changes in process noise, measurement noise, or

deployment geometry from problems associated with locking on to the float trajectories. Training the Kalman filter is a separate problem not addressed here.

The results of the simulations are summarized in Table 5.2 and plotted in Figures 7 and 8. Figure 7 compares the results of Cases 1, 2, 6 and 7 and shows the effects of increased process and measurement noise. Figure 8 compares the results of Cases 1, 3, 4 and 5 and shows the effect of different float deployment geometries.

Table 5.2. Summary of Float Location Simulation Results.

Case	Average RMS Error, meters	
	Kalman Filter	Least Squares Filter
1	0.9	1.4
2	1.6	2.9
3	0.7	1.4
4	0.8	1.5
5	1.2	2.3
6	1.7	1.7
7	2.3	2.7

Conclusions

The simulation results lead one to the following conclusions:

- When the process and measurement noise are low, (Case 1), the error in the least squares position estimate is about 50% greater than that in the Kalman filter estimate.
- Increasing the process noise increases the error in the Kalman filter estimate but has no effect on the least squares estimate. As the process noise increases, the Kalman filter estimate error approaches the least squares estimate error. At sufficiently high process noise, the two filters perform comparably.
- When the process noise is low, increasing measurement noise has a stronger negative effect on the least squares estimate error than on the Kalman filter estimate error. This becomes less true as the process noise is increased.
- Moving the mid-water column float array a large distance out of the triangle formed by the bottomed floats does not appreciably affect either filters' performance.
- When the mid-water column array remains within the triangle formed by the bottomed floats, losing one of the bottomed floats does not appreciably affect either filters' performance.
- Deploying the mid-water column floats in a vertical line array increases the error in the Kalman and least square filter estimates by 30 and 50%, respectively. When the

floats are stacked vertically, their interfloat ranges contain little information about horizontal displacements, and the filters are forced to rely exclusively on ranges between the mid-water column and bottomed floats to determine the x and y coordinates of the drifting floats. The Kalman filter fairs somewhat better than the least squares filter because of its ability to track the floats' motion.

6. Summary

We have evaluated a series of programs which process Swallow float travel time measurements to produce float position estimates. Simulations were run to compare the performances of a Kalman filter and a least squares estimator under several deployment geometries and noise conditions. The Kalman filter performed better than the least squares filter under every simulation in which the floats experienced small random accelerations (low process noise). When the floats experience greater accelerations between measurements, the Kalman filter estimate error increases and approaches that of the least squares estimator.

The Kalman filter functions better than the least squares filter in the presence of high measurement noise when the process noise is low. This is because of its ability to track float motion and effectively smooth noisy measurements. When both the process and measurement noise are increased, the Kalman filter estimation error approaches that of the least squares filter.

Both filters were found to be generally insensitive to changes in deployment geometry which might have been expected to increase estimation error. This is in part because our simulation did not include error in the average sound speed estimate, which would magnify errors in long travel times. One geometry, in which the mid-water column floats were reconfigured from a planar array to a vertical line array, did increase the estimation error in both filters, apparently because it reduces information about horizontal float displacements.

Acknowledgments

This work was supported by the Office of Naval Research, Code 220, under contract N00014-82-K-0147. The paper owes much of its clarity to critical readings and excellent suggestions offered by Dr. Richard K. Brienzo of the Marine Physical Laboratory.

References

1. Hodgkiss, W. S. and V. C. Anderson, "Hardware dynamic beamforming," *J. Acoust. Soc. Am.*, vol. 69, pp. 1075-1083, 1981.
2. Hawes, R., W. S. Hodgkiss, V. C. Anderson, J. C. Nickles, and G. L. Edmonds, "Freely Drifting Swallow float Array: Surface Echo Detection and Tracking," Marine Physical Laboratory, Scripps Institution of Oceanography, San Diego, CA, MPL TM-348, 1982.
3. Hodgkiss, W. S. and V. C. Anderson, "Acoustic positioning for an array of freely drifting sensors," *IEEE J. Oceanic Eng.*, vol. OE-8, pp. 116-119, 1983.
4. Culver, R. L., "Infrasonic ambient ocean noise spectra from freely drifting sensors," Scripps Institution of Oceanography, San Diego, CA, SIO Reference 85-22, 1985. Also, Master's thesis, University of California, San Diego, 1988.
5. Culver, R. L., W. S. Hodgkiss, V. C. Anderson, J. C. Nickles, and G. L. Edmonds, "Freely drifting Swallow float array: Initial estimates of interelement range," Marine Physical Laboratory, Scripps Institution of Oceanography, San Diego, CA, MPL TM-380, 1985.
6. Hodgkiss, W. S., V. C. Anderson, G. Edmonds, J. C. Nickles, and R. L. Culver, "A freely drifting infrasonic sensor system," *Fourth Working Symposium on Oceanographic Data Systems*, February 4-6, 1986.
7. Culver, R. L., G. L. Edmonds, W. S. Hodgkiss, V. C. Anderson, and J. C. Nickles, "Freely Drifting Swallow Float Array: September 1985 Trip Report," Marine Physical Laboratory, Scripps Institution of Oceanography, San Diego, CA, MPL TM-383, 1986.
8. Culver, R. L., W. S. Hodgkiss, G. L. Edmonds, and V. C. Anderson, "Freely Drifting Swallow Float Array: September 1986 Trip Report," Marine Physical Laboratory, Scripps Institution of Oceanography, San Diego, CA, MPL TM-391, 1987.
9. Culver, R. L., W. S. Hodgkiss, V. C. Anderson, J. C. Nickles, and G. L. Edmonds, "Removing Resonant Oscillation Signals from Swallow Float Data," Marine Physical Laboratory, Scripps Institution of Oceanography, San Diego, CA, MPL TM-395, 1987.
10. Culver, R. L., W. S. Hodgkiss, V. C. Anderson, and G. L. Edmonds, "Low Frequency Oscillations in 1986 Swallow Float Data," Marine Physical Laboratory, Scripps Institution of Oceanography, San Diego, CA, MPL TM-394, 1988.
11. Culver, R. L., G. L. D'Spain, and William S. Hodgkiss, "Vertical Oscillation in Freely Drifting Swallow Floats," Marine Physical Laboratory, Scripps Institution of Oceanography, San Diego, CA, MPL TM, under preparation.
12. Culver, R. L., G. L. D'Spain, and William S. Hodgkiss, "Estimating Travel Times and Travel Time Errors from Swallow Float Acoustic Range Data," Marine Physical Laboratory, Scripps Institution of Oceanography, San Diego, CA, MPL TM, under preparation.
13. Sorenson, H. W., *Parameter Estimation*. New York: Marcel Dekker, 1980.
14. Lawson, C. L. and R. J. Hanson, *Solving Least Squares Problems*. Englewood Cliffs, New Jersey: Prentice-Hall, 1974.
15. Kalman, R. E., "New results in linear filtering and prediction theory," *J. Basic Eng.*, vol. 83D, 1960.

16. Meditch, J. S., *Stochastic Optimal Linear Estimation and Control*. New York: McGraw-Hill, 1969.
17. Sorenson, H. W., "Kalman filtering techniques," in *Advances in Control Systems*, C. T. Leondes, Ed. New York: Academic Press, 1966.
18. Anderson, B. D. O. and John B. Moore, *Optimal Filtering*. Englewood Cliffs, New Jersey: Prentice-Hall, 1979.
19. Jazwinsky, A. H., *Stochastic Processes and Filtering Theory*. New York: Academic Press, 1970.
20. Hodgkiss, W. S., "Kalman Filters, Phase Locked Loops, and Optimal (MAP) Demodulation," Naval Undersea Center (NUC), San Diego, Ca., NUC Technical Note 1772, 1977.

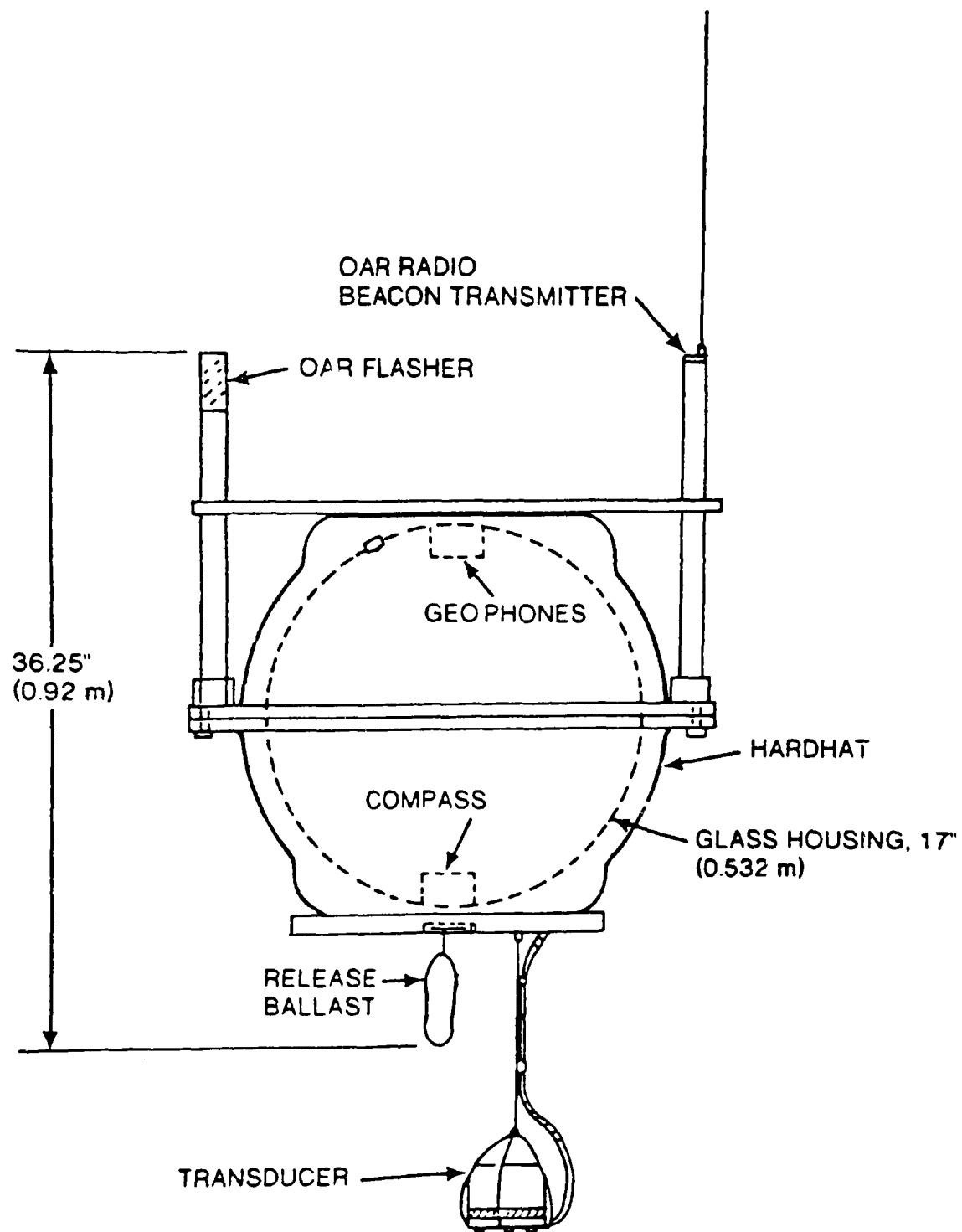


Figure 1

Float 4, 86 deployment: range from float 5

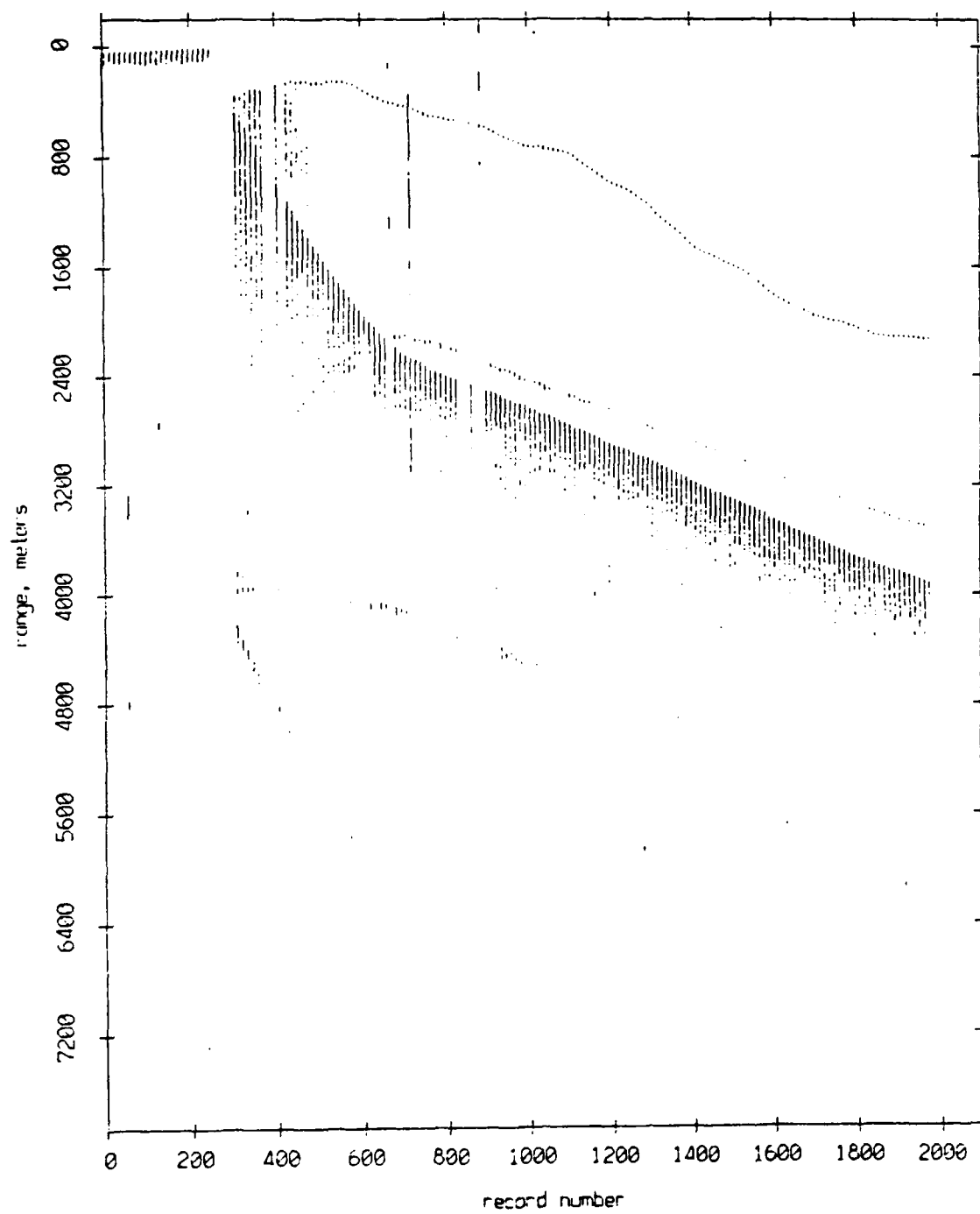


Figure 2

Floot 4, 86 deployment: range to floot 3

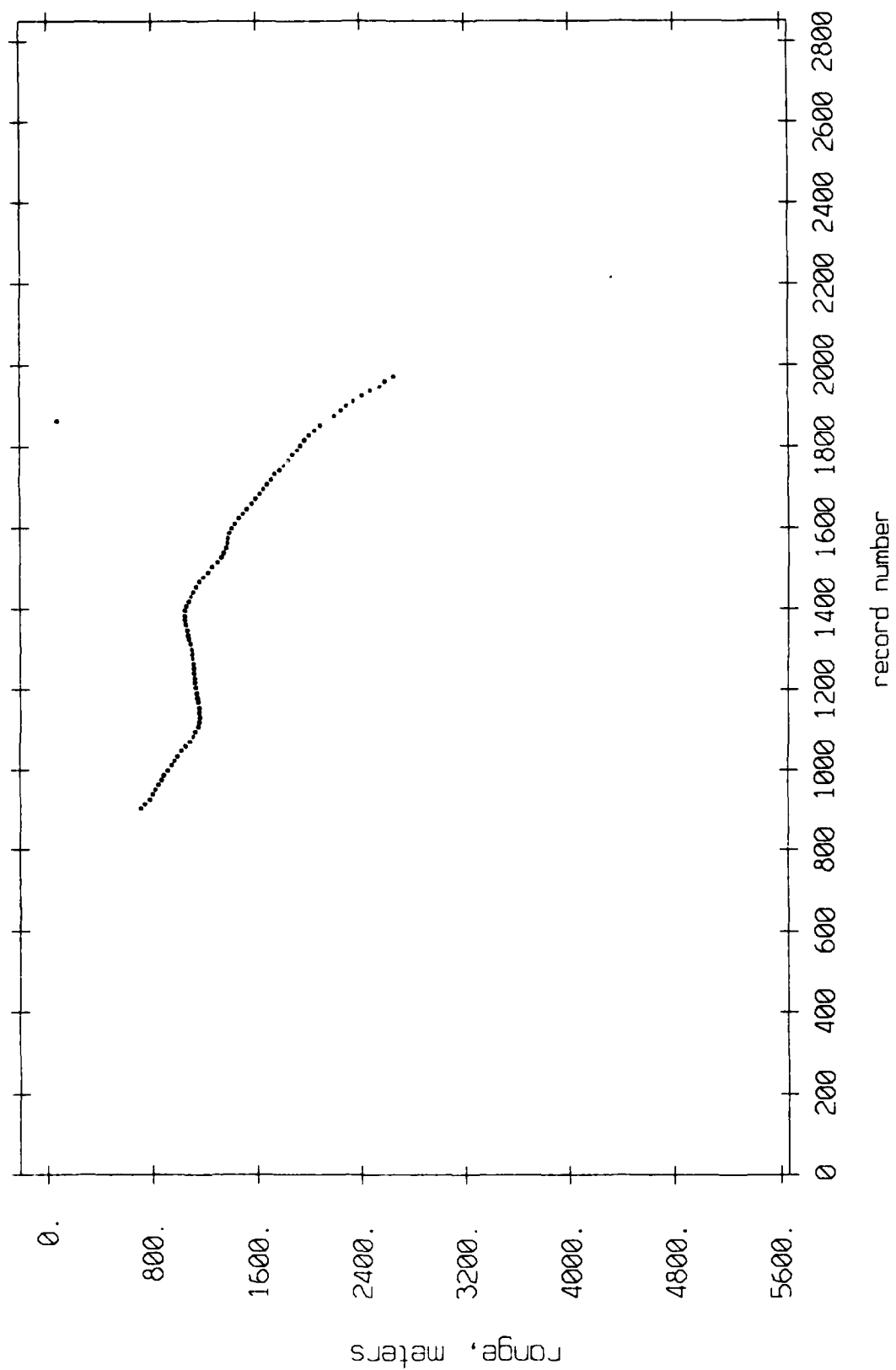


Figure 3

Figure 4. Processing Swallow float travel time measurements to estimate float positions.

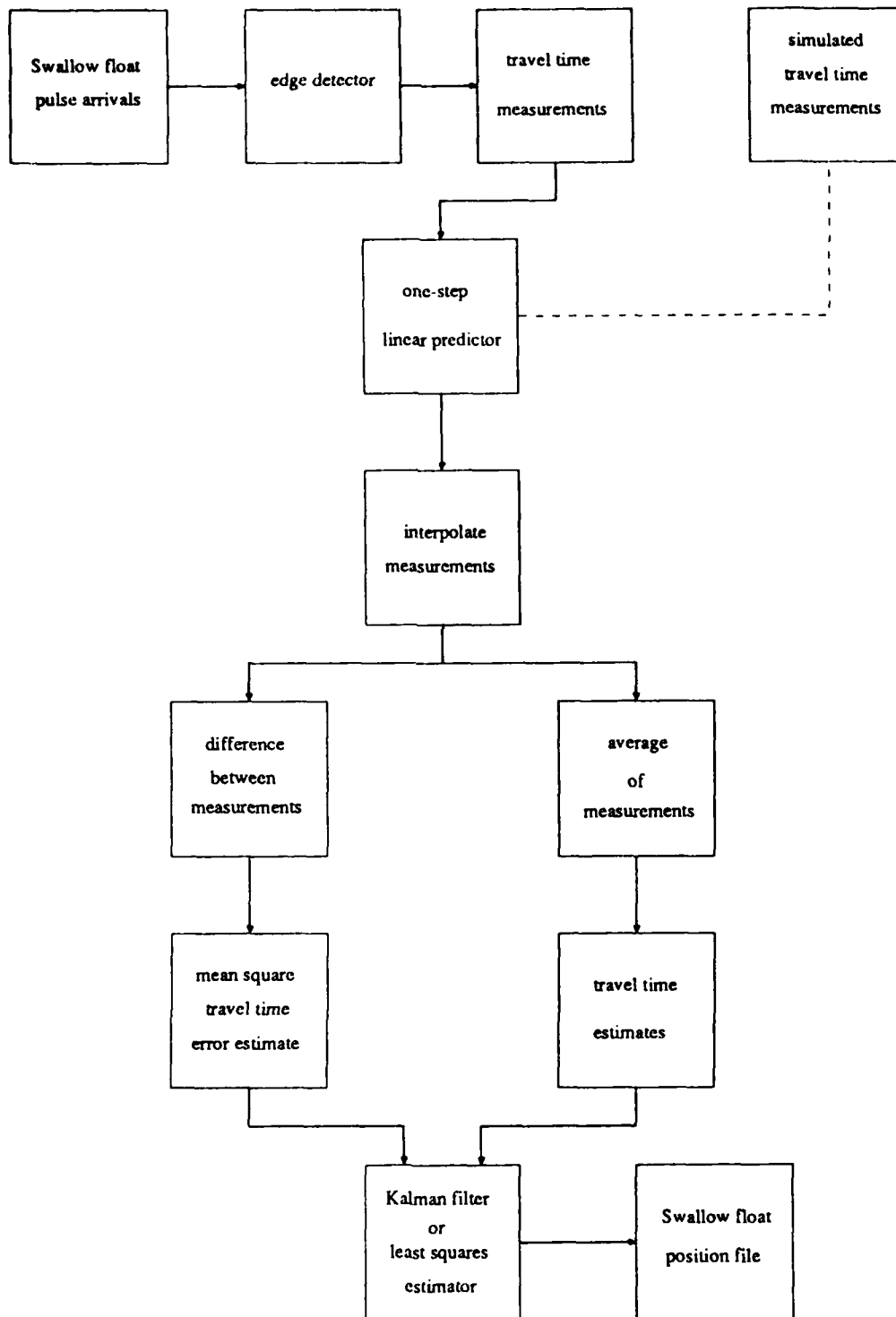


Figure 5. Simulating Swallow float travel time measurements.

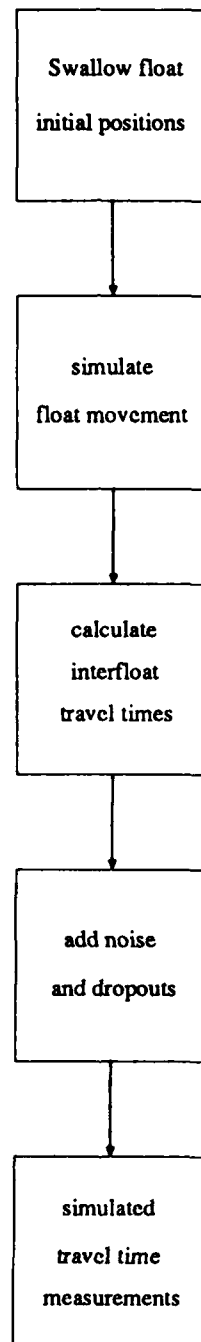


Figure 6. Swallow float localization simulations.

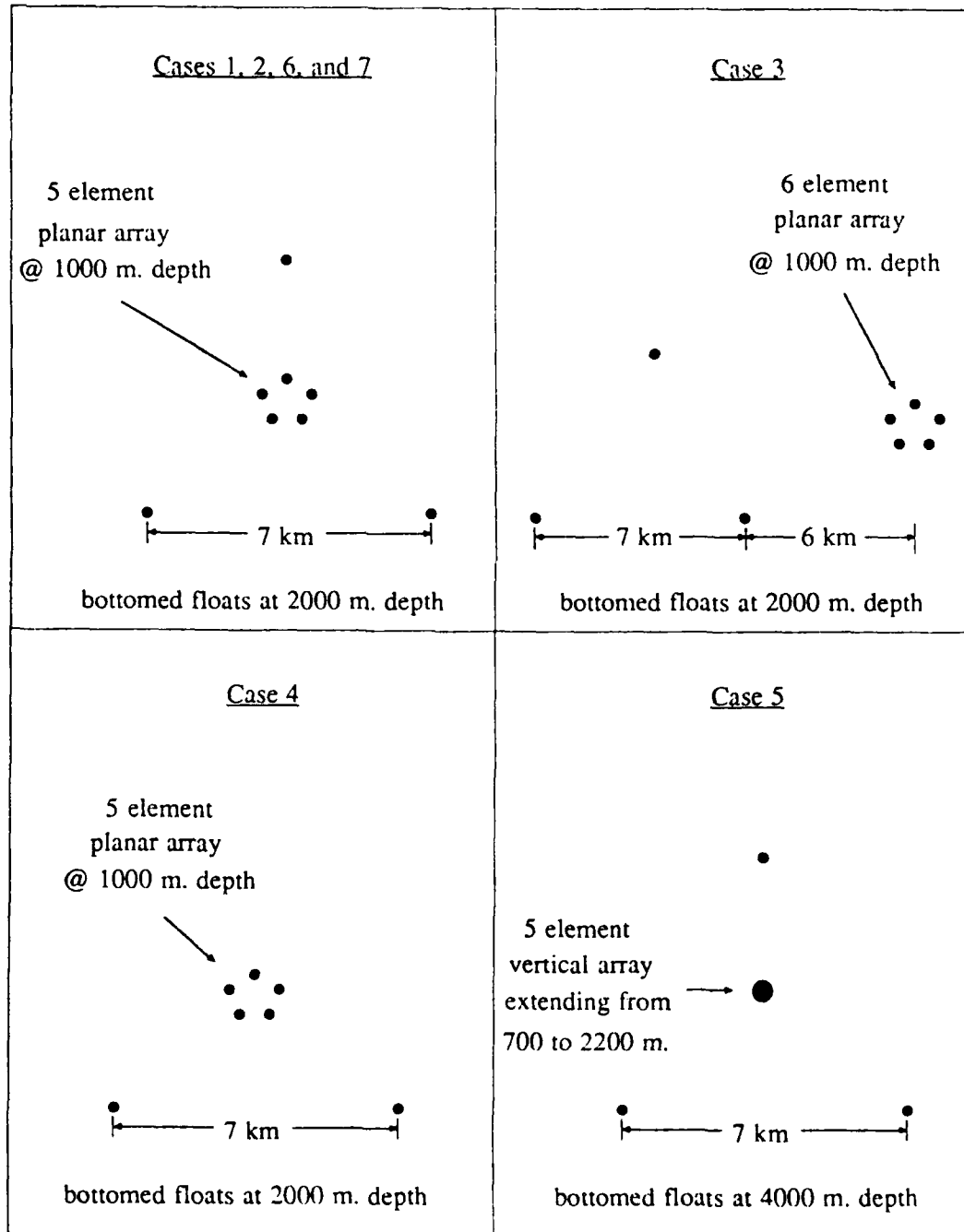


Figure 7. Effect of Process and Measurement Noise on Filter Performance

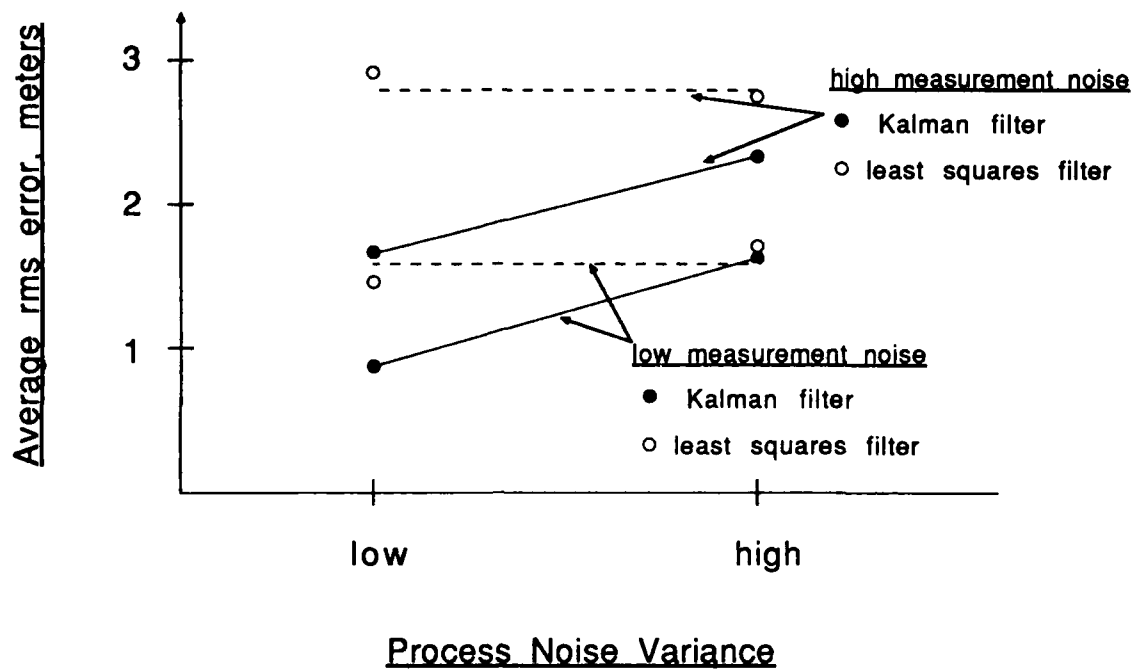
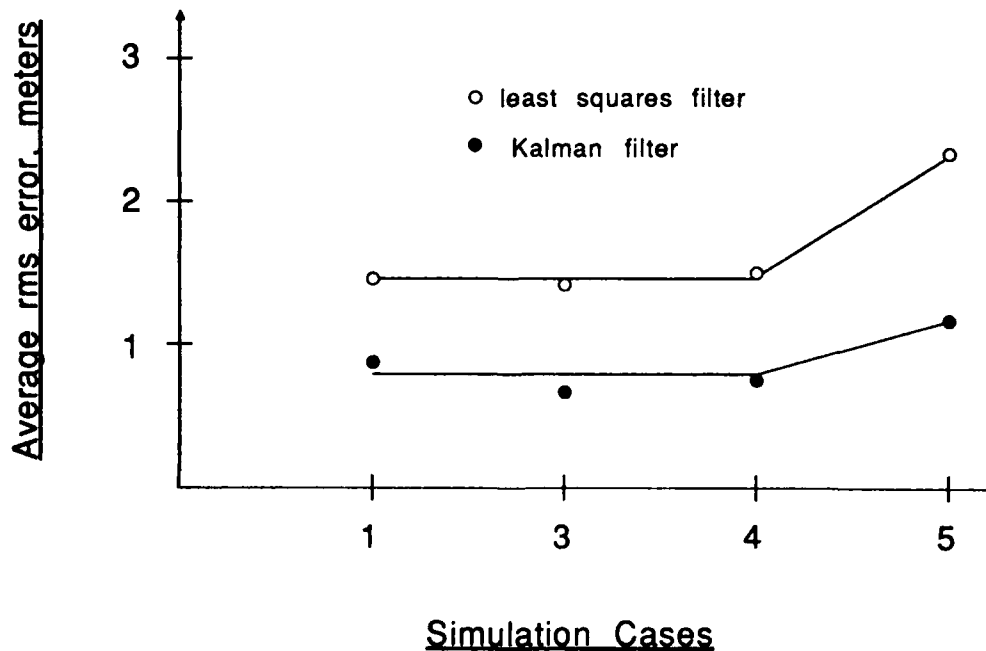


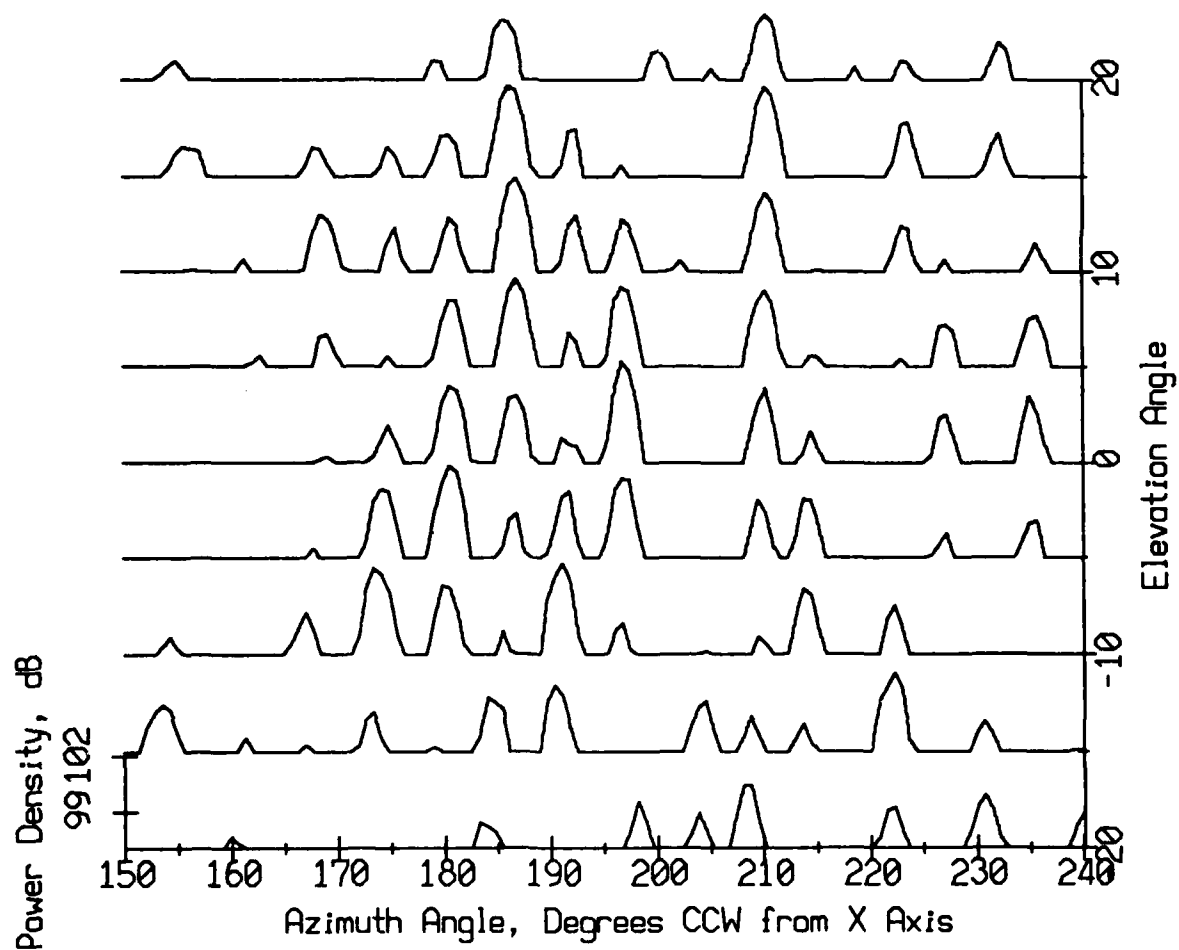
Figure 8. Effect of Deployment Geometry on Filter Performance



APPENDIX D

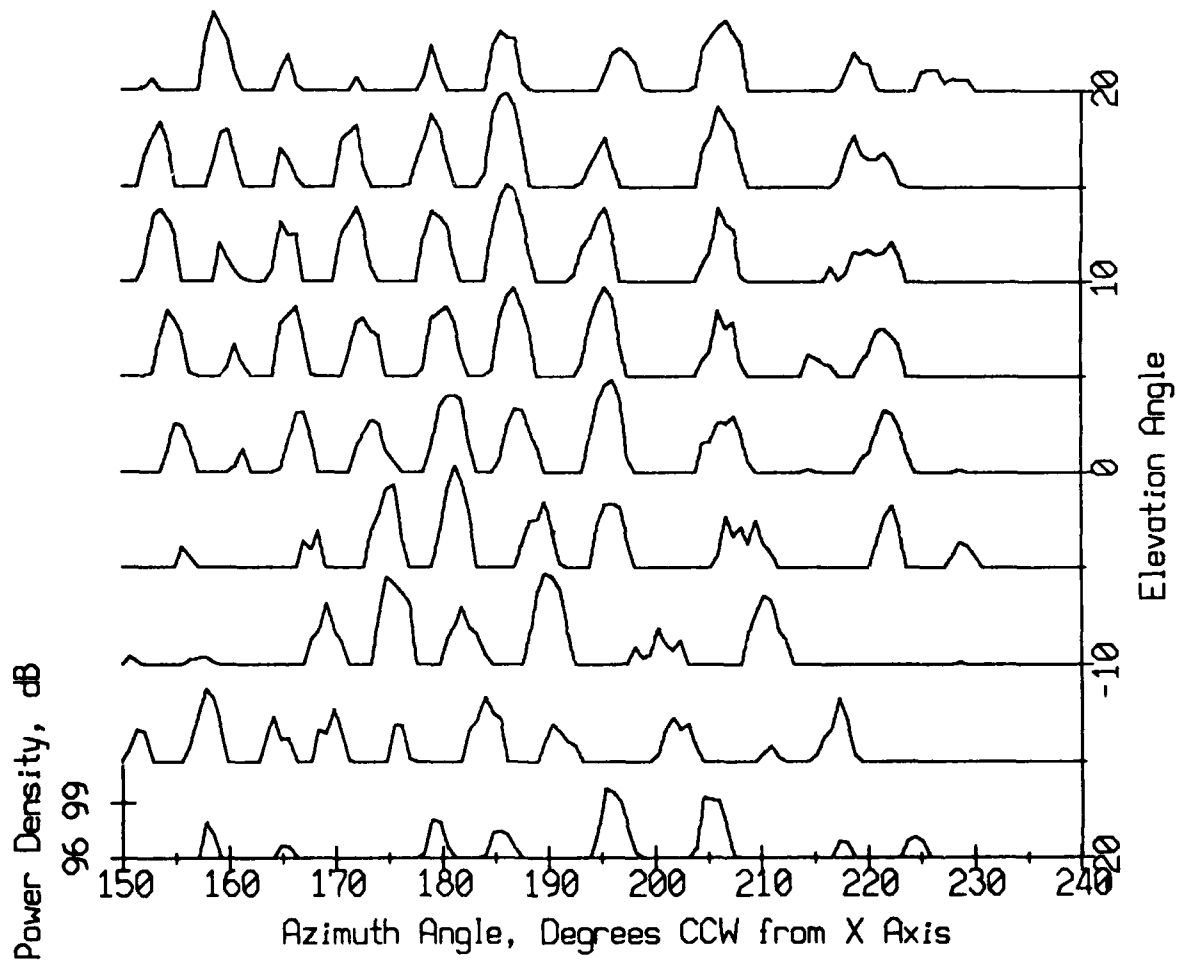
Three-Dimensional Beamforming Results

Beamformer Output vs. Look Direction Angles
Record 1802, 9 Hz.

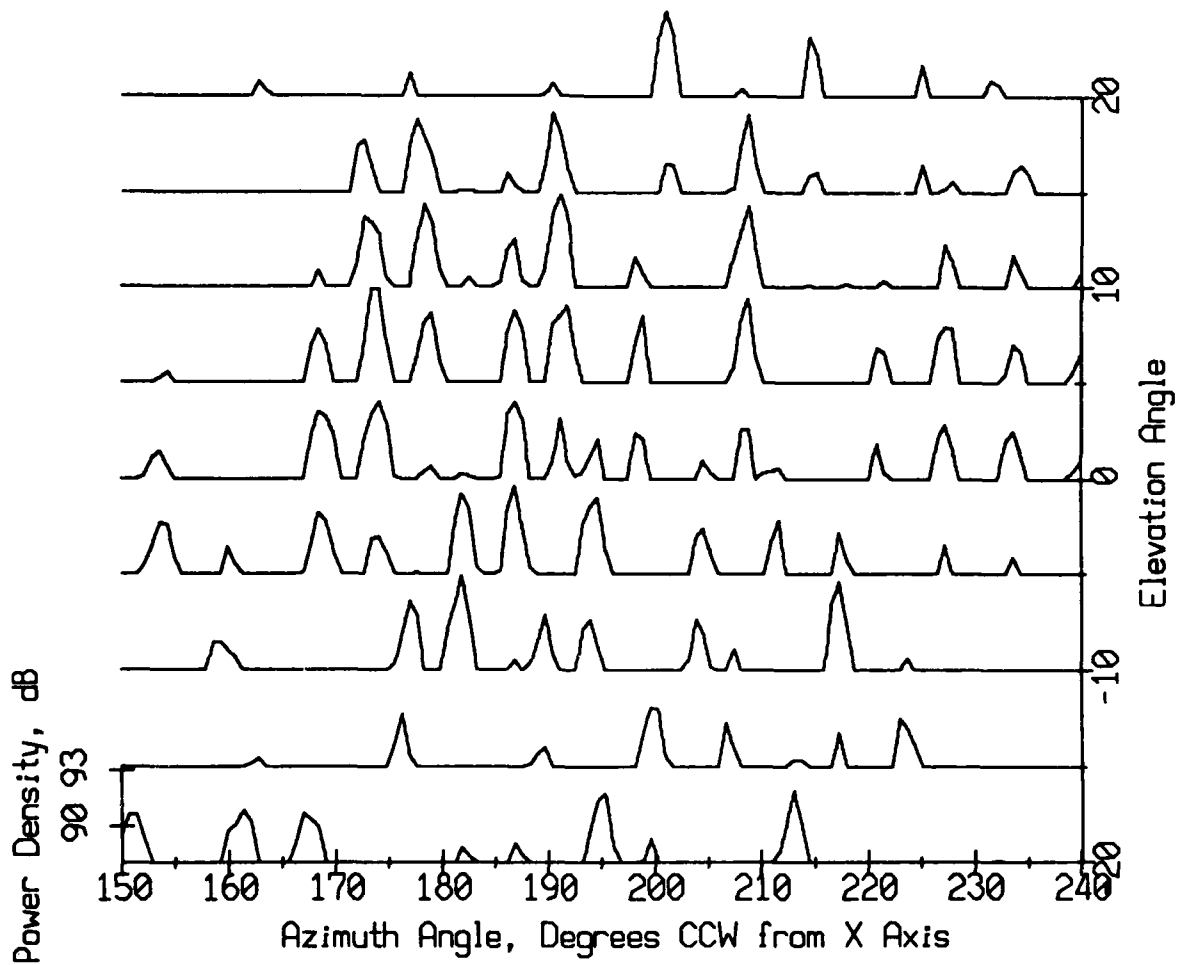


Beamformer Output vs. Look Direction Angles

Record 1802, 10.3 Hz.

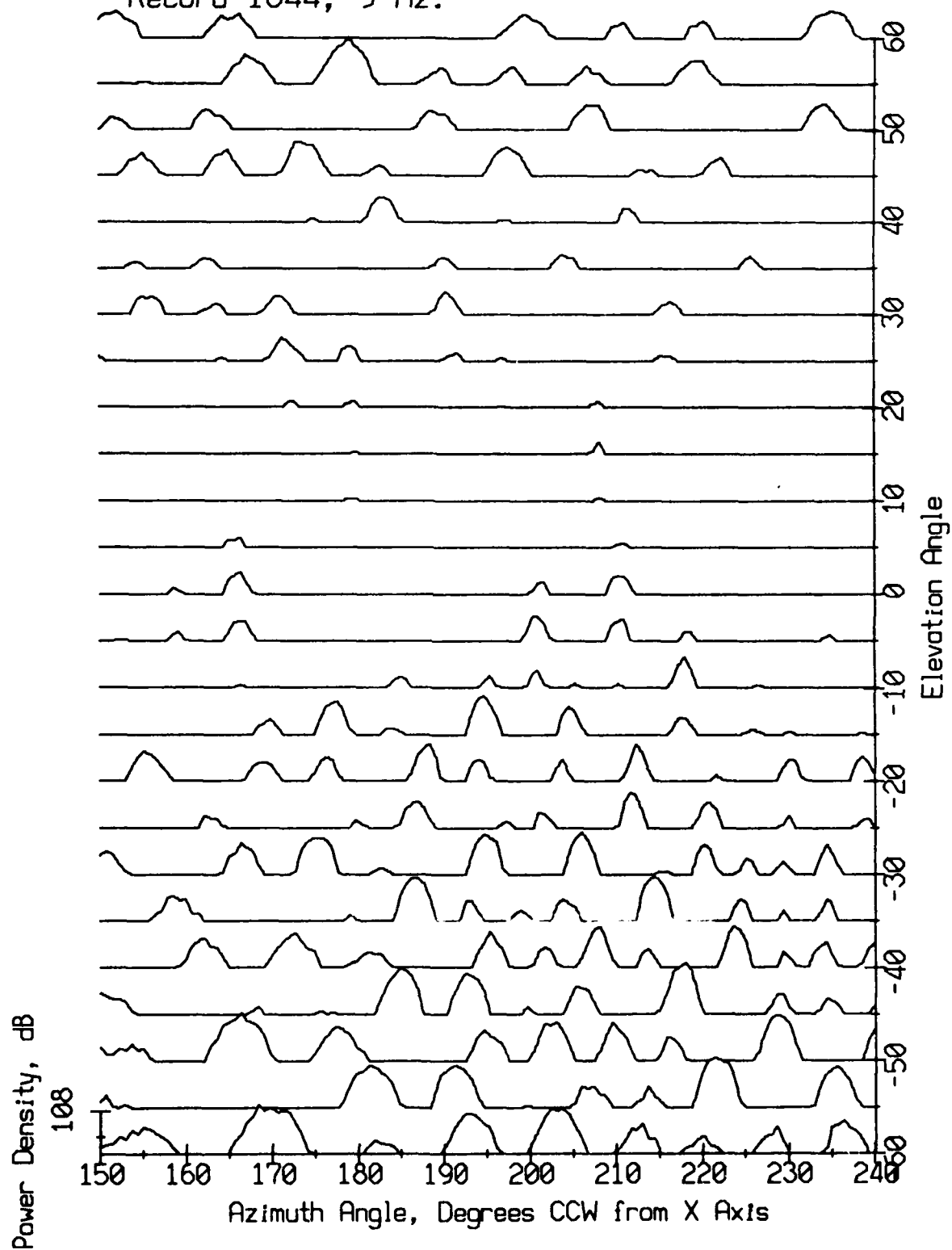


Beamformer Output vs. Look Direction Angles
Record 1802, 12.2 Hz.

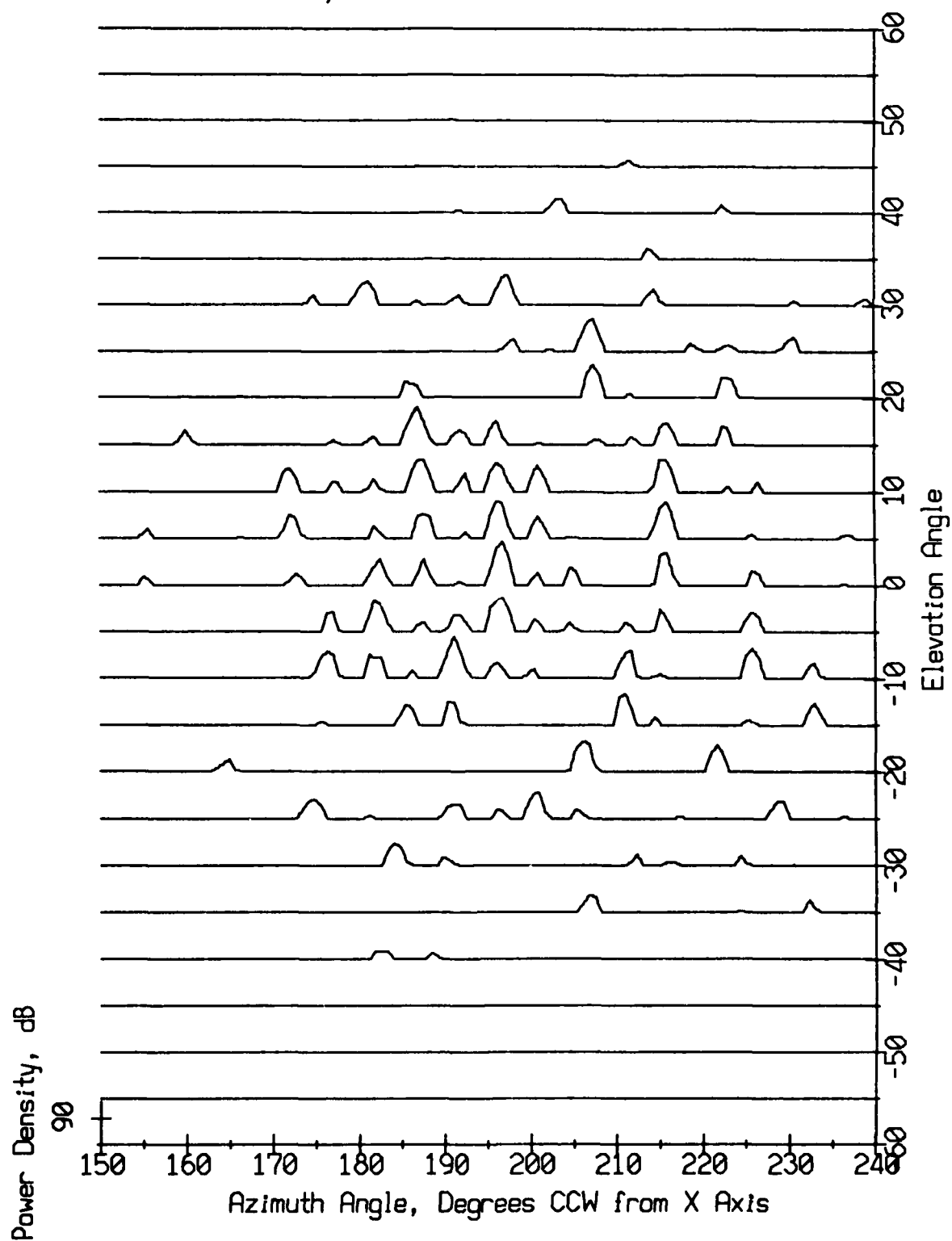


Beamformer Output vs. Look Direction Angles

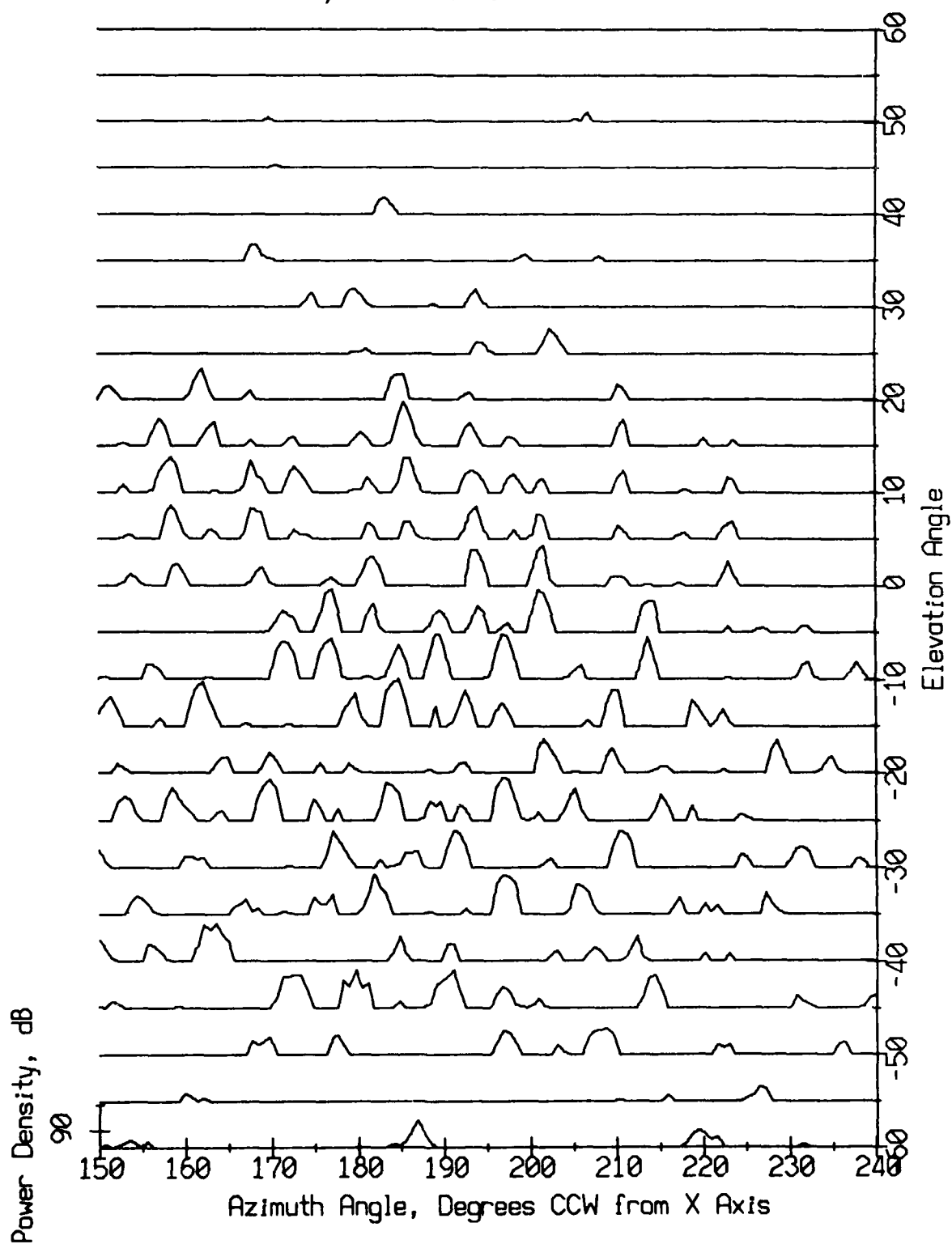
Record 1844, 9 Hz.



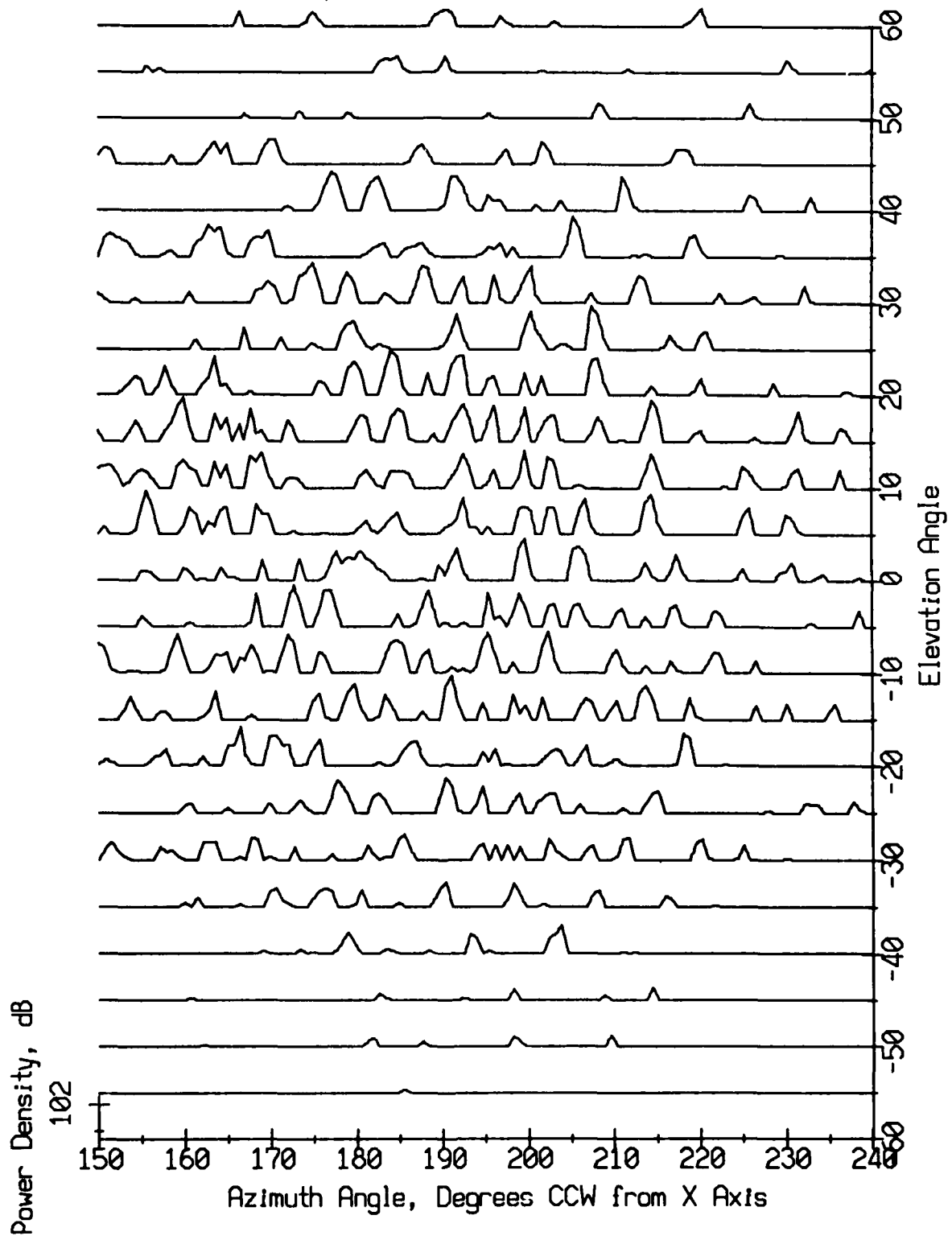
Beamformer Output vs. Look Direction Angles
Record 1844, 10.3 Hz.



Beamformer Output vs. Look Direction Angles
Record 1844, 12.2 Hz.



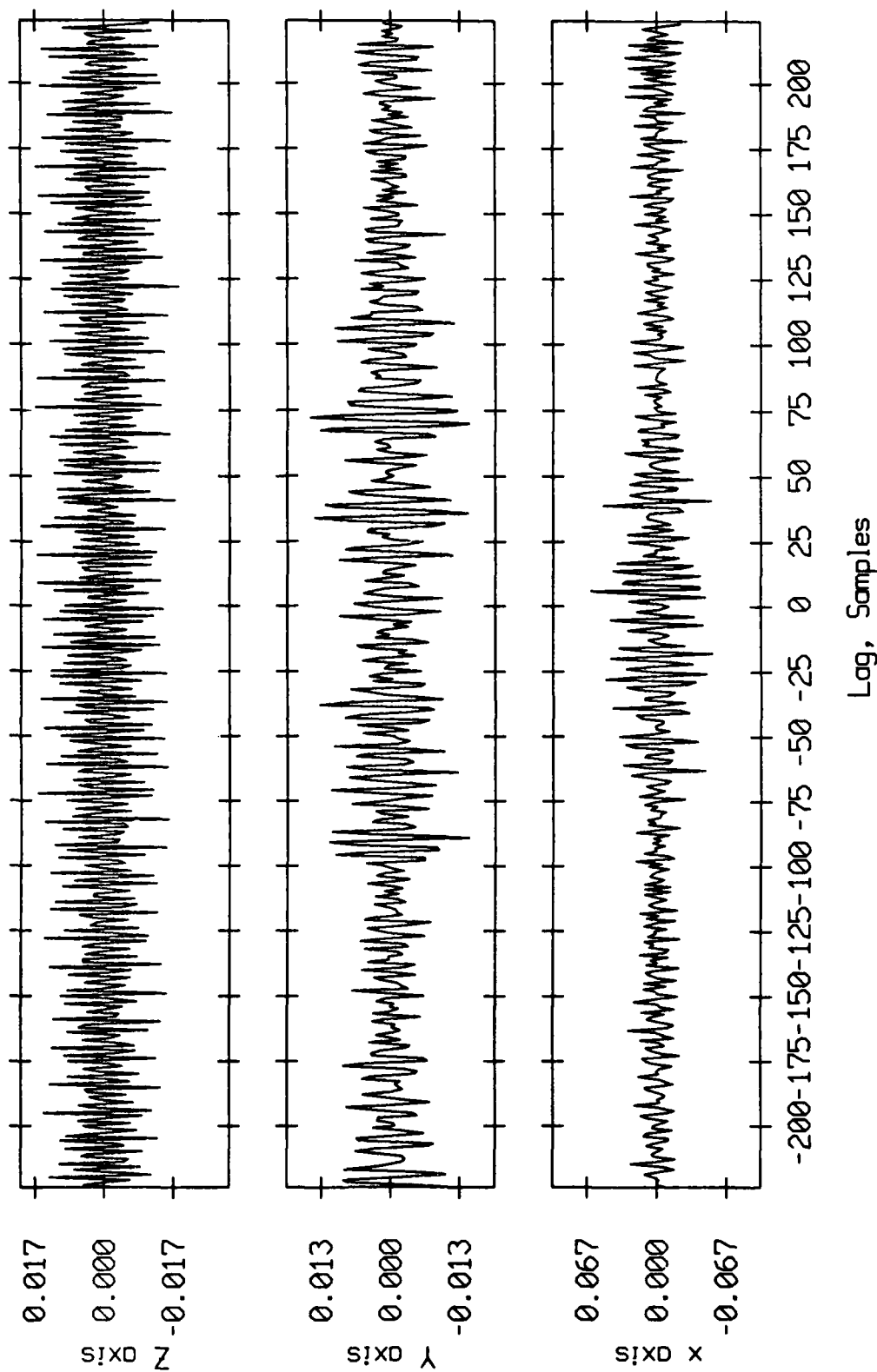
Beamformer Output vs. Look Direction Angles
Record 1844, 13.5 Hz.



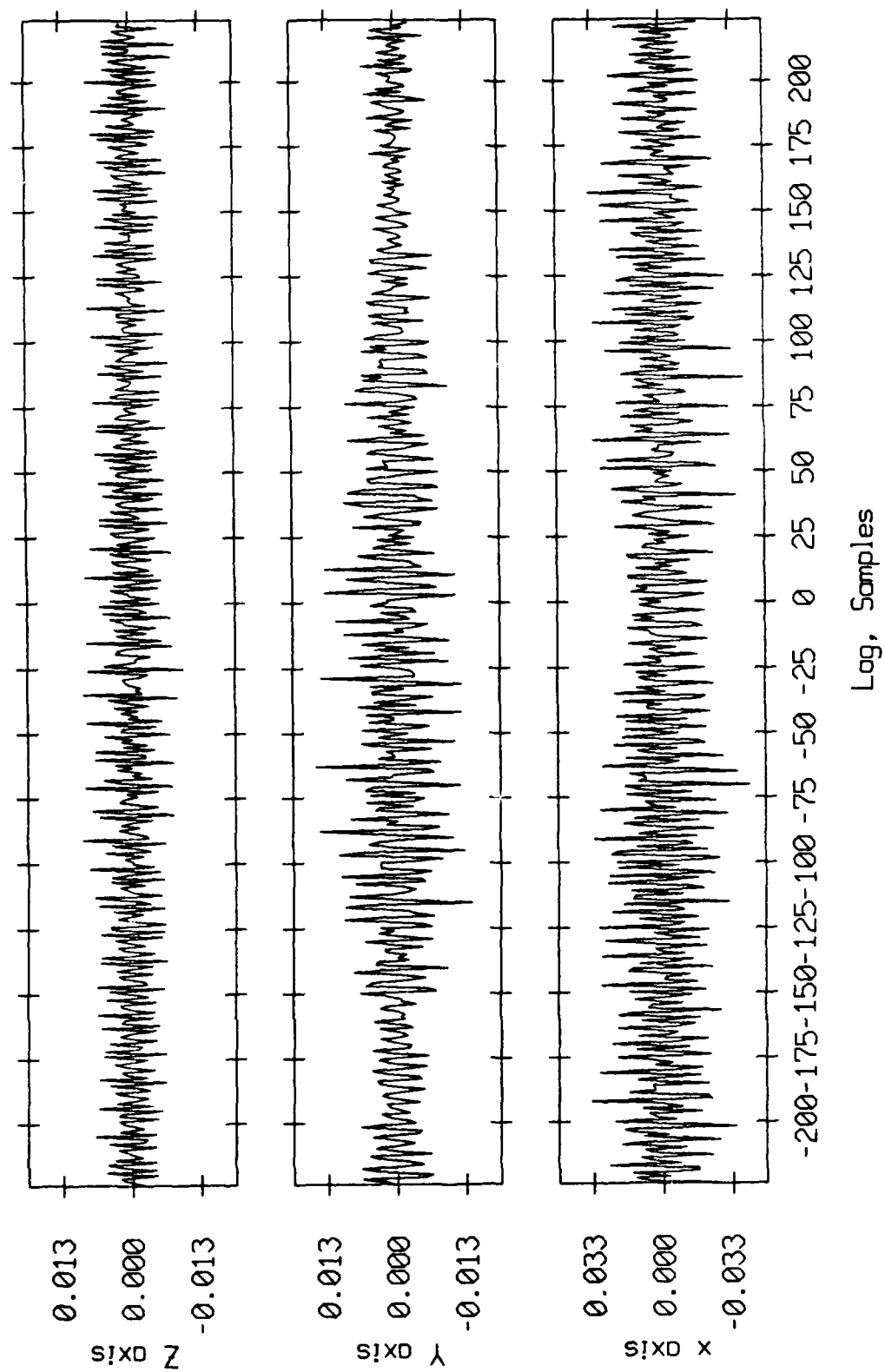
APPENDIX E

Geophone Cross-Correlation

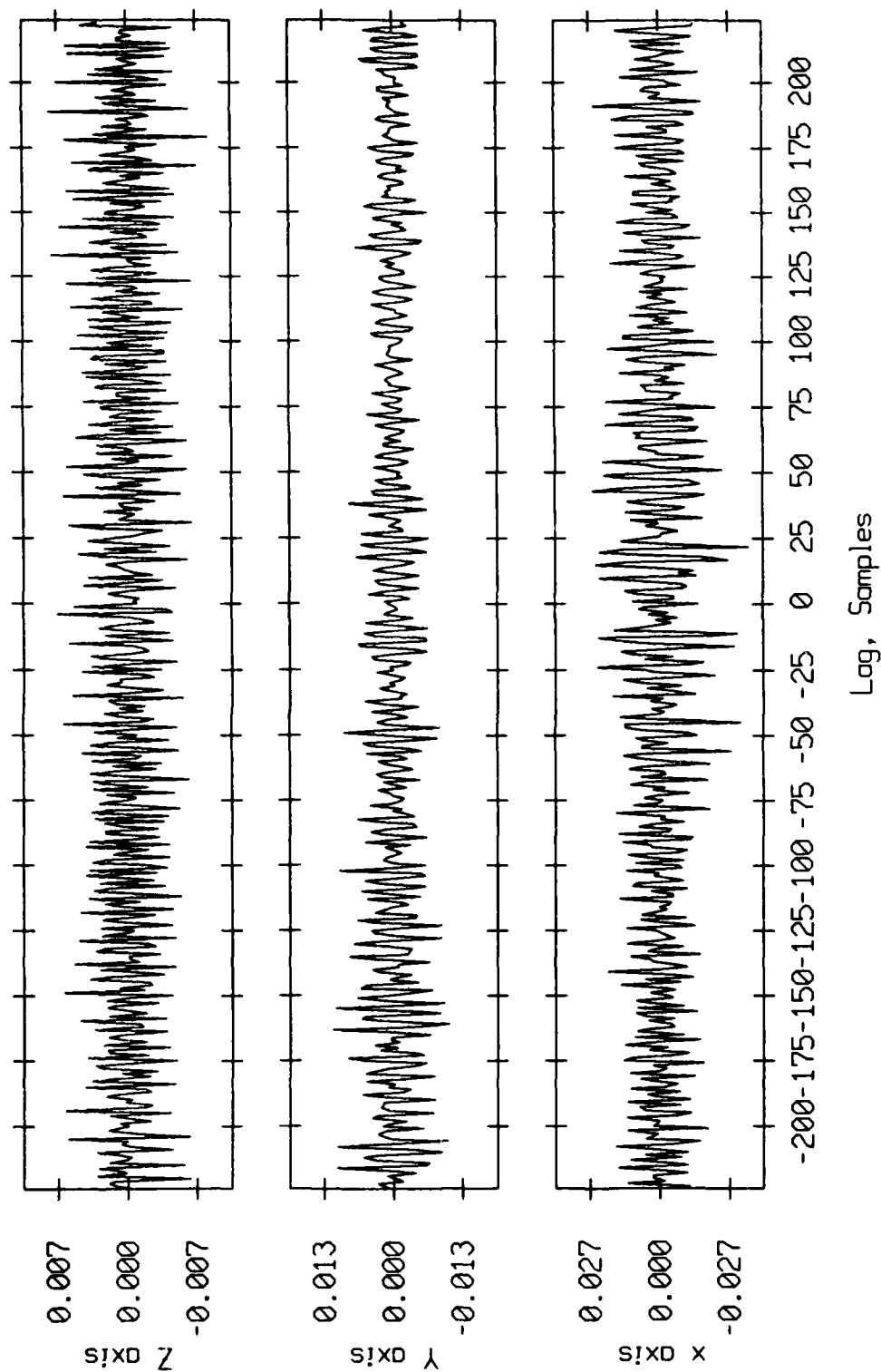
Cross-Correlation of 9, 10.3, 12.2, 13.5, 18, & 22.5 Hz, Record 1820
Channel Impulse Response, Floats 35, 24 Bin Mask



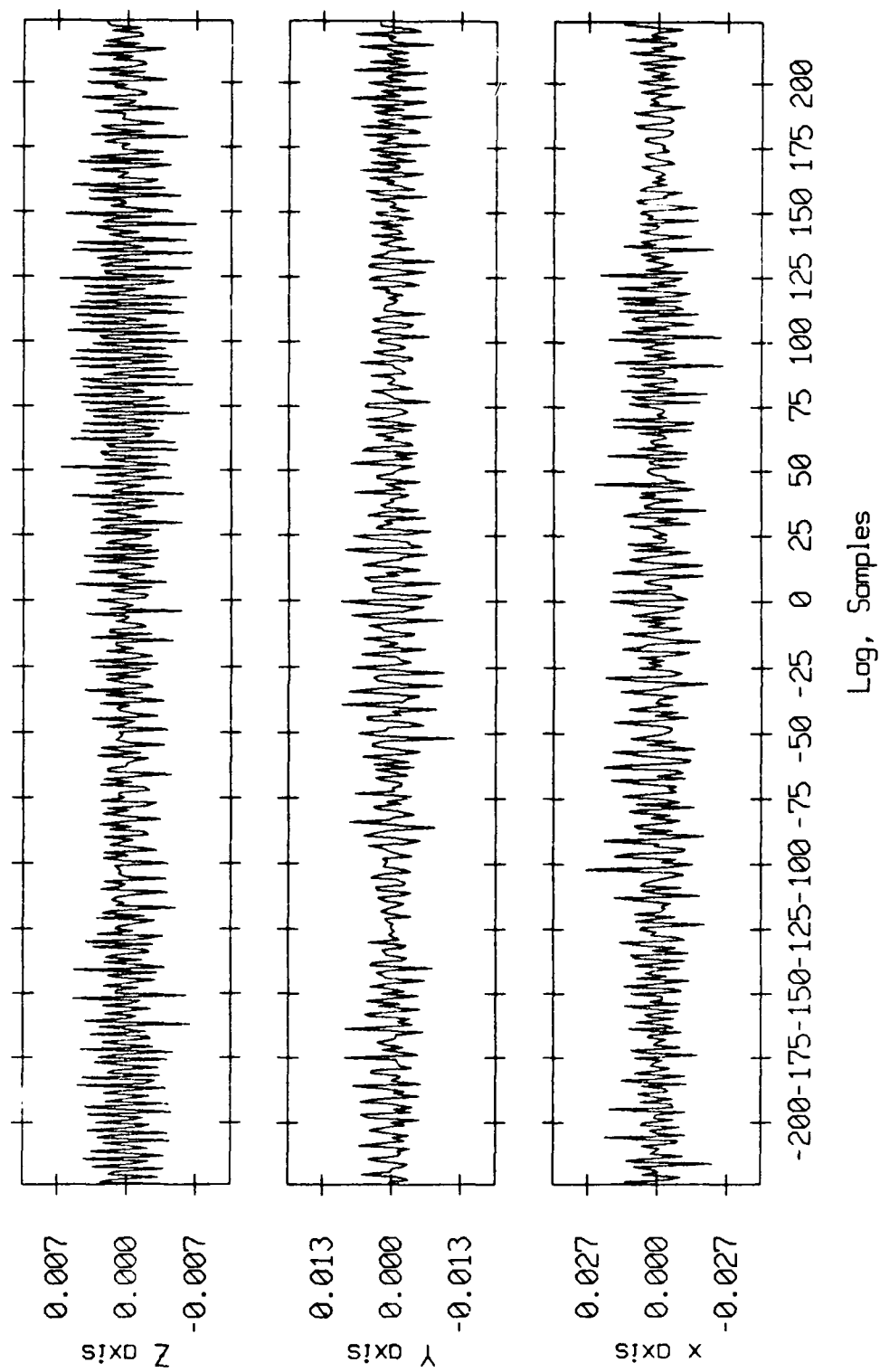
Cross-Correlation of 9, 10.3, 12.2, 13.5, 18, & 22.5 Hz, Record 1820
Channel Impulse Response, Floats 39, 24 Bin Mask



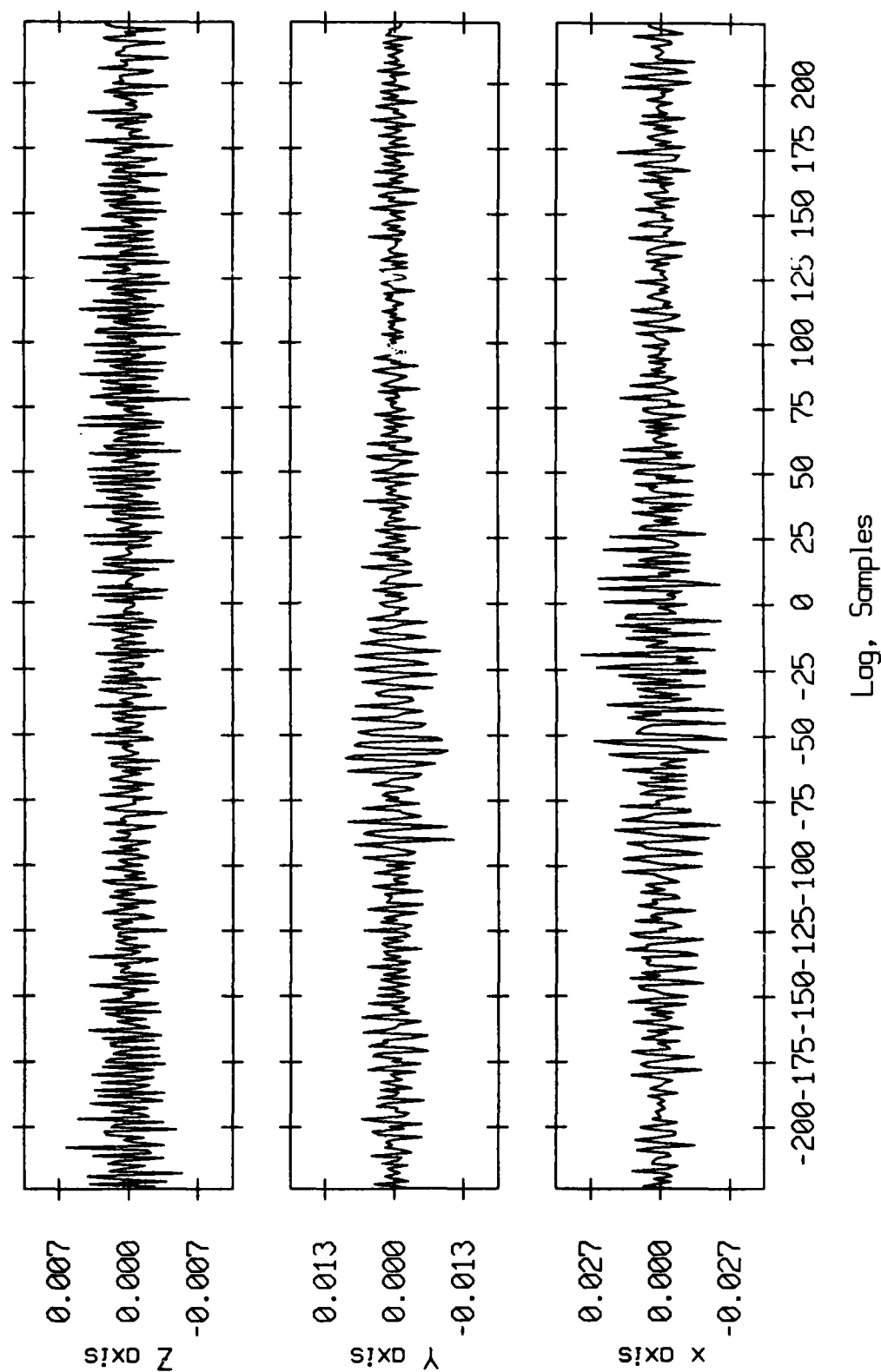
Cross-Correlation of 9, 10.3, 12.2, 13.5, 18, & 22.5 Hz, Record 1820
Channel Impulse Response, Floats 3a, 24 Bin Mask



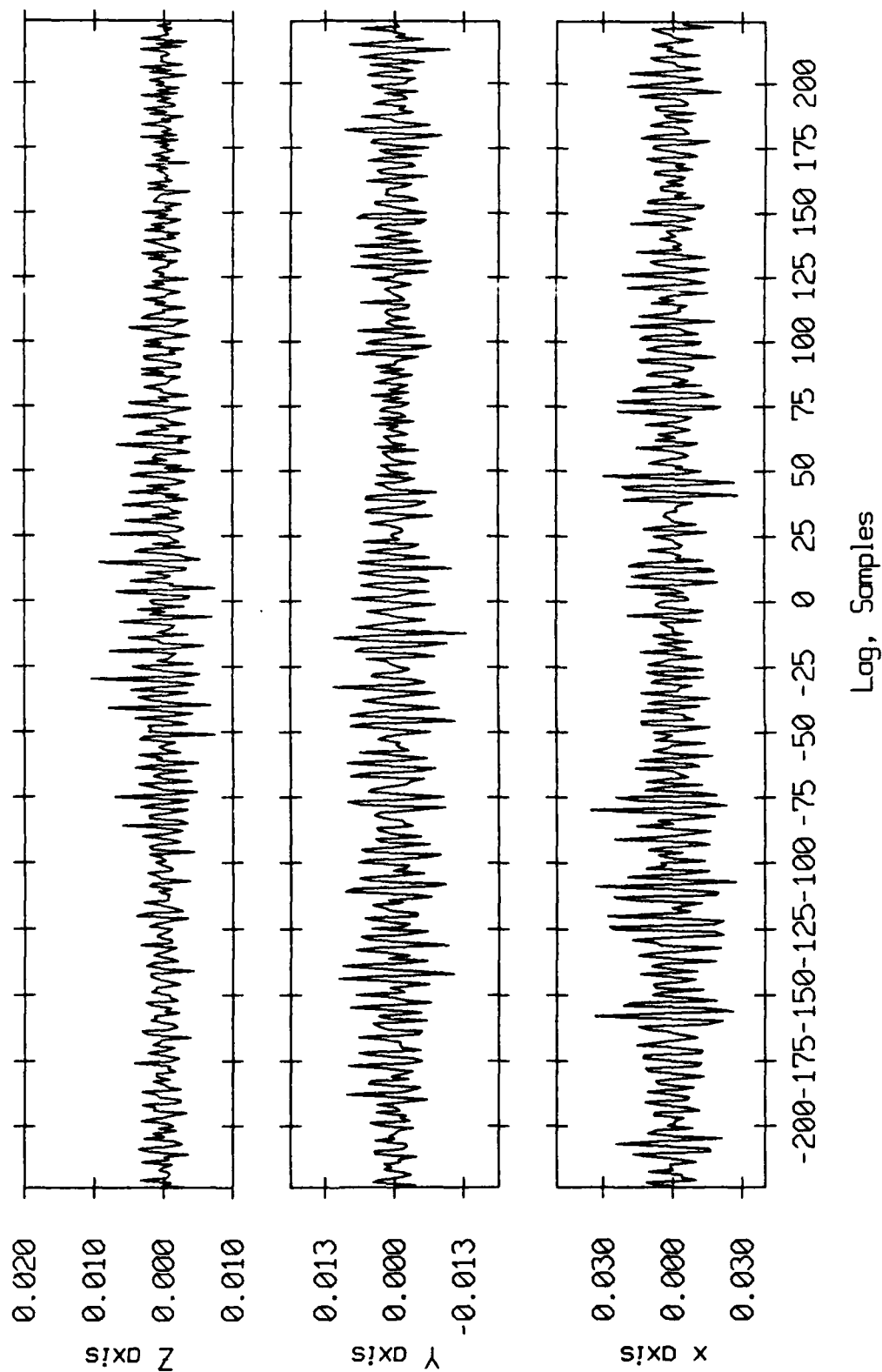
Cross-Correlation of 9, 10.3, 12.2, 13.5, 18, & 22.5 Hz, Record 1820
Channel Impulse Response, Floats 59, 24 Bin Mask



Cross-Correlation of 9, 10.3, 12.2, 13.5, 18, & 22.5 Hz, Record 1820
Channel Impulse Response, Floats 5a, 24 Bin Mask



Cross-Correlation of 9, 10.3, 12.2, 13.5, 18, & 22.5 Hz, Record 1820
Channel Impulse Response, Floats 9a, 24 Bin Mask



ONR/MPL GENERAL DISTRIBUTION LIST

Chief of Naval Research
Department of the Navy
Arlington, Virginia 22217-6000
Code 12, 122(2), 102C
111, 112, 113,
1122PO, 425-AC, 480

ONRDET
NSTL Station
Bay St. Louis, Mississippi 38629-6004
Code 112, 1121, 1122CS, 422CB,
1122PO, 112GG

Director
Office of Naval Research
Branch Office
1030 East Green Street
Pasadena, California 91106-2485

Commander
Naval Sea Systems Command
Washington, D. C. 20382
Code 63, 63R, 63R-23

Commanding Officer
Naval Ocean Research and
Development Activity
NSTL Station
Bay, St. Louis, Mississippi 38629-6004
Code 100, 110, 300, 330,
340, 360, 380, 600

Commander
U.S. Naval Oceanographic Office
NSTL Station
Bay St. Louis, Mississippi 38622-6004
Atten: Bill Jobst

Assistant Secretary of the Navy
(Research Engineering & Systems)
Department of the Navy
Washington, D. C. 20350

Defense Advanced Res. Proj. Agency
TTO - Tactical Technology Office
1400 Wilson Boulevard
Arlington, Virginia 22209-2308
Atten: Capt. Kirk Evans

National Oceanic & Atmospheric
Administration
Ocean Engineering Office
6001 Executive Boulevard
Rockville, Maryland 20852

Commander
Space and Naval Warfare
Systems Command
Washington, D. C. 20380
Code PDW-124, 320A

Commander
Naval Ship Res. & Dev. Center
Bethesda, Maryland 20884

Executive Secretary
Naval Studies Board
National Academy of Sciences
2101 Constitution Avenue, N.W.
Washington, D.C. 20418

Director
Strategic Systems Proj. Ofc. (PM-1)
Department of the Navy
Washington, D. C. 20381
Code NSP-2023

Commander
Naval Ocean Systems Center
San Diego, California 92152
Code 00, 01, 16, 94, 531
5301, 71, 72

Commander
Submarine Development Group ONE
Fleet Post Office
San Diego, California 92152

Commanding Officer
Civil Engineering Laboratory
Naval Construction Battalion Center
Port Hueneme, California 93043
Code L40, L42

Commanding Officer
Naval Underwater Systems Center
Newport, Rhode Island 02844
Atten: Dr. K. A. Kemp, Code 8213

Officer in Charge
Naval Underwater Systems Center
New London Laboratory
New London, Connecticut 06320
Code 900, 906, 910, 930, 960

Director of Research
U.S. Naval Research Laboratory
Washington, D. C. 20375
Code 2920, 2927, 5000, 5100, 5800

Commander
Naval Surface Combat Systems Center
White Oak
Silver Spring, Maryland 20910

Commanding Officer
Naval Coastal Systems Laboratory
Panama City, Florida 32401

STOIC
Battelle Columbus Laboratories
505 King Avenue
Columbus, Ohio 43201

Commander
Naval Air Systems Command
Washington, D. C. 20361
Code 370

Commanding Officer
U.S. Naval Air Development Center
Attention: Jim Howard
Warminster, Pennsylvania 18974

Director
Defense Documentation Center
(TIMA), Cameron Station
5010 Duke Street
Alexandria, Virginia 22314

Institute for Defense Analyses
1801 North Beaupard Street
Arlington, Virginia 22311

Superintendent
U.S. Naval Postgraduate School
Monterey, California 93940

Chief Scientist
Navy Underwater Sound Reference Div.
U.S. Naval Research Laboratory
P.O. Box 6337
Orlando, Florida 32808

Supreme Allied Commander
U.S. Atlantic Fleet
ASW Research Center. APO
New York, New York 09018
Via: ONR 100 M, CNO OP092D1,
Secretariat of Military,
Information Control, Committee

Director
Institute of Marine Science
University of Alaska
Fairbanks, Alaska 99701

Director
Applied Physics Laboratory
Johns Hopkins University
Johns Hopkins Road
Laurel, Maryland 20810
Atten: J. R. Austin

Director
College of Engineering
Department of Ocean Engineering
Florida Atlantic University
Boca Raton, Florida 33431

Director
Marine Research Laboratories
c/o Marine Studies Center
University of Wisconsin
Madison, Wisconsin 53706

Director
Applied Research Laboratory
Pennsylvania State University
P.O. Box 30
State College, Pennsylvania 16802

Director
Applied Physics Laboratory
University of Washington
1013 East 40th Street
Seattle, Washington 98106

Director
The Univ. of Texas at Austin
Applied Research Laboratory
P.O. Box 8029
Austin, Texas 78712

Director
Lamont-Doherty Geological Observatory
Torrey Cliff
Palisades, New York 10964

Director
Woods Hole Oceanographic Institution
Woods Hole, Massachusetts 02543

Director
Inst. of Ocean Science Engineering
Catholic University of America
Washington, D.C. 20017

National Science Foundation
Washington, D. C. 20560

Office of Naval Research
Resident Representative
c/o Univ. of California, San Diego
Mail Code Q023
La Jolla, California 92093

University of California, San Diego
Marine Physical Laboratory
Branch Office
La Jolla, California 92093